Green Carbon Quantum Dots Based Electrochemical Sensors for Analysis of Neurotransmitters

Saheed Eluwale Elugoke

orcid.org/0000-0002-1770-0340

Thesis submitted in fulfilment of the requirements for the degree *Doctor of Philosophy in Chemistry* at the North-West University

Promoter: Prof. E.E. Ebenso
Co-promoter: Prof. O.E. Fayemi
Assistant Promoter: Dr. A.S. Adekunle

Graduation ceremony: November 2022
Student number: 33654735

DECLARATION

I, the undersigned, hereby declare that the dissertation which is hereby submitted to the Department of Chemistry, Faculty of Natural and Agricultural Sciences, North-West University, is my work with the exception of the citations and that the work has not been submitted by me for a degree at any other University.

Student: Saheed Eluwale Elugoke

Signature: ……………………...

Date: 07/10/2022 …………………………..

Promoter: Prof. E.E Ebenso

Signature: ……………………..

Date: …………………………..

Co-promoter: Prof. O.E Fayemi

Signature: ……………………..

Date: …………………………..

Assistant promoter: Dr. A.S Adekunle

Signature: ……………………..

Date: …………………………..

DEDICATION

This thesis is dedicated to God, the creator of the heaven, the earth, the living, and the dead, for the gift of life.

ACKNOWLEDGEMENTS

My sincere gratitude goes to my promoter, Prof. Eno E. Ebenso, for his support, encouragement, and mentorship. His timely response to questions and advice on academic subjects are highly appreciated. I am also grateful to my co-promoter and assistant promoter, Prof. O.E. Fayemi and Dr. A.S. Adekunle, for their support, patience, and encouragement throughout the program.

I would like to thank the Department of Chemistry, Faculty of Natural and Agricultural Sciences, North-West University, for the opportunity to study and the facilities made available for the execution of the thesis.

Special thanks to the technical staff of the Department of Chemistry, Faculty of Natural and Agricultural Sciences, North-West University. In particular, I wish to appreciate the efforts of Mr. Sizwe, Mr. Peter, Mr. Michael, and Miss Murendeni for making available the materials and the manpower required for the synthesis and characterization of the nanomaterials used for the study.

My profound gratitude goes to my precious Dad (Mr. F.B Elugoke), my wonderful aunt (Mrs. Selimat Musa), my brother (Mr. Azeez E. Elugoke), my extraordinary mother (Mrs. R. Oshodi), a great father figure (Mr. G. Oshodi) and my friend (Mr. Taofeek Muhammed) for the unwavering support. Thank you all for always being there.

Special thanks to my wife and best friend, Mrs. T.F Elugoke, for the encouragement, support, care and for always being there. You are simply priceless.

I sincerely thank my friends and colleagues at the North-West University: Dr. T.W. Quadri, Dr. E. Chima, Dr. Gloria Uwaya, Mr. Sheriff Balogun, Mrs. Funmilola Adesanya, Mr. Monsuru Shobande, Mr. N. Baakene, Mr. Teslim Bolarinwa and Mr. A. Afeez for making my study at the North-West University eventful.

ABSTRACT

The study described the synthesis and characterization of carbon-based quantum dots/copper oxide nanocomposite prior to the modification of a glassy carbon electrode for neurotransmitters detection (dopamine (DA), epinephrine (EP), and norepinephrine (NE)). The two carbon-based quantum dots were prepared from pencil graphite and banana peel precursors and tagged CQDs and bCQDs, respectively. The spectroscopic and microscopic characterization of the carbon based quantum dots (CQs) were achieved through Fourier Transform infrared spectroscopy (FT-IR), UV-visible spectroscopy, x-ray diffraction spectroscopy (XRD), scanning electron microscopy (SEM), and transmission electron microscopy (TEM). The preparation of the banana peel precursor used for the green carbon quantum dots (bCQDs) synthesis, green carbon quantum dots (bCQDs), and carbon quantum dots from pencil graphite precursor (CQDs) was monitored with thermogravimetric analysis (TGA). The electrochemical characterization of the quantum dots (CQDs, bCQDs), copper oxide nanoparticles (CNPs), and the nanocomposites (CQDs/CNPs and bCQDs/CNPs) was done with electrochemical impedance spectroscopy (EIS). Bare GCE and GCE modified with these materials (GCE/CQDs, GCE/bCQDs, GCE/CNPs, GCE/bCQDs/CNPs, and GCE/CQDs/CNPs) in the presence of 5 mM ferricyanide/ferrocyanide ($[Fe(CN)_6]^{3-/4-}$) redox probe were used for electrochemical characterization. The EIS data showed that the composites have lower charge transfer resistance than the individual nanomaterials. The superior electronic properties of the composite relative to the individual nanomaterials show that the combination of the nanomaterials for the composite formation offered a synergy that results in better electron transport properties. The electroanalysis of the analytes (DA, EP, and NE) at the bare and modified electrodes done with cyclic voltammetry (CV) showed that the analytes experienced better electrocatalytic oxidation at the composites modified electrodes (GCE/bCQDs/CNPs and GCE/CQDs/CNPs). The EIS analysis of the analytes at the bare and modified electrode supported the superior electron transfer between the analytes and the two sensors compared to other electrodes.

The electroanalysis of 0.4 mM EP at the bare GCE and the modified electrodes showed that the GCE/bCQDs/CNPs and GCE/CQDs/CNPs gave higher anodic peak currents (I_{ap}) than the bare and the other modified electrodes. The fact that the carbon-based quantum dots (bCQDs and CQDs) modified electrodes and CNPs modified electrode offered significantly lower I_{ap} than the composites modified GCE revealed the significance of the synergy between the components of the composites in EP electroanalysis. The scan rate studies showed an increase in EP anodic and cathodic current responses (I_{ap} and I_{cp}) at GCE/bCQDs/CNPs and GCE/CQDs/CNPs with an increase in scan rate (v). The mechanism of EP oxidation at GCE/bCQDs/CNPs and GCE/CQDs/CNPs was found to be diffusion controlled based on the linear relationship between the peak currents (I_{ap} and I_{cp}) and the square root of the scan rate ($v^{1/2}$). The LoD recorded at GCE/bCQDs/CNPs and GCE/CQDs/CNPs were 15.99 and 24.31 μM over linear dynamic ranges (LDRs) of 10-100 and 1-125 μM, respectively. The sensitivities of the sensors were 0.038 and 0.027 μA μM^{-1}, respectively. The interference studies showed that the detection of EP in the presence of ascorbic acid (AA) at GCE/CQDs/CNPs and GCE/bCQDs/CNPs is feasible. The 22 CV scans of the sensors in EP show that GCE/bCQDs/CNPs is more resistant to fouling. However, the LoD, LDR, sensitivity, and the real sample analysis revealed that GCE/CQDs/CNPs is a better EP sensor than GCE/bCQDs/CNPs.

The electroanalysis of 0.4 mM NE with the bare and modified electrodes showed that higher I_{ap} was obtained with GCE/CQDs/CNPs and GCE/bCQDs/CNPs compared to other electrodes. The EIS analysis of NE at the bare and modified electrodes showed that GCE/CQDs/CNPs and GCE/bCQDs/CNPs have lower charge transfer resistance (R_{ct}) than other electrodes, confirming the superior electron transfer at the sensors compared to other electrodes. The relationship between the peak currents (I_{ap} and I_{cp}) and scan rate (v) (or $v^{1/2}$) suggested that the electron transfer at GCE/CQDs/CNPs and GCE/bCQDs/CNPs are surface-confined and diffusion-controlled, respectively. The LoD recorded at GCE/CQDs/CNPs and GCE/bCQDs/CNPs were 14.47 and 14.66 μM over LDRs of 10-126 and 1-131 μM, respectively. The sensitivities of the sensors were 0.024 and 0.025 μA μM^{-1}, respectively. The 22 CV scans of the sensors in NE show that the green carbon quantum dots-based sensor (GCE/bCQDs/CNPs) offered greater resistance to fouling. Based on the LoD, LDR, and reproducibility, the two sensors gave similar performance for the detection of NE. However, the GCE/bCQDs/CNPs was better in terms of resistance to fouling, while GCE/CQDs/CNPs was a better sensor for NE recovery from banana peel solution.

The electroanalysis of 0.4 mM DA with the bare and modified electrodes showed that GCE/CQDs/CNPs and GCE/bCQDs/CNPs offer higher I_{ap} than other electrodes. The EIS data obtained with the bare and modified electrodes showed that these two sensors possess lower R_{ct} than the other electrode, justifying better electron transfer across the two sensors, which culminated in a better current response. The relationship between the peak currents (I_{ap} and I_{cp}) and v (or $v^{1/2}$) suggested that the electron transfer at GCE/CQDs/CNPs and GCE/bCQDs/CNPs are surface-confined and diffusion controlled, respectively. The LoD recorded at GCE/CQDs/CNPs and GCE/bCQDs/CNPs were 13.27 and 25.41 μM, respectively. The LDRs for the sensors were 10-180 and 50-200 μM, respectively. The stability studies revealed that both sensors are susceptible to fouling. Considering the LoD, LDR, and the recovery of DA from dopamine hydrochloride injection solution, GCE/CQDs/CNPs is a better DA sensor.

Keywords: Green carbon quantum dots; Dopamine; Epinephrine; Norepinephrine; Sensors

TABLE OF CONTENTS

DECLARATION i

DEDICATION ii

ACKNOWLEDGEMENTS iii

ABSTRACT iv

TABLE OF CONTENTS vi

LIST OF ABBREVIATIONS x

LIST OF FIGURES xii

LIST OF TABLES xvii

LIST OF SCHEMES xix

LIST OF SYMBOLS xx

CHAPTER 1 1

1.0 Introduction 2

1.1 Background to the study 2

1.2 Justification/significance of the study 4

1.3 Problem statement 5

1.4 Aim of the study 5

CHAPTER 2 7

2.0 Literature review 8

2.1 The neuron 8

2.2 Transmission of impulse 9

2.3 Neurotransmitters 10

2.4 Classification of neurotransmitters 11

2.5 Monoamine neurotransmitters 13

- 2.5.1 Dopamine..13
- 2.5.2 Serotonin...14
- 2.5.3 Norepinephrine..14
- 2.5.4 Epinephrine...15

2.6 Interfering biomolecules in neurotransmitters detection.......................16

- 2.6.1 Ascorbic acid...16
- 2.6.2 Uric acid 16

2.7 Determination of neurotransmitters ……………………………………………………………17
    2.7.1 Electrochemical determination of neurotransmitters ……………...........................17
        2.7.1.1 Electrodes and electrolytes in voltammetric/amperometric systems …………………………………………………………………..........18
    2.7.2 Voltammetric analytical techniques ……………………………………………21
        2.7.2.1 Cyclic voltammetry ……………………………………………………...21
        2.7.2.2 Linear sweep voltammetry ………………………………………………23
        2.7.2.3 Differential pulse voltammetry ……………………………………………24
        2.7.2.4 Square wave voltammetry …………………………………………………24
2.8 Materials for neurotransmitters determination ……………………………………….....25
    2.8.1 Quantum dots: applications and classification ………………………………….25
    2.8.2 Carbon based quantum dots ……………………………………………………..26
        2.8.2.1 Synthetic methods for carbon quantum dots (CQs) ………………….........28
        2.8.2.2 Carbon quantum dots (CQs) for monoamine NTs detection ……………30
    2.8.2 Metal oxide nanoparticles ……………………………………………………...34
        2.8.2.1 Synthesis of metal oxide nanoparticles …………………………………37
            2.8.2.1.1 Copper oxide nanoparticles (CNPs) ……………………………......39
                2.8.2.3.1.1 CNPs modified sensors for monoamine NTs detection 39
2.9 Characterization techniques ……………………………………………………………43
    2.9.1 Spectroscopic characterization ………………………………………………….43
    2.9.2 Electrochemical characterization ……………………………………..................45
        2.9.2.1 Electrochemical impedance spectroscopy …………………..................46
    2.9.3 Microscopic characterization ………………………………………….............47
    2.9.4 Thermogravimetric analysis …………………………………………….............48
CHAPTER 3 ………………………………………………………………….................56
3.0 Materials and methods ……………………………………………………………50
    3.1 Materials and reagents …………………………………………………………50
        3.11 Chemicals ……………………………………………………….................50
        3.1.2 Materials and equipments ………………………………………………50
    3.2 Methods ……………………………………………………………………………..51

3.2.1 Preparation of banana peel for green carbon quantum dots synthesis………..51

3.2.2 Synthesis of green carbon quantum dots (bCQDs)……..................................51

3.2.3 Chemical synthesis of carbon quantum dots……………………….............51

3.2.4 Synthesis of copper oxide nanoparticles (CNPs) …………………………...52

3.2.5 Preparation of carbon quantum dots and copper oxide composites …...........52

3.2.6 Characterization of synthesized nanomaterials and composites 52

3.2.7 Electrode pretreatment ……………………………………………………....54

3.2.8 Modification of electrodes ………………………………………………….54

3.2.9 Electrochemical characterization and preliminary electroanalysis procedures …......54

3.2.10 pH studies…………………………………………………………………..55

3.2.11 Scan rate studies……………………………………………………………55

3.2.12 Concentration studies ……………………………………………………...55

3.2.13 Stability and reproducibility studies….……………………………………56

3.2.14 Interference studies ………………………………………………………..56

3.2.15 Real sample analysis ……………………………………………….........56

CHAPTER 4 ………………………………………………………………………57

4.0 Results and discussions ……………………………………………………….....58

4.1 Synthesis of nanomaterials and composites……………………………………...58

4.2 Characterization of carbon based quantum dots and copper oxide nanoparticles..……………58

4.2.1 Microscopic and spectroscopic characterization ……………………………60

4.2.2 FT-IR analysis …………………………………………………...............60

4.2.3 UV-visible spectroscopy ……………………………………………………62

4.2.4 X-ray diffraction (XRD) analysis ………………………....……….........63

4.2.5 Scanning electron microscopy (SEM) analysis ……………………………..67

4.2.6 Transmission electron microscopy (TEM) analysis……………….............67

4.2.7 Thermogravimetric analysis (TGA) …………………………………………70

4.2.8 Electrochemical characterization ……………………………………………72

4.3 Electrochemical detection of epinephrine ……………………………………….77

4.3.1 Electroanalysis of epinephrine at bare and modified electrodes ……………………77

4.3.2 Electrochemical impedance spectroscopy …………………………………......82

4.3.3 Effect of scan rate ……………………………………………………….....85

4.3.4 Effect of pH ……………………………………………………………………90

4.3.5 Effect of concentration ……………………………………………………...92

4.3.6 Interference studies ……………………………………………………………95

4.3.7 Real sample analysis ……………………………………………………..........100

4.3.8 Stability and reproducibility …………………………………………….........101

4.4 Electrochemical detection of norepinephrine ……………………………………...103

4.4.1 Electroanalysis of norepinephrine at bare and modified electrodes ……………..103

4.4.2 Electrochemical impedance spectroscopy …………………………………..........106

4.4.3 Effect of scan rate …………………………………………………………..109

4.4.4 Effect of pH ……………………………………………………………………112

4.4.5 Effect of concentration ……………………………………………………...116

4.4.6 Interference studies ……………………………………………………………118

4.4.7 Real sample analysis ……………………………………………………………..123

4.4.8 Stability and reproducibility ……………………………………………………..124

4.5 Electrochemical detection of dopamine …………………………………………………127

4.5.1 Electroanalysis of dopamine at bare and modified electrodes …………………...127

4.5.2 Electrochemical impedance spectroscopy ……………………………………….130

4.5.3 Effect of pH ……………………………………………………………………133

4.5.4 Effect of scan rate on DA oxidation ……………………………………………..135

4.5.5 Concentration studies ………………………………………………….........139

4.5.6 Interference studies ……………………………………………………………141

4.5.7 Real sample analysis ……………………………………………………………..146

4.5.8 Stability and reproducibility ……………………………………………………..147

CHAPTER 5 …………………………………………………………………………...150

5.0 Conclusion and recommendations ……………………………………………………151

5.1 Conclusion ……………………………………………………………………………151

5.2 Recommendations ………………………………………………………………..........153

APPENDIX ……………………………………………………………………………..........154

LIST OF ABBREVIATIONS

QDs:	Quantum dots
CQs:	Carbon quantum dots
CQDs:	Carbon quantum dots from pencil graphite
bCQDs:	Carbon quantum dots from banana peel
CuO:	Copper oxide
CNPs:	Copper oxide nanoparticles
NTs:	Neurotransmitters
SE:	Serotonin
DA:	Dopamine
NE:	Norepinephrine
EP:	Epinephrine
PBS:	Phosphate buffer solution
FT-IR:	Fourier Transform infrared spectroscopy
SEM:	Scanning electron microscopy
TEM:	Transmission electron spectroscopy
TGA:	Thermogravimetric analysis
R_{ct}:	Charge transfer resistance
R_s:	Solution resistance
CPE:	Constant phase element
Y_o:	Magnitude of the constant phase element
CV:	Cyclic voltammetry
SWV:	Square wave voltammetry
DPV:	Differential pulse voltammetry
ΔE_P:	Peak separation
E_{ap}:	Anodic peak potential
E_{cp}:	Cathodic peak potential

XRD:	X-ray diffraction spectroscopy
GCE:	Glassy carbon electrode
MONPs:	Metal oxide nanoparticles
I_{ap}:	Anodic peak current
I_{cp}:	Cathodic peak current
LoD	Limit of detection
LoQ	Limit of quantitation
LDR	Linear dynamic range
LDRs	Linear dynamic ranges

LIST OF FIGURES

Figure 2.1: A Neuron. Adapted from [52] Copyright Frontiers, 2021 ……………………………..8

Figure 2.2: A chart showing the action and resting potential. Reprinted with permission from [58] ……………………………………………………………………………………………………10

Figure 2.3: Structure of common neurotransmitters ………………………………………………12

Figure 2.4: Chemical structure of ascorbic acid and uric acid …………………………............17

Figure 2.5: Schematic representation of a three-electrode system. Reprinted from [110] ………..20

Figure 2.6: (a) A typical cyclic voltammogram and (b) A chart showing the forward and reverse potential scan. Reprinted from [2] ……………………………………………………………22

Figure 2.7: Graph of (A) potential scan against time and (B) the voltammogram of LSV. Reprinted from [2] ………………………………………………………………………………………23

Figure 2.8: Differential pulse voltammetry showing (A) applied potential step and (B) current against potential. Reprinted from [2] ………………………………………………………………….24

Figure 2.9: Square wave voltammetry showing (A) applied potential step and (B) current against potential. Reprinted from [2] ………………………………………………………………….25

Figure 2.10: (a) Schematic diagram of inorganic quantum dots. Structure of (b) graphene (c) carbon dots and (d) nitrogen doped carbon dots. Reprinted from [2] ……………………………………..27

Figure 2.11: Preparation of GQDs from pyrolysis of citric acid. Reprinted from [2] …………….29

Figure 2.12: Typical (A) Nyquist plot and (B) Bode plot and phase angle diagram from EIS data of two different materials (white and red plot). Reprinted with permission from [303] (Copyright Elsevier, 2017) ……………………………………………………………………………...54

Figure 4.1: FT-IR spectra of (a) BP and bCQDs (b) CQDs/CNPs, CQDs and CNPs and (c) bCQDs, CNPs and bCQDs/CNPs ………………………………………………………………………65

Figure 4.2: UV-visible spectra of (a) CQDs and bCQDs (b) CQDs, CNPs and CQDs/CNPs………68

Figure 4.3: XRD spectra of (a) bCQDs, CQDs, (b) CQDs/CNPs, (c) CNPs and bCQDs/CNPs…….70

Figure 4.4: SEM micrograph of (a) CNPs (b) CQDs (c) CQDs/CNPs (d) bCQDs and (e) bCQDs/CNPs……………………………………………………………………………………..73

Figure 4.5: TEM micrograph of (a, c) CQDs and bCQDs. Particle size distribution chart of (b,d) CQDs and bCQDs ……………………………………………………………………………74

Figure 4.6: TGA curves of (a) BP and bCQDs and (b) CQDs ……………………………………75

Figure 4.7: Cyclic voltammograms of bare GCE, GCE/CQDs, GCE/CNPs, GCE/bCQDs, GCE/bCQDs/CNPs and GCE/CQDs/CNPs in 5 mM $[Fe(CN)_6]^{3-/4-}$ ……………………...........77

Figure 4.8: EIS spectra (Nyquist plot) of (a) bare GCE, CQDs, bCQDs, CNPs and CQDs/CNPs modified GCE in 5 mM $[Fe(CN)_6]^{3-/4-}$ (pH 7) (inset: enlarged EIS spectra of the bare and modified electrodes) (b) equivalent electrochemical circuit of the EIS data at (a)……………………………78

Figure 4.9: Cyclic voltammograms of the (a) bare GCE, CQDs, bCQDs, CNPs, bCQDs/CNPs and CQDs/CNPs modified GCE in 0.4 mM EP and (b) bare GCE, CQDs/CNPs and bCQDs/CNPs modified GCE in 0.1 M PBS (scan rate: 25 mV s^{-1}, pH 7) …………………………………………84

Figure 4.10: Cyclic voltammograms of (a) bare GCE, GCE/CQDs, GCE/CNPs and GCE/CQDs/CNPs and (b) bare GCE, GCE/bCQDs, GCE/CNPs and GCE/bCQDs/CNPs in 0.4 mM EP (scan rate: 25 mV s^{-1}, pH 7) ……………………………………………………………………86

Figure 4.11: EIS spectra (Nyquist plot) of (a) Bare GCE, CQDs, bCQDs, CNPs and CQDs/CNPs modified GCE in 0.4 mM EP (pH 7) (inset: enlarged EIS spectra of the bare GCE, GCE/CNPs, GCE/bCQDs, GCE/CQDs/CNPs and GCE/bCQDs/CNPs) (b) equivalent electrochemical circuit of the EIS data at (a) ……………………………………………………………………………..87

Figure 4.12: (a) Cyclic voltammograms of GCE/CQDs/CNPs in EP over a scan rate range (25 – 400 mV s^{-1}) at pH 7 (b) plot of the anodic and cathodic peak current against the square root of the scan rate and (c) plot of the anodic and cathodic peak potential against log v …………………………..91

Figure 4.13: (a) Cyclic voltammograms of GCE/CQDs/CNPs in EP over a scan rate range (25 – 400 mV s^{-1}) at pH 7 (b) plot of the anodic and cathodic peak current against the square root of the scan rate and (c) plot of the anodic and cathodic peak potential against log v …………………………..93

Figure 4.14: (a, c) Cyclic voltammograms of GCE/CQDs/CNPs and GCE/bCQDs/CNPs in 0.4 mM EP at pH 3-9 (scan rate: 25 mV s^{-1}) (b,d) plot of the anodic peak current and potential of EP against pH, recorded at GCE/CQDs/CNPs and GCE/bCQDs/CNPs ………………………………………96

Figure 4.15: (a, c) Square wave voltammograms of GCE/CQDs/CNPs and GCE/bCQDs/CNPs over EP concentration range of 10-116.4 µM and 1-125.3 µM, respectively at pH 7 (b,d) plot of current versus concentration extracted from (a) and (c), respectively ……………………………………..98

Figure 4.16: (a) Cyclic voltammograms of bare GCE and GCE/CQDs/CNPs, (b) square wave voltammogram and (c) differential pulse voltammogram of GCE/CQDs/CNPs in 0.4 mM EP and 1

mM AA (d) square wave voltammograms of EP concentration increase (52.2 – 114.3 µM) with constant AA concentration (1 mM) at GCE/CQDs/CNPs (pH 7, scan rate: 25 mV s^{-1}) …………101

Figure 4.17: (a) Cyclic voltammograms of bare GCE and GCE/bCQDs/CNPs, (b) square wave voltammogram and (c) differential pulse voltammogram of GCE/bCQDs/CNPs in 0.2 mM AD and 1 mM AA (d) square wave voltammograms of EP concentration increase (70.3 – 120.6 µM) with constant AA concentration (1 mM) at GCE/CQDs/CNPs (pH 7, scan rate: 25 mV s^{-1}) …………103

Figure 4.18: Cyclic voltammograms of (a) GCE/CQDs/CNPs and (b) GCE/bCQDs/CNPs in 0.4 mM EP (pH 7) after 22 scans (scan rate: 25 mV s^{-1}) ………………………………………………..105

Figure 4.19: Cyclic voltammograms of (a) GCE/CQDs/CNPs and (b) GCE/bCQDs/CNPs in 0.4 mM EP (pH 7, scan rate: 25 mV s^{-1}) for three different trials of electrode modification……………….106

Figure 4.20: Cyclic voltammograms of bare GCE, CQDs, bCQDs, CNPs, CQDs/CNPs and bCQDs/CNPs modified GCE in 0.4 mM NE at pH 7 (scan rate: 25 mV s^{-1}) ……………………..108

Figure 4.21: Cyclic voltammograms of (a) bare GCE, GCE/CQDs, GCE/CNPs and GCE/CQDs/CNPs and (b) bare GCE, GCE/bCQDs, GCE/CNPs and GCE/bCQDs/CNPs in 0.4 mM NE (scan rate: 25 mV s^{-1}, pH 7) …………………………………………………………...110

Figure 4.22: EIS spectra (Nyquist plot) of (a) Bare GCE, CQDs, bCQDs, CNPs and CQDs/CNPs modified GCE in 0.4 mM NE (pH 7) (b) equivalent electrochemical circuit of the EIS data at (a) ……………………………………………………………………………………………..112

Figure 4.23: (a) Cyclic voltammograms of GCE/CQDs/CNPs in NE over a scan rate range (25 – 400 mV s^{-1}) at pH 7 (b) plot of the anodic and cathodic peak current against the square root of the scan rate and (c) plot of the anodic and cathodic peak potential against log v …………………………115

Figure 4.24: Figure 4.23: (a) Cyclic voltammograms of GCE/bCQDs/CNPs in NE over a scan rate range (25 – 400 mV s^{-1}) at pH 7 (b) plot of the anodic and cathodic peak current against the square root of the scan rate and (c) plot of the anodic and cathodic peak potential against log v ……………………………………………………………………………………………..117

Figure 4.25: (a, c) Cyclic voltammograms of GCE/CQDs/CNPs and GCE/bCQDs/CNPs in 0.4 mM NE at pH 3-9 (scan rate: 25 mV s^{-1}) (b,d) plot of the anodic peak current and potential of NE against pH, recorded at GCE/CQDs/CNPs and GCE/bCQDs/CNPs ……………………………………..119

Figure 4.26: (a, c) Square wave voltammograms of GCE/CQDs/CNPs and GCE/bCQDs/CNPs over NE concentration range of 10-126.4 µM and 1-131.1 µM, respectively at pH 7 (b,d) plot of current versus concentration extracted from (a) and (c), respectively……………………………...…121

Figure 4.27: (a) Cyclic voltammograms of bare GCE and GCE/CQDs/CNPs, (b) square wave voltammogram and (c) differential pulse voltammogram of GCE/CQDs/CNPs in 0.4 mM NE and 1 mM UA (d) square wave voltammograms of NE concentration increase (12.9 – 66.7 µM) with constant AA concentration (1 mM) at GCE/CQDs/CNPs (pH 7, scan rate: 25 mV s^{-1})……………125

Figure 4.28: (a) Cyclic voltammograms of bare GCE and GCE/CQDs/CNPs, (b) square wave voltammogram and (c) differential pulse voltammogram of GCE/CQDs/CNPs in 0.4 mM NE and 1 mM UA (d) square wave voltammograms of NE concentration increase (12.9 – 57.1 µM) with constant AA concentration (1 mM) at GCE/CQDs/CNPs (pH 7, scan rate: 25 mV s^{-1})…………..127

Figure 4.29: Cyclic voltammogram of (a) GCE/CQDs/CNPs and (b) GCE/bCQDs/CNPs in 0.4 mM NE (pH 7) after 22 scans (scan rate: 25 mV s^{-1}) ……………………………………………..129

Figure 4.30: Cyclic voltammograms of (a) GCE/CQDs/CNPs and (b) GCE/bCQDs/CNPs in 0.4 mM NE (pH 7, scan rate: 25 mV s^{-1}) for three different trials of electrode modification………………130

Figure 4.31: Cyclic voltammogram of the bare GCE, CQDs, bCQDs, CNPs, bCQDs/CNPs and CQDs/CNPs modified GCE in 0.4 mM DA (scan rate: 25 mV s^{-1}, pH 7)………………………...132

Figure 4.32: Cyclic voltammogram of (a) bare GCE, GCE/CQDs, GCE/CNPs and GCE/CQDs/CNPs and (b) bare GCE, GCE/bCQDs, GCE/CNPs and GCE/bCQDs/CNPs in 0.4 mM DA (scan rate: 25 mV s^{-1}, pH 7) ……………………………………………………………………………..133

Figure 4.33: EIS spectra (Nyquist plot) of (a) Bare GCE, CQDs, bCQDs, CNPs and CQDs/CNPs modified GCE in 0.4 mM DA (pH 7) (inset: enlarged EIS spectra) (b) equivalent electrochemical circuits of the EIS data at (a)…………………………………………………………………136

Figure 4.34: (a, c) Cyclic voltammograms of GCE/CQDs/CNPs and GCE/bCQDs/CNPs in 0.4 mM EP at pH 3-9 (scan rate: 25 mV s^{-1}) (b, d) plot of the anodic peak current and potential of DA against pH, recorded at GCE/CQDs/CNPs and GCE/bCQDs/CNPs ………………………………….…138

Figure 4.35: Cyclic voltammograms of GCE/CQDs/CNPs in DA over a scan rate range (25 – 400 mV s^{-1}) at pH 7 (b) plot of the anodic and cathodic peak current against the square root of the scan rate and (c) plot of the anodic and cathodic peak potential against log v ……………………..……141

Figure 4.36: Cyclic voltammograms of GCE/bCQDs/CNPs in DA over a scan rate range (25 – 400 mV s^{-1}) at pH 7 (b) plot of the anodic and cathodic peak current against the square root of the scan rate and (c) plot of the anodic and cathodic peak potential against log v ………………………….142

Figure 4.37: Square wave voltammograms of GCE/CQDs/CNPs and GCE/bCQDs/CNPs over DA concentration range of 10-180 µM and 50-200 µM, respectively at pH 7 (b,d) plot of current versus concentration extracted from (a) and (c), respectively ………………………………………....144

Figure 4.38: Cyclic voltammograms of bare GCE and GCE/CQDs/CNPs, (b) square wave voltammogram and (c) differential pulse voltammogram of GCE/CQDs/CNPs in 0.4 mM DA and 1 mM AA (d) square wave voltammograms of EP concentration increase (100 – 125 µM) with constant AA concentration (1 mM) at GCE/CQDs/CNPs (pH 7, scan rate: 25 mV s^{-1})…………………….148

Figure 4.39: Cyclic voltammograms of bare GCE and GCE/CQDs/CNPs, (b) square wave voltammogram and (c) differential pulse voltammograms of GCE/CQDs/CNPs in 0.4 mM DA and 1 mM AA (d) square wave voltammograms of EP concentration increase (120 – 170 µM) with constant AA concentration (1 mM) at GCE/CQDs/CNPs (pH 7, scan rate: 25 mV s^{-1})………………….…150

Figure 4.40: Cyclic voltammograms of (a) GCE/CQDs/CNPs and (b) GCE/bCQDs/CNPs in 0.2 mM DA (pH 7) after 22 scans (scan rate: 25 mV s^{-1}) ………………………………………………….152

Figure 4.41: Cyclic voltammograms of (a) GCE/CQDs/CNPs and (b) GCE/bCQDs/CNPs in 0.2 mM DA (pH 7, scan rate: 25 mV s^{-1}) for three different trials of electrode modification………………153

LIST OF TABLES

Table 2.1: Classification of neurotransmitters ……………………………………………………..13

Table 2.2: Figures of merit describing the performance of carbon-based QDs for dopamine detection (Reprinted from [2]) ………………………………………………………………………………..33

Table 2.3: Table of the figures of merit of other monoamine NTs (EP, SE and NE) determination using graphene and carbon quantum dots (GQDs & CQDs) (Reprinted from [2]) …..……………35

Table 2.4: Some metal oxide based sensors for monoamine NTs detection and their figures of merit……………………………………………………………………………………………...46

Table 4.1: Notable functional groups and absorption bands in the nanomaterials and composite……………………………………………………………………………………………66

Table 4.2: Cyclic voltammetry data of the bare and modified electrodes in 5 mM $[Fe(CN)_6]^{3-/4}$.................…………………………………………………………………………………79

Table 4.3: EIS parameters of the bare and modified electrodes ……………………………......80

Table 4.4: Cyclic voltammetry data of bare GCE and modified GCE in EP ………………………85

Table 4.5: EIS parameters of bare and modified electrode in EP …………………………………89

Table 4.6: Kinetic parameters of CQDs/CNPs and bCQDs/CNPs modified electrodes in EP...……………………………………………………………………………………………94

Table 4.7: Comparison of the proposed sensors with past EP sensors ……………………………100

Table 4.8: AA-EP peak difference of past and present EP sensors ………………………………102

Table 4.9: EP analysis in epinephrine injection at GCE/CQDs/CNPs and GCE/bCQDs/CNPs….104

Table 4.10: Cyclic voltammetry data of bare GCE and modified GCE in NE ……………………109

Table 4.11: EIS parameters of bare and modified electrodes in NE ………………………………111

Table 4.12: Kinetic parameters of CQDs/CNPs and bCQDs/CNPs in NE ………………………116

Table 4.13: Figures of merit of the past and current NE sensors ………………………………...123

Table 4.14: UA-EP peak difference of past and present NE sensors ……………………………..125

Table 4.15: Real sample analysis of NE in banana peel …………………………………………128

Table 4.16: Cyclic voltammetry data of bare GCE and modified GCE in DA…………………..134

Table 4.17: EIS parameters of bare and modified electrode in DA ………………………………136

Table 4.18: Kinetic parameters of CQDs/CNPs and bCQDs/CNPs modified electrode in DA……………………………………………………………………………………………140

Table 4.19: Comparison of the proposed sensors with past DA sensors …………………………145

Table 4.20: AA-DA peak difference of past and present DA sensors ……………………………146

Table 4.21: Dopamine analysis in dopamine hydrochloride injection ……………………………151

LIST OF SCHEMES

Scheme 1: Schematic representation of the synthesis of (a) bCQDs (b) CQDs and (c) CNPs…...59

Scheme 2: Mechanism of epinephrine redox reactions ………………………………………..82

Scheme 3: Epinephrine redox peaks …………………………………………………………..83

Scheme 4: Mechanism of NE oxidation and reduction ………………………………………107

Scheme 5: Mechanism of dopamine oxidation ………………………………………………131

LIST OF SYMBOLS

δ	Standard deviation of the intercept of the linear calibration curve
k_s	Charge transfer rate constant
v	Scan rate
I	Current
A	Surface area
d	Interplanar spacing
λ	Wavelength
R	Molar gas constant
T	Temperature
μ	Micro
b	Tafel slope
$b1$	Slope of a plot of E_{ap} against log v
$b2$	Slope of a plot of E_{cp} against log v
n	Number of electrons transferred
F	Faraday’s constant
α	Charge transfer coefficient
D_o	Diffusion coefficient

CHAPTER ONE

INTRODUCTION

1.0 Introduction

1.1 Background to the study

The central and the peripheral nervous system have huge impact on every action of an individual. The interaction of the nervous system with the effector muscles is actualized with the communication between neurons at both ends. The mode of communication could either be electrical or chemical [1]. Chemical transmission has been studied over time because it is considered slow and controllable as opposed to the fast spontaneous electrical signal [2]. Essentially, the chemical signal molecules, otherwise called neurotransmitters are transported from one end of a presynaptic neuron to the other end of the postsynaptic neuron across a junction called synapse [3]. These chemical messengers are important in the day-to-day activities of every individual because they control actions such as learning, sleeping, heart rate, emotion, mental alertness, mood among others [4]. The monoamine class of neurotransmitters such as serotonin (SE), dopamine (DA), epinephrine (EP) and norepinephrine (NE) have played a prominent role in the control of a good number of the actions. Consequently, their imbalance in the human extracellular fluid has been ascribed to the ailments suffered by patients with psychological disorders and other related diseases. Specifically, schizophrenia, Parkinson’s disease, Alzheimer, Tourette’s syndrome, high blood pressure, autism and other chronic ailments have been linked to the upset in the body balance of these chemicals [5-7].

The quest for a point-of-care diagnostic medium for prompt response to these health challenges gave rise to the development of scientific means of detection of neurotransmitters. Chromatography [8], capillary electrophoresis [9], mass spectrometry [10] and spectroscopy [11] have been attempted for the detection of these neurotransmitters with good detection limits. However, none of these methods can boast of cost efficiency, portability, speed and easy manipulation that characterizes the electrochemical technique [12]. Electrochemical methods have been found to possess these qualities and as such has been widely applied for neurotransmitters detection. The design of electrochemical sensors prioritizes the modification of the major electrode across which the electrochemical reactions take place – the working electrode. Carbon nanotubes (CNTs), graphene oxide, graphene, conducting polymers, metal and metal oxide nanoparticles have been used for the modification of conventional electrodes such as glassy carbon, screen printed, carbon paste, platinum and gold electrode with the singular aim of achieving very sensitive electrochemical sensing platforms [13]. Similarly, quantum dots have also been applied individually and in addition to some other materials to provide highly sensitive electrochemical sensing platforms for monoamine neurotransmitters [14-16].

Quantum dots (QDs) are nanomaterials with very small particle size. The small particle size which is often < 10 nm is a product of their zero-dimensional structure. Interestingly, the optical properties of QDs can be altered by controlling their size and shape [17]. This is possible because the band gap is size dependent and therefore, various colours are emitted by QDs depending on the size of the QDs. As a result, they have been widely applied in solar cells [18], television panels [19] and biological labelling [20] where this optical property is grossly harnessed. The good conductivity and large surface area of QDs have endeared electrochemists to the adoption of QDs for sensor fabrication. The relatively high cytotoxicity of QDs prepared from inorganic materials such as Zn, Cd, Te, As, Se, S informed the need for alternative QDs with more biocompatibility and low cytotoxicity. Carbon based QDs made from biological waste [21-24], carbohydrates [25], citric acid [26], graphene [27] among others have since been developed to combat this challenge. Thankfully, the carbon based quantum dots namely carbon and graphene QDs have been successfully incorporated into sensing platforms for biomolecules with huge success [26, 27]. It is noteworthy, that carbon based QDs with biomass precursors (green carbon QDs) are expected to offer lower cytotoxicity than the carbon based QDs made from precursors such as graphite, p-toluenesulfonic acid, and poly(acrylamide).

Green carbon QDs synthesized from carbon sources such as corn cob [28], lemon peel [29], orange juice [30], banana juice [31], onion extract [32], orange peel and some other biomass [33] have been applied for the fabrication of fluorescence sensors for heavy metals due to their excellent optical properties. In certain instances, green carbon quantum dots from precursors such as *Hibiscus sabdariffa* [34], edible carrot [35], walnut shells [36] and banana peel [37] have been used for bioimaging. The electrocatalytic activity of carbon quantum dots from chemical sources and metal oxide composites towards the oxidation of biomolecules have been reported for some electrochemical sensors fabricated with these composites [38, 39]. Meanwhile, the combination of green carbon dots with metal oxide nanocomposites for sensors fabrication is hardly attempted. It is expected that the combination of green carbon quantum dots and metal oxide nanoparticles will offer good electrocatalytic activity towards the oxidation of catecholamine NTs leading to the production of a sensor with low toxicity and high sensitivity. The expectation is largely based on the performance of cuprous oxide and carbon QDs in a carbon quantum dots/cuprous oxide/nafion nanocomposite in the electrochemical detection of dopamine [40]. The synergy between the carbon QDs and Cu_2O nanoparticles in the composite manifested in the anionic nature of the carbon QDs and the good conductivity of Cu_2O nanoparticles which collectively enhanced dopamine detection.

Accordingly, carbon based quantum dots and copper oxide nanocomposites were applied for the modification of glassy carbon electrode in the present study (working electrode) with the motive to obtaining a better sensing platform than the pre-existing ones.

Justification/significance of the study

Electrochemical sensors have proven to be reliable tools for NTs detection. Carbon nanomaterials such as carbon nanotubes, carbon based QDs, graphene, nanodiamonds and graphene oxide belong to a class of nanomaterials with outstanding electrocatalytic activity towards NTs oxidation. Beyond the sensitivity and low detection limits offered by sensors fabricated with these carbon nanomaterials, low toxicity and low cost of sensor fabrication are desired. The low toxicity of carbon QDs, its proven stability and low detection limits earlier reported for some carbon QDs based electrode [27, 41, 42] suggested that the incorporation of carbon dots into a composite with metal oxide will give rise to very reliable electrochemical sensors. It is expected that electrochemical sensors based on green carbon QDs will offer much lower toxicity compared to carbon QDs from chemical precursors. On the other hand, metal oxide nanoparticles (MONPs) individually have huge reputation for good electrocatalytic effect on neurotransmitters [43-45], suggesting a possible synergy between the carbon based QDs and MONPs.

The foregoing has been substantiated by several studies. One of such is a research conducted by Huang et al., [40] in 2015 on the determination of dopamine using cuprous oxide nanoparticles, carbon quantum dots and nafion composite modified glassy carbon electrode. The synergy between the metal oxide and the quantum dot manifested in good electrocatalytic activity of the electrode while nafion ultimately played the role of ionic discrimination. The findings from the study suggested that the combination of carbon quantum dots and copper oxide nanoparticles (CNPs) would offer sufficient electrocatalytic effect on the oxidation of monoamine neurotransmitters (NTs) such that their detection down to very low concentrations would be achieved. In addition, the green nature of the carbon dots in the study could significantly lower the cumulative toxicity of the resultant sensor.

1.2 Problem statement

The ailments associated with the depletion or rise in the level of monoamine neurotransmitters are capable of reducing the quality of life at early stage with the possibility of causing death at advanced stage. The chromatographic, spectroscopic and colorimetric method of quantifying these neurotransmitters are either too complex to handle or time consuming for point-of-care application. To solve this problem, a lot of electrochemical sensors were designed for the analysis of neurotransmitters but few challenges such as high detection limit, instability, considerable toxicity of the electrode modifiers as well as low sensitivity of a host of existing sensors persist. The low toxicity of carbon based QDs relative to the highly toxic QDs of inorganic origin, its proven stability and low detection limits earlier reported for some carbon QDs based electrodes [46, 47] suggested that incorporation of carbon dots into a composite with metal oxide will give rise to very reliable electrochemical sensors. Also, it is already established in literature that copper oxide nanoparticles have good electrocatalytic effect on neurotransmitters [44, 45]. The need to design a more sensitive electrochemical sensor than the pre-existing ones with requisite low toxicity for routine point-of-care determination of monoamine neurotransmitters has led to the generation of the following objectives.

1.3 Aim of the study

Development of an electrochemical sensor based on green carbon QDs/copper oxide nanocomposite for the detection of some monoamine neurotransmitters.

Objectives of the study are to:

- synthesize green carbon quantum dots from banana peels (bCQDs) and pencil graphite (CQDs)
- synthesize CuO nanoparticles (CNPs) and form composites containing CNPs and the carbon based quantum dots (CQDs/CNPs and bCQDs/CNPs) for glassy carbon electrode (GCE) modification.
- characterize bCQDs, CQDs, CNPs, CQDs/CNPs, and bCQDs/CNPs nanocomposite using microscopic, electrochemical and spectroscopic techniques.
- investigate the effect of pH, scan rate, and analyte concentration on the electroanalysis of dopamine, epinephrine, and norepinephrine at the composites modified GCE (GCE/bCQDs/CNPs and GCE/CQDs/CNPs).
- determine the sensitivity, reproducibility and stability of GCE/bCQDs/CNPs and GCE/CQDs/CNPs towards dopamine, epinephrine, and norepinephrine detection.

- determine the ability of the composites modified GCE to detect the analytes in real samples and in the presence of interfering molecules.
- compare the performance of the green carbon QDs based sensor (GCE/bCQDs/CNPs) to that of the chemical based carbon QDs (GCE/CQDs/CNPs).

CHAPTER TWO

LITERATURE REVIEW

2.0 Literature review

2.1 The neuron

Neurons, otherwise called nerve cells can be considered the fundamental unit of the nervous system. There are quite a number of them that make the coordination of the actions of the entire body system achievable. Basically, they are composed of the cell bodies (soma), dendrites and axon (Fig. 2.1). The cell bodies are important for keeping the neuron alive due to the fact that they accommodate the nucleus of the neuron [48]. Nervous impulses are sent out from one end of a neuron to the other via the axon and the dendrites. While the dendrites receive the stimulus, the axon sends it out to the next dendrite [2]. Based on their functions, nerve cells can be classified as; motor neurons, inter neurons and sensory neurons. As the name implies, sensory neurons have close proximity with the sensory organs while the motor neurons are connected to the effector muscles or glands. Precisely, the sensory neurons send nerve impulses to the brain or spinal cord while the motor neurons receive the signal for execution by effectors [49, 50]. The inter neurons simply connect one neuron to the other. The nerve impulses that travel along the neurons can either be electrical or chemical. Electrical signals are very fast and much more difficult to control. Chemical signals on the other hand are slow and can therefore can be controlled [2]. This explains why the chemical means of impulse transmission along neurons is mostly studied. Between the axon and the dendrite of two different neurons, there is a connection across which chemical signals are transported. Such gap junction is referred to as the synapse [51].

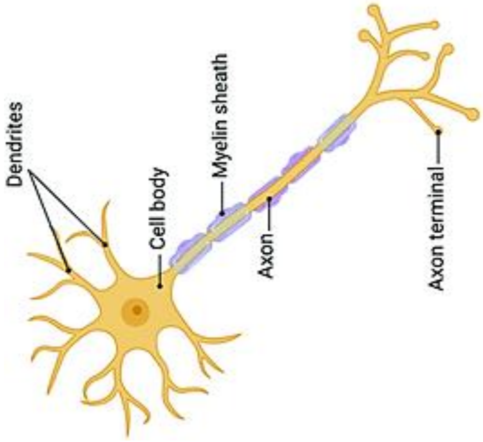

Figure 2.1: A Neuron. Adapted from [52] Copyright Frontiers, 2021

2.2 Transmission of impulse

The transmission of chemical signals along the nerve cells is made possible by the excitable nature of the neuron. The neural membrane experience changes in polarity as inner and outer surface witness change in composition. The inner part of a neuron has a high concentration of K^+ and amino acid molecules while the outer surface is majorly composed of Na^+ and Cl^-. In order to permit the exchange of these ions, the neuron contains ion-gated channels which are specific for each ion (mostly Na^+ and K^+ channels) [53]. The position of the neuron is dictated by the polarity achieved by the migration of these ions. The neuron can assume any of; resting, graded and action potential.

Resting potential: This occurs when the neural membrane attains a potential difference of -70 mV [54]. This potential difference is set up by the separation of charge brought about by the movement of Na^+ into the cell while the K^+ moves out. The balance of these ions in and out of the membrane is brought about by the Na^+/K^+ gate. Basically when the voltage across the neuron is exactly -70 mV, it is at its resting potential where it is not transmitting any impulse [55].

Graded potential: The polar neuron at a resting potential gets depolarized when a stimulus leads to the upset in the polarity of the neural membrane. There is voltage gated Na^+ and K^+ ion channels that open up depending on the polarity of the neural membrane. When the impulse leads to the influx of Na^+ into the cell, the Na^+ at the voltage gated channel opens as the potential difference of the neuron gets to the -55 mV mark [54]. This leads to the depolarization of the neuron and the impulse is transferred to the other neuron. At 30 mV the neuron is repolarized by the efflux of K^+ from the cell until it attains a potential difference below the resting potential, thereby leading to the hyperpolarization of the cell. Unfortunately, the potential difference does not get to the -55 mV sometimes. This possibility prevents the cell from firing an action potential. Such neuron can be said to have its potential graded between the resting and the action potential [49].

Action potential: A neuron fires an action potential when it attains a voltage of -55 mV. The actualization of this ‘all or nothing’ potential can be effected by chemical messengers. The action potential could result from the stimulation of a receptor neuron by a chemical messenger. When such molecules bind to the receptor, the Na^+ pump of the chemically gated channel opens up for the influx of Na^+. If this change in the polarity of the cell brings the potential up to -55 mV, depolarization of such cell occurs and the cell is said to fire an action potential [54] (Fig.

2.2). The implication of this is that the impulse is relayed to the axon of the neuron. Along the neuron, the signal jumps over the insulating myelin sheath to the dendrite of the next neuron. Chemical messengers that trigger the opening of the Na^+ channels for the attainment of the -55 mV potential are termed excitatory while those that trigger the opening of the K^+ cells are tagged inhibitory [56, 57]. Noteworthy, the summation of the inhibitory and excitatory signals determines if the neuron fires an action potential or not. If the number of excitatory signals are greater than the inhibitory, the neuron would be expected to fire an action potential.

These chemical messengers are important for the wellbeing of an individual because their chemical nature carries information that controls human behaviour. In essence, the maintenance of their balance in the body is crucial to a clean bill of health. These neurochemical transmitters are popularly called neurotransmitters.

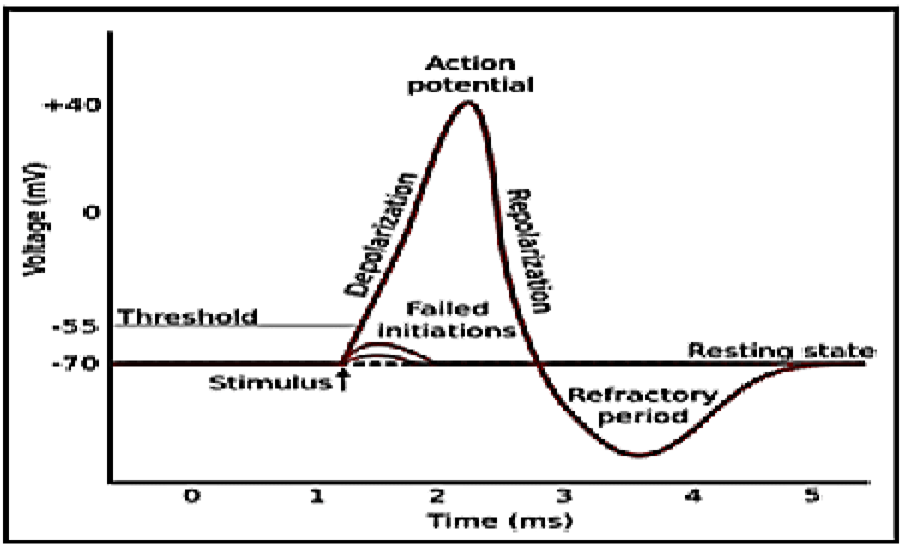

Figure 2.2: A chart showing the action and resting potential. Reprinted from [58].

2.3 Neurotransmitters

Neurotransmitters are chemical substances that control certain human physiological behaviour as they move from the axon of a neuron to the dendrite of the other [50]. They are biomolecules that contribute to the proper running of the entire body system. A good number of them are produced in the central and peripheral nervous system and as such contribute immensely to the actualization of human actions such as sleeping, memory, mental alertness, heart rate, emotion and muscle contraction. When the Ca^+ gates opened as a result of action potential across a presynaptic neuron, Ca^+ binds with the protein around the synaptic vesicles. This action brings about the dissolution of the coating around the synaptic vesicle housing the neurochemical transmitters and they eventually bind to the post-synaptic receptor [56, 57]. The receptors and the neurotransmitters do not always have a lock and key kind of relationship because there is equally a possibility of a neurotransmitter binding to different sites on a receptor – especially when the receptor has sub-receptors [50]. Surprisingly, some neurotransmitters also affect the response of a receptor to another neurotransmitter. Such neurotransmitters are tagged neuromodulators [59]. Depending on the chemical nature of the neurotransmitters, the neuron either fires an action potential or not [54]. Firing the action potential has a corresponding physiological response. The physiological response due to the release of these chemical messengers can be hampered when there is an upset in their level in the human system. This imbalance often leads to chronic health issues that often reduce the quality of life. Few of the debilitating effects of the abnormal concentration of these chemicals are; schizophrenia, Parkinson's disease, autism, high blood pressure, anxiety and depression [12]. The level of neurotransmitters in extracellular fluids has been considered as a possible means of diagnosis for patients suffering from any of these diseases. Hence, the importance of extensive study on neurotransmitter detection. Before looking into the detection of these important biomolecules, it is important to have an idea of what these neurotransmitters look like structurally and their various classes.

2.4 Classification of neurotransmitters

Neurotransmitters are mostly organic compounds such as amino acids, amines, nucleotides and peptides. Inorganic compounds such as nitric oxide (NO) and carbon monoxide (CO) have shown neurotransmitting tendencies [60, 61]. The classification of neurotransmitters can be based on two different categories (Table 2.1) namely

- classification based on mechanism of transmission
- classification based on structure

Classification based on mechanism of transmission is a form of classification that identifies neurotransmitters (NTs) as either inhibitory or excitatory. This classification stems from the effect the neurotransmitter has on the polarity of the neural membrane after the stimulation of the post synaptic receptor. As earlier stated, those NTs that succeeded in raising the potential of the neural membrane to the -55 mV benchmark are termed excitatory while those that acted otherwise are tagged inhibitory [54]. Interestingly, some neurotransmitters can act have both excitatory and inhibitory effect. Example of excitatory neurotransmitters are dopamine, epinephrine, norepinephrine, acetylcholine, glutamate and aspartate. Dopamine and acetylcholine can double as both excitatory and inhibitory NTs. Gamma-aminobutyric acid (GABA), serotonin and glycine are popular inhibitory neurotransmitters [62, 63].

Based on the chemical structure of the neurotransmitters, the commonly studied NTs can be classified as amino acids, gases and amines. Dopamine, epinephrine, norepinephrine, tryptamine and serotonin are collectively termed monoamines because they possess the amino functional group. Specifically, dopamine, epinephrine and norepinephrine are sub-classified as catecholamines - considering the catecholamine backbone in their make-up. Glycine, glutamate, aspartate and GABA are all amino acids due to the presence of the amino and the carboxylic functional group in their chemical structure. As expected, NO and CO are gasotransmitters. Most of the monoamine class of neurotransmitters can also act as neuromodulators [64]. Figure 2.3 showed the chemical structure of notable neurotransmitters.

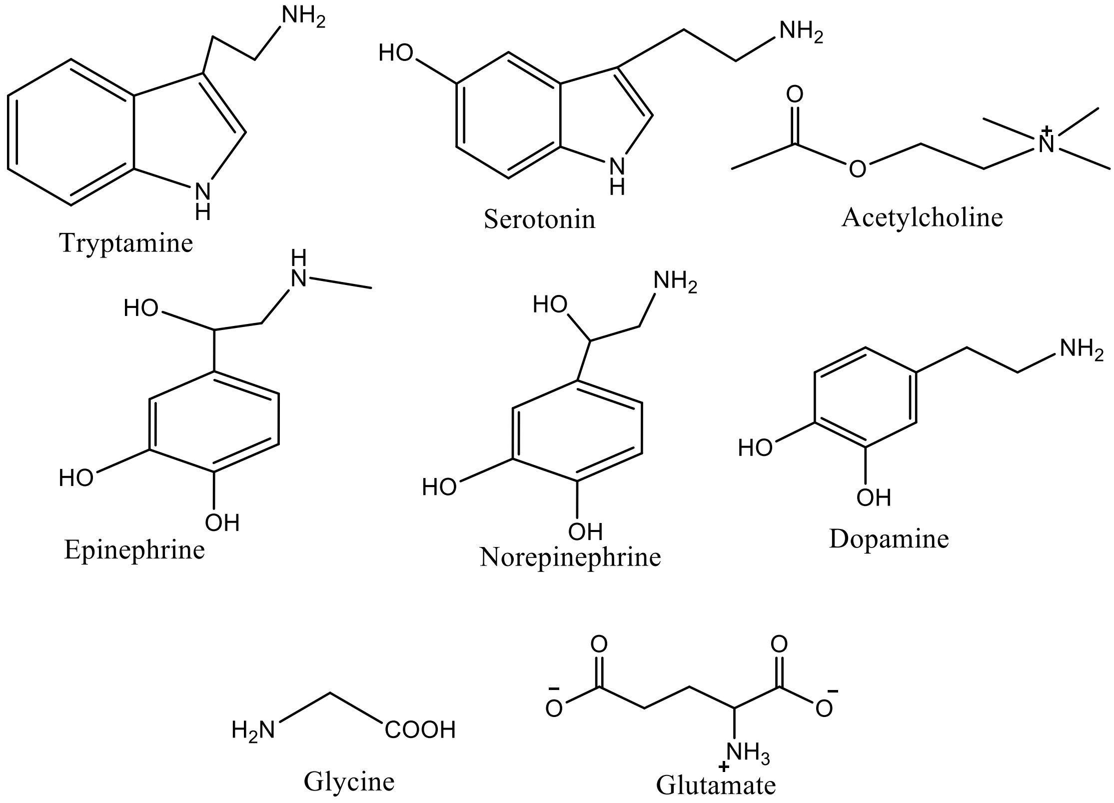

Tryptamine

Serotonin

Acetylcholine

Epinephrine

Norepinephrine

Dopamine

Glycine

Glutamate

Figure 2.3: Structure of common neurotransmitters

Table 2.1: Classification of neurotransmitters

Classification based on mechanism	Classification based on structure
Excitatory	*Monoamine*
Dopamine Epinephrine	[a]Dopamine [a]Epinephrine
Norepinephrine Acetylcholine	[a]Norepinephrine [b]Serotonin Tryptamine
Inhibitory	*Amino acids*
Serotonin GABA	GABA Glycine Aspartate Glutamate
Glycine Dopamine Acetylcholine	*Gasotransmitters*
	Nitric oxide (NO) Carbon monoxide (CO)

a- catecholamines b- indolamine

2.5 Monoamine neurotransmitters

The monoamine class of neurotransmitters have contributed immensely to the smooth running of the entire system because basic human needs such as memory, sleep, emotion, mood and mental alertness are controlled by these NTs [12]. By implication, upset in their body balance and its attendant neurological disorder have singled out this class of NTs for special attention in terms of the design of detection procedures. The attention was partly because the diagnosis of such disorders (schizophrenia, anxiety, Parkinson's disease, dementia and movement disorders) could be near-conclusive with the development of sensors for these NTs. More importantly, this possibility emerged because the cumulative effect of the imbalance of two or three of these NTs could manifest in some of these disorders [50, 65, 66]. This premise explains why there have been the existence of more sensors for the determination of this class of NTs than any other class.

2.5.1 Dopamine

Dopamine (DA) is about the most studied neurotransmitter for electrochemical detection. The popularity of DA stems from its neurological importance. Dopamine is essential for memory, mood, learning and sleep [12]. Its importance in cognitive and behavioural wellness of an individual underscores the massive damage its imbalance could do to the social status of such an individual. Schizophrenia, dementia, attention-deficit hyperactivity (ADH), Parkinson's disease and depression are notable implications of DA imbalance in the body [65-68]. Schizophrenia and Parkinson's disease are the most popular of the lot because of the severity of their symptoms. Symptoms of schizophrenia such as delusion, hallucination and disorganization of behaviour have been ascribed to increase in dopamine activity while cognitive impairment and decreased verbal fluency were associated with decrease in DA level [50, 67, 69]. Parkinson's disease symptoms like severe dementia have also been linked to DA depletion [69]. Noteworthy, the synthetic route of DA in the central nervous system have been found to be the transformation of tyrosine to 3,4-dihydroxyphenylalanine (DOPA) followed by the decarboxylation of DOPA to DA [70]. Since levodopa (L-DOPA) is a precursor of DA, it is administered as drug for the treatment of DA depletion related diseases [50]. This happens basically because L-DOPA can cross the blood-brain barrier. However, L-DOPA has to be handled with extreme care due to the possibility of side effects such as DA toxicity [71]. This side effect which manifests as hypotentia and nausea, has been mitigated with the addition of DA to the L-DOPA formula in order to control the amount of DA to be formed since DA can't surmount the blood-brain barrier [50, 72]. This reality led to the development of dedicated sensors for L-DOPA as well.

2.5.2 Serotonin

Serotonin, also known as 5-HT (5-hydroxytryptamine), can be produced in the central nervous system from tryptophan [73]. It is an inhibitory NT responsible for the regulation of mood, sleep, anxiety, memory, appetite and learning. Muscle contraction and some cardiovascular functions have been ascribed to the presence of SE at optimum level in the body [74]. Anxiety, depression, aggression, memory impairment and reduced muscle movement have been connected to low SE level while high levels of SE have manifested in sedation and decrease in sexual drive [75]. Extremely high SE level causes SE syndrome with symptoms such as insomnia, uncontrollable trembling, aggression, nausea and profuse sweating. Selective serotonin reuptake inhibitors (SSRIs) are drugs that can be used for the treatment of anxiety related disorders such as obsessive –compulsive disorder, social phobia and depression [76, 77]. The apparent importance of SE has inspired the design of numerous sensors for its detection. As seen in some cases, the relationship between SE and tryptophan has motivated scientists to develop a sensitive and selective sensor for SE detection in the presence of tryptophan.

2.5.3 Norepinephrine

Norepinephrine (NE), otherwise referred to as noradrenaline is an excitatory neurotransmitter produced in the central nervous system from DA in a synthetic pathway similar to that of DA - except for the transformation of DA to NE by dopamine β-hydoxylase (Spector). After the re-uptake of NE, it can be broken down further by monoamine oxidase (MAO) [78]. NE which equally doubles as a stress hormone is popularly referred to as the ‘flight or fight’ NT because of its ability to activate the sympathetic nervous system in moments of danger [79]. It is responsible for the regulation of heart rate, blood pressure, memory, body metabolic rate and temperature. Consequently, high levels of NE has been ascribed to anxiety, panic and insomnia while low levels of NE has manifested in depression, poor memory and loss of mental alertness [50]. Precisely, anxiety related disorders such as obsessive compulsive disorder (OCD), post-traumatic stress disorder (PTSD) and panic disorder have been treated with MAO [80, 81]. Like every other monoamine NTs, the health implication of the imbalance of NE has triggered the development of several electrochemical and fluorescence sensors for its detection. More often than not, it takes the determination of other NTs responsible for a specific disorder caused by NE and such NTs to arrive at a conclusive diagnosis of the patient. This underscores the need to design sensors specific for the monoamine NTs which are known to be responsible for some disorders outside their optimum levels.

2.5.4 Epinephrine

Epinephrine, otherwise called adrenaline is another excitatory NT. EP doubles as a hormone produced by the adrenal gland. Just like NE, it can as well be regarded as a ‘flight of fight’ NT because it equally prepares the body for emergency. Again, like NE it can be synthesized from tyrosine [82]. Apart from the apparent difference in structure, EP has a more limited role in ‘flight or fight’ response of the body compared to NE [83]. It is responsible for heart rate, memory, mental alertness and regulation of blood glucose level, which explains why the imbalance of EP had manifested in ailments such as Parkinson’s disease, hypoglycemia, schizophrenia, diabetes and hypertension [12, 45]. It is therefore unsurprising that EP has been administered for the treatment of certain heart conditions. A standard EP concentration of 90-690 pg/mL is expected in a normal human body. Chronic ailments such as myocardial infarction (which limits blood flow to the human heart) have been linked to the upset in the EP balance of the human body system [84].

Considering the importance of these NTs, several methods have been applied for their detection both *in vivo* and *in vitro*, so as to make informed decision on the diagnosis of ailments associated with their abnormal presence in biological systems.

2.6 Interfering biomolecules in neurotransmitters detection

2.6.1 Ascorbic acid

Ascorbic acid (AA), otherwise called vitamin C, is a notable biomolecule with good antioxidant attributes. The dietary sources of AA include fruits and vegetables. Its presence in the extracellular fluids in large concentration is therefore inevitable. It has been reported that the level of AA in the cerebrospinal fluid and the brain could be as high as 10 mM and 400 µM, respectively [43]. Specifically, the level of AA *in vivo* is valued at about 100 – 1000 times the concentration of NTs [85]. Although independent electrochemical detection of AA has been attempted, it has more often been treated as an interfering molecule in the presence of the monoamine neurotransmitters. Given the fact that AA is detected at a potential similar to that of notable monoamine NTs such as DA, the performance of some NTs sensor have also been measured by their ability to effect discriminatory AA and NTs detection. In a number of publications, AA-DA peak resolution have been achieved with the AA peak recorded at a lower potential than the monoamine NTs [86-89]. This precedence and the fact that AA is readily available explain the choice of AA as one of the interfering molecules used in this study.

2.6.2 Uric acid

Uric acid is a byproduct of the breakdown of purine [90]. Purine can be found in many food substances such as peas, liver, and seafood. The consumption of these food items and many more increases the purine content of the body and consequently raises the level of UA in extracellular fluid. Although UA is considered an antioxidant, its high level in the human system has been reported to cause gout and nephropathy [91]. UA has been reported to exist in extracellular fluids at higher concentration than the NTs (about 100-1000 times higher than DA) [92]. Several reports on the selective detection of NTs in the presence of UA show that UA is detected at a higher potential than DA, EP and NE [93-95]. The variation in potential enables the simultaneous and selective detection of these NTs in the presence of UA. In some instances, the detection of NTs in the presence of AA and UA was attempted [96-99]. The ability of sensors to selectively detect NTs in the presence of AA and UA is a useful metric for assessing the practical application of sensors in real samples such as urine and blood serum.

Figure 2.4 showed the chemical structure of AA and UA.

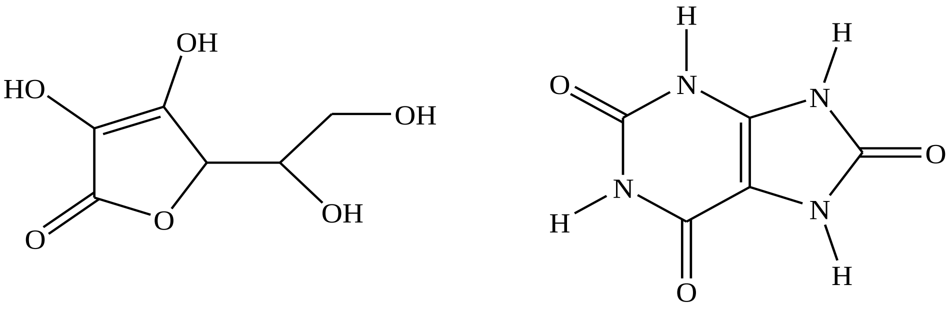

Ascorbic acid **Uric acid**

Figure 2.4: Chemical structure of ascorbic acid and uric acid

2.7 Determination of neurotransmitters

Neurotransmitters have clearly been very important biomolecules of clinical significance. They have huge impact on the smooth running of the entire body system and therefore come with detrimental effect when they exist at levels outside their respective optimum concentrations. In order to accurately detect these NTs for diagnostic purposes, several methods have been applied. Notable methods of NT detection are; chromatography, spectroscopy, mass spectrometry, chemiluminescence (ECL) and capillary electrophoresis [8-11]. Most of these techniques have limitations that often limit their use for easy, fast and cost-effective NT detection. For instance, the high performance liquid chromatography (HPLC) technique requires a highly skilled analyst coupled with the huge cost of procurement of the equipment. Mass spectrometry equally suffers from the requirement of skilled analyst and the need to often couple it with chromatography which often raises the cost of NTs detection. Some of these methods have low sensitivity while those with high sensitivity take long time for analysis. To solve this problem, researchers have developed numerous electrochemical sensors which are capable of rapid detection of analytes of interest to the lowest possible concentration at a very low cost. Beyond this, electrochemical sensors have proven to be very reliable when selectivity of an analyte in the presence of interferents is required. Notable instances are seen in the selective detection of DA in the presence of interferents such as ascorbic acid (AA) and uric acid (UA) which often exist at much higher concentrations than DA [14, 26, 42].

2.7.1 Electrochemical determination of neurotransmitters

Electrochemical determination of analytes is done using electroanalytical methods. Regardless of the working principle of the method, analysis is done at an electrochemical workstation. A typical electrochemical workstation comprises of current/voltage controller (galvanostat/potentiostat), electrodes, electrolyte compartment and a signal display (monitor).

Just like the conventional electrolysis, electrochemical means of analysis stand to measure the voltage/current resulting from driving an originally non-spontaneous chemical reaction. These techniques can broadly be divided into three namely; potentiometric, amperometric and voltammetric techniques.

Potentiometric techniques involve the measurement of voltage difference between two electrodes while controlling the current [100]. This principle is widely used in a class of titration known as the potentiometric titration.

Voltammetry is a very popular and widely used electroanalytical technique that measures the current response of an analyte while the potential is being controlled. Depending on the type of voltammetry, the applied potential range is imposed such that the theoretical potential at which the electroactive specie undergoes a reduction or oxidation reaction is not left out. On the other hand, amperometry requires continuous measurement of current while the potential is fixed [101]. A typical voltammetric or amperometric technique uses a three or two electrode system. The three electrode system comprises of the working electrode, reference electrode and the counter (auxiliary) electrode (Fig. 2.5). The two electrode system is almost the same as the three electrode system except for the absence of the counter electrode. In these systems, each electrode has its designated function which will be discussed in the next section.

2.7.1.1 Electrodes and electrolytes in voltammetric/amperometric systems

Voltammetry is a very popular electroanalytical technique. Numerous literature where these techniques have been used for analysis have established the sensitivity of these techniques. A very large percentage (if not all) of literature make use of an electrochemical cell with a three electrode system [26, 102, 103]. The three electrodes in an electroanalytical system have their specific functions. A good knowledge of the functions of each of these electrodes is important for understanding the mode of operation of an electrochemical sensor.

The working electrode is the actual sensor. It is made of conducting chemically inert materials such as carbon, platinum, silver or gold [104, 105]. Sometimes, it is made from graphite worked into a paste to form a carbon paste electrode [16]. The reactions of the electroactive species take place at the working electrode. For instance, in a redox reaction of a specie, electron for the reduction of the oxidized form of the analyte comes from the working electrode. This is made possible by varying the potential at the working electrode with a potentiostat. The current flow between the working electrode and another electrode within the circuit (counter electrode) is measured by the potentiostat [101]. More often than not, the current response of the analyte has a direct proportion with the analyte concentration. The relationship has been the basic principle upon which most electrochemical sensors were built. The working electrode, compared to the other electrodes is expected to have the lowest possible surface area [106]. Electron enters the electrolyte solution through the working electrode. In order to obtain a very sensitive working electrode, the surface of the working electrode is modified with materials capable of improving its conductivity, selectivity (occasionally), sensitivity and interaction with the analyte. For instance, modification of a glassy carbon electrode (GCE) with carbon nanotube (CNTs) improves the conductivity of GCE and its interaction with DA via π- π stacking. When the CNTs are functionalized, electrostatic attraction between the positively charged DA and the negatively charged CNTs improves electron transfer kinetics [107]. Apart from CNTs, metal and metal oxide nanoparticles, graphene oxide, conducting polymers, imprinted polymers and ion-exchange materials such as nafion have been used for the modification of working electrodes to obtain sensors with improved conductivity, sensitivity and/or selectivity [25, 108, 109].

The reference electrode maintains a constant potential relative to the working electrode. The potentiostat imposes a constant potential to the reference electrode and the electrolyte such that the potential of the electrode can be controlled relative to that of the reference electrode in a three electrode system. Notable reference electrode includes; Ag/AgCl, standard calomel electrode (Hg/Hg_2Cl_2/ KCl) and the standard hydrogen electrode (SHE) [106]. The Ag/AgCl electrode is often used because it doesn’t require temperature adjustment while the difficulty involved in the preparation of SHE makes it rarely used [101]. The reference electrode is placed close to the working electrode to improve the potential the analyte experiences.

The counter electrode majorly exists to complete the circuit and that explains why some electrochemical cells (two-electrode systems) can operate without it. Electrons go into the electrolyte solution through the working electrode while they leave via the counter electrode. Just like the working electrode, it is often made of chemically inert material like platinum [101, 106]. To ensure that the counter electrode does not interfere with the reaction at the working electrode, it is made such that its surface area is a lot larger than that of the working electrode [106]. Essentially, the current flow between the counter and the working electrode is recorded by the potentiostat.

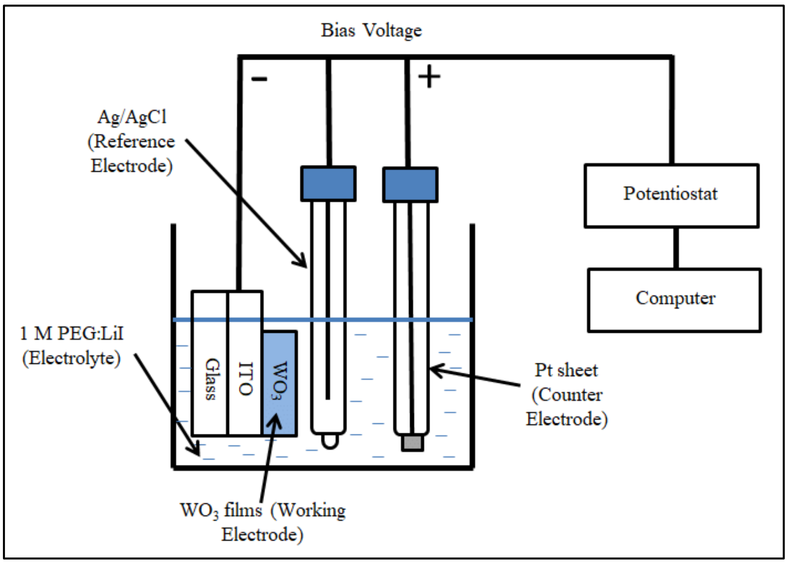

Figure 2.5: Schematic representation of a three-electrode system. Reprinted from [110].

The analyte to be analyzed requires a medium in which it can be dissolved. The medium is referred to as the electrolyte. The electrolytes are salts which are expected to be at higher concentration than the analyte. Beyond this, they are particularly expected to be highly conducting to ensure a fast electron transfer between the analyte and the working electrode [111, 112]. The electrolyte solutions otherwise called the supporting electrolyte help to complete the circuit in the sense that they supply ions to counter the electrons coming from the working electrode. In most existing electrochemical set-up, KCl has been used as a supporting electrolyte dissolved in distilled water as solvent [44]. In some instances, ammonium salts dissolved in acetonitrile or dichloromethane (solvents) have also been used. In cases where the pH of the medium is essential for the dissolution of the analyte or the reproduction of a biological medium, a buffer solution can be used as the electrolyte. Notable example is the phosphate buffer saline (PBS) which is made from phosphate salt and its corresponding weak acid [103]. It is important to note that the supporting electrolyte must be pure and chemically inert with respect to the analyte under the conditions of the electrochemical reaction.

There are a number of voltammetric techniques that have proven to be very sensitive platform for electroanalysis. Notable techniques such as cyclic voltammetry, square wave voltammetry, differential pulse voltammetry, stripping voltammetry and linear sweep voltammetry have given high sensitivity. The next section highlights the mode of operation of some of these techniques based on the frequency with which they surface in literature. The voltammetric techniques have been extensively discussed because of their significance to the current study.

2.7.2 Voltammetric analytical techniques

Cyclic voltammetry, differential pulse voltammetry, square wave voltammetry and linear sweep voltammetry are analytical techniques that are commonly used for the detection of neurotransmitters. Each of these techniques has its strengths and weaknesses as will be seen in this section.

2.7.2.1 Cyclic voltammetry

This is a very popular voltammetric method of evaluating the redox behavior of an analyte at a modified or unmodified bare electrode. It gives a lot of information such as the redox current and potential as well as the reversibility of a redox process at a glance. By implication, evaluating the mechanism and the kinetics of redox reactions from the CV is quite easy. Generally, a CV is generated when the current response emanates from imposing a certain potential on the redox system. The potential imposed such that a potential scan starts from a starting potential (E_1) and switches back to the starting potential (now stop potential, E_s) after attaining a switch potential (E_2) [113] (Fig. 2.6). The resultant voltammogram often showedtwo different peaks at the end of the potential sweep. The peak current obtained during the forward sweep before attaining the switch potential is the anodic peak current (I_{ap}) while the one obtained from the reverse sweep is the cathodic peak current (I_{cp}) (Fig. 2.6). The potentials at which each of these currents are obtained are regarded as the anodic (E_{ap}) and cathodic peak (E_{cp}) potentials, respectively [106]. Noteworthy, this potential sweep is time dependent and as a result, a quantity known as the scan rate obtained from the ratio of potential change (ΔE) and time change (Δt) determines the current response [114]. The reversibility of a redox process can be estimated by calculating the difference between E_{ap} and E_{cp} which is expected to be as close as possible to a value of 59/n mV for a reversible process at room temperature [105]. A reversible process is also expected to have the value of I_{ap}/I_{cp} as 1, meaning that the closer this value is to 1, the more reversible the process [115].

Migration, diffusion and convection are the three major mass transport mechanisms by which an electroactive specie approaches the electrode [106]. Chemical or physical interaction between the analyte and the electrode leads to adsorption of analyte to the surface of the electrode. The mass transport process is referred to as migration. Mass transport by diffusion is most desired as it makes it possible to obtain a more reversible process given that almost the same concentration of the oxidized form of the analyte might also be available for reduction. Convection leads to fluid movement due to temperature changes. The possibility of this in redox systems is mitigated by stirring the solution before experiments [113].

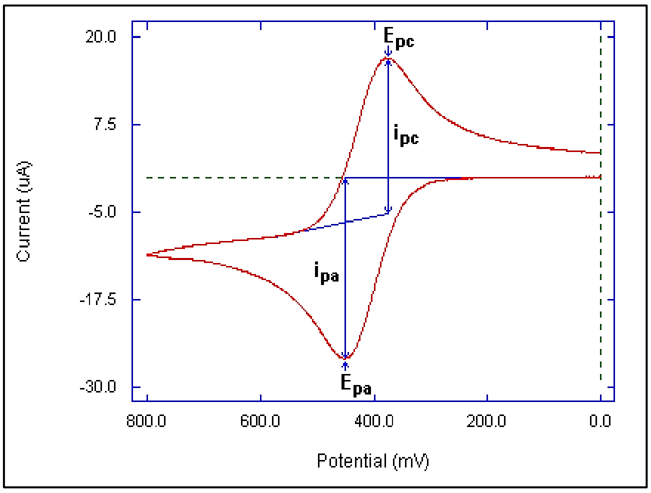

Figure 2.6: A typical cyclic voltammogram. Reprinted from [2]

The mechanism of the redox process at the surface of an electrode could either be adsorptive or diffusive. In some cases, there could be a mixture of the two. A surface confined process (adsorptive process) is defined by the linear relationship between peak current i_p and the scan rate (v) while such linear relationship between I_p and the square root of v suggested a diffusion controlled process [16, 116, 117]. When the latter and the former prevail at lower and higher scan rates, respectively, the process is controlled by both mechanism [16]. Using Randle Sevcik equation (Equation 2.1), a plot of √v against i_p gives a curve from which the surface area of the electrode can be obtained given that n, F, A, R, D_o, C_o and T represent the number of electrons, Faraday's constant (C mol^{-1}), electrode's surface area (cm ^{2}), molar gas constant ($J.mol.K^{-1}$), diffusion coefficient (cm^2 s^{-1}), concentration of the analyte (mol. cm^{-3}) and absolute temperature (K). The electroactive surface coverage of the electrode can be obtained from Equation 2.2.

$$i_p = 0.446nFAC^0\left(\frac{nFvD_0}{RT}\right)^{1/2} \qquad \text{(Eqn 2.1)}$$

$$i_p = \left(\frac{n^2F^2}{4RT}\right)vAr \qquad \text{(Eqn 2.2)}$$

If the quantity of charge is known, the number of electrons transferred can be obtained from Equation 2.3.

$$i_p = \frac{nFQv}{4RT} \qquad \text{(Eqn 2.3)}$$

The kinetics of redox processes at an electrode can be investigated using the Laviron equation [118]. The slope of any of Equations 2.4 and 2.5 from a plot of ln v against peak potentials helps in getting the charge transfer coefficient (α). The rate constant, k_s can be calculated from Equation 2.6.

$$E_{pa} = a + \left(\frac{RT}{(1-\propto)nF}\right)\ln v \qquad \text{(Eqn 2.4)}$$

$$E_{pc} = b - \left(\frac{RT}{\propto nF}\right)\ln v \qquad \text{(Eqn 2.5)}$$

$$\log k = \propto \log(1-\propto) - \log\left(\frac{RT}{nFv}\right) - \propto (1-\propto)\frac{nF\Delta E}{RT} \qquad \text{(Eqn 2.6)}$$

The presence of charging current significantly affects the sensitivity of CV. Consequently, it gives current response that does not sufficiently represent what the redox system experiences. Pulse voltammetry has significantly addressed this challenge and therefore offers greater sensitivity. However, the mechanism and kinetics of redox processes are much easier to investigate from CV.

2.7.2.2 Linear sweep voltammetry

The linear sweep voltammetry (LSV) is a technique often applied for electrochemical analysis of slow reactions [114]. This places LSV over SWV (which is much faster) when sluggish reactions are to be studied. Basically, voltammograms in LSV are obtained through a fixed potential scan between a specified lower and upper limit (Fig. 2.7 (a)) which consequently provokes a peak current response at a particular potential based on the analyte-electrode interaction [119]. The resultant voltammogram is a plot of potential against current response (Fig. 2.7 (b)). For reversible process with fast kinetics, a change in current response accompanies a change in the scan rate. Shift in potential and decline in current response characterizes slow and irreversible reactions under similar condition.

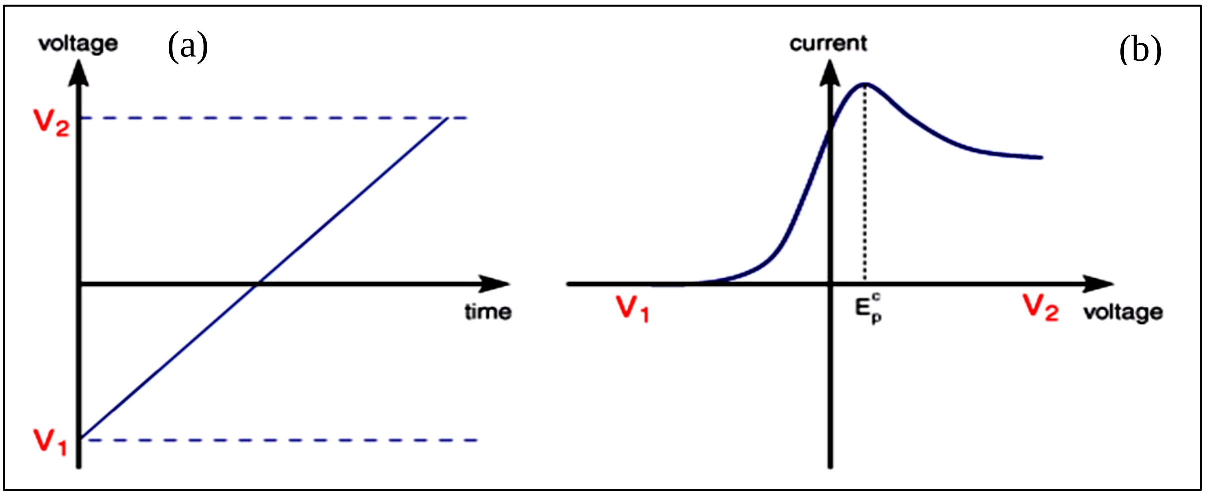

Figure 2.7: Graph of (a) potential scan against time and (b) the voltammogram of LSV. Reprinted from [2].

2.7.2.3 Differential pulse voltammetry

Beyond the current recorded due to electron transfer between the analyte and the electrode (Faradaic current), current flow without such electron transfer is equally possible. This occurs when a double layer formation between the electrolyte and the electrode surface emerges, thus giving a charging current that undermines the Faradaic current recorded at the potentiostat [114]. The phenomenon is most prevalent in cyclic voltammetry because the actual current response should have been the combination of the Faradaic and the non-faradaic current [120]. To mitigate the challenges contributed by the charging current, pulse voltammetry significantly reduce charging current by applying short pulse for a specific time frame. The application of the pulse is such that the difference between current response at the beginning (I_2) and the end (I_1) of the pulse applied within a particular potential step is recorded [101] (Fig. 2.8 (a)). The differential pulse voltammogram (DPV) is a plot of the potential applied against the cumulative current obtained over a specific potential range (Fig 2.8 (b)). This way, the DPV gives a better sensitivity than the CV and as a result often applied for selectivity studies in sensor fabrication since analytes discrimination based on individual potential of detection is feasible with better resolution [120].

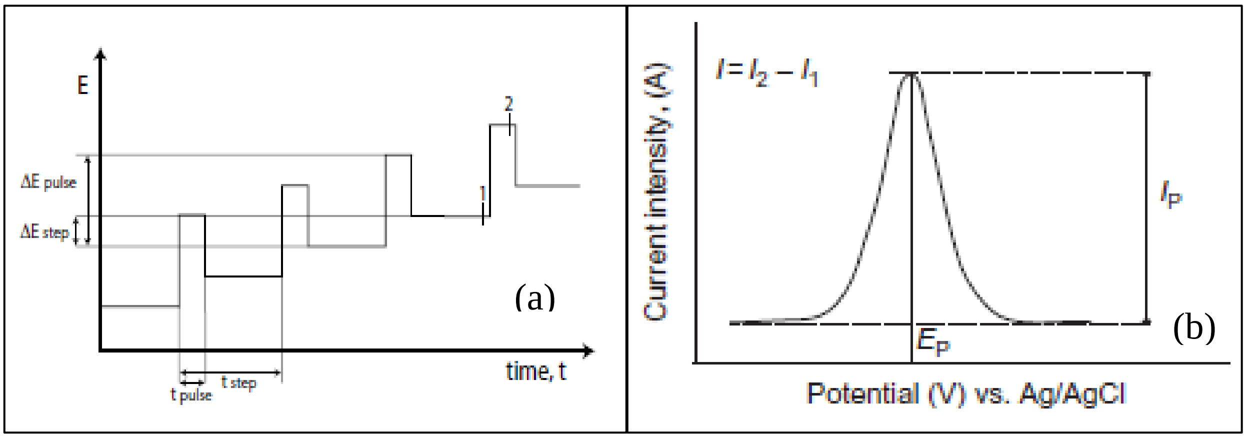

Figure 2.8: Differential pulse voltammetry showing (a) applied potential step and (b) current against potential. Reprinted from [2].

2.7.2.4 Square wave voltammetry

A voltammetric technique that combines both the advantages of the mechanistic deductions of CV and the high sensitivity of DPV is the square wave voltammetry (SWV). Specifically, the SWV offers better sensitivity compared to DPV, probably because SWV operates at a faster scan rate [121]. Just like DPV potential pulse are imposed within a step as such step increases with time (Fig. 2.9 (a)). Also, the net peak current (ΔI) at SWV is the change in current response obtained from the applied forward potential (at the terminal end of the forward pulse) and the backward applied potential (at the end of backward pulse) [101]. The charging current in both directions are similar in magnitude, therefore this net current is devoid of the effect of charging current which would have been subtracted in the process of obtaining ΔI [114]. As seen in Figure 2.9 (b), the square wave voltammogram looks very much like that of a CV before subtracting the current response in both directions. The SWV is used when very high sensitivity is required. Consequently, it is applied for the electrochemical detection of trace level of analytes as well as the simultaneous detection of various analytes [44].

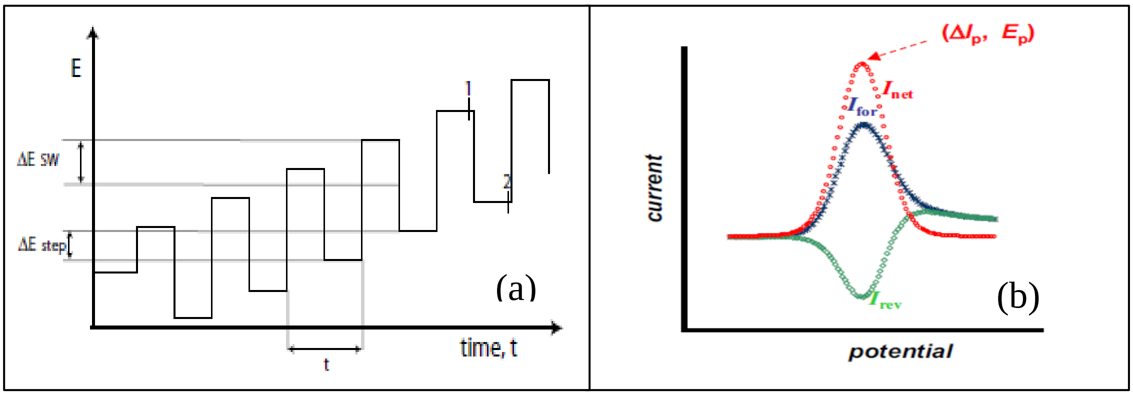

Figure 2.9: Square wave voltammetry showing (a) applied potential step and (b) current against potential. Reprinted from [2].

2.8 Materials for neurotransmitters determination

2.8.1 Quantum dots: applications and classification

Quantum dots (QDs) are widely known as zero-dimensional nanomaterials with extremely small particle size (often < 10 nm) [17]. Interestingly, QDs have optical properties that have a direct link with their size. Precisely, the band gap between the valence and the conduction band increases with decrease in the size of the QDs particles such that the movement of electrons is limited to discrete energy levels [122]. This phenomenon is tagged ‘quantum confinement’ simply because the hole left at the valence band and the electron at the conduction band are within the small dimensions of QDs which contain few atoms. QDs are also called artificial atoms because they can be synthesized to possess quantum confinements similar to a conventional atom of interest [123]. The optical feature of QDs has been linked with the variation in the wavelength of light emitted by QDs particles of different band gaps. As a result, QDs of different sources have been made and utilized in electronics such as television sets and solar cells where this special optical feature is needed [18, 19]. Also, the light emitting characteristics of QDs have been harnessed to serve as substitute for organic dye commonly used for cell bioimaging [124]. The resistance of QDs to photobleaching and the bright photoluminescence they offer placed them over other materials for this purpose [122]. The optical properties, small particle size, electrical conductivity and the large surface area of quantum dots have inspired scientists to fabricate electrochemical and optical sensors with very high sensitivity towards various analytes [16, 26, 103]. QDs have equally been used in drug delivery due to the ease with which they can be functionalized with various drug substances such as folic acid (FA), doxorubicin, Adriamycin among others [24, 125-127]. Biosensors for the detection of biomolecules such as adenosine triphosphate (ATP), FA, Lysozyme and neurotransmitters have been developed with the use of QDs. These applications of QDs however came with their challenges of which the most significant is the cytotoxicity.

In terms of chemical composition, QDs can either be inorganic or carbon based. The inorganic QDs are composed of two major parts namely the core and the shell. Beyond this, they can have stabilizing layers, dopants and ligands (Fig. 2.10). The core and the shell are made up of binary compounds made up of Zn, Cd, S, Te, P, Cu, Ga, N and O. For instance, the core could be CdTe, CdS, GaP, CuCl or GaAs while the shell could be any of CdSe, PbS, ZnO, ZnS, ZnTe or ZnSe [128-133]. The dopants are mostly metallic cations introduced in order to improve the luminescence of the QDs. The QDs have performed well for the various purposes earlier discussed, but they tend to have high level of cytotoxicity [17]. In a bid to find an alternative to these metallic QDs, scientists came up with the carbon based quantum dots which have cheaper precursor and much lower cytotoxicity. This class of QDs are referred to as the carbon based quantum dots.

The carbon based QDs that have been commonly used in the preparation of electrochemical sensors in recent times are the graphene quantum dots and the carbon quantum dots (loosely called carbon dots). This project is centred on the use of carbon based quantum dots for the determination of monoamine NTs. Accordingly, carbon quantum dots and their application in this regard would be discussed in the next section.

2.8.2 Carbon based quantum dots

The prominent carbon based quantum dots are the graphene QDs (GQDs) and the carbon QDs (CQs). Although these two types of carbon based quantum dots are both zero dimensional carbon nanomaterials with sp^2 hybridized carbon atoms with characteristic quantum confinement, they are still different in some respect [134-136]. GQDs are largely crystalline carbon nanomaterials made up of fewer graphene sheets compared to CQs [134]. As the name implies, GQDs are mostly prepared via the top-down approach with the use of graphene as the precursor. Basically, the differences between the GQDs and the CQs are the synthetic route, crystallinity and graphene content.

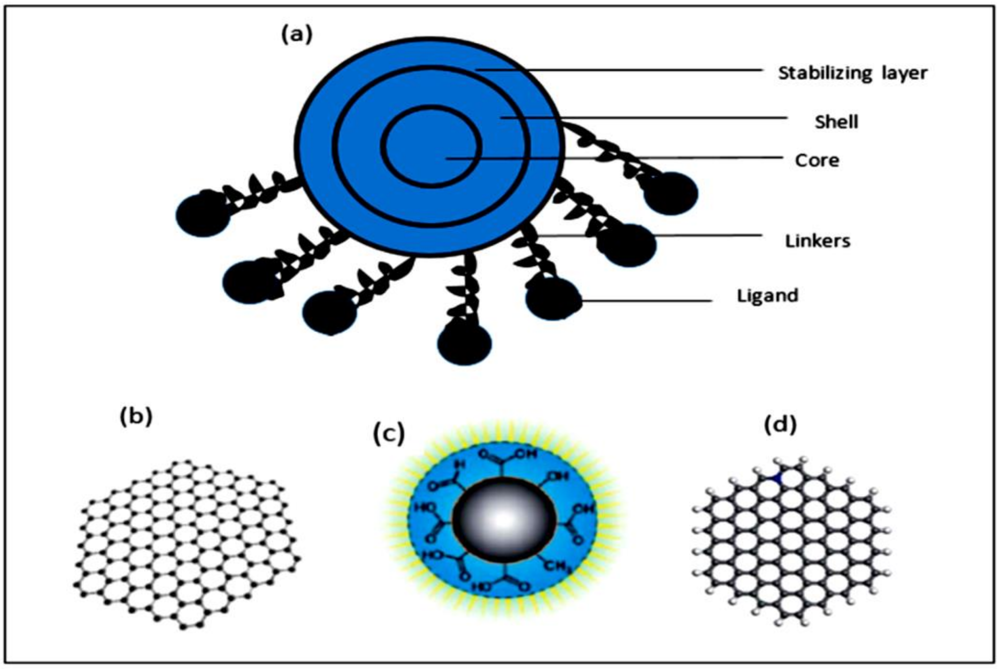

Figure 2.10: (a) Schematic diagram of inorganic quantum dots. Structure of (b) graphene (c) carbon dots and (d) nitrogen doped carbon dots. Reprinted from [2].

CQs are relatively new class of carbon nanomaterials, considering their discovery in 2004. They have tunable fluorescence and can be synthesized from cheap precursors such as biological wastes and other environmentally benign materials such as pawpaw [23]. Apart from the low cytotoxicity, CQs are chemically inert materials with good biocompatibility that makes them suitable for incorporation into matrices for biomolecules sensor fabrication. The synthesis of CQs have been divided into two broad categories regardless of the chemical, physical or electrochemical method of synthesis.

The first category is the top-down approach which involves the use of carbon source such as carbon nanotubes (CNTs), graphite, activated carbon and nanodiamonds for the preparation of QDs. Techniques such as arc-discharge, laser ablation and the electrochemical method have been used to accomplish the top-down approach [137]. The bottom-up approach on the other hand involves the use of biomass, carbohydrates, organic acids and natural products for CQDs synthesis. Sucrose, citric acid, water melon peel, starch, sweet potato, grass, pomelo peel, plant root and leaves have been used as precursor for the bottom-up approach for CQs synthesis using the hydrothermal, plasma, microwave, solvothermal or the chemical treatment [21, 22, 138-140].

The properties of various materials such as the nanodiamonds (NDs) and CNTs have been modified to suit a specific purpose by doping these materials with atoms or some other materials of interest [13, 45]. CQs have equally been doped with atoms such as nitrogen and boron to obtain doped quantum dots with desired luminescence and conductivity. For instance, Jiang et al., [141] suggested that doping carbon nanomaterials with nitrogen can induce charge delocalization in such material and this would be expected to be the case with nitrogen doped carbon QDs (N-CQDs). A number of N-CQDs have been prepared for the fabrication of sensors for monoamine NTs detection in recent times with good sensitivity [142]. Similarly, a lot of GQDs based sensors for NTs detection are available in literature (Table 2.2). The current study is predicated on the use of CQs for NTs detection. Consequently, the next section is dedicated to the discussion of synthesis of CQs and the application of CQs for monoamine NTs detection.

2.8.2.1 Synthetic methods for carbon quantum dots (CQs)

The synthesis of CQs can be achieved through the top-down and the bottom-up approach using the appropriate precursor. These two approach have been accomplished with the help of some physical and electrochemical methods. Some of these methods would be discussed in this section.

Carbonization: Carbonization of various biomass has been used for the preparation of CQs of various sizes. This method has been deployed for the preparation of green CQs using cheap precursors such as the watermelon peel [138], pepper [143] and hair fibre [21]. Organic acids such as citric acid and glucose as well as carbon based precursors such as carbon black have also been deployed for CQs preparation through carbonization [14, 42, 117]. This is often achieved through the hydrothermal means which involves heating the precursor at elevated temperature and pressure. This is because the hydrothermal technique is more environmentally friendly and cost effective than the chemical oxidation or the thermal decomposition method [144]. Gomes and his group reported CQs synthesis via the hydrothermal means of carbonization from chitin, chitosan and graphite by subjecting the precursors to heating at 200 ^{o}C for 6 hours [145]. The hydrothermal synthesis of CQs from CA and glucose has also been reported by Shen et al., [146]. Carbonization through thermal decomposition of precursors have also been attempted with huge success. This basic principle involves a solvent free carbonization of precursor at very high temperature. This method was adopted by Martindale and his team for the preparation of CQs via citric acid pyrolysis at 180 ^{o}C [147]. Pyrolysis of citric acid is a very significant synthetic route for carbon based quantum dots (Figure 2.11).

Chemical oxidation: From the instrumentation point of view, the chemical oxidation means of CQs synthesis is a very convenient and cheap method of large scale CQs synthesis [144]. On the other hand, this method requires the use of a large quantity of chemicals to an extent that the toxicity of the resultant CQs is of great concern. Generally, it involves the combination of the precursor with an inorganic oxidant such as inorganic acids and hydrogen peroxide [148]. For instance, Chen et al., reported the synthesis of CQs from the chemical oxidation of pencil graphite with hydrofluoric acid and potassium permanganate to give very conducting CQs subsequently applied for DA electrochemical detection[27]. Similarly, Yan et al., reported the synthesis of highly fluorescent CQs from starch chemical oxidation with H_2O_2 [61]. This synthesis combines both carbonization and chemical oxidation considering the initial carbonization of starch prior to chemical oxidation.

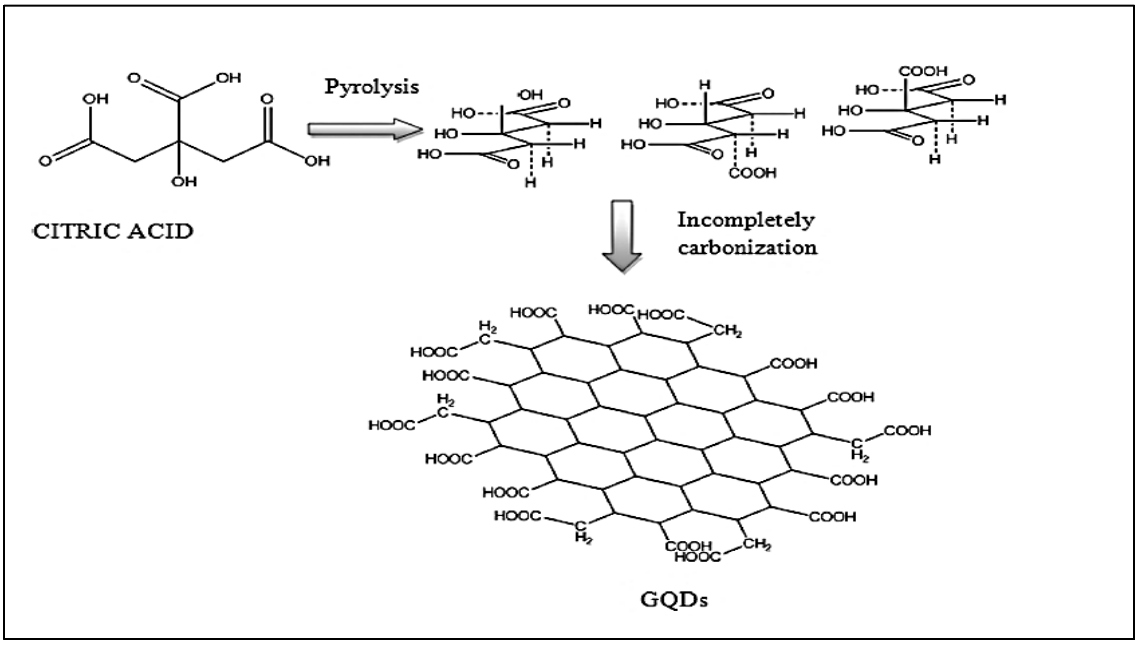

Figure 2.11: Preparation of GQDs from pyrolysis of citric acid. Reprinted from [2]

Electrochemical oxidation: This is about the most popular method of CQs synthesis via the top-bottom approach using precursors such as graphite and CNTs. The electrochemical oxidation technique offers CQs with high yield, purity, reproducibility as well as low cost of production [144]. CQs preparation from graphite electrode electrochemical oxidation in alkaline alcohol was attempted by Liu and his group to obtain carbon dots of ~ 4 nm average diameter [47]. The authors also showed that the storage of the CQs have an effect on their particle sizes by obtaining different particle size distribution for particles stored at room temperature and 4 ^{o}C. Devi et al., also reported the electrochemical CQs synthesis from graphite rod (used as cathode and anode) in alkaline ethanol electrolyte [115]. The resultant CQs gave green fluorescence under a UV of 365 nm wavelength and average particle size of 7 nm.

Microwave-assisted synthesis: Compared to the hydrothermal synthesis, the microwave-assisted method helps to shorten the reaction time and provide a platform for uniform heating of the precursor for CQs synthesis, thus producing CQs of uniform size [137, 140]. The microwave provides the required energy to break bonds between substrate, thus limiting the introduction of too many chemicals as seen in the chemical oxidation method. Microwave-assisted CQs synthesis has been successfully done by Pires et al., using various biomass such as cashew gum to obtain CQs of 9 nm average particle size [149]. Similarly, highly fluorescent CQs were prepared by Hu and his team from orange peels using a 900 W microwave [150]. Noteworthy, the particle distribution of the CQs particles spans a range of 2-21 nm which suggested irregular particle size. The CQs had an average particle size of ~ 3 nm and gave green fluorescence under a wavelength of 420 nm. Interestingly, the particles of the CQs were nearly uniform because the size distribution had a narrow range of 3-5 nm.

Laser ablation, which depends on the physical interaction between precursors such as graphite and laser beams have also been applied for CQs synthesis. Noteworthy, the nature of the laser beam has been found to contribute significantly to the particle size of the resultant CQs [151]. Also, the arc-discharge method and the ultrasonic treatment of carbon containing precursors have also yielded large quantity of CQs with high quantum yield [152, 153]. These and many other methods have been applied for CQs synthesis but the highlighted techniques are much easier to achieve and therefore likely to be applied during the course of this project.

2.8.2.2 Carbon quantum dots (CQs) for monoamine NTs detection

The significance of the monoamine neurotransmitters as earlier discussed inspired scientists to attempt the use of CQs for monoamine NTs sensors fabrication. Compared to the number of such publications available on the application of some other materials such as graphene (Gr), graphene oxide (GO), polymers, metal oxide nanoparticles, CNTs and metal nanoparticles, fewer data are available on the application of CQs for this purpose [2]. Also, the largest percentage of the CQs based sensors were glassy carbon electrodes (GCE) modified with composites containing CQs and some other materials such as metal nanoparticles, single-walled CNTs (SWCNTs), chitosan, GO and nafion among other materials (Table 2.2).

Compared to other monoamine NTs, dopamine (DA) was the most determined NTs with CQs modified electrode in the last ten years. The quantum dots used for this purpose were mostly synthesized with the use of carbohydrates such as glucose, sucrose and collagen as precursor (Table 2.2). Carbonized glucose was used for the synthesis of CQs by Li et al., prior to the modification of GCE with the prepared CQs [154]. Following the drop-casting of the CQs on GCE, the modified electrode was used for DA detection. This sensor provided a sensitivity sufficient for DA detection in human serum. Similarly, Huang and his group presented another CQs modified GCE with glucose as precursor [109]. In this case, polyethylene glycol was added to glucose for the synthesis of the CQs which was subsequently incorporated into chitosan (CS) for the formation of the composite for GCE modification. The resultant sensor was able to detect DA in DA injection sample with good recovery. Using sucrose as precursor, two different articles were presented for DA detection in the last decade. In one of those articles presented by Huang et al., a combination of sucrose and oil acid was carbonized for the preparation of CQs which was combined with AuNPs and CS for the formation of a composite for DA detection [116]. Another article by the same author used the CQs prepared using the same method for the preparation of CQs which were combined with nafion and Cu_2O for the preparation of a composite for DA detection [40]. The sensors offered very high sensitivity to DA in human serum and DA injection. N-CQDs was synthesized from a mixture of NH_3 and collagen using the hydrothermal method. The N-CQDs was further modified with nafion prior to the modification of GCE with the N-CQDs in order to obtain a more stable sensor. This sensor was applied for the selective detection of DA in solutions containing ascorbic acid (AA) and uric acid (UA).

Carbon nanomaterials have also been used for the preparation of CQs using the top-down approach. Devi and his team prepared one of such CQs through the exfoliation of graphite via an electrochemical means[115]. This was accomplished by subjecting two graphite electrodes to a direct current in the presence of NaOH, ethanol and water. The resultant CQDs were applied for coating the surface of GCE and a screen printed carbon electrode (SPCE) for a comparative DA detection in the presence of AA. Pencil graphite was used for the preparation of the CQDs prepared by Algarra and his team for the fabrication of CQs modified GCE [155]. However, the sensor was used for DA detection in the absence of interfering species.

Pyrolysis of citric acid (CA) is another common synthetic route for CQs. Chen and his team prepared CQs using this method and incorporated the CQs into a composite with β-cyclodextrin (β-CD) for the modification of GCE [156]. The sensor obtained was eventually applied for the determination of DA in the presence of UA and tryptophan (trp). Also, a simple electrode composed of GCE modified with CQs prepared from 1-propanol through the electrochemical method was fabricated by Canevari and his group [15]. The summary of the performances of these CQs modified electrodes as seen on Table 2.2 showed that these sensors are capable of DA detection to a very low concentration. In addition, the application of the electrodes for the determination of DA in real samples is equally apparent. Table 2.2 also revealed that the electroanalysis of DA with the CQs modified electrodes has been undertaken mostly with DPV due to the higher sensitivity of the technique relative to some other voltammetric technique.

Other monoamine neurotransmitters such as EP, SE and NE have equally been analysed with the aid of CQs modified electrodes. Compared to the sensors of this nature available for DA detection, the ones dedicated for this purpose are fewer (Table 2.3). In recent times, EP and SE have enjoyed greater attention in this regard. Specifically, there is paucity of data on the determination of NE with CQs based electrochemical sensor. Molecularly imprinted polymers (MIPs) have been combined with N-CQDs prepared from urea and CA for the determination of EP. Yola and Atar combined the EP imprinted MIPs with N-CQDs and graphitic carbon nitride (g-C_3N_4) to form a composite for GCE modification [157]. This electrode showed a very high sensitivity to EP in the presence of UA, AA, DA, NE, tyrosine and tryptophan. Shankar et al., also designed a CQs based sensor for EP detection by combining CQs made from styrene with carbon paste [158]. The resultant CQs/CPE was applied for AA, SE and EP determination individually and simultaneously with very wide peak difference and high sensitivity. In recent times (over a decade), NE determination has not been attempted with the aid of a CQs modified electrode but such electrode made from GQDs abound.

The electrochemical detection of monoamine NTs with CQs of the green origin has not been reported. The green CQs based monoamine NTs sensors in literature are fluorescence sensors [159, 160]. This explains the decision to adopt the CQs from banana peel as a component of the monoamine NTs sensors in this study. Interestingly, the results obtained at the green CQs based sensor will be compared with that of the synthetic CQs (from pencil graphite) based sensor.

Table 2.2: Figures of merit describing the performance of carbon-based QDs for dopamine detection (Reprinted from [2])

Electrode Support	Electrode	QD precursor	Method	LOD (nM)	LDR (μM)	Peak difference (mV)			pH	Validating sample	References
						AA-DA (DA-tyr)	UA-DA (DA-EP)	AA-UA (UA-trp)			
GQDs	GQDs/GCE	CA	DPV	50	0.4-100	148	-	-	7.0	DA injection	[14]
	Au-GQDs/Nafion/GCE	Carbon black	DPV	840	2-50	-	-	-	7.4	Human urine (HU)	[117]
	CS/N-GQDs/SPCE	Glucose	DPV	145	1-200	171	46	-	7.0	HU	[42]
	GQDs-Nafion/GCE	Graphite	DPV	0.45	0.005-100	-	-	-	7.0	DA injection	[161]
	GQDs-eth/GCE	CA	DPV	115	1-150	288	194	-	7.0	DA injection	[162]
	SnO2/PANI/N-GQDs/GCE	Glucose	DPV	220	0.5-200	288	199	-	7.0	-	[25]
	GQDs-TMSPED-AuNCs/GCE	Glucose	AP	5	0.005-2.1	-	(412)	-	7.0	DA injection & HU	[102]
	H-GQDs-GMA	CA	DPV	0.29	0.001-80	-	-	-	7.0	Rat brain	[103]
	GQDs/MWCNTs/GCE	Glucose	DPV	95	0.25-250	-	-	-	7.0	Human serum (HS)	[41]
	GQDs/SPE	CA	DPV	500	1-900	(435)	-	-	7.0	DA ampoule & Urine	[26]
CQs	CD-CQs/GCE	CA	DPV	140	4-220	-	(150)	(420)	7.0	Urine	[156]
	GCE/CQs	Propanol	DPV	4.6	0.05-2	-	-	-	7.0	Urine	[15]
	GCE-CQs	Graphite	LSV	2700	0.19-11.81	-	-	-	7.0	-	[27]
	CQs-CS/GCE	Glucose	DPV	11.2	0.1-30	-	-	-	7.0	DA injection	[109]
	IL-graphene/CQs/GCE	Graphene oxide	DPV	30	0.1-600	-	-	-	6.5	Bovine serum	[108]
	NCQDs-nafion/GCE	Collagen	DPV	1.0	0.0-1000	-	760	340	7.4	-	[142]
	NCQDs/GCE	DEA	DPV	1.2	0.05-800	580	-	-	6.5	HS and HU	[141]
	CQs/GCE	Glucose	DPV	26	0.15-150	-	-	-	6.0	Human plasma	[154]
	AuNP/CQs-CS/GCE	Sucrose	DPV	1.0	0.1-30	-	-	-	7.0	DA injection	[116]
	Cu_2O-CQs/Nafion/GCE	Sucrose	DPV	1.1	0.05-45	-	-	-	7.0	HS	[40]
	CQs/SPCE	Graphite	CV	99	1-7	-	-	-	7.4	HU	[115]

2.8.2 Metal oxide nanoparticles (MONPs)

Metal oxide nanoparticles (MONPs) are very significant materials in nanotechnology and applied electrochemistry. This is largely due to the ease of preparation, large surface area, huge intrinsic conductivity, and the low cost of production of these materials. By implication, metal oxide nanoparticles have formed a part of various electrochemical sensor, drug delivery system, fuel cells and semiconductors. Metal oxide nanoparticles have also been used as antimicrobials as well as very efficient photocatalyst. The versatility of MONPs have been linked to their very small size (nanometers).

The periodicity of elements which affects metals has been the major reason for the difference in the properties of MONPs prepared from different metals. MONPs prepared from the combination of group 3-12 metals with oxygen give metallic and semiconducting properties while those formed with other metals are insulating in nature. Semiconducting MONPs are broadly divided into three namely; intrinsic (i-type), electron deficient (p-type) and the electron-rich type of semiconductor (n-type) [163, 164]. The p and n-type semiconductors are collectively referred to as extrinsic semiconductors when foreign dopants are present. The electron deficiency of the p-type semiconductors stems from the fact that they possess excess holes which are the major charge carriers while the excess electrons in the n-type semiconductor are the major charge carriers [164]. The nature of the dopant in a semiconducting material determines its classification as either n or p-type semiconductor. For instance, ZnO nanoparticles are considered n-type semiconductors because it is widely believed that during the growth of the particles, hydrogen served as an unintended dopant while the oxygen vacancy was considered as the reason for the n-type nature of ZnO nanoparticles in some cases [165, 166]. Regardless of what the reason behind this identity is, it has been confirmed that excess electrons are the charge carrier in this material. Also, copper oxide nanoparticles are referred to as p-type semiconductors as a result of the copper vacancies [167]. Just like a typical semiconductor, the i-type MONPs act as both conductor and insulator. This is because i-type semiconductors are generally dopant free.

The antimicrobial properties of MONPs have been a huge relief considering the resistance of pathogens to antibiotics. This is possible due to the improved solubility, catalytic activity and mass transfer of the MONPs which accompanied the small particle size of the metal oxide

Table 2.3: Table of the figures of merit of other monoamine NTs (EP, SE and NE) determination using graphene and carbon quantum dots (GQDs & CQs). Reprinted from [2]

Monoamine NTs	Electrode Support	Electrode	QDs precursor	Technique	LOD (nM)	LDR (µM)	pH	Validating sample	References
Epinephrine	GQDs	GQDs/CS/CPE	CA	CAP	0.3	0.36-380	7.0	Blood serum & EP injection	[16]
		GCE/GQDs/Lac	CA	CV	83.0	1-120	5.2	EP injection	[168]
	CQs	MIP/g-C_3N_4/NCQDs/GCE	CA	DPV	0.0003	0.001-1	7.5	Human urine	[157]
		CQDs/CPE	Styrene	DPV	6.0	0.02-20	7.4	EP injection	[158]
Serotonin	GQDs	MIP/h-BN/GQDs/GCE	Graphite	DPV	0.0002	0.001-10	7.0	Human urine	[169]
	CQs	CQs/CPE	Styrene	DPV	4.0	0.01-8	7.4	-	[158]
Norepinephrine	GQDs	GQDs-AuNPs/GCE	CA	SWSV	150	0.5-7.5	7.0	NE injection & rat brain tissue	[170]
		GQDs/IL/CPE	CA	DPV	60	0.2-400	7.0	NE injection & human urine	[171]

nanoparticles (MONPs) [172]. Although the actual mechanism of the antimicrobial effect of MONPs on pathogens is hardly known, it is expected that the toxicity of the free metal on the nanoparticles surface as well as its solubility played a significant role in this regard. The physicochemical properties of these nanomaterials have also been reported to have significantly influence its antimicrobial properties [173, 174]. Specifically, Dizaj and his group [172] pointed out in a review of the antimicrobial properties of various MONPs that shape, size, concentration, roughness, pH and crystal structure of MONPs are significant factors affecting its antimicrobial properties. In the same vein, MONPs have anti-inflammatory and antioxidant properties. They perform this function by preventing the inflammation of some parts of human body through the reduction in the level of production of substances that triggers such body response. For instance, ZnO nanoparticles have been reported to have performed anti-inflammatory functions by bringing down the level of lymphopoietin produced by epithelial cells [175].

Beyond the therapeutic functions of MONPs, they have proven to be a very important class of nanomaterials in the fabrication of electrochemical sensors for a wide range of analytes. This has been achieved due to the high conductivity, large surface area and their compatibility with a broad spectrum of other nanomaterials. Specifically, MONPs have been comfortably couples with polymers, carbon nanotubes, nanodiamonds, phthalocyanines, graphene and quantum dots for the preparation of electrochemical sensors with very high sensitivity. In most cases, these other materials act as support for the MONPs which have electrocatalytic effect on the analyte. The synergy between the composite containing these materials and MONPs have resulted in the actualization of platforms that gave better current response than what could have been achieved with the MONPs alone. Notable mention is the detection of neurotransmitters with carbon nanotube (CNTs) supported metal oxide nanoparticles targeted towards neurotransmitters detection where the CNTs support provided the requisite synergistic effect on MONPs for the preparation of a sensor sensitive beyond the nanomolar level [44]. Also, phthalocyanines have been reported to offer great synergy with metal oxide nanoparticles and CNTs for the neurotransmitter detection [45]. The significant sensitivity of conventional bare electrodes towards the oxidation of these neurotransmitters after MONPs nanoparticles modification is reflective of their catalytic effect. The detection of notable water pollutants such as the dihydroxybenzenes by MONPs modified electrodes down to the nanomolar level have also been reported. A very good instance can be found in the detection of hydroquinone and catechol at a graphene oxide supported MgO nanoparticles [176].

MONPs have also enjoyed a great deal of patronage in the photocatalytic degradation of pollutants such as dye molecules by acting as a photocatalyst that actively breaks down such pollutants. It has been reported that the utilization of UV-light for electron-hole pair generation in MONPs has been exploited in the initiation of various photocatalytic processes leading to the degradation of dye molecules such as murexide [177], methylene blue [178], malachite green (MG) [179], eriochrome black T (EBT) [177] and malachite blue (MB) [179]. For example, Chanu et al., [180] achieved up to 97 % degradation efficiency for the time dependent photocatalytic degradation of MB and MG with ZnO and SnO nanoparticles. The authors concluded that the degradation was achieved through the adsorption of the dye prior to the mineralization by the photocatalytic degradation.

The very few applications of MONPs highlighted in this section point to the fact that MONPs are very versatile in nanotechnology and as expected, several means have been adopted for their synthesis. These synthetic routes are discussed in the next section.

2.8.2.1 Synthesis of metal oxide nanoparticles

The synthesis of MONPs, metal nanoparticles and some other nanoparticles can broadly be classified into two namely; classification based on precursor and the classification based on the technique of synthesis.

The classification of the MONPs synthesis based on the precursor refers to the nature of the starting materials used for their preparation which are either the traditional chemical synthetic route or the green method of synthesis. The chemical method of synthesis involves the application of the salt of the metal of interest and a reducing agent or surfactant of the chemical origin such as sodium hydroxide, sodium borohydride among others [181-183]. It is very easy to achieve the chemical synthesis of MONPs especially when the toxicity of the resultant material is not top priority. However, like every other nanoparticle the chemical means of MONPs synthesis is more expensive considering the cost of the chemical reductants. The green method of synthesis involves the use of microbial extract, plant extracts, seeds, sprouts and some other plant parts as substitute for the reducing agent. These starting biological materials are used because they possess alkaloids, phenolic compounds, terpenoids and proteins that can act in place of the conventional chemical reductants [184, 185]. The application of these materials for MONPs synthesis has significantly reduced the cost of production of the nanomaterials while making them more environmentally benign. Sutradhar et al., [186] relied on the phenolic components of extracts of coffee, tea and triphala as reductant in combination with aluminum nitrate for the preparation of spherical aluminum oxide nanoparticles. The synthesis of CuO nanoparticles from the leaf extract of Aloe vera and copper nitrate has also been reported [187]. The green nature of this type of MONPs made them more suitable for clinical applications.

The classification based on the method of synthesis refers to either the synthesis via the purely chemical route or the physical means. The chemical method of MONPs synthesis include co-precipitation, electrodeposition, solution combustion, chemical vapour deposition, sol-gel and microemulsion methods [188, 189]. The co-precipitation technique is often used because of its cost-effectiveness as well as the low aggregation and ease of controlling the particle size of the yield [190, 191]. Co-precipitation in MONPs synthesis involves the addition of a precipitating agent such as ammonium hydroxide to the salt of the metal of interest. Preparation of MgO nanoparticles from magnesium nitrate through this technique was reported by Rao and his group [190]. Similarly, preparation of iron oxide nanoparticles with particle size of ~ 20 nm via co-precipitation was reported by Kandpal et al., [191]. Physical method of nanoparticle synthesis includes but not limited to laser and flash spray pyrolysis, laser ablation, physical vapour deposition, ball milling, electrospraying, melt mixing and inert gas enabled condensation [192]. Copper oxide nanoparticle synthesis via laser ablation of copper metal in the presence of water molecules has been reported [193]. The resultant CuO nanoparticles were both crystalline and amorphous. Cathode electrodeposited ZnO nanoparticles have been generated from zinc chloride solution in the presence of oxygen precursor [194]. The hydrothermal method of nanoparticle synthesis is a chemical-physical hybrid method which involves subjecting reacting chemical mixture to a very high temperature (> 100 ^{o}C) and pressure. Arun et al., [195] reported a hydrothermal synthesis of a highly crystalline monoclinic copper oxide nanoparticles (27 nm particle size) from copper sulphate and sodium hydroxide without a surfactant. ZnO-CuO binary nanoparticles for the fabrication of a very sensitive glucose sensor prepared through hydrothermal means has also been reported [196].

Several metal oxide nanoparticles have been adopted for monoamine NTs detection. Notably, MnO_2 [197], MoO_3 [198], NiO [199, 200], Fe_3O_4 [87], ZrO_2 [201], Fe_2O_3 [202], SnO_2 [203, 204], Cu_2O[40], CeO_2 [205], WO_3 [206], $FeMoO_4$ [207], $ZnFe_2O_4$ [208], $FeTiO_3$ [209], Co_3O_4 [210], YO [211], $NdFeO_3$ [212], RuO_2 [213], Ni_6MnO_8 [214], Nd_2O_3 [215], $MnCr_2O_4$ [216], CuO [217], TiO_2 [218], and ZnO nanoparticles [219] and a host of other metal oxide nanomaterials have been incorporated into monoamine NTs sensors. The performance of copper oxide nanoparticles (CNPs) as sensing material for various neurotransmitters underscores their suitability for monoamine NTs electroanalysis. Accordingly, the next few sections of this chapter focus on CNPs properties and their application for neurotransmitters sensors fabrication.

2.8.2.1.1 Copper oxide nanoparticles (CNPs)

Copper based nanoparticles exist in three major forms namely copper, copper I oxide (Cu_2O) and Copper II oxide (CuO) nanoparticles. Cu_2O (cuprous oxide) nanoparticles are a product of partial oxidation of nanosized copper and therefore can be further oxidized to the more stable CuO (cupric oxide) nanoparticles. The copper oxide nanoparticles in this section and subsequent ones refer to the more stable cupric oxide (CuO) nanoparticles. Copper oxide nanoparticles (CNPs) are monoclinic p-type semiconducting material with band gap energy < 2 eV and a dark brown colouration [220, 221]. It has found tremendous application in catalysis, solar cells development, batteries manufacture, superconductors fabrication and electrochemical sensing. CNPs have also showed excellent antimicrobial activity towards microbes among other applications [222]. The large surface area, high electrical conductivity and good photovoltaic attributes of CNPs are responsible for its versatility. Precisely, its small size contributed immensely to its application as an antimicrobial, thus serving as alternative to antibiotics which microbes are fast becoming highly resistant to [223]. Jadhav et al., [223] attributed the antibacterial properties of CNPs to their stability in colloidal medium where such bacteria are present which hastens the modulation of its phosphotyrosine profile, thus impairing its growth. The application of CNPs in electrochemical sensors has been a significant area of research in electrochemistry in the last few years. CNPs have been combined with polymers, graphene, graphene oxide, MWCNTs and some other materials to form composites with much better catalytic activity towards various analytes than CNPs [224-229]. CNPs have also been applied as the sole modifier of conventional electrodes for sensor fabrication [230]. NTs are one of the various classes of analytes that have been extensively analysed with the aid of CNPs modified electrodes. As would be seen in the next section, these sensors offered exceptional sensitivity to monoamine neurotransmitters.

2.8.2.1.2 CNPs modified sensors for monoamine NTs detection

Dopamine detection with CNPs modified electrodes has been attempted to a much greater extent than that of the ZNPs modified electrodes with huge success. These sensors are either fabricated by the modification of conventional electrodes with only CNPs or a composite containing CNPs. One of the sensors made via the modification of GCE with CNPs was presented by Sandar et al. Green CNPs synthesized from a copper salt, sodium hydroxide and a fruit extract was used for the modification of GCE prior to DA detection with the resultant CNPs/GCE [217]. The sensor gave a detection limit of 0.1 µM over a linear range of 0.1 - 105 µM when applied for varying DA concentration using DPV. Using the hydrothermal technique, Baloach and his group synthesized CNPs and subsequently applied them as modifier of a bare GCE [230]. The resultant sensor gave a similar detection limit (0.11 µM) to the one reported by Sandar et al., albeit over a narrow linear range (5 - 40 µM) [217]. Through the electrochemical oxidation of copper nanoparticles supported on a pencil graphite electrode, Bahrami and his team [226] fabricated a DA sensor with a higher detection limit (1.06 µM) over a wider linear range (0.3 – 53 µM) than that of Nafady et al., [230]. On the other hand, CNPs have been combined with other materials such as MWCNTs [231], graphene oxide [232], metal nanoparticles [233], other MONPs [234], graphitic carbon nitride (g-C_3N_4) [235, 236], polymers [237, 238]. For instance, Reddy et al., [239] investigated the impact of the shape of CNPs on the electrocatalytic oxidation of DA by using CNPs of different shapes and poly(glycine) as CPE modifier. The sensor containing the flake shaped CNPs gave a lower detection limit and a better peak separation (with respect to AA) than the electrode modified with poly(glycine) and a rod-shaped CNPs. Another notable CNPs based sensor fabricated from a combination of 2-dimensional g-C_3N_4 and CNPs. This sensor offered a very low detection limit (0.1 nM) over a very wide linear range (2 nM - 71.1 µM) [236]. In some cases, CNPs formed a part of a ternary composite for improved catalytic effect on DA oxidation [231, 240, 241]. A sensor of this architecture was presented by Yang et al., by combining CNPs, MWCNTs and nafion for GCE modification [231]. This sensor offered a detection limit of 0.4 µM for DA detection over a linear range of 1.0 -80 µM using the differential pulse anodic stripping voltammetry (DPASV). Compared to the data on DA detection with CuO modified electrodes, fewer sensors are available on the detection of SE, NE and EP. One of such sensors targeted towards SE detection presented by Ashraf et al., [242] was fabricated by depositing Pt nanoparticles on CNTs/Cu_2O-CuO nanocomposite initially immobilized on GCE [242]. This sensor offered a detection limit of 3 nM using the amperometry technique. EP detection using CNPs with colorimetry and fluorimetry [243, 244] has been reported but CNPs modified electrochemical sensor for EP detection are almost inexistent in literature. In the same vein, CNPs modified electrode for NE detection are unavailable up to this moment of writing this report.

Table 2.4 showedsome figures of merit for some CNPs modified electrodes. It could be seen at a glance that quite a number of materials have been combined with CNPs for the preparation of electrochemical sensors for dopamine (DA) and serotonin (SE) detection. However, the application of CNPs modified electrodes for the detection of other monoamine NTs was hardly investigated. Also, the combination of CNPs with carbon based nanomaterials such as CNT, GO and rGO gave very sensitive electrodes with detection limits not less than the micromolar level. It could also be inferred from Table 2.4 that DPV was often used to prosecute the determination of the calibration curve for most of the sensors in the presence of the monoamine NTs. The findings of this literature survey and the reliable electrocatalytic activity of CNPs in the presence of monoamine neurotransmitters informed the choice of CNPs in the present study. Also, the paucity of data on the combination of CNPs with carbon nanomaterials as electrochemical sensing platform for NE and EP as well as the established electrocatalytic activity of CNPs towards DA oxidation contributed to the selection of CNPs in the present study.

Moreover, Table 2.4 showed that the class of carbon based materials that was not combined with any of these MONPs (TNPs, CNPs and ZNPs) is the carbon based quantum dots. Considering the large surface area, biocompatibility and the electrical conductivity of carbon nanomaterials, it is expected that the combination of CNPs with carbon based QDs would yield electrochemical sensors with high sensitivity to the monoamine neurotransmitters. The high expectation, the need for novel NTs sensors, and the quest for an environmentally benign electrochemical sensor is the premise for undertaking the present study.

Table 2.4: Some metal oxide based sensors for monoamine NTs detection and their figures of merit

Analyte	Electrode	Technique	Detection limit (µM)	Linear range (µM)	Real sample	References
DA	GCE/CuO	AP	0.11	5-40	Human serum	[230]
	CPE/polyglycine/rCuO	DPV	0.18	0.3-20	-	[239]
	CPE/polyglycine/fCuO	DPV	0.055	0.6-20	-	[239]
	MIPs (pNA)/CuO/GCE	CV	0.008	0.02-25	Human serum	[245]
	NiO-CuO/GR/GCE	SWV	0.17	0.5-20	Human serum	[241]
	ZnO-Cu_xO-PPy/GCE	DPV	0.04	0.1-130	DA injection & human urine	[234]
	2D g-C_3N_4/CuO/GCE	AP	0.0001	0.002-71.1	Human serum	[236]
	Ag/CuO/ITO	CV	7.0	0.04-10	Human serum	[233]
	GCE/CuO/g-C_3N_4	DPV	0.06	0.2-78.7	Human serum	[235]
	CuO/GCE	DPV	0.1	0.1-0.105	-	[217]
	CuO/MWCNTs/Nafion/GCE	DPASV	0.4	1-80	DA injection	[231]
	GO/CuO/CPE	CV	0.5	-	DA injection	[232]
	Cu/Cu_xO/PGE	DPV	1.07	0.3-53	-	[226]
	rGO/Pd@PPy/GCE	DPV	0.056	1000-15000	Human serum	[240]
	CPE-PPy/CuO	DPV	0.02	0.06-1000	Human serum	[238]
SE	CNTs-Cu_2O-CuO/Pt	AP	0.003	0.015-3000	Liver cell	[242]

2.9 Characterization techniques

Characterization is essential for identifying materials. In some cases characterization of industrial materials has been carried out to confirm the suspected shape, size, crystal structure, surface area and elemental composition of such materials. On the other hand, characterization of materials serves to give details about some other properties of the material such as the wettability, tensile strength, hardness, Young modulus, conductivity, resistance, impedance, elongation at break among others. Specifically, nanomaterials have been largely characterized through the spectroscopic, microscopic, and the electrochemical methods. Thermogravimetric analysis has also proven very useful for nanomaterials characterization.

2.9.1 Spectroscopic characterization

Spectroscopic characterization of nanomaterials is dependent on the information that can be obtained from the interaction between nanomaterials and light. Infrared spectroscopy (IR), mass spectrometry (MS), nuclear magnetic resonance (NMR), Raman spectroscopy (RS), ultraviolet-visible (UV-visible) spectroscopy, optical emission spectroscopy (OES), atomic emission spectroscopy (AES), energy dispersive x-ray spectroscopy (EDS), electron spin resonance spectroscopy (ERS), x-ray diffraction spectroscopy (XRD) and x-ray photoelectron spectroscopy (XPS) are few of the routine spectroscopic characterization techniques in nanotechnology. Although all of these techniques are important in nanotechnology and material science at large, few of them will be given special attention in this section.

i. **Infrared spectroscopy:** The infrared (IR) spectroscopy can be used for obtaining the functional groups present in a materials as a result of the vibrational motion provoked by the interaction between infrared light (wavelength between 2.5-25µm) and the materials [246]. The fact that each chemical bond absorb the IR light at different wavelengths gives diagnostic information about the different functional groups present in a material. The IR spectrum is a graph of the wavenumber (cm^{-1}) against the percentage transmittance. The higher the transmittance at a given wavenumber, the lower the intensity of such absorption. The spectrum obtained using an advanced form of the dispersive IR spectrometer (DIR) called Fourier-Transform IR (FT-IR) spectrometer is often reported. This spectrometer is so named because it uses a mathematical operation called the Fourier Transform to convert a time domain spectrum to a frequency domain spectrum which is identical to that of the DIR spectrometer [247]. FT-IR spectrometer generates spectrum at a faster rate than the DIR.

ii. **Raman spectroscopy:** Raman spectroscopy helps in functional group identification, especially when the IR-spectroscopy fails. This is because not all molecules are IR-active. Bond whose dipole moment does not change with the incoming electromagnetic radiation in IR-spectroscopy cannot be detected by the IR spectrometer. Raman spectroscopy is based on the frequency shifts that occur when monochromatic visible light is focused on a material, hence no restriction as regards the type of functional groups to be detected [248, 249]. Frequency shifts take place because the scattered light from the material which is naturally expected to be of the same frequency as the incident light has a certain percentage with frequency above and below this incident light. A plot of the intensity of the scattered light and the frequency shit gives the Raman spectrum [249]. Similar to the IR spectrum with wavenumber scale of 4000 – 400 cm^{-1}, the frequency shift is reported in the wavenumber format (4000 -20 cm^{-1}). Contrary to what obtains in IR spectroscopy, change in electronic polarizability of the bonds during vibration is of utmost importance in Raman spectroscopy [250].

iii. **UV-visible spectroscopy:** This involves getting information about the electronic transition that ensues when light in the UV-visible region of the electromagnetic spectrum interacts with a material under study. These electronic transitions often help in gathering data (such as the maximum absorption wavelength, λ_{max}) on the functional groups present in a certain material and the possible position of such functional groups within such material. Noteworthy, the electronic transitions are often from the lowest unoccupied molecular orbital (LUMO) and the highest occupied molecular orbital (HOMO) [247]. The UV-visible spectroscopy can as well help in drawing a convincing inference about the functional groups earlier suspected in the FT-IR spectroscopy. For instance, a material with C=C and C=O confirmed from FT-IR spectroscopy can further be characterized with UV-visible spectroscopy to confirm the relationship between the two functional groups. Also, the maximum absorption (λ_{max}) obtained from a compound could be unique to such material, thus aiding its identification. A typical UV spectrum is a plot of wavelength against absorbance.

iv. **X-ray diffraction (XRD):** XRD spectroscopy basically gives information about the crystal structure of materials based on resultant diffraction pattern after interaction with x-ray. This gives information that helps in obtaining the crystallite particle size, lattice constants, phases of such material, degree of crystallinity among other properties [251, 252]. In nanotechnology, the reliance on the unique diffraction pattern of a particular material, even in complex mixtures makes XRD spectroscopy a very significant characterization tool. The Debye Scherrer

($D=0.9\lambda/\beta\cos\theta$) equation can be used to obtain the crystallite particle size of a material from a x-ray diffractogram given that D, λ, β and θ represent the crystallite particle size, wavelength of the x-ray, full width of the peak at half maximum (FWHM) and Bragg's angle (diffraction angle in radians), respectively [253]. Bragg's law ($n\lambda=2d\sin\theta$) can be used to obtain the interlayer spacing between layers of a nanomaterial. For instance, the interlayer spacing (d) of graphene sheets in carbon nanotubes have a unique value that makes the identification of graphitic materials through XRD spectroscopy easier [254]. The symbols θ, n and λ in Bragg's equation represent the diffraction angle (in degrees), order of reflection and wavelength of the x-ray, respectively. Also, the strain in the particles as a result of imperfection of the crystals (lattice strain, ε) can be obtained using the equation $\varepsilon=\beta/4\tan\theta$ with the variables retaining their usual identity. Lattice strain is a product of crystal imperfections like lattice dislocation and stacking faults and has been reported to equally be responsible for peak broadening, just like the crystallite size [255]. Using Williamson-Hall (W-H) equation ($\beta\cos\theta = \varepsilon(4\sin\theta) + k\lambda/D$), the lattice strain and the crystallite particle size can also be obtained by plotting a graph of $\beta\cos\theta$ against $4\sin\theta$. Lattice strain, ε and the crystallite size, D can then be obtained from the linear relationship obtained from this plot [255, 256]. Noteworthy, every variable in W-H equation retains their usual identity.

v. **Energy dispersive x-ray spectroscopy (EDS):** EDS is an efficient elemental analysis tool used in combination with the scanning electron microscopy (SEM). The basic principle of this technique is the emission of an x-ray when a high energy charges are focused on the surface of a material. This interaction gives different energy profiles depending on the composition of the material under study [257, 258]. Apart from the fact that the wavelength of the x-ray emitted is specific for each element, the percentage of such element in the sample can as well be obtained by recording the rate at which such x-rays are generated [258]. This makes the EDS both a qualitative and quantitative tool for characterization in material science.

2.9.2 Electrochemical characterization

Among other techniques, the electrochemical characterization of a material can be done through the voltammetric technique and the electrochemical impedance spectroscopy (EIS). The voltammetry method is often carried out with the aid of cyclic voltammetry by generating voltammograms which originally gives information about the redox nature of the analyte after interaction with an electrocatalytic material. The surface area of the material can as well be obtained using the data from the voltammogram. The EIS is a very important characterization technique in nanotechnology and material science at large. For this fact, detailed information concerning its mode of operation and output would be discussed in the next section.

2.9.2.1 Electrochemical impedance spectroscopy

Optical spectroscopy produces diagnostic information from the interaction of a sample with light in the electromagnetic spectrum. The electrochemical impedance spectroscopy on the other provides information about a material when subjected to an alternating current (AC) potential. According to Ohms law, the current and resistance offered to the flow of such direct current are in phase. The resistance in this case is independent of frequency and cannot sufficiently describe every properties of a material. Impedance which is a measure of the resistance to the flow of an AC through a material is frequency dependent. This is because impedance (Z) is mathematically a ratio of the out-of-phase potential and current amplitudes which are frequency dependent. This ratio gives complex numbers such that the EIS data obtained are reported in the complex plane among some other forms [259].

The Nyquist plot is a plot of the real against the imaginary part of the impedance (Fig. 2.12 (a)). The Nyquist plot gives information about the various forms of resistance, capacitance and the deviation from the ideal capacitive and resistive behavior of a material (CPE) [140]. The relationship between the magnitude of CPE and its exponent n is a complex number. The values of n vary from -1 to 0 where n values of 0, 1, -1, suggest that the material is a perfect resistor, capacitor and inductor, respectively with respect to the experimental conditions. The possibility of mass transfer towards the material through diffusive mechanism can be obtained from this plot via the Warburg impedance (W). This appears as a straight line at the terminal end of a semicircle in a Nyquist plot [260]. Figure 2.12 (a) showed a typical Nyquist plot and some basic circuit elements.

The plot of the logarithm of frequency against the modulus of impedance is referred to as the Bode plot. The modulus of impedance is a measure of the ability of the material to prevent current flow. As a result, it is often used as an index of the conductivity of nanomaterials and some other materials such as polymers and protective coatings in corrosion studies [261]. The phase angle diagram is a plot of the logarithm of frequency against the phase angle. This explains why the Bode plot and the phase angle diagram are often represented by a single plot (Fig. 2.12 (b)). The deviation of the phase angle obtained for a material from an ideal phase angle of -90 ^{o} is a deviation from an ideal capacitive or resistive behavior [262]. This is because the experimental phase angles are obtained as product of n and 90 ^{o} (n x 90 ^{o}). Figure showedtypical Bode and phase angle diagram.

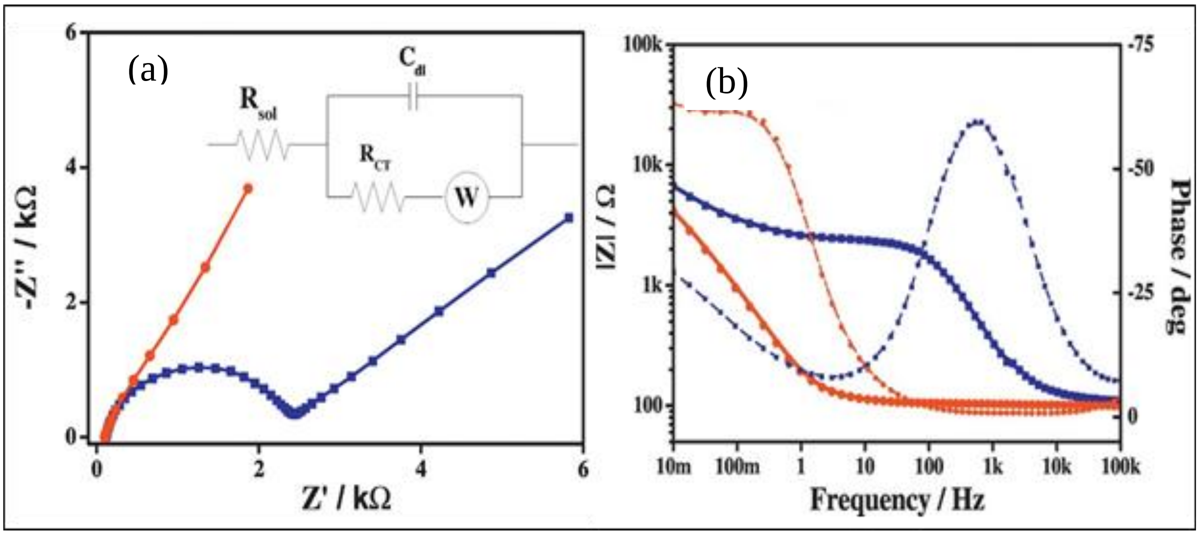

Figure 2.12: Typical (a) Nyquist plot and (b) Bode plot and phase angle diagram from EIS data of two different materials (white and red plot). Reprinted with permission from [260] (Copyright Elsevier, 2017).

2.9.3 Microscopic characterization

Microscopic techniques in material science are mostly used for surface characterization of materials in order to obtain details about either the surface morphology of internal structure of such materials. Three of these microscopic techniques namely scanning electron microscopy (SEM), transmission electron microscopy (TEM) and atomic force microscopy (AFM) would be discussed in this section.

i. **Scanning electron microscopy (SEM):** This involves the use of electron microscope to obtain information about the topography and the morphology of the surface of a material [263]. This information technically called micrograph are generated when low-energy electron beam (primary electrons) are focused on a sample and the image obtained due to backscattered secondary electrons [253]. The particle size of such material can as well be obtained from SEM micrograph (Fig. 13 A). SEM can be coupled with EDS for determination of the elemental composition of a material. SEM micrographs give detailed information about the surface of a sample depending on the magnification and the resolution of the microscope.

ii. **Transmission electron microscope (TEM):** TEM can be applied for the determination of the internal structure of a material. Just like the SEM micrograph, it helps in obtaining the particle size distribution and by implication the average particle size of a material. As opposed to the image collection due to backscattered electrons from the sample's surface in SEM, TEM micrographs are obtained as a result of scattered electron beams travelling through a very thin version of the sample [264]. TEM gives a more precise particle size and spatial resolution of higher quality than the SEM. Consequently, it is preferred over SEM for the determination of the particle size of nanomaterials [264, 265].

2.9.4 Thermogravimetric analysis (TGA)

Thermogravimetric analysis is a method used for estimating the weight of a sample with changes in temperature (or time). The sample may be subjected to heating at a constant temperature or heating rate. In some cases, the temperature programs may be non-linear as seen in sample controlled thermogravimetric analysis [266, 267]. TGA analysis can be conducted in an inert or reactive atmosphere. Depending on the nature of the sample and the information required from the analysis, the atmospheric state can be adjusted during sample analysis [266]. The changes in the weight of the sample as the temperature changes give a TGA profile that reveal the material's thermal stability. This information has been beneficial for the characterization of polymers and nanomaterials [268, 269]. The temperature at which changes such as loss of volatile components, oxidative decomposition, water loss (or uptake), and thermal decomposition occur in a sample can be monitored with TGA, thus providing valuable information about the physical and chemical properties of the sample. The TGA curve is often a plot of the weight percent against temperature [268, 269].

CHAPTER THREE

MATERIALS AND METHODS

3.0 Materials and methods

The reagents, equipment, and other materials used for the synthesis of the nanomaterials and composites have been highlighted in the present chapter. Furthermore, the methodologies for the synthesis and characterization of the nanomaterials and composites used in the study were discussed. The preliminary electrode treatment and the electrochemical parameters applied in each of the electrochemical experiments were also outlined in this chapter.

3.1 Materials and reagents

3.1.1 Chemicals

Potassium permanganate (97 % $KMnO_4$), copper sulphate pentahydrate (98 % $CuSO_4.5H_2O$), sodium hydroxide (99 % NaOH), hydrofluoric acid (75 % HF), dimethyl formamide (99.8 % $(CH_3)_2CONH$), ethanol (99.9 % C_2H_5OH), acetone ($(CH_3)_2CO$), hydrogen peroxide (H_2O_2), sulphuric acid (99 % H_2SO_4), calcium hypochlorite (99 % $Ca(ClO)_2$), dichloromethane (99.9 % CH_2Cl_2), ascorbic acid (99 %), uric acid (> 99 %), dopamine hydrochloride (99 %), epinephrine hydrochloride (99 %), norepinephrine hydrochloride (> 98 %), distilled water, dopamine hydrochloride injection (200 mg/5mL) and epinephrine injection (1:1000 solution). Disodium hydrogen phosphate (99 % Na_2HPO_4) and sodium dihydrogen phosphate (99 % NaH_2PO_4) were used for the preparation of pH 7 phosphate buffer solution. A combination of potassium hexacyanoferrate III (99 % $K_3[Fe(CN)_6]$) and potassium hexacyanoferrate II (99 % $K_4[Fe(CN)_6]$) was used for the preparation of the 5 mM redox probe. All reagents were of analytical grade and supplied by Merck, Sigma Aldrich chemicals (South Africa).

3.1.2 Materials and equipment

The materials used in the study include autoclave, centrifuge, conical flasks, beakers, burette, fume hood, Whatman filter paper, hot plate, magnetic stirrer, dry air oven, bar magnet, and glassy carbon electrode (2 mm diameter). The Opus Alpha-P FT-IR spectrophotometer used for functional group analysis was supplied by Bruker Optics, Germany. The Uviline 94000 UV-visible spectrophotometer was supplied SI analytics, Germany. XRD spectroscopy data were collected with Rontgen PW3040/60 X'Pert Pro diffractometer supplied by PANalytical, USA. Scanning electron microscopy analysis was done with the Quanta FEG 250 scanning electron microscope supplied by ThermoFisher Scientific, USA. TEM analysis was carried out with JEM-1400 transmission electron microscope supplied by JEOL Ltd., USA. Thermogravimetric analysis was done using SDT Q600 thermogravimetric analyser procured from TA instruments, USA. Pencil graphite was obtained from HB pencils procured from shop rite, megacity mall, Mafikeng, Mmabatho, South Africa. Banana peels were collected from banana purchased from same location as the HB pencils.

All electrochemical studies were done at an Autolab PGSTAT 302N electrochemical work station (three-electrode system) with glassy carbon working electrode, platinum counter electrode and Ag/AgCl reference electrode with 3 M KCl. The work station ran on the Nova 2.1.3 software. The workstation and the software were supplied by Metrohm, South Africa.

3.2 Methods

3.2.1 Preparation of banana peel for green carbon quantum dots synthesis

The banana peel (BP) precursor for green carbon quantum dots (bCQDs) synthesis was washed with copious amount of distilled water and dried in a dry air oven at 50 ^{o}C. Afterwards, the dry BP was crushed and grounded using a mortar and pestle to obtain fine BP particles. The fine BP particles were stored in clean sample bottles for bCQDs synthesis.

3.2.2 Synthesis of green carbon quantum dots (bCQDs)

The synthesis of the green carbon quantum dots was achieved using a hydrothermal technique presented by Tyagi et al., [29]. The dried banana peels were made into a powdery form using mortar and pestle to provide large surface area for the hydrothermal process. About 4 g of the powdery banana peels were transferred into a beaker 100 mL of 0.2 M H_2SO_4. Then, the suspension was washed with distilled water several times and dried in an oven at 100 ^{o}C for 5 hours. The dried sample was subsequently dispersed in 100 mL of calcium hypochlorite for 5 hours. The sample was then washed with distilled water until it attains a pH of 7. The hydrothermal synthesis of the aqueous mixture of the banana peels was done using an autoclave at 210 ^{o}C for 10 hours. The product obtained from the autoclave was mixed with dichloromethane to remove unreacted organic components. The aqueous solution of the dark brown carbon dots was centrifuged and subsequently dried at 90 ^{o}C for 24 hours to obtain dry carbon dots.

3.2.3 Chemical synthesis of carbon quantum dots

Using the Hummer method as presented by Algarra et al., [27], the synthetic carbon quantum dots were prepared from a pencil graphite precursor. Initially, about 1 g of the pencil graphite was dispersed in a conical flask containing a mixture of hydrofluoric acid (50 mL HF) and potassium permanganate (6 g of $KMnO_4$). The mixture was transferred into a Teflon reactor and refluxed at 100 ^oC for 1 hour. About 10 mL of hydrogen peroxide was added to this mixture after cooling at room temperature. The resultant mixture was diluted with distilled water and centrifuged for 30 minutes at 3000 rpm. The upper fluorescent suspension was separated from the lower less fluorescent deposit and dried at 100 ^oC for 12 hours.

3.2.4 Synthesis of copper oxide nanoparticles (CNPs)

The synthesis of copper nanoparticles was done using a chemical precipitation method proposed by Hwa et al., [270] with slight modification. Copper sulphate pentahydrate ($CuSO_4.5H_2O$) solution (40 ml of 0.2 M) and 1 M sodium hydroxide (20 ml) solution were prepared in separate conical flask. The copper sulphate solution was placed under magnetic stirring for about 10 minutes before the addition of sodium hydroxide solution in drops from a burette. The mixture was continuously stirred for about 3 hours. The resultant precipitate was allowed to settle overnight and washed with copious amount of water and ethanol through centrifugation at 3000 rpm for 15 minutes. The precipitates obtained was dried in a dry air oven at 60 ^0C for 12 hours and calcinated at 300 ^oC in a furnace.

3.2.5 Preparation of carbon based quantum dots and copper oxide nanocomposites

About 5 mg of the synthetic carbon dots (CQDs) were added to the same mass of copper oxide nanoparticles (CNPs). The resultant mixture was dispersed in N,N-dimethyl formamide (DMF) and mixed continuously in sonicator at room temperature for 24 h. The formation of composite involving the green banana peel carbon quantum dots (bCQDs) was achieved through the same method using 5 mg bCQDs and 10 mg of the CNPs. The homogeneous paste of the composites was stored at room temperature for further use.

3.2.6 Characterization of synthesized nanomaterials and composites

The formation of the nanomaterials was confirmed through the spectroscopic and microscopic techniques. The methods applied were the transmission electron microscopy (TEM), scanning electron microscopy (SEM), x-ray diffraction spectroscopy (XRD), UV-vis spectroscopy, FT-IR spectroscopy and thermogravimetric analysis (TGA). The electrochemical characterization of the materials was done using CV and EIS in the presence of the $[Fe(CN)_6]^{3-/4-}$ redox probe and the analyte. JOEL microscope (USA) was used for TEM analysis.

FT-IR analysis was done with the solid samples of the banana peel (BP), nanomaterials (CQDs, bCQDs and CNPs) and composites (CQDs/CNPs and bCQDs/CNPs) using the FT-IR spectrometer powered by the Opus software. After the background analysis, about 5 mg of the samples were placed in the sample compartment of the FT-IR spectrophotometer sensor held in position by the lid of the sample compartment. The acquired spectra were smoothened, normalized and saved for further processing.

The UV-visible analysis was done with liquid samples of the nanomaterials and composites. The samples were dissolved in N,N-dimethyl formamide (DMF) and subsequently diluted with DMF to about 10 µM. After adjusting the UV-visible spectrophotometer to a wavelength range of 200 – 800 nm, a blank measurement using the solvent was done prior to the acquisition of the UV-visible spectra with individual diluted samples. The acquired spectra were saved for further processing.

XRD analysis was also done with the solid form of the nanomaterials and the composites. About 10 mg of the samples were placed in a sample holder (one sample at a time) and pressed further into the sample holder with a pressing block. Excess particles of the materials were removed with a brush before inserting the sample holder into the sample compartment of the diffractometer. The scan rate was adjusted to 2^{o} min^{-1} and the diffractograms were recorded. The diffractograms were saved for further processing. The data recorded using FT-IR, UV-visible and XRD spectrophotometers were processed with Origin 2021 software.

SEM analysis was done by placing about 20 mg of the nanomaterials and composites on a mounting pin containing a carbon sticker (one sample at a time). The mounted materials were calibrated to obtain the optimum height for the samples before analysis. The mounting pin was transferred to the specimen page and the electron gun was activated. The magnification and resolution of the microscope were adjusted to obtain the desired details of the SEM images.

The TEM images were acquires by placing about 10 mg of the samples on a copper grid with the aid of a sample rod. The samples were inserted into the microscope through the air lock and the filament is switched on. The resolution and magnification of the microscope were adjusted to capture TEM images with the desired details.

Thermogravimetric analysis (TGA) was done by putting about 18.861, 5.588, and 18.833 mg of BP, CQDs, and bCQDs in a sample pan (one sample at a time). The sample pan loaded with the sample was placed in the furnace and the furnace was subsequently closed. The TGA profile of the samples was generated in air with the aid of the TA Universal Analysis 2000 software by setting the temperature range of the thermogravimetric analyser to 0 -1400 ^{o}C.

3.2.7 Electrode pretreatment

The bare glassy electrode was cleaned over a cleaning pad containing aqueous aluminum oxide in a spiral fashion and immediately rinsed with distilled water. The electrode was transferred into methanol to remove organic impurities yet unremoved before finally washing with distilled water under ultrasonication. The cleaned electrode was dried in the oven at 50 ^{o}C and kept at room temperature for further use.

3.2.8 Modification of electrodes

The modification of electrodes was done via the drop casting technique. Briefly, about 10 µL of the paste of the nanomaterials and composites were dropped on the surface of the clean bare GCE and placed in a dry air oven at 50 ^{o}C for 4 minutes to obtain the modified electrodes. The modified electrode were coded GCE/CNPs, GCE/CQDs, GCE/bCQDs, GCE/CQDs/CNPs and GCE/bCQDs/CNPs.

3.2.9 Electrochemical characterization and preliminary electroanalysis procedures

Using the earlier described electrochemical work station, electroanalytical characterization of the nanomaterials and the composites was done using cyclic voltammetry (CV) over a potential window of -0.4 - 0.9 V (or as specified) with the modified electrodes in $Fe[(CN)_6]^{3-/4-}$ redox probe prepared with PBS of pH 7. The voltammograms obtained with the bare electrode and electrode modified with individual nanomaterial and composites (GCE/CNPs, GCE/CQDs, GCE/bCQDs, GCE/CQDs/CNPs and GCE/bCQDs/CNPs) were used to obtain the anodic and cathodic peak current (I_{ap} and I_{cp}) and potentials (E_{ap} and E_{cp}) as well as the peak separation of the anodic and peak currents (ΔE_p). The experiment was repeated using the analytes (DA, EP and NE) instead of the redox probe. Using the redox probe, the surface area of these materials and the reversibility of the redox process were determined using the Randle Sevcik equation (Equation 2.1) and the I_{ap}/I_{cp} ratio, respectively. The scan rate studies were done with CV over a range of 25-400 mVs^{-1} using the analytes (DA EP and NE) for the determination of the mechanism of interaction of the analytes with the modified electrode. A plot of the scan rate (or square root of the scan rate) against the peak currents (I_{ap} and I_{cp}) gave

The electrochemical characterization of the modified electrodes through EIS was done over a frequency range of 10^{-2} – 10^{5} Hz with 0.05 V rms sinusoidal modulation. The EIS data were obtained at the anodic peak potential or at the formal potential E^{o} for a reversible process. The formal potential is the average of the anodic and the cathodic peak potentials (E_{ap} and E_{cp}). The

EIS parameters of each of the materials with respect to the analytes such as charge transfer resistance (R_{ct}), constant phase element (CPE), Warburg impedance (W), capacitance (C) and the solution resistance (R_s) were obtained after fitting the EIS data with the respective equivalent circuit obtained with each material.

3.2.10 pH studies

The effect of pH on the electroanalysis of DA, EP, and NE was investigated using the same approach. Firstly, the pH of the electrolyte (0.1 M PBS) was adjusted to approximately 3, 5, 7, and 9 using 0.1 M HCl or 0.1 M NaOH solutions, depending on the desired pH. Afterwards, 0.4 mM of the neurotransmitters (NTs) were prepared using the electrolytes with the adjusted pH (pH 3-9). The cyclic voltammogram of the neurotransmitter solutions prepared at various pH (conducted at 25 mV s^{-1}) showed the variation of peak currents and potentials with pH. The cyclic voltammetry experiments were carried out with the modified electrodes (GCE/CQDs/CNPs and GCE/bCQDs/CNPs) to investigate the effect of pH of the NTs at the two sensors.

3.2.11 Scan rate studies

The effect of scan rate on the electroanalysis of DA, EP and NE was investigated using the same method. Cyclic voltammetry was conducted at pH 7 using GCE/CQDs/CNPs and GCE/bCQDs/CNPs for the electroanalysis of each of the NTs over a scan rate range of 25 – 400 mV s^{-1}. The variation of the anodic peak currents and potentials with changes in scan rate revealed the effect of scan rate on the electroanalysis of the NTs.

3.2.12 Concentration studies

The effect of concentration of individual analytes (in PBS of pH 7.0) on current response was investigated at the modified electrodes using the square wave voltammetry due to its superior sensitivity compared to cyclic voltammetry (CV). The limit of detection (LoD), limit of quantitation (LoQ) and linear dynamic range (LDR) of the electrodes with respect to an analyte was obtained from the calibration curve recorded from a plot of the concentration of analytes against the peak current. Noteworthy, the LoD detection limit was calculated using the relationship 3.3 δ/m where m and δ represented the slope of the calibration curve and the standard deviation of the intercept of the calibration curve, respectively. The LoQ was calculated from the relationship 10 δ/m, where each variable retained their usual meaning.

3.2.13 Stability and reproducibility studies

Stability of the electrodes toward the detection of DA, EP, and NE was investigated by running 22 cyclic voltammetry scans with GCE/CQDs/CNPs and GCE/bCQDs/CNPs in the presence of 0.4 mM of each of the NTs. The percentage current loss at the end of the 22 CV scans was used to estimate the stability of the sensors for the detection of the NTs. The current loss estimated from the CV scans was used to assess the resistance of the sensors to fouling by the oxidation products of the NTs. The reproducibility of the sensors was investigated by triplicate electroanalysis of the NTs with sensors fabricated three different times using cyclic voltammetry at a scan rate of 25 mV s^{-1} (pH 7). The reproducibility of each sensor was estimated by the percentage relative standard deviation (% RSD) of the anodic current responses of the three trials.

3.2.14 Interference studies

The interference of 1 mM AA (or 1 mM UA) (pH 7) signal with that of 0.4 mM of each neurotransmitter was investigated using the modified electrodes as working electrode and adopting SWV (or DPV where appropriate) as the voltammetric technique. The SWV parameters applied include a potential step of 0.005 V, frequency of 25 Hz and modulation amplitude of 0.02 V. On the other hand, potential step of 0.05 V, modulation time of 0.05 s and modulation amplitude of 0.025 V were applied for the DPV experiments. The voltammogram which showed increase in concentration of the analyte while keeping constant the interfering AA concentration was recorded over the desired potential range (0.0 – 0.8 V).

3.2.15 Real sample analysis

The real sample analysis was done using diluted pharmaceutical or food samples containing the analyte of interest using the standard addition technique. The concentration of the respective analytes obtained from the unspiked real sample (A_o) and that of the samples spiked with a known concentration of the analyte (A2) were recorded. The concentration of the analytes added to the unspiked sample was also recorded (A1). The percentage recovery (% recovery) was obtained from Equation 3.1. The experiments were done in triplicates for each sample.

$$\% \text{ recovery} = \frac{A_1}{A_2 - A_o} \text{ x } 100 \ \% \qquad \text{(Eqn 3.1)}$$

CHAPTER FOUR

RESULTS AND DISCUSSION

4.0 Results and discussions

The preparation and characterization of nanomaterials (CQDs, bCQDs and CNPs) and the composites (CQDs/CNPs and bCQDs/CNPs) as well as the modified electrodes prepared by the modification of the bare glassy carbon electrode (GCE) was discussed in the present chapter. Also, the electroanalysis of the neurotransmitters (DA, EP, and NE) at the composites modified electrode (GCE/CQDs/CNPs and GCE/bCQDs/CNPs) was investigated. Specifically, the effect of changes in pH and scan rate on the electroanalysis of the NTs were investigated. In addition, the stability of the sensors, the analytical application of the sensors in real samples containing the NTs and the ability of the sensors to detect each of the NTs in the presence of interfering molecules (ascorbic acid or uric acid) were discussed in the current chapter.

4.1 Synthesis of nanomaterials and composites

The synthesis of the green carbon quantum dots (bCQDs) and the chemical-based quantum dots (CQDs) by the hydrothermal route gave powdery materials with different colours. The green carbon quantum dots (bCQDs) were fine dark brown nanoparticles (Scheme 1 (a)). On the other hand, the chemical based quantum dots were fine dark grey particles (Scheme 1 (b)). The copper oxide nanoparticles prepared via the chemical precipitation approach were black coarse grains (Scheme 1 (c)). The composites used in the study (bCQDs/CNPs and CQDs/CNPs) were prepared by combining CNPs with the quantum dots (bCQDs and CQDs) in the presence of dimethylformamide (DMF).

4.2 Characterization of CQDs and metal oxide nanoparticles

The characterization of the nanomaterials (CQDs, bCQDs, and CNPs) and the composites (CQDs/CNPs and bCQDs/CNPs) with Fourier Transform infrared (FT-IR) spectroscopy, UV-visible spectroscopy, X-ray Diffraction (XRD) spectroscopy, scanning electron microscopy (SEM), transmission electron microscopy (TEM) and thermogravimetric analysis (TGA) were discussed in the present section. Also, electrochemical characterization of the bare and modified electrodes using cyclic voltammetry (CV) and electrochemical impedance spectroscopy (EIS) was discussed in the current section.

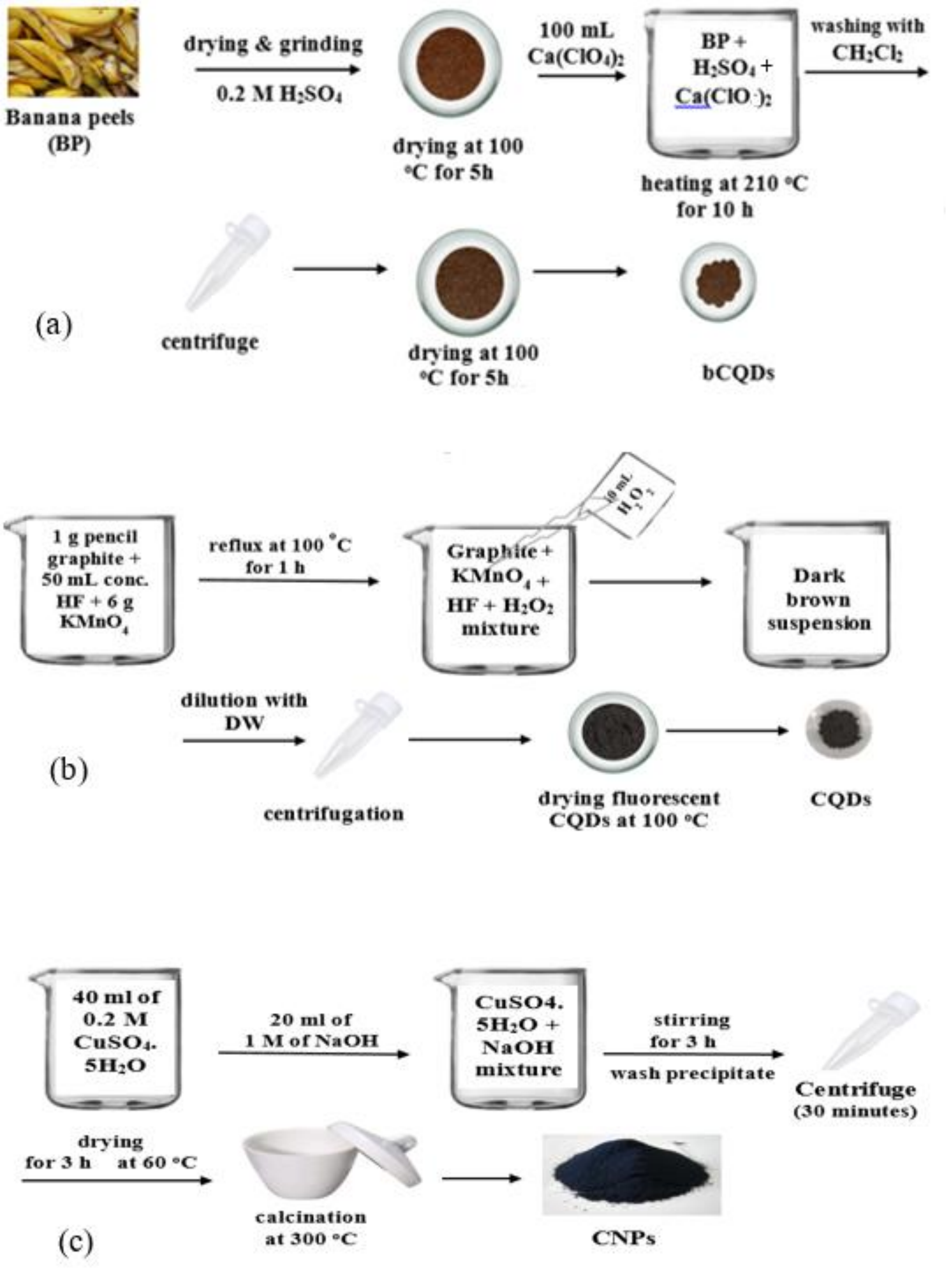

Scheme 1: Schematic representation of the synthesis of (a) bCQDs (b) CQDs and (c) CNPs

4.2.1 Microscopic and spectroscopic characterization

4.2.2 FT-IR analysis

Figure 4.1 (a) showed the FT-IR spectra of the banana peel (BP) and the carbon quantum dots synthesized from BP (bCQDs). The absorption bands at 3295, 2914, 1600, 1363 and 1048 cm^{-1} can be attributed to the presence of –OH stretching, C-H stretching, COO$^-$ stretching, bending –OH, and ester C-O stretching vibrations, respectively. A similar spectrum has been reported for banana peel [271]. The transformation of BP to bCQDs showed that the peak at 3295 cm^{-1} became broader after the hydrothermal bCQDs synthesis. The result implied that the bCQDs retained the –OH/-NH group in the BP. In addition, a peak emerged at 2320 cm^{-1} on bCQDs spectrum which was almost non-existent on the BP spectrum, indicating that the bCQDs probably have –C≡N group which was absent in the precursor. The absorption bands at 2915, 1601, and 1048 cm^{-1} suggest that the bCQDs contain the –C-H, -C=C and C-O functional groups, respectively. Similar absorption bands have been reported for the FT-IR spectrum of carbon quantum dots synthesized from lemon peel [29]. The peak at 1239 cm^{-1} on bCQDs spectrum can be attributed to the presence of C-N bond (originally at 1363 cm^{-1} on BP).

Figure 4.1 (b) showed the FT-IR spectra of carbon quantum dots synthesized from pencil graphite (CQDs), copper oxide nanoparticles (CNPs), and the nanocomposite (CQDs/CNPs). The absorption peaks at 1046, 1639, and 3202 cm^{-1} recorded for CQDs suggested the functional groups C-O, C=C, and –OH, respectively, are present in CQDs. The –OH was suspected to be the -OH of –COOH, which emerged after oxidizing the graphite precursor. The C-O was probably the C-O of –COOH/-OH and the C=C was probably due to the presence of graphitic core in CQDs. The peak at 718 cm^{-1} was due to the presence of C-F bond in CQDs. The source of the fluorine could be traced to the presence of trace amount of fluorine from the HF used for the digestion of the pencil graphite. Fortuitously, the functional groups suspected from the FT-IR spectra of CQDs have been reported in the FT-IR spectrum of some carbon-based quantum dots [15, 156]. The FT-IR spectrum of CNPs showed peaks at 485 and 688 cm^{-1} due to Cu-O stretching vibration, while the peak at 3382 cm^{-1} referred to the possible presence of adsorbed moisture in CNPs. A similar spectrum has been reported for copper oxide nanoparticles [272]. The spectrum of CQDs/CNPs showed absorption peaks at 1086, 1742, and 3020 cm^{-1}, suggesting C-O, C=O, and –OH, respectively are present in the composite. The peak at 1742 cm^{-1} was probably the C=O peak of –COOH, originally at 1755 cm^{-1} on CQDs spectrum.

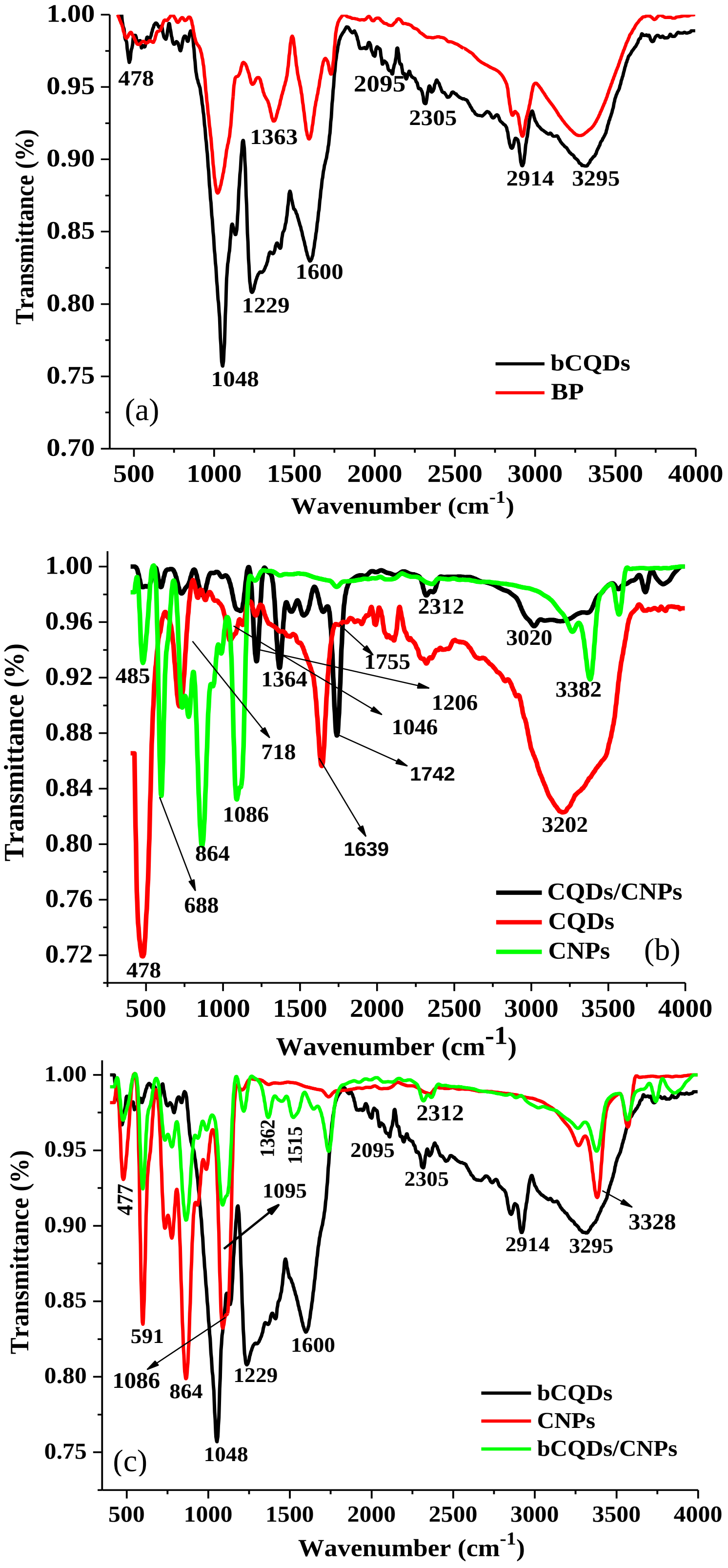

Figure 4.1: FT-IR spectra of (a) BP and bCQDs (b) CQDs/CNPs, CQDs and CNPs and (c) bCQDs, CNPs and bCQDs/CNPs

The peak at 3020 cm^{-1} wass broader than the one on CQDs found at about the same wavenumber. The peaks found in the CNPs spectrum at 1200-400 cm^{-1} remained intact in CQDs/CNPs spectrum, except for a slight variation in wavenumber. The similarities and differences in the spectrum of the nanomaterials (CQDs and CNPs) and the composite (CQDs/CNPs) confirmed that the composite was prepared from the nanomaterials.

Figure 4.1 (c) showed the FT-IR spectra of bCQDs, CNPs, and bCQDs/CNPs. The bCQDs/CNPs spectrum show absorption bands at 1048, 1600, and 3328 cm^{-1}, suggesting the presence of –C-O, -C=C, and -OH, respectively. The peak at 1048 cm^{-1} representing –C-O (which can also be found in bCQDs spectrum) remained intact in the composite spectrum. The peak at 1600 cm^{-1} in the bCQDs spectrum appeared very weak in the composite. It is worthy to note that the addition of CNPs to bCQDs to form the composite led to the disappearance of the peaks between 1800 and 2312 cm^{-1} in bCQDs/CNPs spectrum (which were initially in bCQDs spectrum). Also, the broad peak at about 3295 cm^{-1} in bCQDs spectrum became less broad in the composite, probably because the hydrogen bond in the bCQDs became less prevalent after composite formation. Figure 4.1 (c) also revealed that most of the peaks in CNPs spectrum remained intact in the composite, suggesting the stabilization of CNPs in the composite. Table 4.1 summarizes of the functional groups in banana peel, the nanomaterials, and the nanocomposites, as well as their corresponding wavenumbers.

Table 4.1: Notable functional groups and absorption bands in the nanomaterials and composite

	Notable functional groups and wave number (cm^{-1})						
Samples	-C-O	-OH/-NH	-C=C	–C≡N	-C=O	-C-N	Cu-O
BP	1048	3295	1601	-	-	1363	-
bCQDs	1048	3295	1601	2320	-	1239	-
CQDs	1046	3202	1639	-	1755	-	-
CNPs	-	3382	-	-	-	-	485 & 688
bCQDs/CNPs	1048	3328	1600	2320	-	-	477 & 591
CQDs/CNPs	1086	3020	1639	-	1742	-	485 & 688

4.2.3 UV-visible spectroscopy

Figure 4.2 (a) showed the UV-visible spectrum of bCQDs and CQDs. The spectrum of bCQDs show two peaks at 291 nm and 361 nm. Several CQDs have been reported to show absorption at similar wavelengths as bCQDs [273, 274]. The CQDs showed a very strong peak at 290 nm.

Similar absorption wavelengths have been reported for CQDs prepared from various precursors. The absorption at about 290 nm in both quantum dots was due to the n-π^* transition of C=O present in the carbon quantum dots [275]. The difference in the UV spectrum of the two carbon dots suggested that they were made from different precursors. The variation in the precursor for carbon-based quantum dots have also manifested in differences in UV-visible spectra. A notable example can be found in the difference between the UV-visible spectrum of carbon quantum dots prepared from lemon peel and citric acid [29, 273].

Figure 4.2 (b) showed the UV-visible spectra of CNPs, bCQDs/CNPs, and CQDs/CNPs. The spectrum of CNPs showed absorption at 291 nm and 339 nm due to surface plasmon resonance [276]. Specifically, the peak at the higher wavelength (339 nm) has been widely reported in the UV-visible analysis of copper oxide nanoparticles from various precursors [277-279]. The spectrum of CQDs/CNPs showed absorption peaks at 291 nm and 348 nm. The peak at 348 nm is probably due to the shift of the peak at 339 nm in CNPs to a higher wavelength after composite formation. Similarly, the spectrum of bCQDs/CNPs showed two peaks at 299 nm and 437 nm. The weak peak at 437 nm was due to the shift of the peak at 339 nm in CNPs to a higher wavelength after composite formation.

The appearance of the two strong peaks on the spectrum of the composites at a wavelength similar to that of their components confirmed the composite's formation from the components. However, the absorption peaks in the composites are found at higher wavelengths than the peaks in the individual nanomaterials, confirming the formation of materials different from the individual components after composite formation.

4.2.4 X-ray diffraction (XRD) analysis

The XRD analysis is a critical method for identifying nanomaterials. Also, the crystallite particle size and the interlayer (d) spacing can be calculated from the XRD spectrum of nanomaterials. In this section, the crystallite particle size (D) has been calculated from the peaks with the highest intensity using Scherrer's equation (Eqn 4.1), where k (0.9) is the shape factor, Θ is the diffraction angle, λ is the X-ray's wavelength (0.154 nm), and β is the full width at half maximum (in Radians). The interlayer (d) spacing was calculated using Bragg's equation (Eqn 4.2), where n = 1 and other parameters retained their meaning as earlier described.

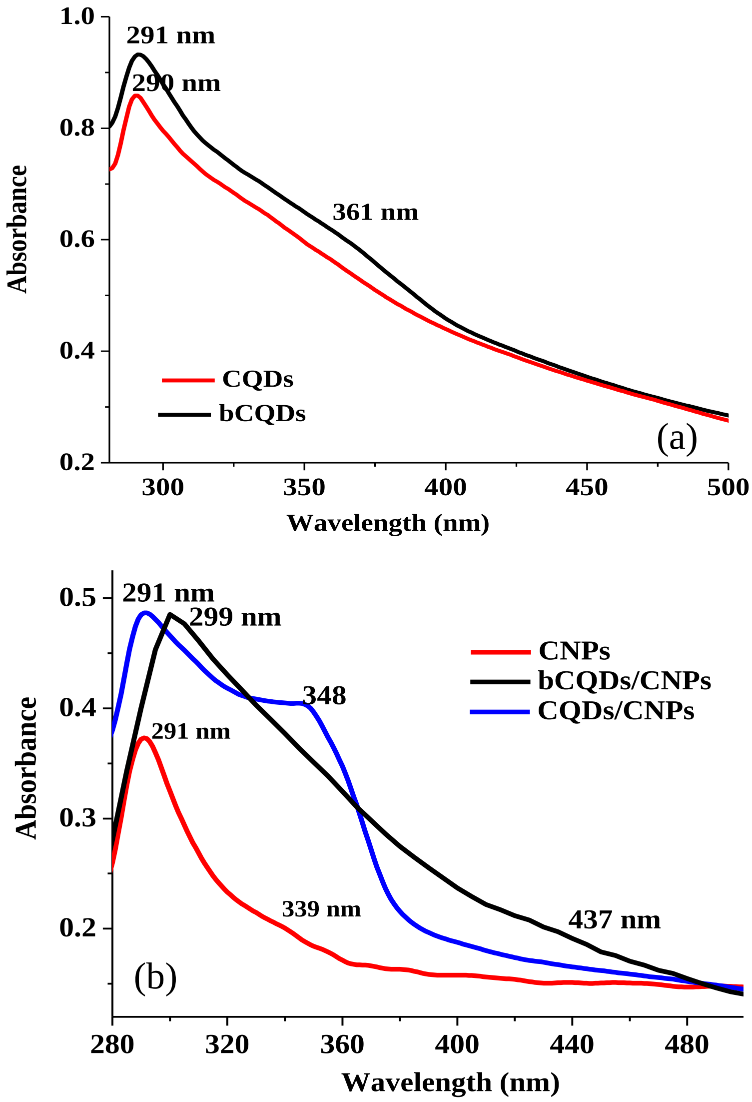

Figure 4.2: UV-visible spectra of (a) CQDs and bCQDs (b) CQDs, CNPs and CQDs/CNPs.

Figure 4.3 depicts the XRD spectra of nanomaterials, and the composites made with bCQDs and CQDs. Figure 4.3 (a) showed the XRD spectra of the bCQDs and CQDs. The CQDs spectrum showed prominent peaks at 20.8^{o}, 23.2^{o}, 27.6^{o} and 42.3^{o}. The broad peak at 23.2^{o} and 42.3^{o} indicate the presence of graphene-like carbon in CQDs [280]. The interlayer spacing of CQDs calculated from the broad peak at 23.2^{o} (0.38 nm) was greater than the interlayer spacing of graphite (0.33 nm), suggesting poor crystallinity of the CQDs [275]. The bCQDs spectrum showed prominent peaks at 22^{o}, 28.7^{o} and 42.3^{o}. The peaks at 22^{o} and 42.3^{o} suggested the presence of graphene-like carbon in bCQDs [280]. The interlayer spacing calculated from the very broad peak at 22^{o} is higher than the graphitic interlayer spacing, indicating bCQDs possessed poor crystallinity. The poor crystallinity of the QDs was probably due to the oxygen-containing functionalities in the QDs [275].

Figure 4.3 (b) showed the XRD spectrum of CQDs/CNPs. The peaks at 21.9^o and 26.5^o on CQDs/CNPs spectrum are probably from the CQDs (peaks at 23.2^o and 27.6^o on CQDs spectrum). Typically, peaks on carbon quantum dots XRD spectra become less broad in composites [281, 282]. The change in peak size was evident in the sharper CQDs peaks in the XRD spectrum of CQDs/CNPs (Fig. 4.3 (b)). The peaks at 32.6^o (110), 35.7^o (002), 38.8^o (111), 48.9^o (202), 58.5^o (202), 61.6^o (113), and 68.1^o (113) are suspected to have emerged from the CNPs because they appeared at similar diffraction angles to that of CNPs. These peaks confirmed the presence of CNPs in the composite.

Figure 4.3 (c) showed the XRD spectra of CNPs and bCQDs/CNPs. CNPs spectrum showed peaks at 32.6^o (110), 35.5^o (002), 38.8^o (111), 48.8^o (202), 53.7^o (020), 58.3^o (202), 61.6^o (113), 66.3^o (311), 68.1^o (113), 72.6^o (311) and 75.1^o (004). The emergence of peaks at these diffraction angles and the corresponding miller indices (in parenthesis) agreed with the x-ray diffractogram of CNPs in the monoclinic phase [222, 272]. The presence of no other peaks apart from the CNPs peaks suggested that the CNPs are of high purity and devoid of impurities such as Cu_2O and $Cu(OH)_2$. The CNPs crystallite particle size calculated from Equation 4.2 was 16.3 nm.

$$D = \frac{k\alpha}{\beta\cos\theta} \qquad \text{(Eqn 4.1)}$$

$$2d\text{Sin}\theta = n\lambda \qquad \text{(Eqn 4.2)}$$

The sharpness of the peaks and the small crystallite particle size suggest the crystalline nature of CNPs [283]. Figure 4.3 (c) showed the XRD spectrum for bCQDs/CNPs. The spectrum show the diffraction pattern of the constituent metal oxide nanoparticles (as depicted by their miller indices) and the bCQDs (depicted by the diffraction angle in a circle) (Fig. 3 (c)). The presence of the peaks corresponding to CNPs on the spectrum of bCQDs/CNPs confirmed the composite’s successful formation. A similar XRD pattern has been reported for a carbon nanomaterial and CNPs composite [283-285].

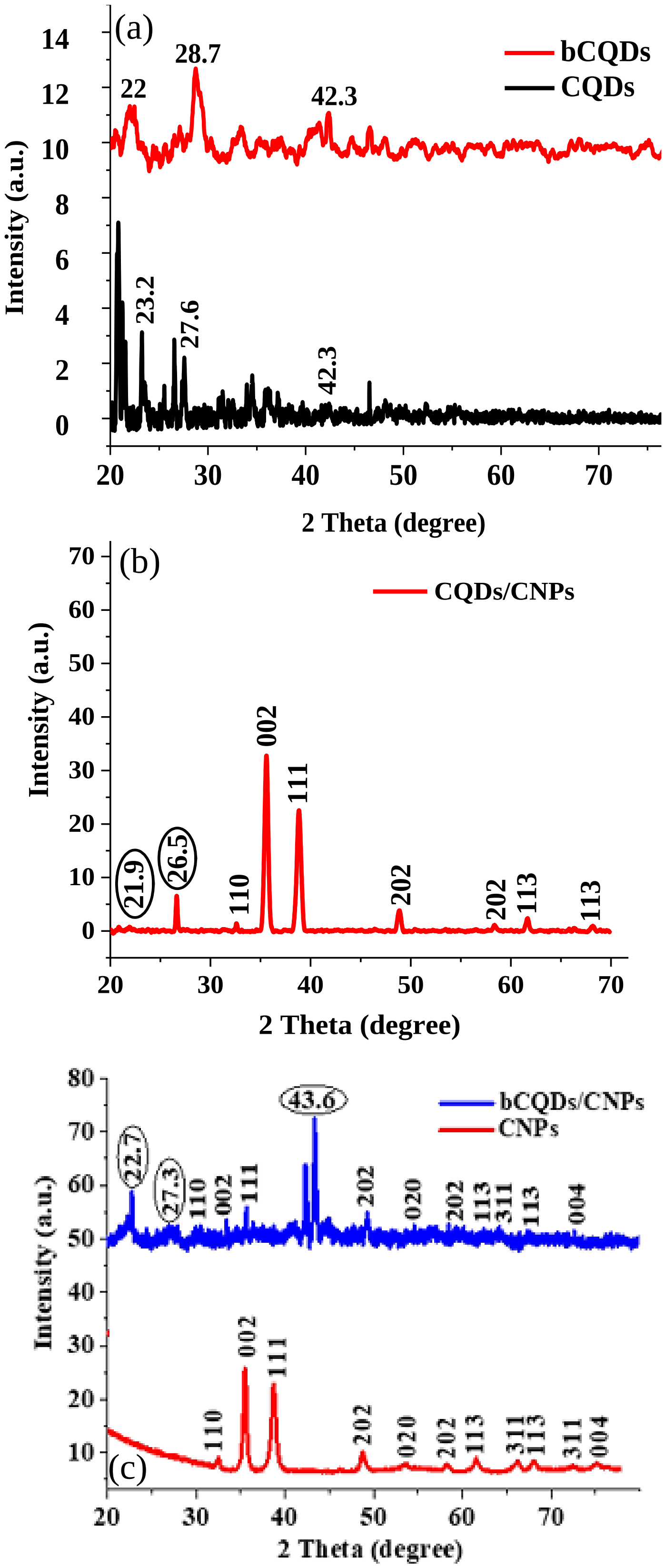

Figure 4.3: XRD spectra of (a) bCQDs, CQDs, (b) CQDs/CNPs, (c) CNPs and bCQDs/CNPs.

4.2.5 Scanning electron microscopy (SEM) analysis

The SEM analysis is essential for establishing the surface morphology of materials. Figures 4.4 represented the SEM micrograph of the CNPs, CQDs, bCQDs, and the nanocomposites. The SEM image of CNPs showed that CNPs are pseudo-spherical particles (Fig. 4.4 (a)). The pseudo-spherical masses fuse to form layers of pseudo-spherical nanomaterials (blue circle). These clusters were organized into irregularly spaced colonies of nanomaterials. SEM images with similar pseudo-spherical masses have been reported for CNPs [286-288]. The SEM image of CQDs (x 100, 000 magnification) revealed that the CQDs are fused pseudo-spherical carbon flakes (Figure 4.4 (b)).

The inset of Figure 4.4 (b) showed the SEM micrograph of CQDs at a lower magnification (x 5, 000), and hence indicated that a large proportion of the CQDs are fused carbon flakes. The carbon flakes aggregated to form a brush-like figure containing irregular pores. The SEM image of the bCQDs revealeded perfectly ordered pseudo- spherical particles. Green carbon quantum dots of similar morphology have been reported [289]. The SEM image of CQDs/CNPs showed that the pseudo-spherical CNPs adorned the surface of the CQDs flakes (see red circles). This SEM image also revealed that the pseudo-spherical CNPs were sandwiched between layers of the CQDs flakes. Figures 4.4 (e) showed the SEM images of bCQDs/CNPs. The SEM micrograph of bCQDs/CNPs showed that the composite is a fusion of the bCQDs (see yellow arrow) and CNPs (see red arrow). Some parts of the SEM image show aggregates of CNPs sandwiched in between layers of the pseudo-spherical bCQDs (see red arrow) (Fig. 4.4 (e)).

4.2.6 Transmission electron microscopy (TEM) analysis

TEM analysis is famous for the characterization of QDs. The analysis of various carbon-based quantum dots with TEM showed that most carbon-based QDs have particle sizes < 10 nm [27, 42]. This particle size determination with TEM analysis has proven to be significant in QDs characterization. Accordingly, TEM analysis was adopted to characterize the as-synthesized carbon dots in the study.

The TEM micrograph of CQDs showed that the carbon dots have a pseudo-spherical shape (Fig. 4.5 (a)). The darker part of the micrograph is due to the aggregation of CQDs, which form two different CQDs aggregates. The average particle size of the CQDs calculated from the analysis

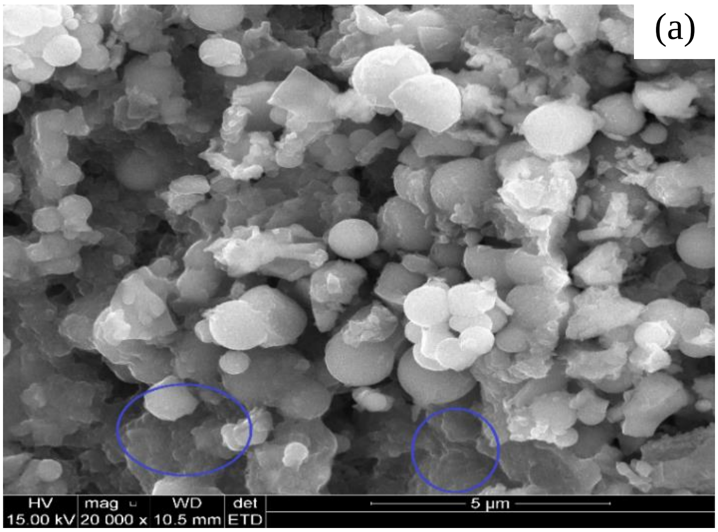
(a)
HV 15.00 kV
mag 20 000 x
WD 10.5 mm
det ETD
5 µm

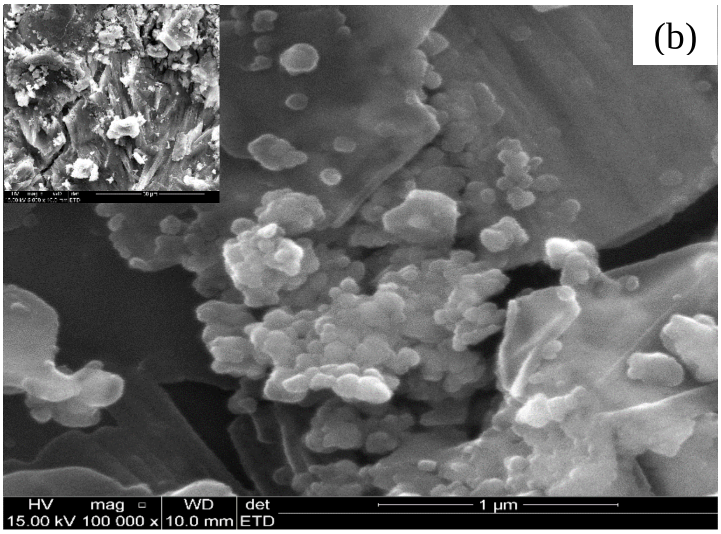
(b)
HV 15.00 kV
mag 100 000 x
WD 10.0 mm
det ETD
1 µm

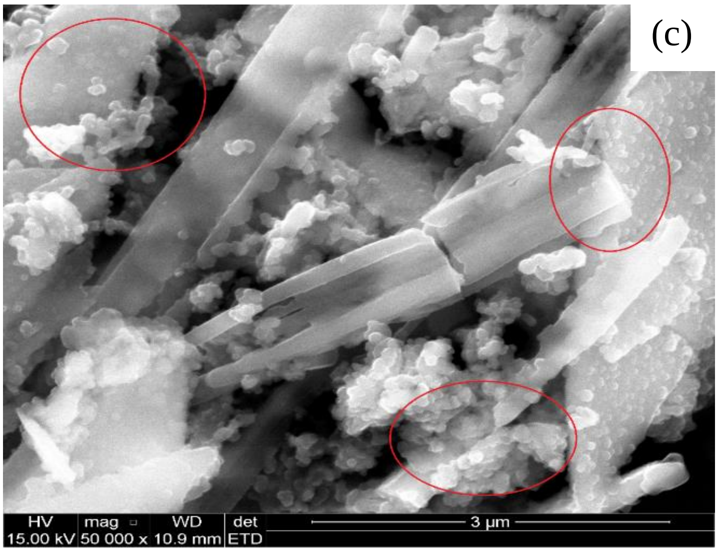
(c)
HV 15.00 kV
mag 50 000 x
WD 10.9 mm
det ETD
3 µm

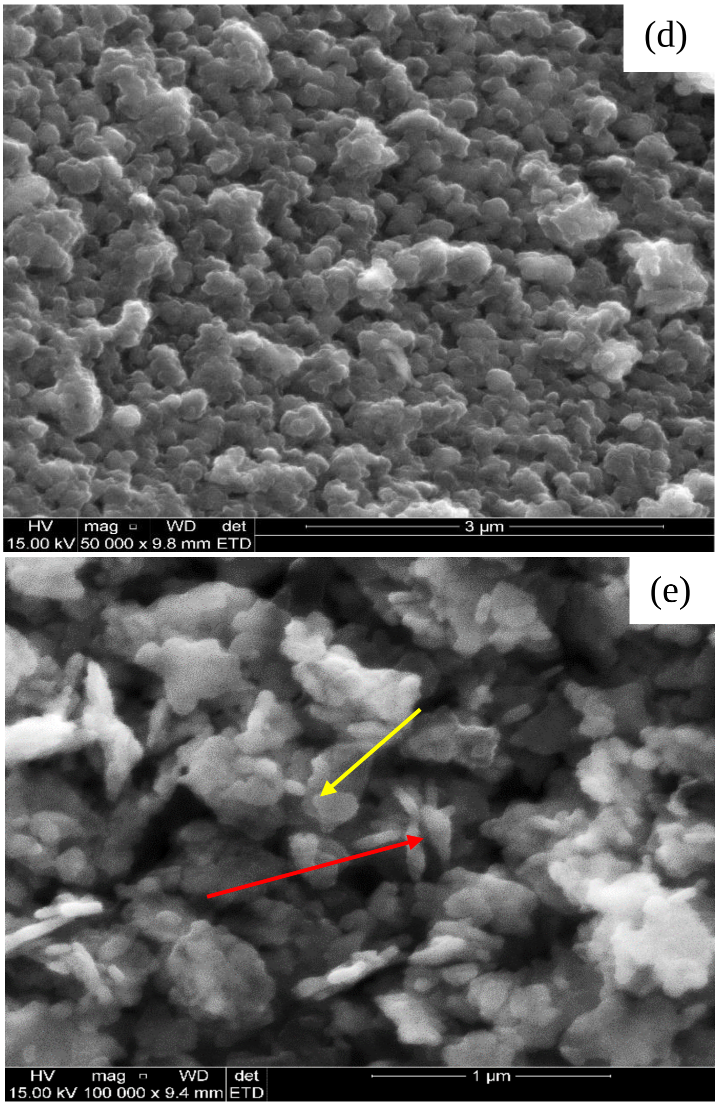

Figure 4.4: SEM micrograph of (a) CNPs (b) CQDs (c) CQDs/CNPs (d) bCQDs and (e) bCQDs/CNPs

of the TEM micrograph is the average frequency distribution (AFD) of the carbon dots diameter (9.021 ± 0.178). However, the particle size distribution chart showed that the particle size of CQDs range from 6-12 nm (Fig. 4.5 (b)). Average particle size of 9.02 nm obtained for CQDs agrees with the average particle size of < 10 nm previously reported for carbon-based QDs [27, 42, 290, 291].

The TEM micrograph of the carbon dots prepared from the green source (bCQDs) (Fig. 4.5 (c)) confirmed the pseudo-spherical shape of the particles as depicted by the SEM micrograph. The bCQDs particle size distribution chart showed the AFD of bCQDs particle size (7.512 ±

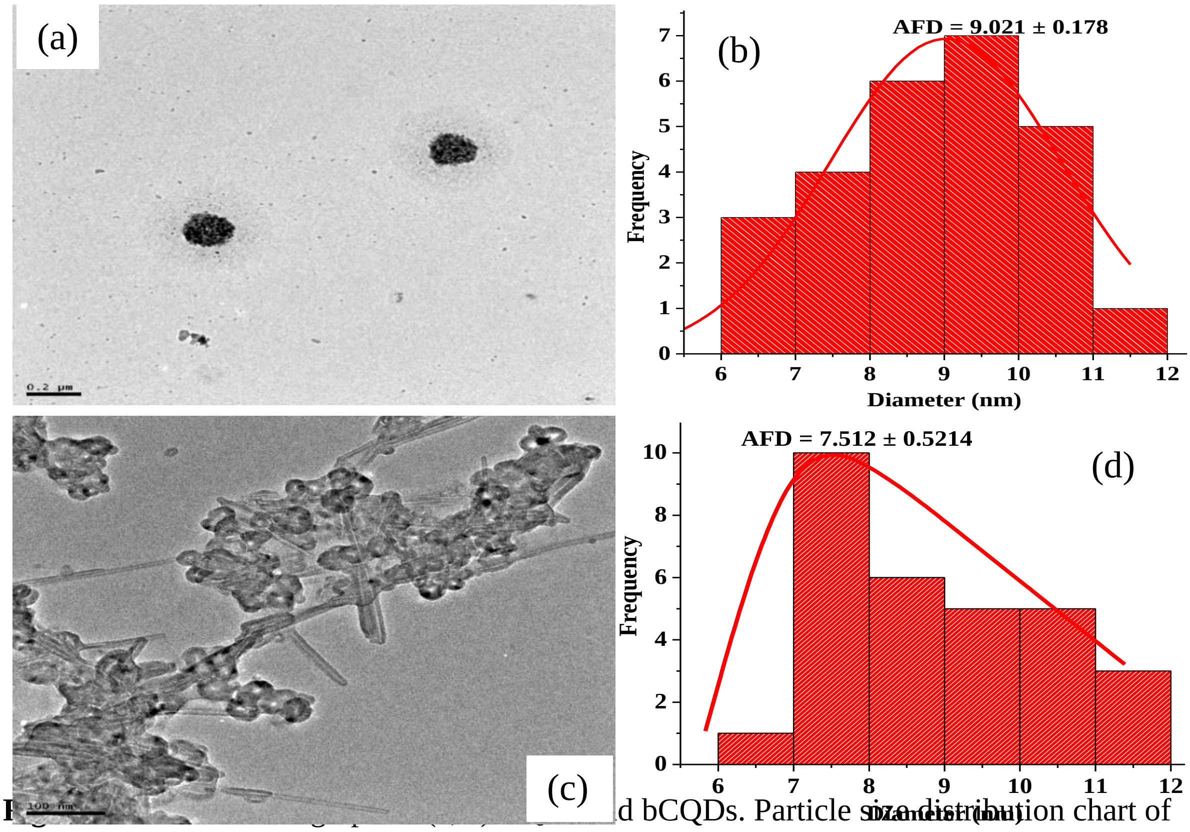

F d bCQDs. Particle size distribution chart of (b,d) CQDs and bCQDs

0.521) and the particle size range of bCQDs (6-12 nm) (Fig. 4.5 (d)). The results implied that the average particle size of bCQDs is 7.51 nm. Average particle size of 7.51 nm for bCQDs agrees with the average particle size of < 10 nm reported for some carbon-based QDs prepared from the green source [29, 290-292]. CQDs and bCQDs have the same particle size range (6-12 nm).

4.2.7 Thermogravimetric analysis (TGA)

Thermogravimetric analysis of the banana peel (BP) and the quantum dots was carried out using 18.861, 5.588, and 18.833 mg of BP, bCQDs, and CQDs, respectively. The TGA profile of BP revealed that the degradation of the banana peels occurred in two different stages (Fig. 4.6 (a)). The first stage was the 64 % weight loss between 175 – 687 ^{o}C. The second stage of degradation was a 19.8% weight loss observed between 759 – 1170 ^{o}C. The weight loss at 175 – 687 ^{o}C was due to the combustion of the organic matter in BP [293]. Specifically, the occurrence at 337 ^{o}C represents the loss of CO_2 [294]. The significant weight loss at 759-1170 ^{o}C could be ascribed to the decomposition of the carbonates in the banana peel. The TGA profile of bCQDs also showed two stages of degradation. Weight loss of 49 % and 36 % were recorded at 175 – 485 °C and 510 -1060 °C, respectively. The 49 % weight loss can be attributed to the loss of organic compounds present in bCQDs. The decomposition of graphite in the air has been reported to occur at 600 °C [295, 296]. The 36 % weight loss can be attributed to the decomposition of graphite. The two-stage decomposition depicted by bCQDs TGA profile was similar to the TGA curve reported for carbon quantum dots synthesized from cashew gum [149]. The differences in the TGA profile of BP and bCQDs confirmed the transformation of BP. The event at 782 °C (in the bCQDs TGA profile) suggested oxidative degradation of the graphitic core in bCQDs. Noteworthy, the TGA profile of BP and bCQDs showed water loss up to 175 °C.

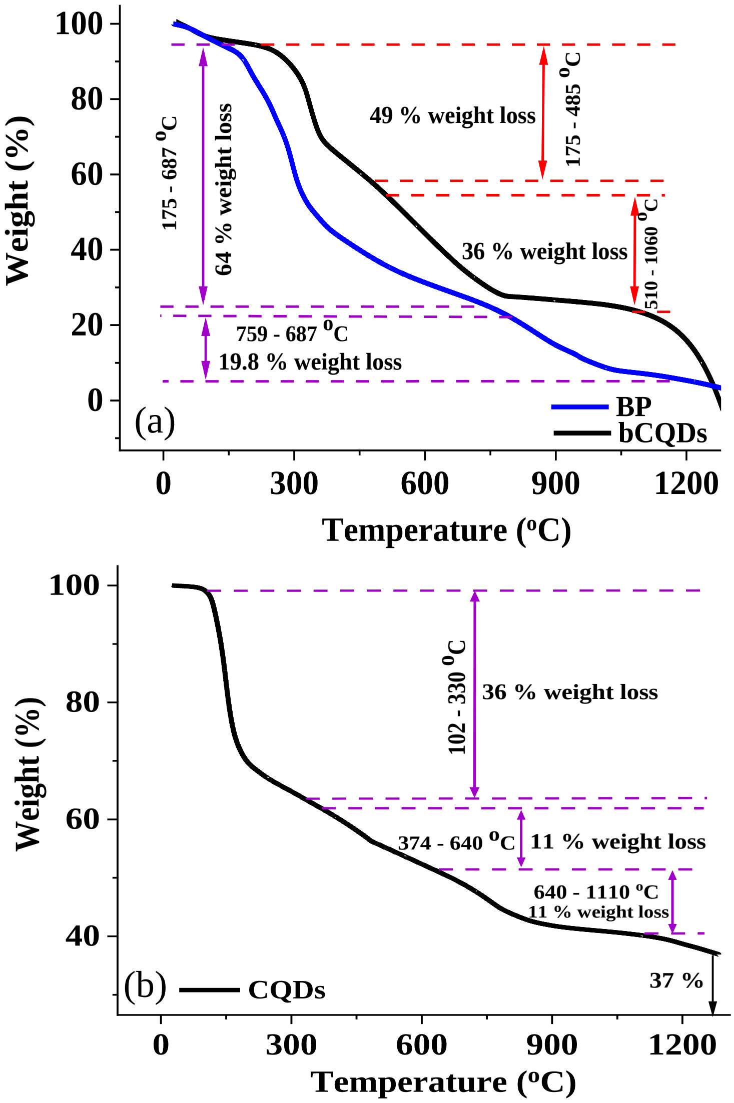

Figure 4.6: TGA curves of (a) BP and bCQDs and (b) CQDs

The TGA curve of CQDs showed three degradation stages after the initial water loss up to 100 ^{o}C (Fig. 4.6 (b)). The first degradation stage occurred between 102 – 330 ^{o}C, with 36 % weight loss due to the loss of the carboxyl functionality around CQDs [297]. The second stage occurred over a temperature range of 374 – 640 ^{o}C with a weight loss of 11%. The degradation can be attributed to the loss of other oxygen-containing functional groups in the carbon dots [298, 299]. Another 11 % weight loss was recorded at the third degradation stage (640-1110 ^{o}C). The degradation at this stage was due to the decomposition of the CQDs graphitic core [295, 296]. Noteworthy, the CQDs witnessed significant thermal stability after 1267 ^{o}C such that about 37 % of the initial CQDs mass remain intact. The 37 % residual mass may contain undecomposed carbon particles. The fact that a thermal stability of this degree was not recorded with bCQDs suggested that CQDs possess greater thermal stability than bCQDs.

4.2.8 Electrochemical characterization

The electrochemical characterization of the bare electrode and modified electrodes was done in 5 mM $[Fe(CN)_6]^{3-/4-}$ redox probe at a pH of 7. Figure 4.7 depicts the cyclic voltammogram recorded with the bare GCE, CNPs modified GCE, and CQDs/CNPs modified GCE at a scan rate of 25 mV s^{-1}. The Bare GCE, GCE/CQDs, GCE/CNPs, GCE/CQDs/CNPs, GCE/bCQDs, and GCE/bCQDs/CNPs gave anodic peak current (I_{ap}) of 17.89 µA (0.27 V), 7.19 µA (0.28 V), 7.04 µA (0.14 V), 19.69 µA (0.37 V), 6.66 µA (0.52 V), and 18.44 µA (0.39 V), respectively at their respective peak potentials (E_{ap}) (in parenthesis). The cathodic peak currents (I_{cp}) recorded were -18.93 µA (0.16 V), -5.92 µA (-0.06 V), -12.89 µA (0.07 V), -12.11 µA (0.15 V), -0.86 µA (0.16 V), -18.93 µA (0.09 V), -4.28 µA (0.07 V) and -4.35 µA (-0.27 V), -7.89 µA (-0.27 V), -21.18 µA (-0.06 V), respectively at their respective peak potential (E_{cp}, in parenthesis). The closer the value of I_{ap}/I_{cp} to unity the better the reversibility of a redox process. The values of I_{ap}/I_{cp} in Table 4.2 showed that the bare GCE and CQDs/CNPs modified GCE have I_{ap}/I_{cp} values of 0.94 and 0.97, respectively, suggesting that they have better reversibility than the other electrodes. The difference between E_{ap} and E_{pc} (ΔE) can also be used to estimate the reversibility of a redox process. A reversible one-electron process is expected to have ΔE value of 59 mV. A quasi-reversible process has ΔE value greater than 59 mV [300]. The ΔE values in Table 4.2 showed that all the electrodes have ΔE values greater than 59 mV, suggesting that all the redox processes at the surface of the bare and modified electrodes are quasi-reversible. The surface area of the bare and modified electrodes was calculated from Equation 4.3, where i_p, n, v, D_o, A, and C represent the peak current (A), number of electrons, scan rate (V s^{-1}), diffusion coefficient (cm ^{2} s^{-1}), surface area (cm ^{2}) and bulk concentration of analyte (mol. cm^{-3}), respectively. The diffusion coefficient of the redox probe was taken as 7.6 × 10^{-6} cm^2 s^{-1} [301].

$$i_p = 2.69 \times 10^5 \, n^{3/2} \, A D_o^{1/2} C v^{1/2} \qquad \text{(Eqn 4.3)}$$

The surface areas of bare GCE, GCE/CQDs, GCE/bCQDs, GCE/CNPs, GCE/CQDs/CNPs, and GCE/bCQDs/CNPs were calculated as 9.65, 3.88, 3.68, 3.80, 10.62, and 9.91 cm ^{2}, respectively. The CQDs/CNPs modified electrode possesses the highest I_{ap} and greatest surface area, suggesting that modification of GCE with CQDs/CNPs improved surface area and possibly conductivity of the electrode. The improved electronic conductivity of the electrode fosters faster electron transfer between the modified electrode and redox probe. It is noteworthy that CQDs and bCQDs modified electrodes have ΔE values very far from the theoretical value of 59 mV. The outcomes showed that the surface of bCQDs and CQDs modified electrodes could not support a reversible process in the presence of the redox probe.

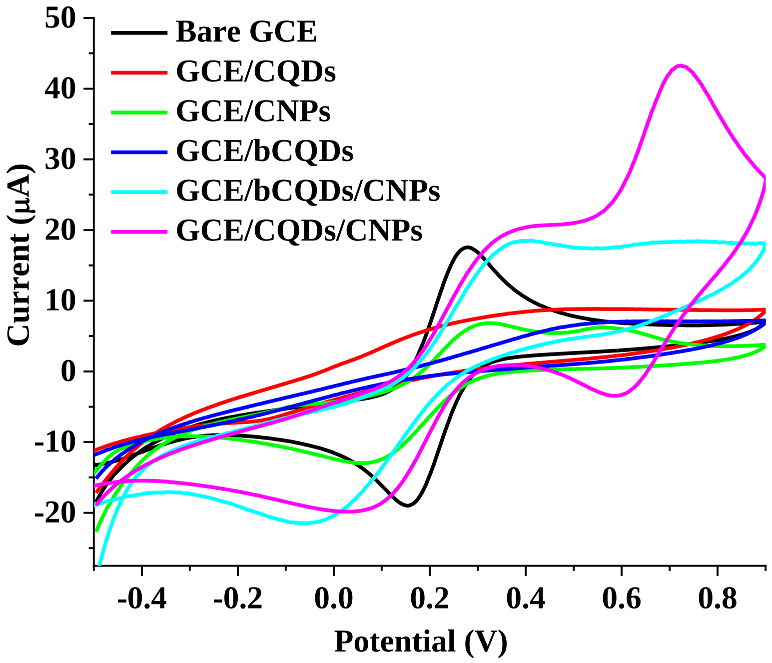

Figure 4.7: Cyclic voltammograms of bare GCE, GCE/CQDs, GCE/CNPs, GCE/bCQDs, GCE/bCQDs/CNPs and GCE/CQDs/CNPs in 5 mM $[Fe(CN)_6]^{3-/4-}$

The electrochemical impedance spectroscopy (EIS) analysis was also applied for the characterization of the bare and modified electrodes in 5 mM $[Fe(CN)_6]^{3-/4-}$. Figure 4.8 (a) showed the Nyquist plot obtained with bare GCE, CNPs, CQDs, bCQDs, and the composites modified GCE. The inset of Figure 4.8 (a) depicts the enlarged Nyquist plot of Bare GCE, GCE/TNPs, GCE/CNPs, and GCE/CQDs. Figure 4.8 (b) showed the equivalent circuits adopted for fitting the EIS data obtained with this electrode. The circuit X in Figure 4.8 (b) was used for fitting the data obtained with GCE/CQDs, GCE/ZNPs, GCE/CQDs/CNPs, and GCE/CQDs/TNPs. On the other hand, circuit Y in Figure 4.8 (b) showed the equivalent circuit for fitting the data recorded with Bare GCE, GCE/CNPs, GCE/TNPs, and GCE/CQDs/CNPs. The charge transfer resistance (R_{ct}), solution resistance (R_S), Warburg impedance (W), the magnitude of the constant phase element (Y_o), and its exponent (N) obtained after fitting the EIS data have been itemized in Table 4.3. Noteworthy, the errors associated with the parameters used for fitting the EIS data have been put in parenthesis (Table 4.3). A similar treatment was given to all EIS data reported in the study.

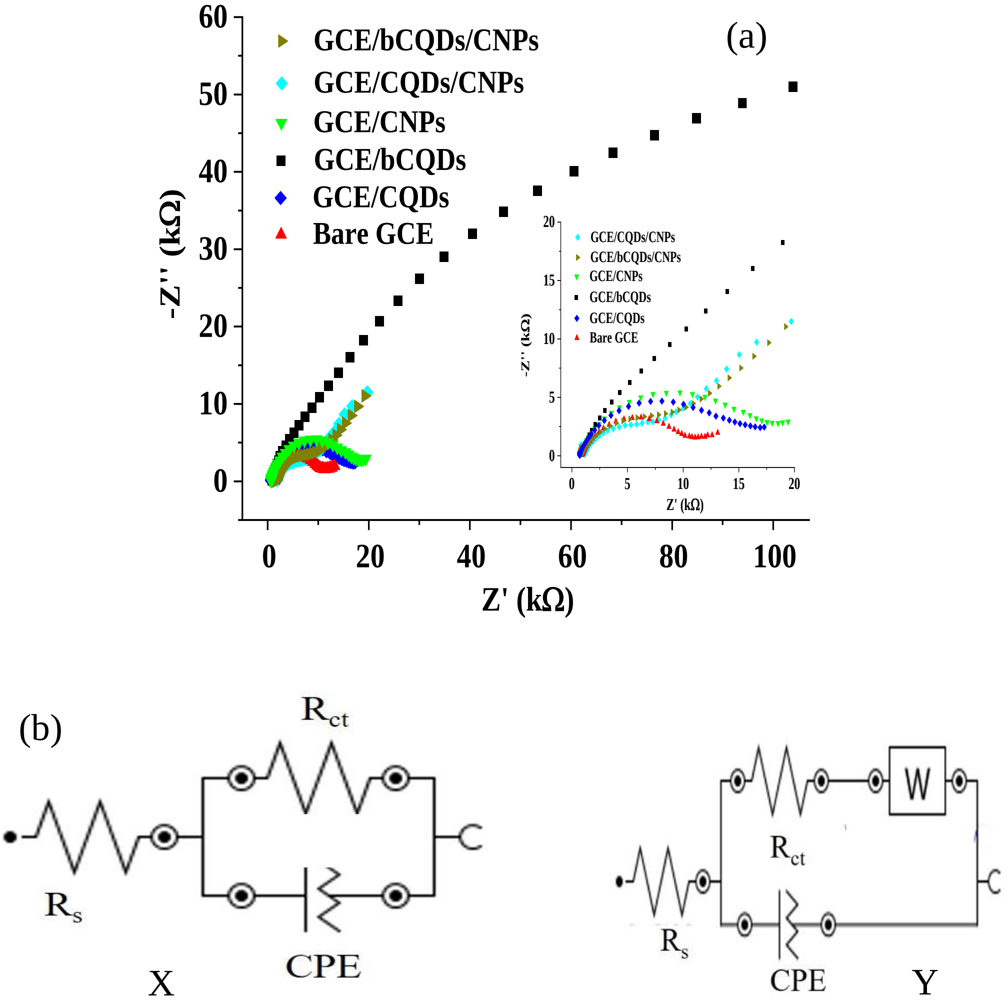

Figure 4.8: EIS spectra (Nyquist plot) of (a) Bare GCE, CQDs, bCQDs, CNPs and CQDs/CNPs modified GCE in 5 mM $[Fe(CN)_6]^{3-/4-}$ (pH 7) (inset: enlarged EIS spectra of the bare and modified electrodes) (b) equivalent electrochemical circuit of the EIS data at (a)

The charge transfer resistance (R_{ct}) showed the extent of a surface's resistance to charge transfer. Highly conducting surfaces are expected to possess low charge transfer resistance. The R_{ct} values in Table 6 showed R_{ct} follows the order GCE/CQDs/CNPs (6.92 kΩ) < GCE/bCQDs/CNPs (8.19 kΩ) < Bare GCE (9.87 kΩ) < GCE/CQDs (15.54 kΩ) < GCE/CNPs (16.19 kΩ) < GCE/bCQDs (107.11 kΩ). The trend is in agreement with the anodic current response obtained with cyclic voltammetry in the redox probe. For instance, GCE/CQDs/CNPs with the highest current response in CV possessed the lowest R_{ct} compared to the bare GCE and the modified GCE. On the other hand, GCE/bCQDs with the lowest current response with CV gave the highest R_{ct}. The results suggested that the modification of the bare GCE with CQDs/CNPs composite improved the conductivity of the electrode (reduces R_{ct} of the electrode) and consequently increased the electron transfer kinetics of the electrode. Several carbon nanomaterials based/metal oxide nanocomposite modified electrodes exhibited the same behaviour [87, 302, 303]. Also, the fact that GCE/CQDs and GCE/CNPs possessed higher R_{ct} than the composite modified GCE implied that the combination of CQDs and CNPs is essential for forming a more conducting surface.

Table 4.2: Cyclic voltammetry data of the bare and modified electrodes in $[Fe(CN)_6]^{3-/4-}$

Electrodes	I_{ap} (A)	I_{cp} (A)	E_{ap} (V)	E_{cp} (V)	I_{ap}/I_{cp}	ΔE (V)	A (cm^2)
Bare GCE	17.89	-18.934	0.273	0.155	-0.945	0.118	9.649
GCE/bCQDs	6.813	-6.65	0.531	-0.185	-1.025	0.716	3.675
GCE/CQDs	7.199	-5.92	0.282	-0.06	-1.216	0.342	3.883
GCE/CNPs	7.039	-12.886	0.139	0.067	-0.546	0.072	3.797
GCE/CQDs/CNPs	19.69	-18.93	0.365	0.094	-1.040	0.271	10.620
GCE/bCQDs/CNPs	18.373	-21.31	0.379	-0.063	-0.862	0.442	9.910

The electron transfer rate constant (k_s) of the electrodes calculated from Equation 4.4 (all variables retain usual meaning) and depicted in Table 4.3 revealed that GCE/CQDs and GCE/CNPs possess very high k_s in the presence of the redox probe. The result implied that modifying the bare GCE with these two materials (CQDs and CNPs) increases the electron transfer rate across the electrode. The synergy between the two materials culminated in forming a composite (CQDs/CNPs) which gave a surface with an intermediate k_s (0.72×10^{-6} s^{-1}) when applied for GCE modification. The high I_{ap} value, low R_{ct}, large surface area, and a reasonably high k_s value recorded with GCE/CQDs/CNPs suggested that it might possess the requisite electronic properties for the electrocatalytic oxidation of biomolecules. Considering the widely reported improvement in electronic conductivity of electrodes after CNPs modification and the small particle size of CQDs [42, 217], it can be inferred that the synergistic effect of the combination of CQDs and CNPs could have emanated from large surface area of CQDs and good conductivity of CNPs.

$$k_s = \frac{RT}{n^2F^2AR_{ct}C} \qquad \text{(Eqn 4.4)}$$

Furthermore, it is essential to note that GCE/bCQDs/CNPs also possess a very low R_{ct} (close to the R_{ct} of GCE/bCQDs/CNPs). The low R_{ct} value suggested that the modification of GCE with bCQDs/CNPs gave a surface with little resistance to charge transfer from the redox probe. The R_{ct} values and the large surface earlier reported for GCE/bCQDs/CNPs showed that the combination of bCQDs and the CNPs give composites with better conductivity and larger surface areas than their component nanomaterials. The conductivity of CNPs, as depicted by their relatively low R_{ct} also played a significant role in the improved conductivity witnessed at GCE/bCQDs/CNPs.

Table 4.3: EIS parameters of the bare and modified electrodes

Electrodes	R_s (kΩ)	R_{ct} (kΩ)	Y_o ($\mu\Omega^{-1}$.s^N)	N ($\mu\Omega^{-1}$.s^N)	W ($\mu\Omega^{-1}$.s)	k_s (μs^{-1})	X^2
Bare GCE	1.32	9.87	4.06	0.73	497.00	0.56	0.5272
	(2.98)	(6.12)	(19.18)	(4.20)	(39.79)		
GCE/ bCQDs	0.78	107.11	3.88	0.66	-	0.14	0.6249
	(3.89)	(9.71)	(7.76)	(1.99)			
GCE/CQDs	0.66	15.54	4.36	0.73	-	0.88	0.3372
	(2.47)	(3.09)	(8.99)	(1.98)			
GCE/CNPs	0.66	16.19	3.71	0.75	333.78	0.87	0.2929
	(2.27)	(4.28)	(9.39)	(1.96)	(30.53)		
GCE/CQDs/CNPs	1.75	6.92	4.98	0.72	81.31	0.72	0.6412
	(3.39)	(15.87)	(37.84)	(8.13)	(9.71)		
GCE/bCQDs/CNPs	1.59	8.19	4.58	0.73	81.56	0.66	0.5799
	(3.11)	(13.1)	(29.8)	(6.38)	(10.04)		

4.3 Electrochemical detection of epinephrine

4.3.1 Electroanalysis of epinephrine at bare and modified electrodes

The electroanalysis of EP was done using cyclic voltammetry at a scan rate of 25 mV s^{-1} in the presence of 0.4 mM EP prepared in PBS (pH 7). Figure 4.9 (a) showed the cyclic voltammograms (CV) recorded using bare GCE, CNPs, CQDs, bCQDs, and the composite modified electrodes. The voltammograms show GCE/CQDs/CNPs gave the highest I_{ap} and $I_{cp,}$ confirming the suspected superiority of GCE/CQDs/CNPs to other electrodes earlier established with the characterization of all electrodes with $[Fe(CN)_6]^{3-/4-}$ redox probe. Using the bare GCE, GCE/CQDs/CNPs, and GCE/bCQDs/CNPs electrode for cyclic voltammetry, the peaks emerging from the presence of EP in PBS were absent in PBS alone (blank) (Fig. 4.9 (b)). The peaks observed with GCE/CQDs/CNPs in PBS alone appeared at a potential where none of the EP peaks were found. The peaks are suspected to emerge from CQDs/CNPs composite itself. The emergence of peaks outside the potential window of the analytes has been reported for some CNPs-supported composites in blank solutions [304, 305]. The results and the fact that no peaks were found with bare GCE (in PBS alone) confirmed the electroanalysis of EP at bare and modified electrodes in EP solution.

It is worthy to note that the CV of EP at the electrodes showed four different peaks. The voltammograms is similar to the CV reported by Sainz et al., for EP electroanalysis at a graphene nanoribbons-modified electrode [306]. Electroanalysis of EP led to the formation of three other compounds (epinephrinechrome, epinephrinequinone, and leucoepineprine-chrome) as identified by electronspray ionization mass spectrometry and reported in literature [307, 308]. As a result, the four peaks represent the peaks corresponding to the three compounds and the peak associated with EP itself. The mechanism of EP redox processes in Scheme 2 showed that the formation of epinephrinechrome (EPC) from epinephrinequinone (EPQ) by Michael addition is highly favoured. The mechanism also revealed that leucoepinephrinechrome (LEC) is an intermediate product of the transformation of EPQ to EPC. The anodic peaks include the peak designated A1 (found at 0.2-0.3 V) associated with EP oxidation and the peak tagged A2, representing the peak associated with LEC oxidation. The cathodic peaks include C1 (found at 0.2-0.3 V) and C2 (found at -1 to -0.2 V), representing the reduction of EPQ and EPC, respectively (Scheme 3). The EP oxidation peak current has been considered the diagnostic peak for EP electrochemical oxidation due to its prominence.

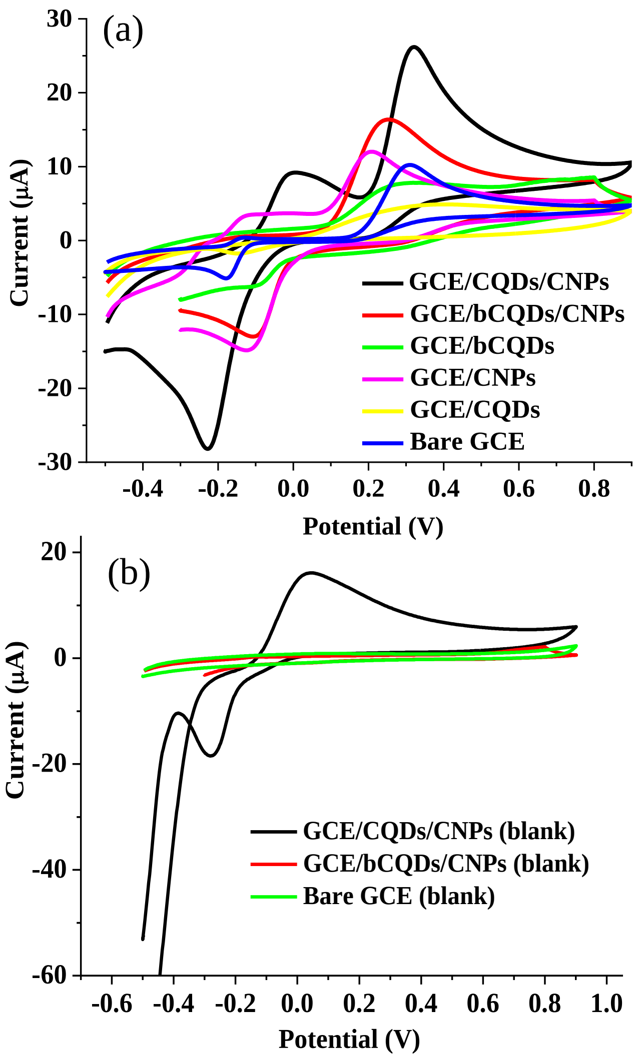

Figure 4.9: Cyclic voltammogram of the (a) bare GCE, CQDs, bCQDs, CNPs, bCQDs/CNPs and CQDs/CNPs modified GCE in 0.4 mM EP and (b) bare GCE, CQDs/CNPs and bCQDs/CNPs modified GCE in 0.1 M PBS (scan rate: 25 mV s^{-1}, pH 7).

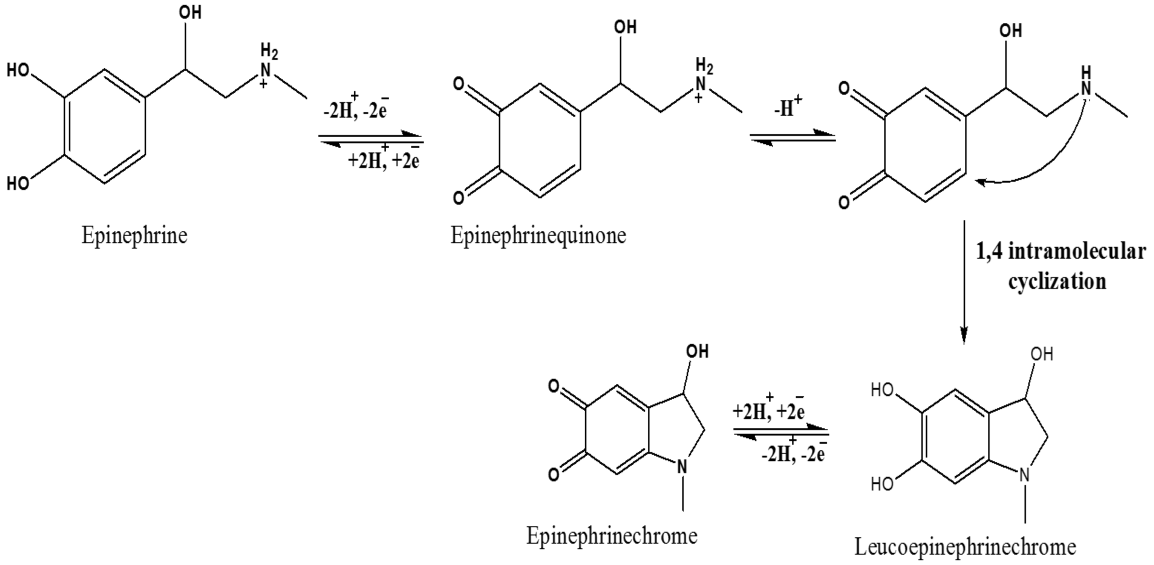

Scheme 2: Mechanism of epinephrine redox reactions

In the present study, the anodic peak current referred to the EP oxidation peak current (A1) and peak C2 represent the cathodic peak current.

Figure 4.10 showed the CVs of the bare GCE, CNPs, CQDs, bCQDs, and the composites modified electrodes in EP. The voltammograms gave a clear picture of the superiority of the composite modified GCE to that of the component individual nanomaterials and the bare GCE.

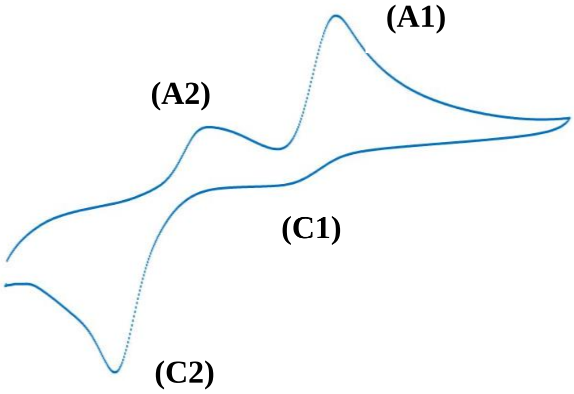

Scheme 3: Epinephrine redox peaks

Figure 4.10 (a) showed the CV for the bare GCE, GCE/CQDs, GCE/CNPs and GCE/CQDs/CNPs with anodic peak currents (I_{ap}) of 10.24 µA (0.31 V), 4.91 µA (0.31 V), 12.22 µA (0.21 V) and 26.99 µA (0.32 V), respectively. The I_{ap} at GCE/CQDs/CNPs was higher than twice the value at GCE/CNPs, about three times the value at bare GCE, and close to six times the value at GCE/CQDs. The cathodic peak currents (I_{cp}) of bare GCE, GCE/CQDs, GCE/CNPs and GCE/CQDs/CNPs were -6.91 µA (-0.18 V), -3.83 µA (-0.13 V), -15.20 µA (-0.13 V), and -28.50 µA (-0.23 V), respectively. The ratio of the I_{ap} to I_{cp} (A1 to C2) for these electrodes are in the order bare GCE (1.48) < GCE/CQDs (1.29) < GCE/CNPs (0.80) < GCE/CQDs/CNPs (0.95). The results showed that GCE/CQDs/CNPs provide a platform for a more reversible process compared to other electrodes. The outstanding performance of GCE/CQDs/CNPs can be ascribed to the synergy between CQDs and CNPs, which culminated in better current response than what was obtained at GCE/CQDs and GCE/CNPs. The synergy is probably a product of the large surface area and good biocompatibility of CQDs and the excellent conductivity of CNPs.

The synergy between carbon nanomaterials and metal oxide nanoparticles has produced composites with better electronic properties than the individual nanomaterials. In instances where such materials have been combined as composite for neurotransmitters (NTs) sensor fabrication, improved electrocatalytic activity of the sensor towards the oxidation of the NTs have been reported [200, 214, 309, 310]. A notable mention is the improved electrocatalytic activity of CNPs modified electrode towards EP oxidation after incorporating multi-walled carbon nanotubes (MWCNTs) [309].

A thorough inspection of the voltammograms in Figure 4.10 (a) revealed that GCE/CNPs possess the highest value of C1, suggesting a favourable reduction of EPC at GCE/CNPs. The voltammogram obtained with GCE/CQDs revealed that the electrode offered the poorest EP electrocatalysis. The fact that peak C1, which appeared on every other electrodes, was absent on the CV of GCE/CQDs supports this assertion. This could be associated with the rapid deprotonation of the EP's quarternary amino functionality than other materials, such that the intermediate EPQ was hardly formed before eventual EPC formation. Also, the highest C2 was recorded at GCE/CQDs/CNPs, suggesting that the synergy between CQDs and CNPs greatly supported the formation of EPC such that its reduction gave a relatively large current output. The shift in the I_{ap} of GCE/CNPs to the left indicated a low overpotential is required for EP oxidation, suggesting that CNPs provided a better electrocatalytic effect than the bare electrode. The oxidation peak potential (E_{ap}) at GCE/CQD shifted slightly to the positive side of the E_{ap} recorded at bare GCE. A similar occurrence has been reported for quantum dots modified electrodes designed for catecholamine neurotransmitter (NTs) detection [102, 115]. Noteworthy, the E_{ap} at GCE/CQDs/CNPs was about the same as that of the bare electrode.

The ΔE_p of the bare and modified electrodes followed the order: GCE/CNPs (340 mV) GCE/bCQDs/CNPs (360 mV) < GCE/bCQDs (380 mV) < GCE/CQDs (440 mV) < bare GCE (490 mV) < GCE/CQDs/CNPs (550 mV). The ΔE_p values of electrodes have been used for estimating the electron transfer rate and the electrocatalytic activity of modified electrodes toward NTs detection. Modified electrodes with small ΔE_p values have been adjudged better than those with large ΔE_p, based on the fact that small ΔE_p value symbolizes better electrocatalytic activity towards NTs oxidation. However, the complexity of the cyclic voltammogram of EP made adopting this data for similar deduction a difficult task. As evident from Table 4.4, GCE/CQDs/CNPs with the higher I_{ap} gave the highest ΔE_p value (550 mV) and GCE/CQDs with the lowest I_{ap} offered a lower ΔE_p. The results and the other ΔE_p values (Table 4.4) suggest that there was probably no connection between the ΔE_p gap and the electrocatalytic activity of the bare and modified electrodes towards EP oxidation. The fact that the potential gap has not been considered for the analysis of EP cyclic voltammogram confirmed the assertion.

Table 4.4: Cyclic voltammetry data of bare GCE and modified GCE in EP

Electrodes	I_{ap} (μA)	I_{cp} (μA)	E_{ap} (V)	E_{cp} (V)	I_{ap}/I_{cp}	ΔE_p (mV)
Bare GCE	10.22	-6.91	0.31	-0.18	1.48	490
GCE/CNPs	12.22	-15.2	0.21	-0.13	0.80	340
GCE/CQDs	4.91	-3.83	0.31	-0.13	1.29	440
GCE/bCQDs	7.71	-6.22	0.27	-0.11	1.24	380
GCE/CQDs/CNPs	26.99	-28.5	0.32	-0.23	0.95	550
GCE/bCQDs/CNPs	16.52	-12.93	0.25	-0.11	1.28	360

Figure 4.10 (b) showed the CV for bare GCE, GCE/bCQDs, GCE/CNPs, and GCE/bCQDs/CNPs. The I_{ap} values (E_{ap} in parenthesis) obtained with these electrodes were 10.24 (0.31), 7.71 (0.27), 12.22 (0.21), and 16.52 μA (0.25V), respectively. The I_{ap} at GCE/bCQDs/CNPs is about 1.6 times the value at bare GCE, 1.5 times the value at GCE/bCQDs and about 1.4 times the value at GCE/CNPs. Relative to the bare electrode, the anodic peak potential of the other electrodes shifted to the negative side, confirming that the oxidation of EP is more favourable at the modified electrodes. The lower overpotential at which EP oxidation occurs relative to bare GCE potential suggested improved electrocatalytic activity of the electrodes after modification with the composite and nanomaterials.

A similar relationship can be observed between the CV of bare GCE and modified electrodes recorded for EP electroanalysis [214, 311]. The cathodic peak current recorded for the electrodes were -15.20 μA (-0.13 V), -12.93 μA (-0.11 V), -6.22 μA (-0.11 V) and -6.91 μA (-0.18 V) for GCE/CNPs, GCE/bCQDs/CNPs, GCE/bCQDs and bare GCE, respectively. The ratio I_{ap}/I_{cp} for the electrodes are in the order GCE/CNPs (0.80) < GCE/bCQDs (1.24) < GCE/bCQDs/CNPs (1.28) < bare GCE (1.48). The outcome implied that the CNPs modified electrode offered better reversibility than the other electrodes.

Contrary to what was obtained in Figure 4.10 (b), where the cathodic peak at GCE/bCQDs/CNPs was the highest of all the electrodes, the cathodic peak current for GCE/CNPs was higher than that of GCE/bCQDs/CNPs. Also, the peak at C1 showed that GCE/bCQDs gave a more prominent C1 peak than GCE/bCQDs/CNPs and other electrodes. In contrast, the C2 peak was absent in the voltammogram of GCE/CQDs. Furthermore, the I_{ap} (peak at A1)

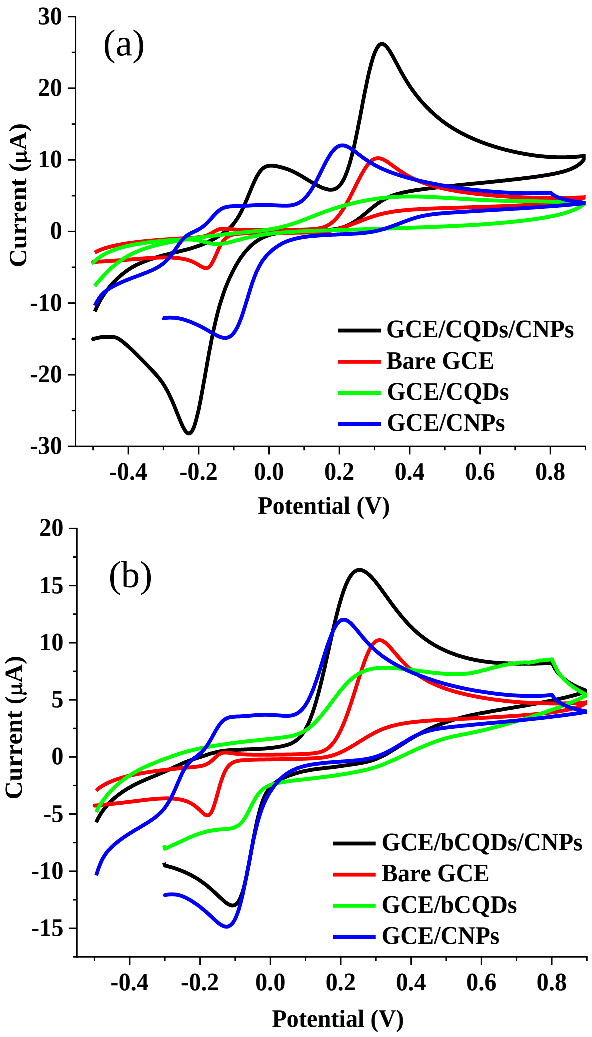

Figure 4.10: Cyclic voltammogram of (a) bare GCE, GCE/CQDs, GCE/CNPs and GCE/CQDs/CNPs and (b) bare GCE, GCE/bCQDs, GCE/CNPs and GCE/bCQDs/CNPs in 0.4 mM EP (scan rate: 25 mV s^{-1}, pH 7).

greater than that of GCE/CQDs (Fig. 4.10 (a)). The outcomes suggested that GCE/bCQDs offered better catalytic activity towards EP oxidation than GCE/CQDs. It is also important to note that the I_{ap} recorded at GCE/CQDs/CNPs (26.99 µA) was higher than that of GCE/bCQDs/CNPs (16.52 µA). Because of the outstanding perfromance of these two electrodes, subsequent EP analysis was carried out using GCE/bCQDs/CNPs and GCE/CQDs/CNPs. EIS analysis of EP with all electrodes was done to affirm the superiority of the two electrodes from the electron transport perspective prior to EP electroanalysis.

4.3.2 Electrochemical impedance spectroscopy (EIS)

Electrochemical impedance spectroscopy (EIS) was also applied for the analysis of EP. Figure 4.11 (a) depicts the Nyquist plot of the EIS data generated with bare GCE, GCE/CNPs, GCE/CQDs, GCE/bCQDs, GCE/CQDs/CNPs, and GCE/bCQDs/CNPs. The inset of Figure 4.11 (a) gave a clearer picture of the initially obscured Nyquist plot of all electrodes except GCE/CQDs. The Randles equivalent circuit in Figure 4.11 (a) represents the circuit used for fitting the EIS data from the Nyquist plot of these electrodes except GCE/CQDs.

Figure 4.11 (b) represents the equivalent circuit for fitting GCE/CQDs EIS data. The parameters used for fitting these circuits include solution resistance (R_S), charge transfer resistance (Rct), constant phase element (CPE), Warburg impedance (W), and capacitance (C) where appropriate. The R_{ct} values obtained with bare GCE, GCE/CQDs, GCE/CNPs, and

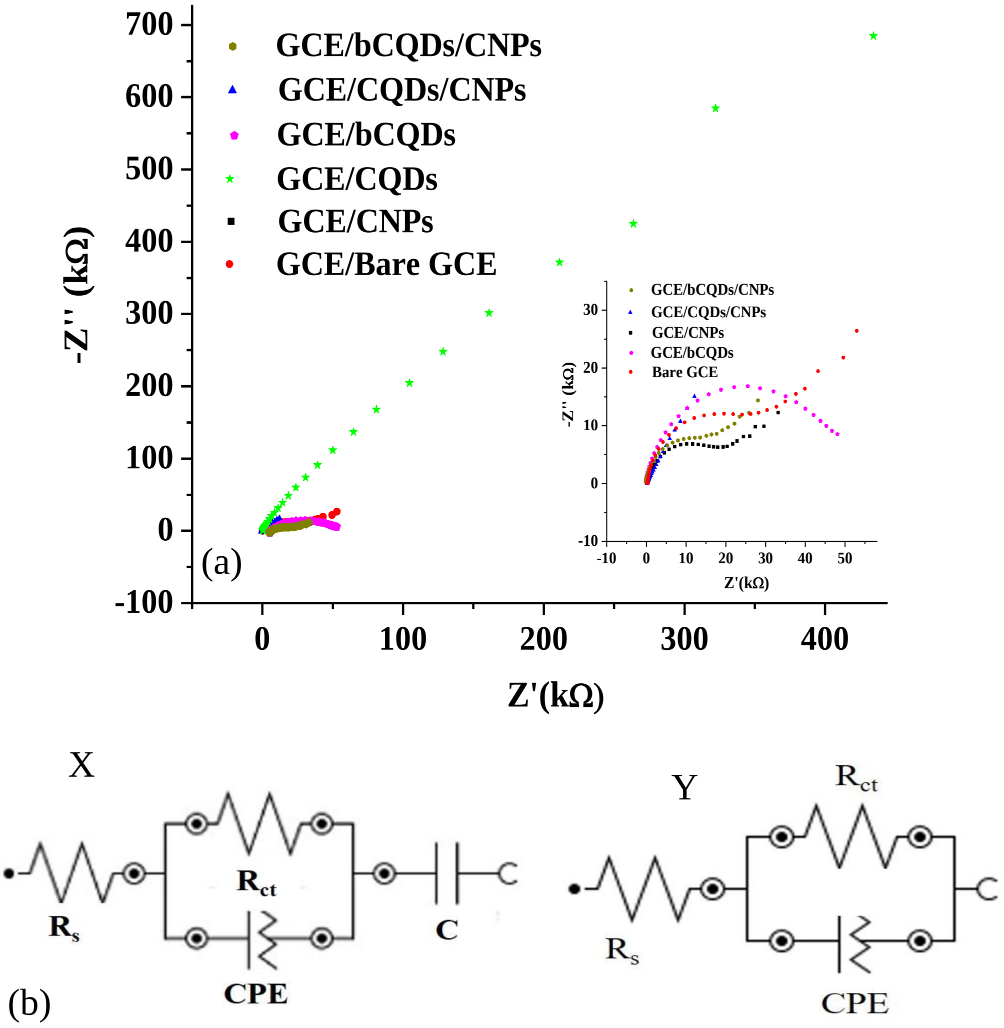

Figure 4.11: EIS spectra (Nyquist plot) of (a) Bare GCE, CQDs, bCQDs, CNPs and CQDs/CNPs modified GCE in 0.4 mM EP (pH 7) (inset: enlarged EIS spectra of the bare GCE, GCE/CNPs, GCE/bCQDs, GCE/CQDs/CNPs and GCE/bCQDs/CNPs) (b) equivalent electrochemical circuit of the EIS data at (a)

GCE/CQDs/CNPs were 24.28, 450.00, 17.22, and 6.72 kΩ, respectively (errors in parenthesis) (Table 4.5). The values show that GCE/CQDs/CNPs have the lowest resistance to charge transfer between the anlayte and the working electrode, suggesting that CQDs/CNPs improved the conductivity of GCE after modification. The fact that CNPs modified GCE have lower R_{ct} than bare GCE and GCE/CQDs also confirmed that CNPs improved the conductivity of GCE. Improved conductivity of GCE after modification with CNPs has been reported [312]. On the other hand, the extremely high R_{ct} obtained with GCE/CQDs showed that CQDs impede the charge transfer process after GCE modification with the CQDs. The outcomes agreed with the anodic current (I_{ap}) recorded with the electrodes using CV, thus confirming that the synergy between the CQDs and CNPs is essential for improved electrocatalytic oxidation of EP at GCE/CQDs/CNPs. The synergy was suspected to have emanated from the large surface area of CQDs and the excellent conductivity of CNPs in the presence of EP. Similar synergy in binary composites designed for neurotransmitters (NTs) detection has been reported [313]. The Warburg impedance in the Nyquist plot of the electrodes in EP (except for GCE/CQDs) showed that the interaction of EP with these electrodes involves diffusion. Equation 4.5 showed the relationship between the impedance of the constant phase element (Z_{CPE}), magnitude of the constant phase element (Y_o) and its exponent (N) (where j and ω represent an imaginary number and angular frequency, respectively) [314, 315]. The higher value of Y_o was recorded at GCE/CQDs/CNPs, suggesting the modified electrode possessed the lowest value of Z_{CPE} compared to other electrodes. The Z_{CPE} result further confirmed the superior conductivity of GCE/CQDs/CNPs. The superior current response obtained with CV and the low R_{ct} recorded with EIS are the reasons GCE/CQDs/CNPs was considered as the working electrode for further EP analysis.

$$Z_{CPE} = 1/\,(Y_o(j\omega)^N \qquad \text{(Eqn 4.5)}$$

Table 4.5 also showed that R_{ct} of bare GCE, GCE/bCQDs, GCE/CNPs, and GCE/bCQDs/CNPs were 24.28, 42.73, 17.22 and 16.12 kΩ, respectively. The fact that GCE/bCQDs/CNPs gave the lowest R_{ct} confirmed the superior conductivity of GCE/bCQDs/CNPs as earlier established with the $[Fe(CN_6)]^{3-/4-}$ redox probe. The higher R_{ct} obtained with GCE/bCQDs compared to bare GCE suggested that bCQDs adversely affected charge transfer across the modified electrode. Compared to bare GCE and GCE/bCQDs, lower R_{ct} was recorded with GCE/CNPs, suggesting that GCE/CNPs possess better conductivity than the other two electrodes. The synergy between bCQDs and CNPs in bCQDs/CNPs gave a composite with a better conductivity than the individual nanomaterials. The synergy is evident in the relatively low R_{ct} of the composite modified electrode. Obtaining the lowest R_{ct} with the bCQDs/CNPs modified electrode and the highest EP current response (I_{ap}) recorded with

GCE/bCQDs/CNPs (using CV) compared to the other three electrodes confirmed its suitability for EP detection. Also, GCE/bCQDs/CNPs possess the highest Y_o value compared to other electrodes. The outcome implied that the GCE possesses a lower Z_{CPE} value after modification with bCQDs/CNPs composite, thus affirming the higher conductivity of GCE/bCQDs/CNPs relative to bare GCE and the other electrodes.

The satisfactory performance of GCE/bCQDs/CNPs and GCE/CQDs/CNPs in the redox probe and EP confirmed that the two electrodes are suitable for comparative study of the contribution of the green carbon dots (bCQDs) and the chemically synthesized carbon dots (CQDs) to EP detection. Consequently, the two electrodes were adopted for further studies.

Table 4.5: EIS parameters of bare and modified electrodes in EP

Electrode	R_{ct} (kΩ)	R_s (kΩ)	Y_o ($\mu\Omega^{-1}s^N$)	N	W ($\mu\Omega^{-1}$.s)	X^2
Bare GCE	24.28 (2.91)	0.25 (1.24)	1.29 (4.23)	0.90 (0.68)	34.8 (4.11)	0.0927
GCE/CNPs	17.22 (3.18)	0.27 (1.59)	1.95 (5.62)	0.84 (0.95)	70.4 (6.27)	0.1186
GCE/bCQDs	42.73 (4.59)	0.25 (2.53)	1.98 (6.26)	0.83 (1.13)	8.98 (23.66)	0.3187
GCE/CQDs	450.0 (15.25)	0.31 (2.07)	1.80 (4.14)	0.81 (0.74)	-	0.2210
GCE/CQDs/CNPs	6.72 (59.5)	0.19 (1.07)	43.8 (12.57)	0.71 (2.63)	33.8 (12.57)	0.0659
GCE/bCQDs/CNPs	16.12 (6.03)	0.22 (2.24)	3.13 (8.03)	0.86 (1.42)	62.5 (8.82)	0.3123

4.3.3 Effect of scan rate

The effect of change in scan rate on EP electrocatalytic oxidation at GCE/CQDs/CNPs and GCE/bCQDs/CNPs was investigated with cyclic voltammetry using 0.4 mM EP at scan rate ranging from 25 – 400 mV s^{-1}. Figure 4.12 (a) showed the CV for EP electrocatalysis at GCE/CQDs/bCQDs over a scan rate range of 25 – 400 mV s^{-1}. These voltammograms showed that the peak A1 corresponding to EP oxidation peak current and the peak C2 (EPQ reduction peak current) increased with an increase in scan rate. Noteworthy, the cathodic peak C2 did not significantly change with scan rate as the anodic peak (A1). The plot of the anodic peak current at A1 (I_{ap}) and the square root of the scan rate ($v^{1/2}$) gave a linear relationship (Equation 4.6) as depicted in Figure 4.12 (b). The relationship between I_{ap} and $v^{1/2}$ became more linear at higher scan rates (≥ 200 mV s^{-1}). The cathodic peak current (peak C2) and the $v^{1/2}$ also gave a linear relationship (Equation 4.7). The linear relationship between I_{ap} and $v^{1/2}$ suggested a diffusion-controlled process at the surface of GCE/CQDs/CNPs. The diffusion-controlled mechanism was in agreement with the diffusion-controlled mechanism reported for EP electrochemical detection at chemically modified electrodes [306, 316]

$$I_{ap} = 3.7205 + 3.1073\ v^{1/2} \qquad (R^2 = 0.9918) \qquad \text{(Eqn 4.6)}$$

$$I_{cp} = -20.8342 - 1.7305\ v^{1/2} \qquad (R^2 = -0.9793) \qquad \text{(Eqn 4.7)}$$

The anodic peak potential also shifted (to the right) with the increase in scan rate, especially after 50 mV s^{-1} (Fig. 4.12 (c)). The anodic peak potential (E_{ap}) and the cathodic peak potential (E_{cp}) have a linear relationship with the logarithm of the scan rate (Equation 4.8). The number of electrons transferred (n) and the electron transfer coefficient (α) were calculated using Laviron equation, given that the slopes of the graphs of E_{ap} and E_{cp} against log v were b1 and b2, respectively (Equations 4.10 and 4.11). The parameters n, R, T and F in these equations retain their usual meaning. The Tafel slope b is calculated from Equation 4.12, suggesting that b is twice the value of b1 (for the anodic peak). Tafel slope b was calculated as 238 mV dec^{-1}. A Tafel slope within the range of 60-120 mV suggested a one-electron process at the rate-determining step. A redox process that leads to the emergence of a Tafel plot greater than 120 mV dec^{-1} suggested an adsorptive process at the surface of the electrode [317]. Adsorption of this nature has been ascribed to the strong binding force between the analyte and the electrode modifier [317, 318]. The Tafel slope for EP oxidation (238 mV dec^{-1}) exceeding 120 mV dec^{-1} suggested an adsorptive process at GCE/CQDs/CNPs [317].

$$E_{ap} = 0.1569 + 0.1188 \log v \qquad (R^2 = 0.9956) \qquad \text{(Eqn 4.8)}$$

$$E_{cp} = -0.1439 - 0.0537 \log v \qquad (R^2 = -0.9767) \qquad \text{(Eqn 4.9)}$$

$$b1 = \frac{RT}{(1-\propto)nF} \qquad \text{(Eqn 4.10)}$$

$$b2 = \frac{RT}{\propto nF} \qquad \text{(Eqn 4.11)}$$

$$E_p = \frac{b}{2} \log v + K \qquad \text{(Eqn 4.12)}$$

The values of α and n were calculated as 0.69 and 1.54, respectively. A similar value of n (~2) has been reported for the overlapping EP oxidation peaks A1 and A2 [308]. The α value reported for this electrode was greater than the values reported for the thin gold film modified electrode (0.52) and dysprosium tungstate modified electrode (0.30) [308, 319]. The disparity between α reported for these electrodes and GCE/CQDs/CNPs was due to the difference in the surface area and conductivity of the modifiers of the electrodes.

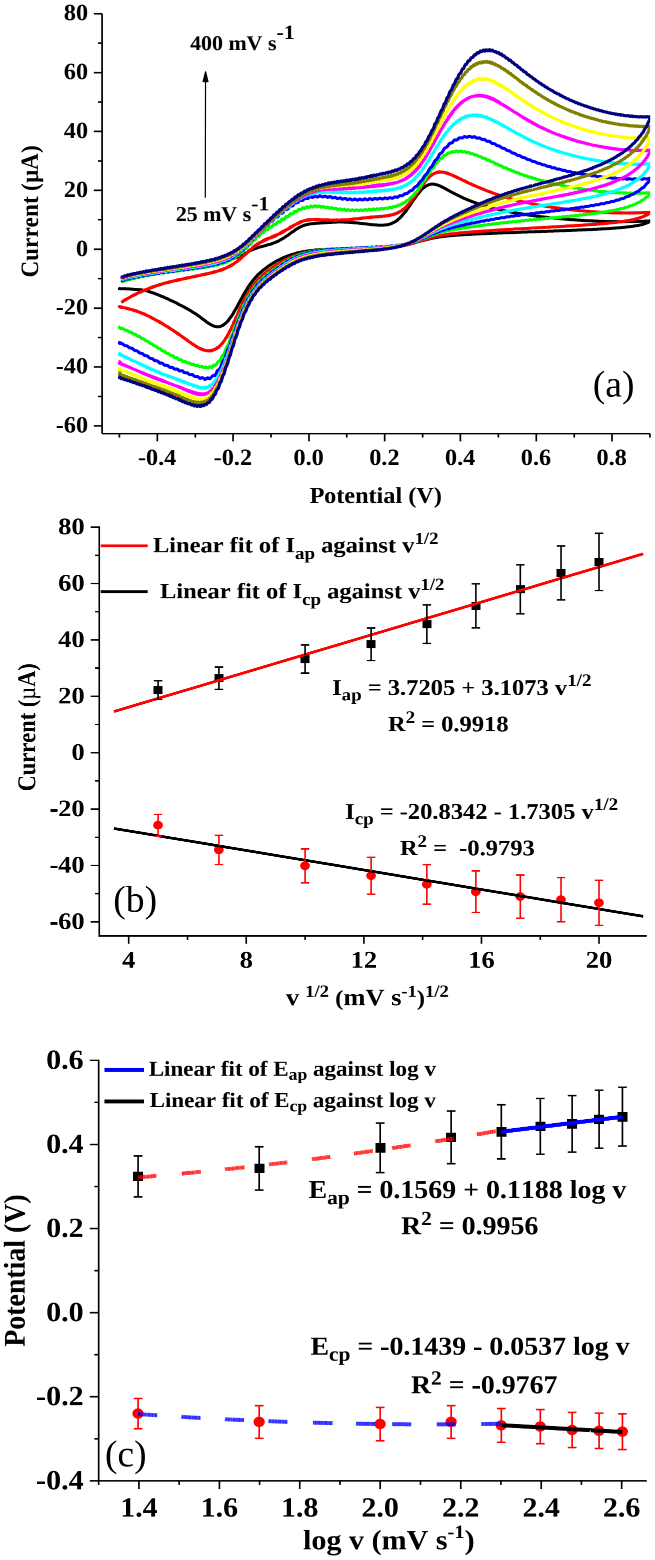

Figure 4.12: (a) Cyclic voltammogram of GCE/CQDs/CNPs in EP over a scan rate range (25 – 400 mV s-1) at pH 7 (b) plot of the anodic and cathodic peak current against the square root of the scan rate and (c) plot of the anodic and cathodic peak potential against log v

$$\log k_s = \propto \log(1-\propto) + (1-\propto)\log \propto - \log\left(\frac{RT}{nFv}\right) - \propto \frac{(1-\propto)nF\Delta E_p}{2.3RT} \qquad \text{(Eqn 4.13)}$$

The charge transfer rate constant (k_s) value calculated from Equation 4.13 is 5×10^{-3} s^{-1}. This value was higher than the value reported for some other modified electrodes for EP detection.

Figure 4.13 (a) showed the cyclic voltammogram of GCE/bCQDs/CNPs in 0.4 mM EP at varying scan rates (25-400 mV s^{-1}). Like the CV of GCE/CQDs/CNPs in Figure 4.12 (a), the anodic peak current (I_{ap}) and the cathodic peak current (I_{cp}) increased with increase in the square root of the scan rate (Fig. 4.13 (b)). The linear regression Equations 4.14 and 4.15 depicted the relationship between peak currents (I_{ap} and I_{cp}) and $v^{1/2}$. The relationship implied that the redox process at GCE/bCQDs/CNPs is also a diffusion-controlled process [308]. Also, the anodic peak potentials shift to the positive side with an increase in the scan rate. This shift was more significant with the anodic peak potentials (E_{ap}) (Fig. 4.13 (a)). Figure 4.13 (c) depicts the linear relationship between the peak potentials and the logarithm of the scan rates (log v). This relationship became more linear after 200 mV s^{-1}. The linear relationships between the peak potentials (E_{ap} and E_{cp}) and log v are represented with linear equations (Equations 4.16 and 4.17).

$$I_{ap} = 1.4989 + 2.0434\, v^{1/2} \qquad (R^2 = 0.9923) \qquad \text{(Eqn 4.14)}$$

$$I_{cp} = -5.6475 - 2.0929\, v^{1/2} \qquad (R^2 = -0.9995) \qquad \text{(Eqn 4.15)}$$

$$E_{ap} = 0.1651 + 0.1358 \log v \qquad (R^2 = 0.9975) \qquad \text{(Eqn 4.16)}$$

$$E_{cp} = -0.0504 - 0.0879 \log v \qquad (R^2 = -0.9897) \qquad \text{(Eqn 4.17)}$$

The values of α and n calculated from Equations 4.16 & 4.17 were 0.61 and 0.48, respectively. These values are lower than the results recorded for GCE/CQDs/CNPs (Table 4.6). In addition, the charge transfer rate constant (k_s) recorded with GCE/bCQDs/CNPs (0.44 s^{-1}) is higher than the k_s recorded with GCE/CQDs/CNPs (0.005). On the contrary, GCE/CQDs/CNPs gave a higher value of α (Table 4.6). The higher α value recorded at GCE/CQDs/CNPs suggested a faster electron transfer at GCE/CQDs/CNPs. The faster electron transfer at the electrode explains the superior anodic peak current recorded at GCE/CQDs/CNPs compared to GCE/bCQDs/CNPs. Also, the lower value of k_s recorded at GCE/CQDs/CNPs compared to GCE/bCQDs/CNPs could be ascribed to the high value of ΔE_p recorded at GCE/CQDs/CNPs.

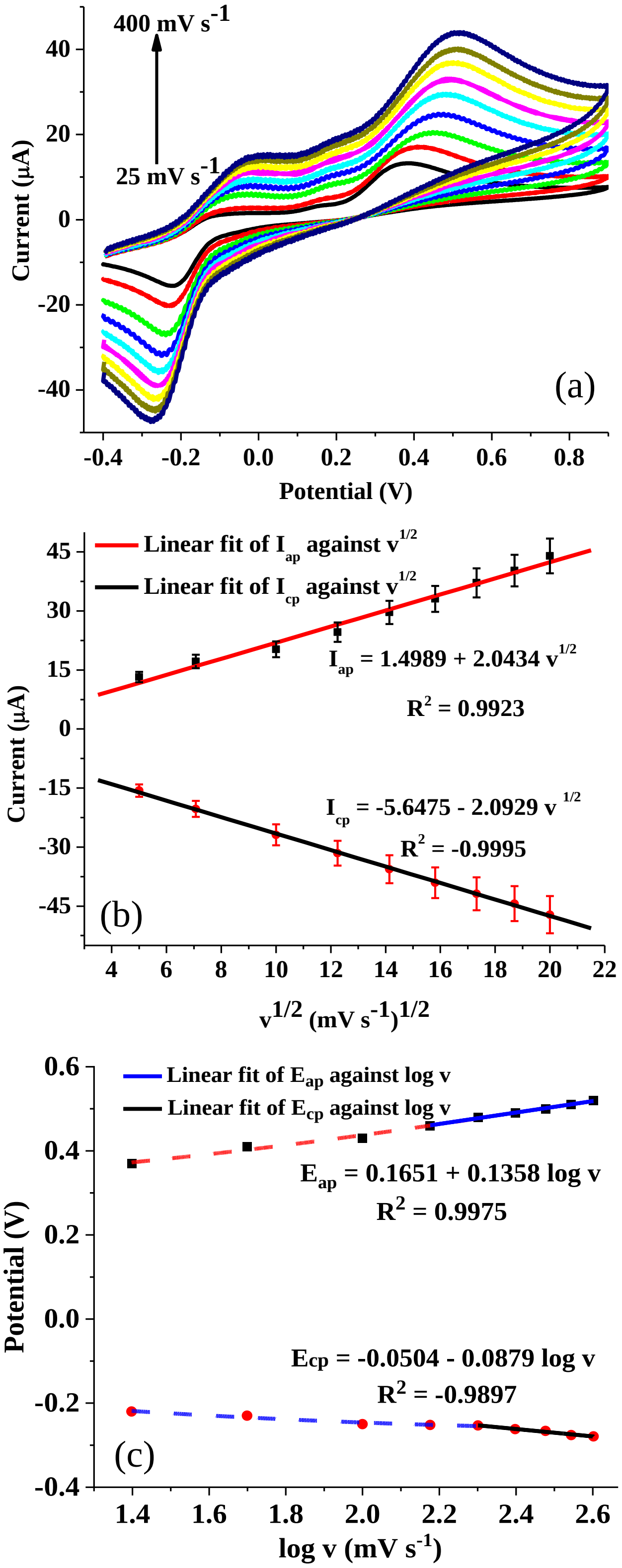

Figure 4.13: (a) Cyclic voltammogram of GCE/bCQDs/CNPs in EP over a scan rate range (25 – 400 mV s^{-1}) at pH 7 (b) plot of the anodic and cathodic peak current against the square root of the scan rate and (c) plot of the anodic and cathodic peak potential against log v

Table 4.6: Kinetic parameters of CQDs/CNPs and bCQDs/CNPs modified electrodes in EP

Electrode	α	n	k (s^{-1})	b (mV dec^{-1})
GCE/CQDs/CNPs	0.69	1.54	0.005	238
GCE/bCQDs/CNPs	0.61	0.48	44	272

Given the relationship between log k_s and ΔE_p, the absence of a direct link between I_{ap} and ΔE_p, and the complexity of the EP redox process, it could be inappropriate to use k_s to estimate the rate of electron transfer between EP and the modified electrodes. Noteworthy, the Tafel slope (b) recorded at GCE/bCQDs/CNPs (272 mV dec^{-1}) also suggested the prevalence of adsorption at the surface of the modified electrode [317].

4.3.4 Effect of pH

The influence of pH on the electrochemical oxidation of EP was studied with cyclic voltammetry at a scan rate of 25 mV s^{-1} using GCE/CQDs/CNPs and GCE/bCQDs/CNPs. Figure 4.14 (a) showed the cyclic voltammograms of EP at pH range of 3-9 using GCE/CQDs/CNPs. The voltammograms showed that the highest I_{ap} (peak A1) was recorded at pH 7 while the lowest peak current was obtained at pH 5. At pH 3.18, an unusually large current response emerged at peak A2. The fact that this peak is much higher than the diagnostic peak A1 suggested that the highly acidic pH supported the oxidation of LEC more than EP oxidation [308]. The outcome could be due to the availability of lone pair of electrons on the nitrogen atom on LEC, which consequently made LEC more susceptible to protonation by the acidic medium than the already protonated nitrogen on EP. The cationic nature of LEC after protonation increased the affinity of the CQDs in GCE/CQDs/CNPs for LEC, thus increasing the current response due to LEC oxidation. Noteworthy, the diagnostic anodic peak current A1 at pH 3.18 was lower than the value recorded at pH 7. At pH 9.3, a very low peak current (peak A1) was recorded. The trend was probably due to the deprotonation of EP, which led to repulsion between the cationic CQDs on GCE/CQDs/bCQDs and the deprotonated EP. With the exception of pH 3.18 where the lowest anodic peak potential was recorded, the anodic peak potential reduced with increase in pH (Fig. 4.14 (b)).

Figure 4.14 (c) depicted the pH dependence of peak currents recorded with GCE/bCQDs/CNPs. At pH 3.18, the voltammogram showed that EP oxidation proceeded like

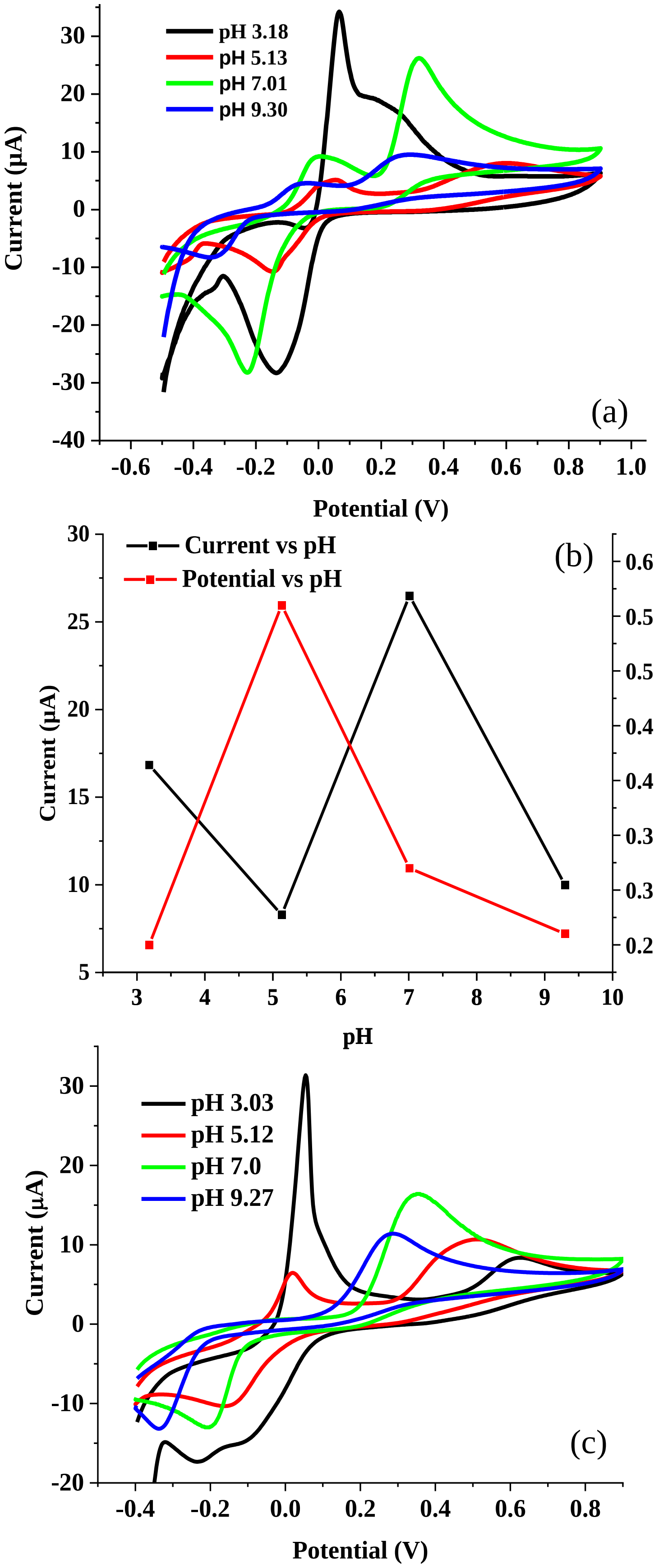
pH 3.18
pH 5.13
pH 7.01
pH 9.30
Current (µA)
Potential (V)
-0.6
-0.4
-0.2
0.0
0.2
0.4
0.6
0.8
1.0
30
20
10
0
-10
-20
-30
-40
(a)
Current vs pH
Potential vs pH
(b)
Current (µA)
Potential (V)
pH
3
4
5
6
7
8
9
10
5
10
15
20
25
30
0.25
0.30
0.35
0.40
0.45
0.50
0.55
0.60
pH 3.03
pH 5.12
pH 7.0
pH 9.27
Current (µA)
Potential (V)
-0.4
-0.2
0.0
0.2
0.4
0.6
0.8
-20
-10
0
10
20
30
(c)

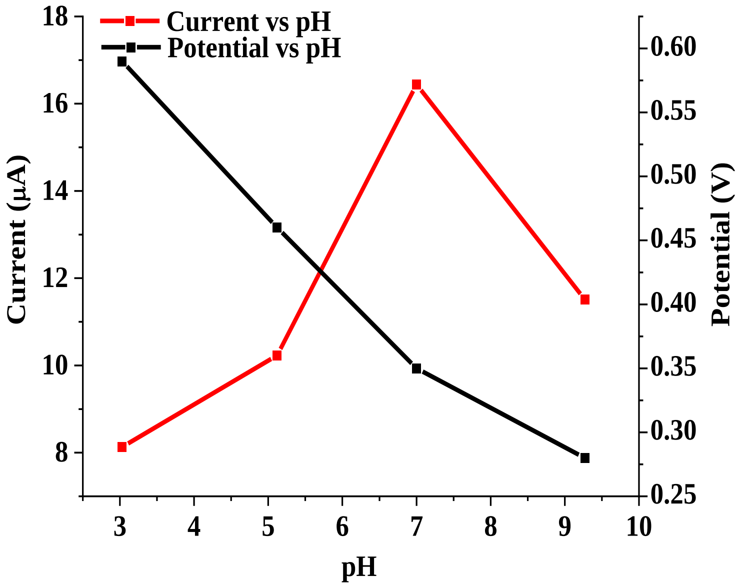

Figure 4.14: (a, c) Cyclic voltammograms of GCE/CQDs/CNPs and GCE/bCQDs/CNPs in 0.4 mM EP at pH 3-9 (scan rate: 25 mV s^{-1}) (b,d) plot of the anodic peak current and potential of EP against pH, recorded at GCE/CQDs/CNPs and GCE/bCQDs/CNPs

the CV obtained with GCE/CQDs/CNPs at a similar pH. However, the peak current A1 recorded with GCE/bCQDs/CNPs was the lowest compared to other pH values. Like the CV obtained with GCE/CQDs/CNPs at pH 7, the highest anodic peak current (peak A1) was recorded at pH 7 using GCE/bCQDs/CNPs. The significantly high anodic peak current recorded at pH 7 using the two electrodes could be attributed to the ability of the carbon-based quantum dots present in the electrodes modifier to attract the EP molecules through electrostatic interaction. The outcome explained why every other electroanalysis was done with these electrodes at pH 7. Interestingly, the electroanalysis of EP at pH 7 has been reported widely reported [213, 320, 321]. It is worth noting that the oxidation peak potentials recorded with GCE/bCQDs/CNPs reduced with increase in pH (Fig. 4.14 (d)). The outcome is similar to what was obtained at GCE/CQDs/CNPs, except that the lowest anodic peak potential at GCE/CQDs/CNPs was recorded at pH 3.18 (Fig. 4.14 (b)).

4.3.5 Effect of concentration

The influence of concentration changes on EP oxidation at GCE/CQDs/CNPs and GCE/bCQDs/CNPs was investigated over a concentration range of 10-116.4 µM and 1-125.3 µM, respectively, using square wave voltammetry (SWV). Figure 4.15 (a) depicted the square wave voltammograms obtained with GCE/CQDs/CNPs with varying concentrations of EP. The EP oxidation peak current recorded with SWV increased with an increase in EP concentration

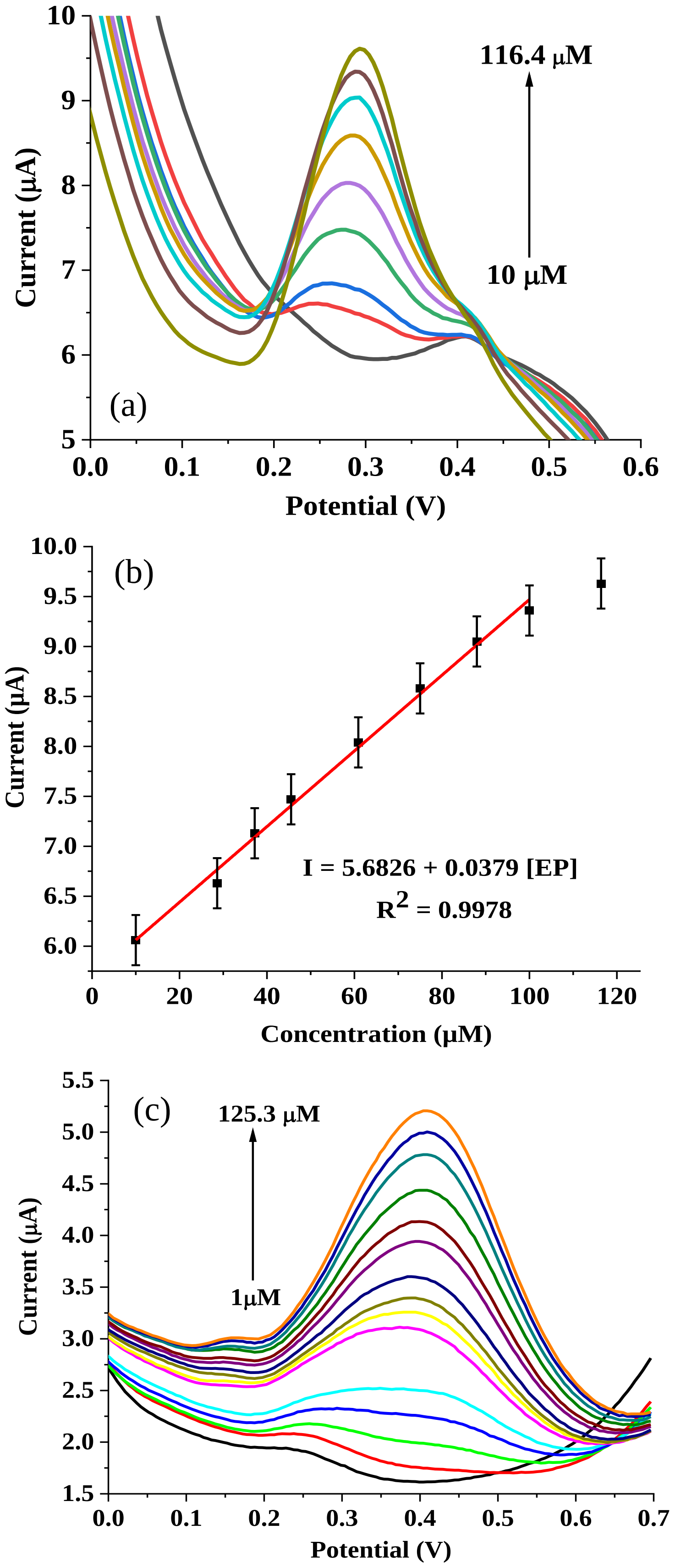
(a)
116.4 μM
10 μM
Current (μA)
Potential (V)
10
9
8
7
6
5
0.0
0.1
0.2
0.3
0.4
0.5
0.6
(b)
I = 5.6826 + 0.0379 [EP]
R^2 = 0.9978
Current (μA)
Concentration (μM)
10.0
9.5
9.0
8.5
8.0
7.5
7.0
6.5
6.0
0
20
40
60
80
100
120
(c)
125.3 μM
1μM
Current (μA)
Potential (V)
5.5
5.0
4.5
4.0
3.5
3.0
2.5
2.0
1.5
0.0
0.1
0.2
0.3
0.4
0.5
0.6
0.7

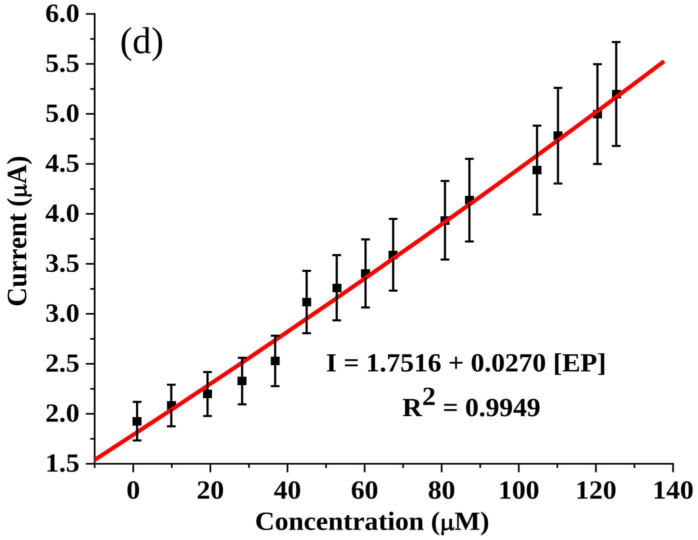

Figure 4.15: (a, c) Square wave voltammograms of GCE/CQDs/CNPs and GCE/bCQDs/CNPs over EP concentration range of 10-116.4 µM and 1-125.3 µM, respectively at pH 7 (b,d) plot of current versus concentration extracted from (a) and (c), respectively.

(Fig. 4.15 (a)). The plot of the current response against EP concentration showed a linear relationship represented by Equation 4.18 (Fig. 4.15 (b)). Figure 4.15 (b) also showed that this relationship was linear over a dynamic range of 10-100 µM. The limit of detection (LoD) for the electrodes was calculated using Equation 4.19, where δ is the standard deviation of the intercept and m is the slope of the calibration curve. The LoD calculated for GCE/CQDs/CNPs is 15.99 µM. Similarly, EP oxidation peak current increased with an increase in concentration when GCE/bCQDs/CNPs was used as the working electrode (Fig 4.15 (c)). This relationship was linear over a dynamic range of 1-125.3 µM (Fig. 4.15 (d)). Equation 4.20 showed the corresponding linear regression equation representing this linear relationship. The limit of quantitation of the sensor was calculated from Equation 4.21 as 48.45 µM.

The LoD calculated for GCE/bCQDs/CNPs is 24.3 µM. The LoD calculated with these electrodes was comparable to the value reported for some sensors earlier fabricated for EP detection (Table 4.7). An LoD of 14.99 µM reported for GCE/CQDs/CNPs was lower than the

$$I = 5.6826 + 0.0379\,[EP] \qquad \text{(Eqn 4.18)}$$

$$\mathrm{LoD} = \frac{3.3\,\delta}{m} \qquad \text{(Eqn 4.19)}$$

$$I = 1.7516 + 0.0270\,[EP] \qquad \text{(Eqn 4.20)}$$

$$\mathrm{LoQ} = 10\frac{\delta}{\mathrm{m}} \qquad \text{(Eqn 4.21)}$$

value reported for GCE/bCQDs/CNPs and some previously fabricated electrodes for EP detection [322, 323] (Table 4.7). On the other hand, the dynamic linear range (LDR) of 1 - 125.3 µM reported for GCE/bCQDs/CNPs was wider than that of GCE/bCQDs/CNPs and the MWCNT/Fe_3O_4/phthalocyanines nanocomposite modified electrode [324]. The limit of quantitation of GCE/bCQDs/CNPs (73.67 µM) was much higher than that of GCE/CQDs/CNPs.

The LoD and LDR recorded with the two electrodes suggested that they are suitable for EP detection at the micromolar level.

4.3.6 Interference studies

The interference of ascorbic acid (AA) with EP in a mixture of AA and EP was investigated using CV, SWV, and the differential pulse voltammetry (DPV). AA exists in extracellular fluid at a much higher concentration than EP [325]. Consequently, the possibility of detecting EP (0.4 mM) in a solution containing a much higher AA concentration was investigated. Figure 4.16 (a) showed the CV of the bare GCE and GCE/CQDs/CNPs in a mixture of 1 mM AA and 0.4 mM EP. With CV, the voltammograms obtained using the bare and the modified electrode (GCE/CQDs/CNPs) showed that the AA and EP peaks were indistinguishable. Specifically, a broad anodic peak was observed with bare GCE. In contrast, a sharper anodic peak at lower potential was observed at GCE/CQDs/CQDs. With DPV, distinct AA (at 0.23 V) and EP (at 0.38 V) peaks with a peak separation of 150 mV was recorded (Fig. 4.16 (b)). On the other hand, SWV gave a voltammogram with sharper EP peaks than that of DPV (Fig. 4.16 (c)). In addition, the peak potentials of AA (found at 0.25 V) and EP (found at 0.51 V) in SWV gave a larger peak difference (260 mV) than the peak separation in DPV (150 mV). The AA-EP peak separation at this electrode (with SWV) was wider than the peak difference reported at some notable EP sensors earlier fabricated [88, 326, 327]. As a result, SWV was adopted for detecting varying concentrations of EP (52.2 – 114.3 µM) in the presence of a constant AA concentration (1 mM) (Fig. 4.16 (d)).

Table 4.7: Comparison of the proposed sensors with past EP sensors

Electrode	Methods	LoD (µM)	LDR (µM)	Sensitivity (µA µM^{-1})	References
GCE/MWCNTs/poly-FA	AP	22.2	73-1406	0.004	[323]
GCE-MWCNT/Fe_3O_4/Nc	DPV	12.3	7.5-48	0.048	[324]
GCE/MWCNT/CA	DPV	10.0	30-170	-	[328]
Nano Au film	CV	19.0	50-1000	-	[322]
$CuFe_2O_4$/ILs/CPE	SWV	0.07	0.1-400	0.059	[329]
GCE/CQDs/CNPs	SWV	15.99	10-100	0.038	This work
GCE/bCQDs/CNPs	SWV	24.31	1-125	0.027	This work

GCE/MWCNTs/poly-FA – Multi-walled carbon nanotubes and poly ferulic acid modified glassy carbon nanotube; GCE-MWCNT/Fe_3O_4/Nc - Multi-walled carbon nanotubes, 2,3-naphthalocyanine and iron oxide nanocomposite modified glassy carbon electrode; GCE/MWCNT/CA - Multi-walled carbon nanotubes; Nano Au film – Nanoporous gold film; $CuFe_2O_4$/ILs/CPE – $CuFe_2O_4$ nanoparticles and ionic liquid composite modified carbon paste electrode.

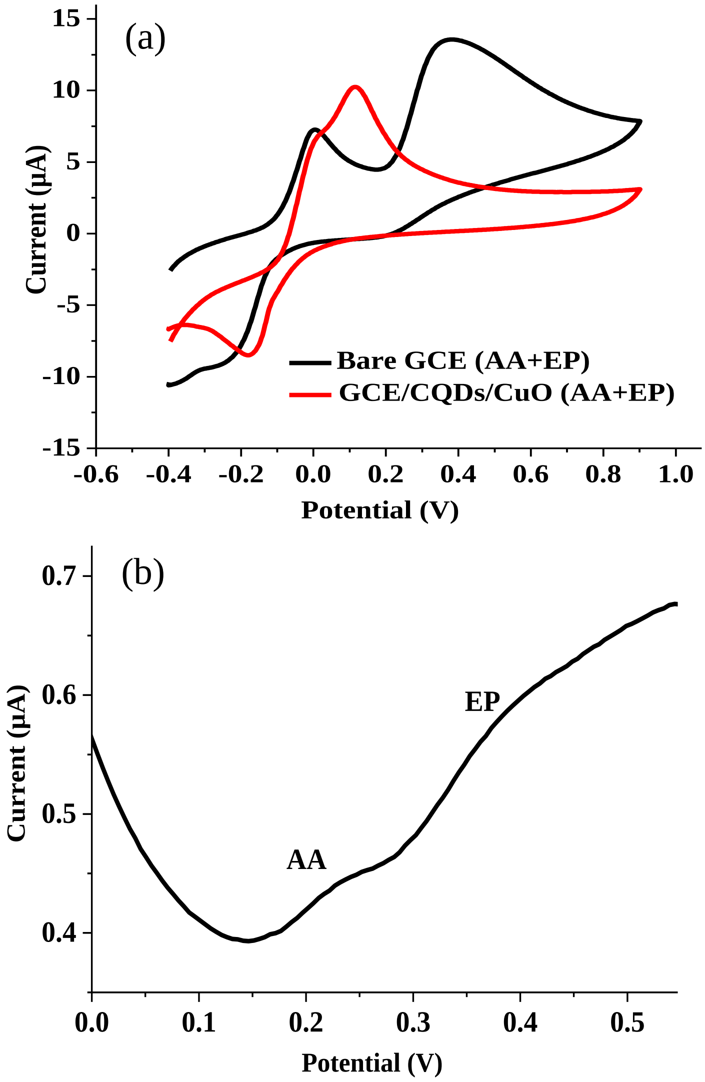

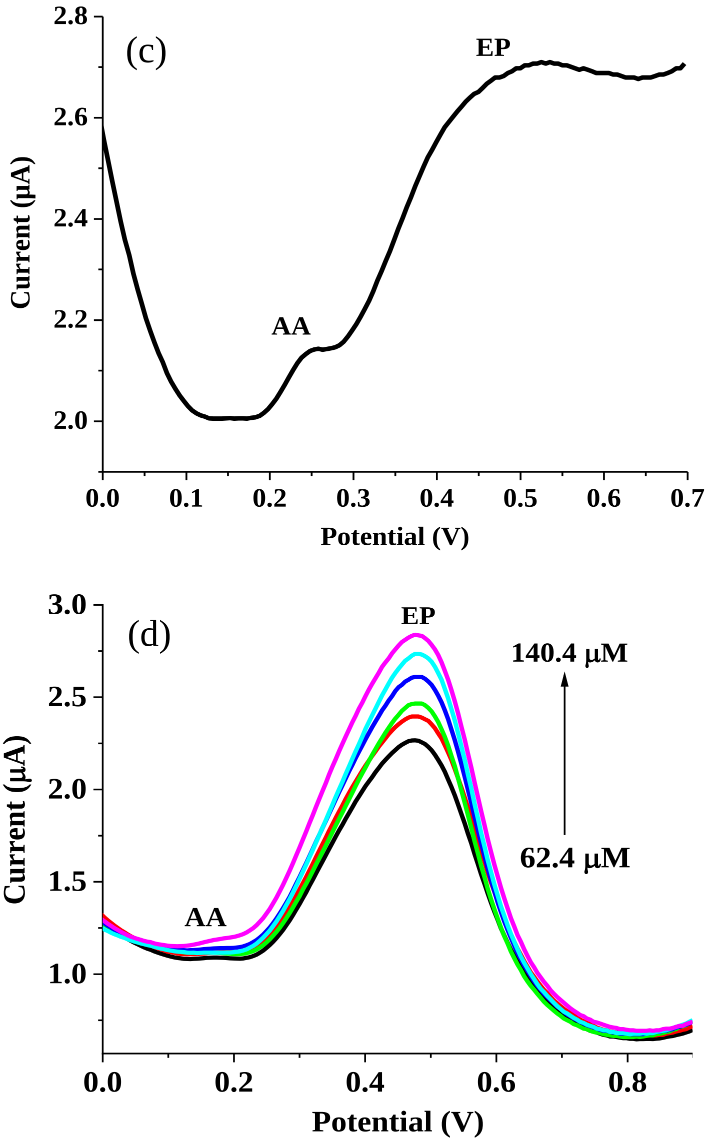

Figure 4.16: (a) Cyclic voltammograms of bare GCE and GCE/CQDs/CNPs, (b) square wave voltammogram and (c) differential pulse voltammogram of GCE/CQDs/CNPs in 0.4 mM EP and 1 mM AA (d) square wave voltammograms of EP concentration increase (62.4 – 140.3 µM) with constant AA concentration (1 mM) at GCE/CQDs/CNPs (pH 7, scan rate: 25 mV s^{-1}).

Figure 4.16 (d) showed that the peak potentials of AA and EP peaks shifted to a lower potential. More importantly, the AA peak remained unchanged with every increase in the EP concentration. This indicates AA's presence did not prevent EP detection at GCE/CQDs/CNPs.

Figure 4.17 showed the CV, SWV, and the DPV recorded from the investigation of the interference of AA with EP in a mixture of 1 mM AA and 0.4 mM EP at GCE/bCQDs/CNPs. Just like with GCE/CQDs/CNPs, the CV in Figure 4.17 (a) showed that the AA and EP peaks are indistinguishable.

Table 4.8: AA-EP peak difference of past and present EP sensors

Electrode	Method	AA-EP peak difference (mV)	References
NDG/PGE	LSV	204	[326]
TTAB/CPE	DPV	188	[88]
GO/CPE	DPV	131	[327]
MCPE/MWCNTs	CV	216	[330]
GCE/bCQDs/CNPs	SWV	170	This work
GCE/CQDs/CNPs	SWV	260	This work

NDG/PGE – nanodiamond/graphite modified pyrolytic graphite electrode; LSV – linear sweep voltammetry; CPE – carbon paste electrode; TTAB/CPE – Tetradecyltrimethyl ammonium bromide modified CPE; GO/CPE - Graphene oxide modified CPE; MCPE/MWCNTs – multi-walled carbon nanotubes modified CPE.

With DPV, the AA and EP peaks emerged at 0.10 V and 0.19 V, respectively, giving a peak-to-peak gap of 90 mV (Fig. 4.17 (b)). On the other hand, SWV gave AA-EP peak separation of 170 mV due to AA and EP peaks emerging at 0.13 V and 0.30 V, respectively (Fig. 4.17 (c)). This peak difference was wider than the AA-EP peak gap reported for some previously fabricated EP sensors (Table 4.8). The wider peak separation obtained with SWV explained why SWV was applied for the electroanalysis of varying EP concentrations (70.3 – 120.6 µM) at GCE/bCQDs/CNPs in the presence of a constant AA concentration.

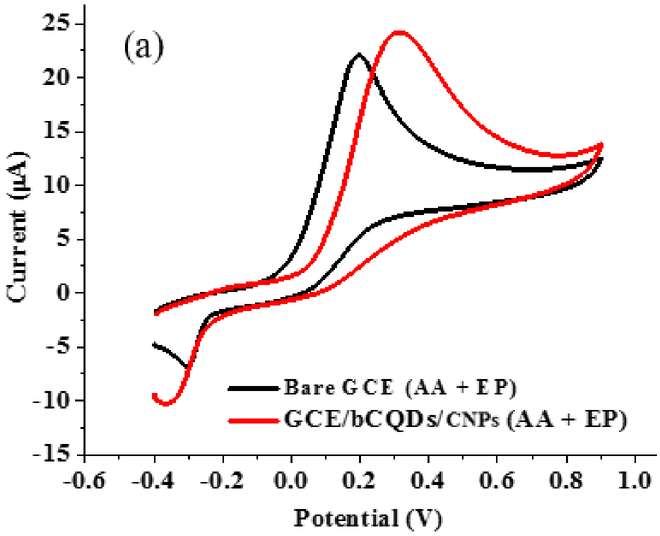

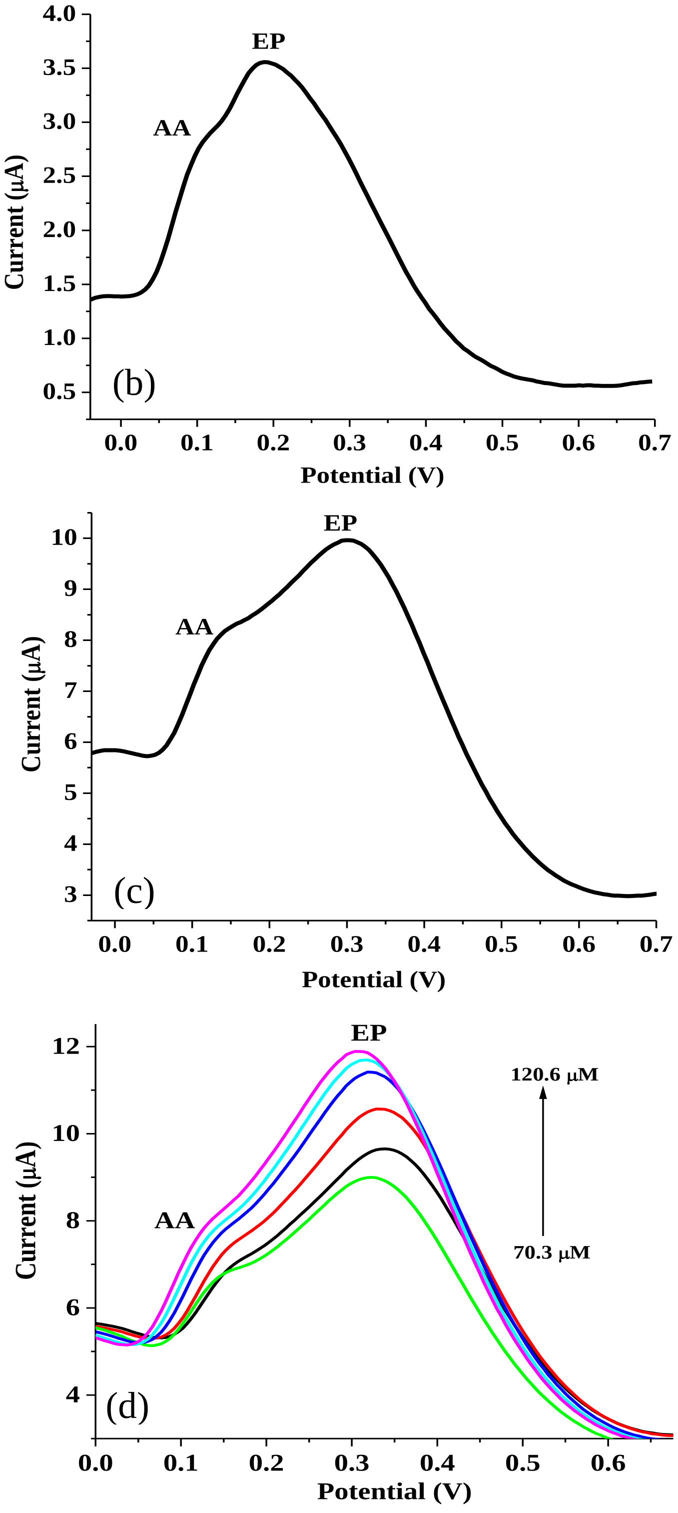

Figure 4.17: (a) Cyclic voltammogram of bare GCE and GCE/bCQDs/CNPs, (b) square wave voltammogram and (c) differential pulse voltammogram of GCE/bCQDs/CNPs in 0.2 mM AD and 1 mM AA (d) square wave voltammograms of EP concentration increase (70.3 – 120.6 μM) with constant AA concentration (1 mM) at GCE/CQDs/CNPs (pH 7, scan rate: 25 mV s^{-1}).

The AA peak did not showed a change as significant as that of the EP concentration. Although the AA peak change became more conspicuous at higher EP concentrations, the modified electrode can be considered a reliable tool for EP detection in the presence of AA (Fig. 4.17 (d)).

The inability of CV to distinguish AA and EP peaks at the bare and modified electrodes could be due to the lower sensitivity of CV compared to DPV and SWV. Also, the fact that EP gave four different peaks made it easy for AA peaks to interfere with EP peaks on the cyclic voltammogram. Also, the peak separations obtained with GCE/bCQDs/CNPs is higher than the value recorded with GCE/bCQDs/CNPs and comparable to the values reported for previously fabricated electrodes for EP detection in the presence of AA [88, 326, 327]. The result showed that GCE/CQDs/CNPs is more suitable for EP detection in the presence of AA.

4.3.7 Real sample analysis

The applicability of the two fabricated sensors for the analysis of EP in real sample was investigated with epinephrine injection using the standard addition technique. The mean percentage EP recovery at GCE/CQDs/CNPs after spiking a solution of the real sample with 45.46 µM EP (in triplicate) is 101.23 %. The percentage relative standard deviation (% RSD) of these measurements was 7.56 % (Table 4.9). With GCE/bCQDs/CNPs, a percentage recovery of 96 % was recorded after triplicate analysis with % RSD of 5.63 %. The results showed that the modified electrodes are suitable for EP detection in a real sample. It is also worth noting that GCE/CQDs/CNPs offered a higher percentage recovery than the bCQDs/CNPs modified electrode.

Table 4.9: EP analysis in epinephrine injection at GCE/CQDs/CNPs and GCE/bCQDs/CNPs

Electrode	Sample	Amount added (µM)	Amount found (µM)	% recovery	% RSD
GCE/CQDs/CNPs	EP injection	45.46	49.2	108.3	7.56
		45.46	46.48	102.3	
		45.46	42.34	93.10	
GCE/bCQDs/CNPs	EP injection	45.46	46.6	102.5	5.63
		45.46	42.1	92.6	
		45.46	42.2	92.9	

4.3.8 Stability and reproducibility

The stability of the electrodes was investigated using the modified electrodes for cyclic voltammetry in 0.4 mM EP at a pH of 7 and scan rate of 25 mV s^{-1}. The modified electrodes were subjected to 22 CV scans each (Fig. 4.18 (a) and (b)). With GCE/CQDs/CNPs, the current dropped to 50.9 % of the initial current response (current of the first scan). The voltammogram generated with GCE/bCQDs/CNPs showed that the bCQDs/CNPs modified electrode was only able to retain 56.4 % of the current response obtained after the first scan. The outcomes suggest that GCE/bCQDs/CNPs was more stable than GCE/CQDs/CNPs. In addition, the two electrodes are considered unstable when their stability was compared to some sensors previously fabricated for EP detection [83, 213, 331]. However, considering the equilibration time and adsorption equilibrium of the sensors in EP, the first two scans can be ignored, suggesting that the two sensors were relatively stable after the first two scans.

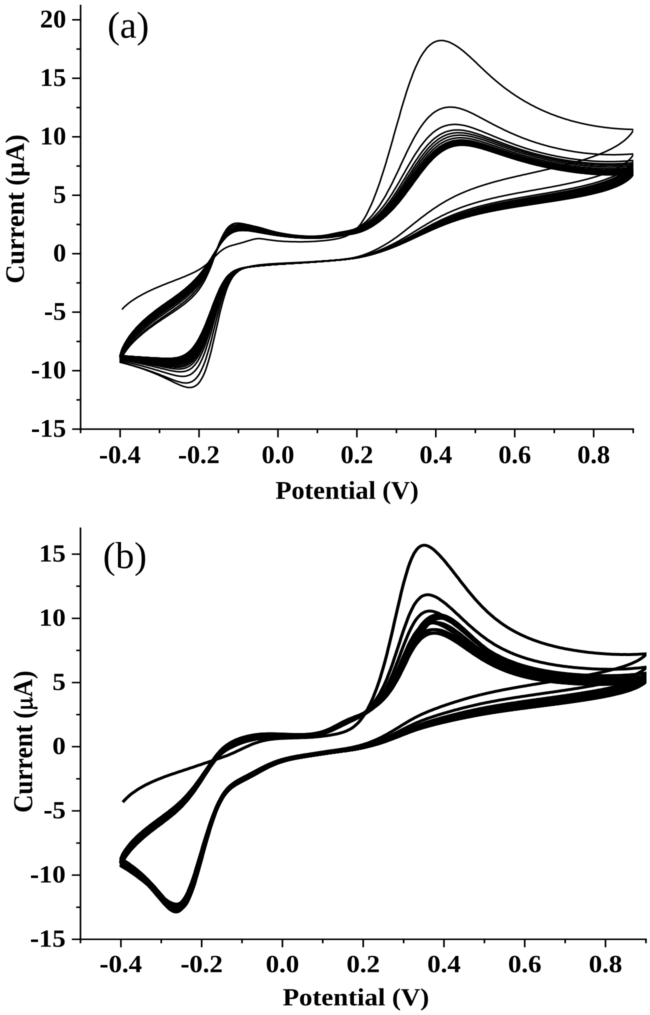

Figure 4.18: Cyclic voltammogram of (a) GCE/CQDs/CNPs and (b) GCE/bCQDs/CNPs in 0.4 mM EP (pH 7) after 22 scans (scan rate: 25 mV s^{-1})

The reproducibility of the electrode was investigated using a single CV scan under the same condition adopted for the reproducibility studies. The CV recorded for determinations made from electrode modified three separate times with the same composite showed the reproducibility of the modified electrodes (Fig. 4.19 (a) and (b)). Using CQDs/CNPs for GCE modification, the percentage relative standard deviation (% RSD) of the current response recorded for the three measurements is 8 %. With GCE/bCQDs/CNPs, the % RSD of the current response is 11 %. The lower % RSD obtained with GCE/CQDs/CNPs compared to that of GCE/bCQDs/CNPs suggested that the CQDs/CNPs modified electrode offered a more reproducible result. Collectively, the two sensors showed a considerable level of reproducibility, suggesting that the fabrication of the electrode can be replicated with reliable current response with minimal error margin.

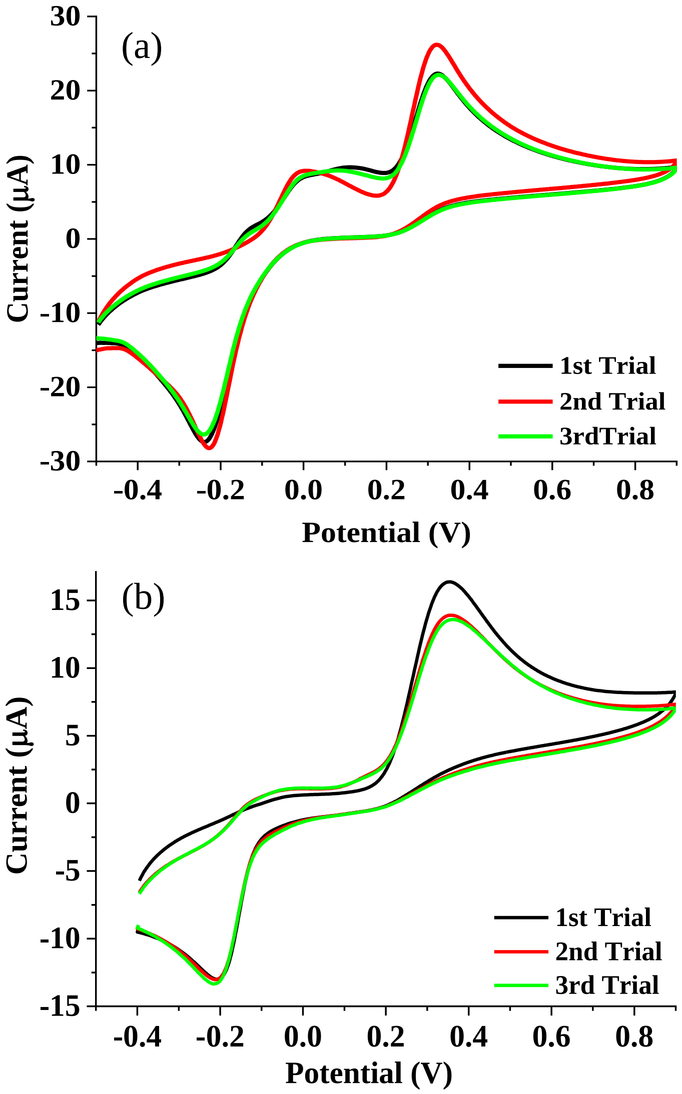

Figure 4.19: Cyclic voltammograms of (a) GCE/CQDs/CNPs and (b) GCE/bCQDs/CNPs in 0.4 mM EP (pH 7, scan rate: 25 mV s^{-1}) for three different trials of electrode modification

4.4 Electrochemical detection of norepinephrine

4.4.1 Electroanalysis of norepinephrine at bare and modified electrodes

The electroanalysis of norepinephrine (NE) at the bare and modified electrodes was done at a scan rate of 25 mV s^{-1} using cyclic voltammetry. The comparative cyclic voltammograms (CV) of the bare GCE, CNPs, CQDs, bCQDs, and the composites modified electrodes showed the current response of the electrodes in the presence of NE (Fig. 4.20 (a)).

In agreement with the result of the electrochemical characterization of the bare and modified electrodes with the $[Fe(CN)_6]^{3-/4-}$ redox probe, GCE/CQDs/CNPs gave the highest anodic peak current (I_{ap}). The anodic peak at 0.31 V was due to NE oxidation to norepinephrine quinone (NEQ) (I_{a1}). Like epinephrine quinone (EPQ), NEQ undergoes cyclization to 2,3,5,5-tetrahydro-1H-indole-3,5,6-triol (THT) which undergoes a redox reaction with 3-hydroxy-2,3-dihydro-1H-indole-5,6-dione (HID) (Scheme 4) [332]. The anodic peak at 0.02 V is due to the reduction of NEQ to NE (I_{c1}). The cathodic peak at 0.21 was due to the conversion of THT to HID (I_{a2}). The cathodic peak at -0.27 was due to the conversion of HID to THT (I_{c2}) (Scheme 3). NE cyclic voltammograms with similar redox peaks have been reported [332-334]. The existence of the products of NE oxidation and reduction have been established using electrospray ionization mass spectrometry [335]. Due to the prominence of I_{a1} and I_{c2} in the voltammograms, they are considered the anodic and the cathodic peak, respectively. Similar to the results recorded with epinephrine (EP), GCE/bCQDs/CNPs gave an anodic peak current (I_{a1}) close to that of GCE/CQDs/CNPs. On the other hand, the highest cathodic peak current

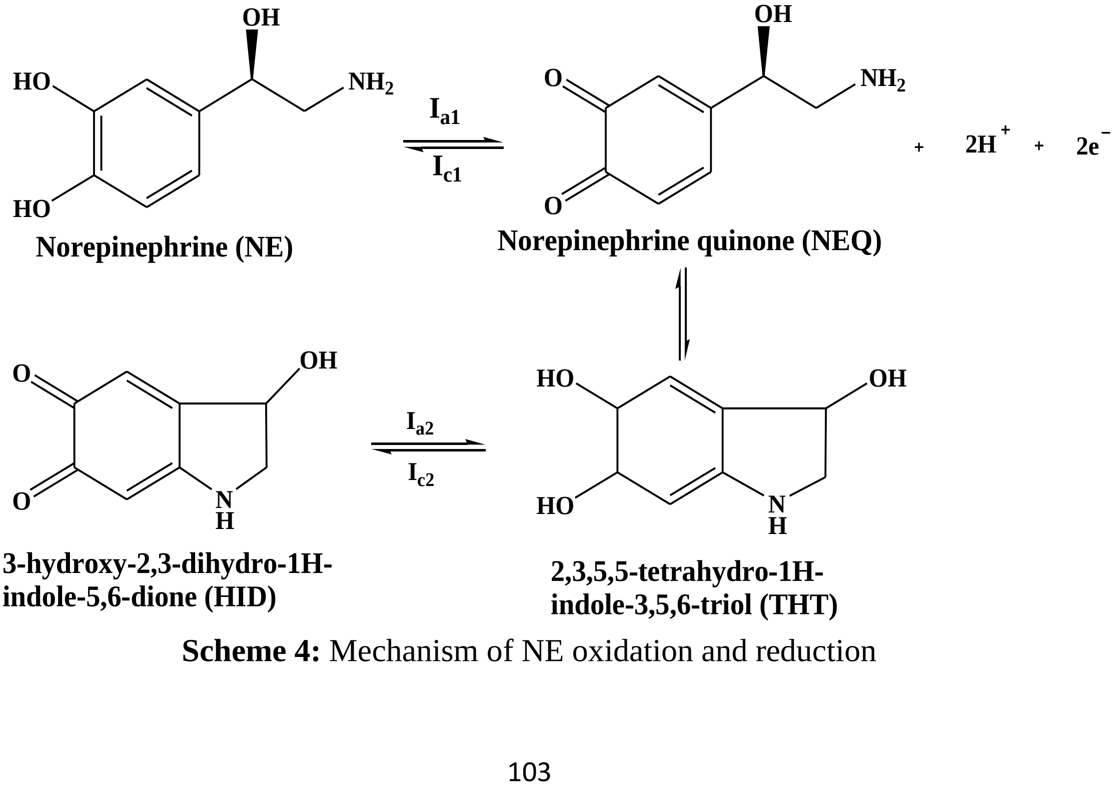

Scheme 4: Mechanism of NE oxidation and reduction

(I_{c2}) was recorded at GCE/CNPs. Because the anodic peak I_{a1} was the most prominent peak of the bare and the modified electrodes, and the fact that it was considered the diagnostic peak for NE electroanalysis [332, 333], GCE/bCQDs/CNPs and GCE/CQDs/CNPs were selected for further comparative NE analysis.

Figure 4.20 showed the relationship between the current signals of the bare electrodes, GCE/CNPs quantum dots, and the composites modified electrodes. The comparative CV showed that the bare GCE, GCE/CNPs, GCE/CQDs, GCE/CQDs/CNPs, GCE/bCQDs, and GCE/bCQDs/CNPs have I_{a1} values (potential in parenthesis) of 6.08 µA (at 0.39 V), 11.00 µA (at 0.28 V), 11.03 µA (at 0.28 V), and 55.69 µA (at 0.31 V), 1.80 µA (at 0.36 V), and 14.5 µA (at 0.22 V), respectively. The cathodic peak (I_{c2}) for these electrodes were -2.36 µA (at -0.21 V), -14.27 µA (at -0.26 V), -3.26 µA (at -0.16 V), and -74.14 µA (-0.28 V), -3.01 µA (at -0.38 V), and -8.59 µA (at -0.10 V), respectively. The ratio I_{a1}/I_{c2} has been used as the index of reversibility of the redox peaks obtained at the electrodes. The values of I_{a1}/I_{c2} recorded at bare GCE, GCE/CNPs, GCE/CQDs

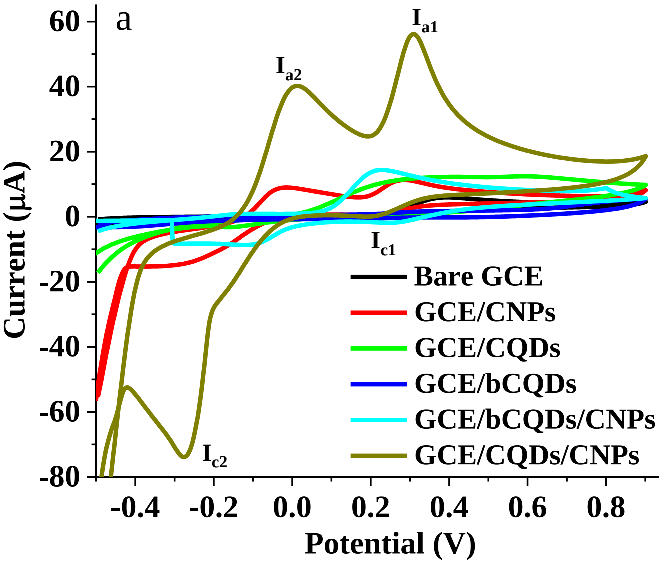

Figure 4.20: Cyclic voltammograms of bare GCE, CQDs, bCQDs, CNPs, CQDs/CNPs and bCQDs/CNPs modified GCE in 0.4 mM NE at pH 7 (scan rate: 25 mV s^{-1})

GCE/CQDs/CNPs, GCE/bCQDs and GCE/bCQDs/CNPs were 2.58, 0.77, 3.38, 0.75, 0.60, and 1.69 respectively. The results suggested that GCE/CNPs gave the most reversible NE peaks. Generally, all electrodes gave quasi-reversible peaks in the presence of NE. The prominent I_{a1} peak recorded at GCE/CQDs/CNPs and GCE/bCQDs/CNPs made these electrodes the chosen candidate for further NE electroanalysis.

Figure 4.21 (a) showed the relationship between the voltammograms of the bare GCE, GCE/CNPs, GCE/CQDs, and GCE/CQDs/CNPs. The voltammograms revealed that the I_{ap} values follow the order: GCE/CQDs/CNPs > GCE/CQDs > GCE/CNPs > bare GCE. In addition, the comparative voltammograms revealed the significantly large difference between the current response recorded at the nanocomposite modified electrode compared to the GCE modified with CQDs or CNPs. On the other hand, Figure 4.21 (b) showed the relationship between the voltammograms of the bare GCE, GCE/bCQDs, GCE/CNPs, and GCE/bCQDs/CNPs. The current responses from the voltammograms followed the order: GCE/bCQDs/CNPs > GCE/CNPs > bare GCE > GCE/bCQDs. In addition, the voltammograms show the closeness between the I_{ap} recorded at GCE/CNPs and GCE/bCQDs/CNPs and the superior cathodic peak current (I_{c2}) recorded at GCE/CNPs.

As it was with EP, the ΔE_p values recorded from the cyclic voltammograms of the bare and modified electrodes show that there was no direct link between the electrocatalytic activity of the electrodes toward NE oxidation and the ΔE_p values. For instance, GCE/CQDs/CNPs which gave the highest I_{ap} value due to the excellent electrocatalytic activity of the electrode towards NE oxidation possessed a significantly high ΔE_p (590 mV). On the other hand, GCE/bCQDs/CNPs which had a much lower I_{ap} gave a very low ΔE_p (320 mV). The relationhip is in contrast with reports on the relationship between electrocatalytic activity and ΔE_p which suggested that low ΔE_p value implied good electrocatalytic activity of the electrode towards the oxidation of the analyte [336]. Summarily, Table 4.10 showed that there was no relationship between I_{ap} and ΔE_p.

Table 4.10: Cyclic voltammetry data of bare GCE and modified GCE in NE

Electrodes	I_{ap} (µA)	I_{cp} (µA)	E_{ap} (V)	E_{cp} (V)	I_{ap}/I_{cp}	ΔE_p (mV)
Bare GCE	6.08	-2.36	0.39	-0.21	1.48	600
GCE/CNPs	11.00	-14.27	0.28	-0.26	0.80	540
GCE/CQDs	11.03	-3.26	0.28	-0.16	1.29	440
GCE/bCQDs	1.80	-3.01	0.36	-0.38	1.24	740
GCE/CQDs/CNPs	55.69	-74.14	0.31	-0.28	0.95	590
GCE/bCQDs/CNPs	14.5	-8.59	0.22	-0.10	1.28	320

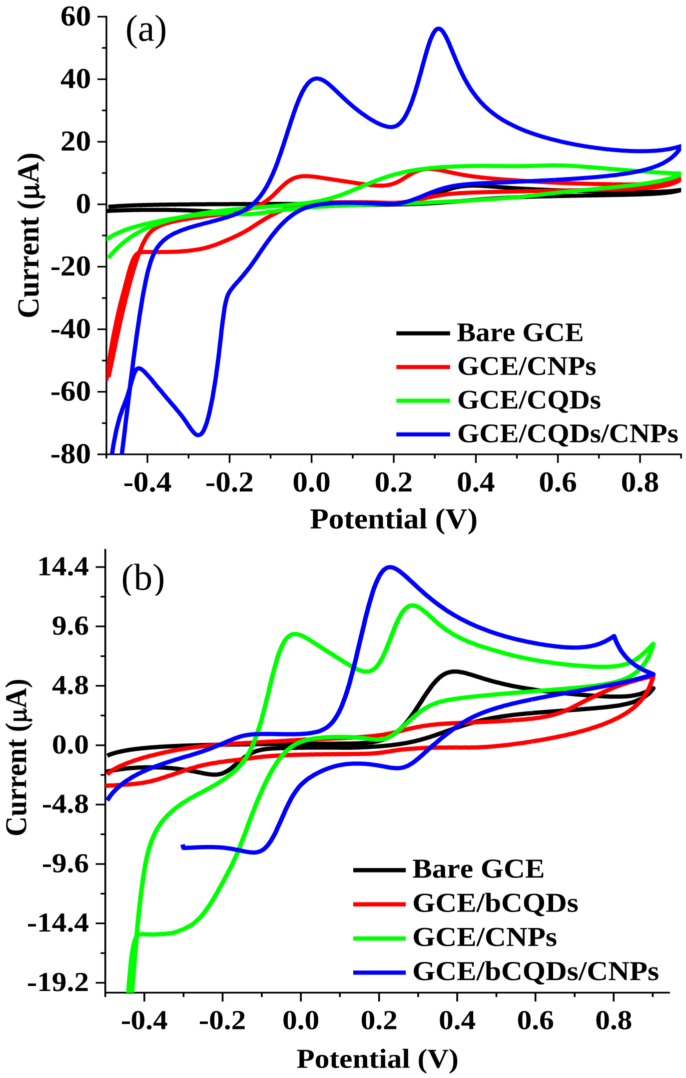

Figure 4.21: Cyclic voltammograms of (a) bare GCE, GCE/CQDs, GCE/CNPs and GCE/CQDs/CNPs and (b) bare GCE, GCE/bCQDs, GCE/CNPs and GCE/bCQDs/CNPs in 0.4 mM NE (scan rate: 25 mV s^{-1}, pH 7).

4.4.2 Electrochemical impedance spectroscopy

To further substantiate the suitability of the electrodes as the working electrodes for NE electroanalysis, EIS was done with the bare electrodes, and the electrodes modified with CNPs, quantum dots, and their composite. Figure 4.22 (a) depicted the Nyquist plot of the EIS data obtained at bare GCE, GCE/CNPs, GCE/CQDs, GCE/bCQDs, GCE/bCQDs/CNPs, and GCE/CQDs/CNPs. Table 1 showed the value of the charge transfer resistance (R_{ct}), capacitance (C), solution resistance(R_s), the magnitude of the constant phase element (CPE) (Y_o), the CPE exponent (N), Warburg impedance (W) and the Chi square (X^2) value recorded after fitting the EIS spectrum.

Table 4.11: EIS parameters of bare and modified electrodes in NE

Electrode	R_{ct} (kΩ)	R_s (kΩ)	Y_o ($\mu\Omega^{-1}s^N$)	N	W ($\mu\Omega^{-1}.s$)	X^2
Bare GCE	80.10 (9.94)	0.21 (2.61)	5.42 (5.38)	0.82 (1.19)	-	0.4376
GCE/CNPs	68.28 (8.35)	0.19 (4.12)	3.68 (7.44)	0.76 (1.53)	-	0.7232
GCE/bCQDs	111.41 (9.75)	0.20 (3.06)	5.05 (6.02)	0.81 (1.31)	-	0.5583
GCE/CQDs	49.41 (35.48)	0.24 (2.95)	-	-	8.04 (11.37)	0.6175
GCE/CQDs/CNPs	19.71 (2.23)	0.21 (2.23)	4.23 (7.32)	0.82 (1.37)	53.29 (9.14)	0.2784
GCE/bCQDs/CNPs	19.98 (8.85)	0.20 (2.35)	1.96 (8.53)	0.85 (1.38)	19.83 (5.24)	0.2734

The EIS data of the bare GCE, GCE/CNPs, GCE/CQDs, and GCE/CQDs/CNPs is shown in Table 4.11. The Nyquist plot of the EIS spectra obtained with the electrodes showed that multiple circuits are required for fitting the spectra (Fig. 4.22 (b)). Therefore, the equivalent circuit X was used for fitting the EIS spectra of bare GCE and GCE/CNPs. On the other hand, equivalent circuits Y and Z were used for GCE/CQDs and GCE/CQDs/CNPs EIS spectra fitting, respectively (Fig. 4.22 (b)). The charge transfer resistance (R_{ct}) obtained at bare GCE, GCE/CNPs, GCE/CQDs, and GCE/CQDs/CNPs were 80.10, 68.28, 49.41, and 19.71 kΩ, respectively. The increase in R_{ct} follows the order: GCE/CQDs/CNPs < GCE/CQDs < GCE/CNPs < bare GCE. This showed that GCE/CQDs/CNPs possess the lowest resistance to charge transfer between NE and CQDs/CNPs composite. Also, the R_{ct} trend agrees with the anodic current (I_{a1}) response recorded with CV. It is also worth noting that the R_{ct} obtained with GCE/CQDs was significantly higher than that of GCE/CNPs even though the anodic current (I_{a1}) response at GCE/CQDs was not so significant. The elationship between R_{ct} and I_{a1} could be due to the fact that the CNPs had a higher surface area than the CQDs which adversely affected the electron transfer between NE and GCE/CNPs. The assertion has also been substantiated by the fact that the Warburg impedance was absent in the equivalent circuit for modeling EIS data obtained with GCE/CNPs because the Warburg impedance in the circuit of GCE/CQDs suggested a diffusive movement of NE towards GCE/CQDs [96, 337]. It was therefore deduced that the movement of NE towards GCE/CNPs must have occurred through a channel other than diffusion, thus retarding the charge transfer process. The capacitance (C1 and C2) in the equivalent circuit at GCE/CQDs confirms the CQDs' capacitive nature. The capacitance C1 and

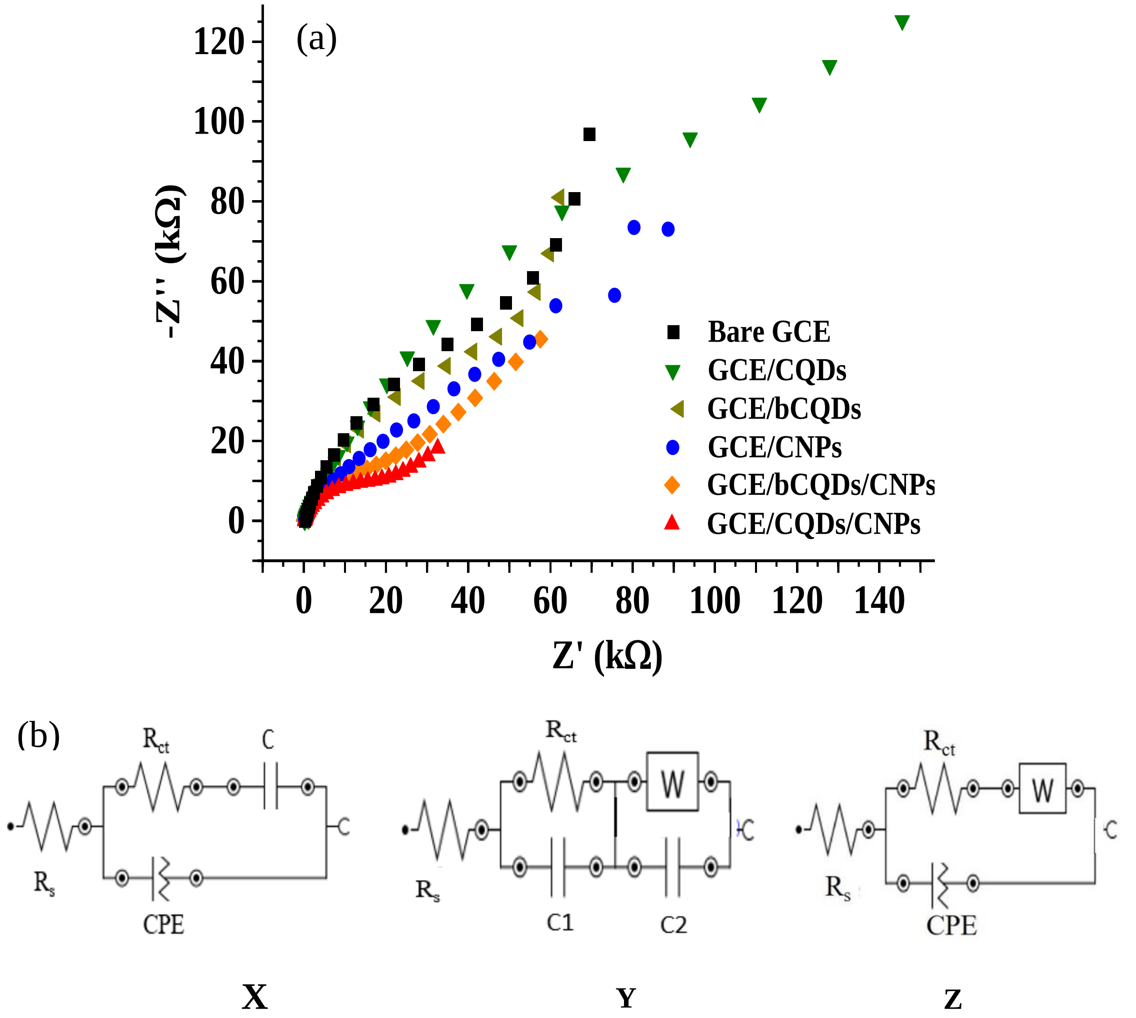

Figure 4.22: EIS spectra (Nyquist plot) of (a) Bare GCE, CQDs, bCQDs, CNPs and CQDs/CNPs modified GCE in 0.4 mM NE (pH 7) (b) equivalent electrochemical circuit of the EIS data at (a)

C2 represent the double layer capacitance and the passivation layer capacitance, respectively [338]. The result suggested that CQDs film has a capacitive tendency with the possibility of forming a passive layer on the bare electrode. The capacitance C in the equivalent circuit of GCE/CNPs and the bare GCE (circuit X) is the double-layer capacitance. The very high R_{ct} obtained at the bare GCE is an indication that the modifiers improved the charge transfer process between the analyte and the electrode.

Figure 4.22 (a) showed the Nyquist plot of the bare GCE, GCE/CNPs, GCE/bCQDs, and GCE/bCQDs/CNPs. The equivalent circuit X was used for fitting the EIS spectra of bare GCE, GCE/bCQDs, and GCE/CNPs. On the other hand, the equivalent circuit Z was used for fitting the EIS spectrum of GCE/bCQDs/CNPs. The R_{ct} values obtained at the bare GCE, GCE/CNPs, GCE/bCQDs, and GCE/bCQDs/CNPs were 80.10, 68.28, 111.41, and 19.98 kΩ, respectively (Table 4.11). The R_{ct} values followed the order: GCE/CQDs/CNPs < GCE/CNPs < bare GCE < GCE/bCQDs. The values agreed with the anodic current response obtained with CV because the anodic current response values followed the reverse order. The trend suggested that the bCQDs/CNPs composite modified electrode possesses the lowest resistance to charge transfer between the electrode and the analyte. Also, the lower R_{ct} obtained with GCE/CNPs and GCE/CQDs showed that the CNPs and CQDs have lower conductivity relative to bCQDs/CNPs. A similar occurrence was recorded with GCE/CQDs, GCE/CNPs, and GCE/CQDs/CNPs. The R_{ct} trend implied that the individual nanomaterials that form bCQDs/CNPs and GCE/CQDs/CNPs have a synergy that raises the conductivity of the composites. The fact that the highest R_{ct} was obtained with GCE/bCQDs implied that bCQDs acted like an insulator on the GCE surface, thus impeding electron transfer between NE and the modified electrode. Such an increase in the R_{ct} of the bare electrode after modification has been reported [237, 339]. In general, GCE/CQDs/CNPs and GCE/bCQDs/CNPs possessed the lower R_{ct} compared to other electrodes considered (Table 4.11). The outcome and the superior current response of these electrodes (with CV) informed the decision to apply these electrodes for further NE electroanalysis.

4.4.3 Effect of scan rate

The effect of scan rate on the peak currents was investigated with GCE/CQDs/CNPs and GCE/bCQDs/CNPs using cyclic voltammetry. The voltammograms recorded at GCE/CQDs/CNPs revealed that the anodic peak currents increased with an increase in scan rate (Fig. 4.23 (a)). It is worth noting that the anodic peak I_{a1} was more intense than the peak I_{a2} at low scan rates (25-50 mV s^{-1}). At higher scan rates, the two peaks were of similar intensity. The occurrence suggested that the oxidation of NE was more dominant at low scan rates, while the oxidation of NE (I_{a1}) and the conversion of 2,3,5,5-tetrahydro-1H-indole-3,5,6-triol (TIT) to 3-hydroxy-2,3-dihydro-1H-indole-5,6-dione (HID) (I_{a2}) share similar kinetics. Figure 4.23 (b) showed the linear relationship between the scan rate (v) and the anodic peak current (I_{a1}). The linear relationship between **v** and I_{a1} has been represented by Equation (Equation 4.22). Similarly, the cathodic peak (I_{c2}) showed a linear relationship with the scan rate (Equation 4.23). As reported in numerous publications, a linear relationship between **v** and the anodic peak current suggested a surface-confined process [340, 341]. Therefore, the outcomes suggested that the interaction between the modified electrode (GCE/CQDs/CNPs) and the analyte could be defined by an adsorptive mechanism.

Figure 4.23 (a) showed a noticeable shift of the anodic peak potential to the positive side with an increase in scan rate. In contrast, based on physical inspection, the change in the cathodic peak current was most noticeable after 100 mV s^{-1}. Figure 4.23 (c) showed the relationship between log v and peak potentials (anodic and cathodic). Equations 4.23 & 4.24 represented the linear relationship between the peak potentials and log v. The relationship between the peak potentials and ln v were more linear at higher scan rates (> 200 mV s^{-1}). Using Equations 4.23 & 4.24, the number of electron (s) transferred (n) and the charge transfer coefficient (α) was calculated as 0.34 and 1.83, respectively. The Tafel slope (b) was found to be 232 mV dec^{-1}. The Tafel value was obtained from the slope of a plot of log v against E_{pa} (Equation 4.24) and Equation 4.12. Similar to what was obtained at EP oxidation, the fact that these Tafel slopes exceed 120 mV dec^{-1} suggested that the occurrence of adsorption at the surface of the modified electrode [317]. The electron transfer rate constant (k_s) calculated from Equation 4.13 was 0.55 s^{-1}.

$$\mathrm{I_{ap}} = 33.8847 + 0.6001\,\mathrm{v} \qquad (\mathrm{R}^2 = 0.9993) \qquad (\text{Eqn } 4.22)$$

$$\mathrm{I_{cp}} = -68.7289 - 0.9382\,\mathrm{v} \qquad (\mathrm{R}^2 = -0.9988) \qquad (\text{Eqn } 4.23)$$

$$\mathrm{E_{ap}} = 0.1213 + 0.1167\log\mathrm{v} \qquad (\mathrm{R}^2 = 0.9855) \qquad (\text{Eqn } 4.24)$$

$$\mathrm{E_{cp}} = 0.1666 - 0.2139\log\mathrm{v} \qquad (\mathrm{R}^2 = -0.9867) \qquad (\text{Eqn } 4.25)$$

Figure 4.24 (a) showed the cyclic voltammogram (CV) for the change in the current response with the increase in scan rate (25-400 mV s^{-1}) using GCE/bCQDs/CNPs as the working electrode. Just like what was obtained at GCE/CQDs/CNPs, the anodic and cathodic current responses increased with the increase in scan rate (Fig. 4.24 (b)). Unlike the case with the voltammograms obtained with GCE/CQDs/CNPs, linear relationships were recorded between the peak currents (anodic and cathodic) and the square root of the scan rate ($v^{1/2}$). Equations 4.26 and 4.27 represent the linear relationship between the peak currents (I_{a1} and I_{c2}) and the square root of the scan rate ($v^{1/2}$). The linear relationship suggested that NE redox process at GCE/bCQDs/CNPs was diffusion-controlled [230, 342]. Figure 4.24 (c) depicted the linear relationship between the peak potentials (cathodic and anodic) and the logarithm of the scan rate (log v). Similar to the data obtained with GCE/CQDs/CNPs, the relationship between the potentials and log v was most linear at a higher scan rate (> 200 mV s^{-1}).

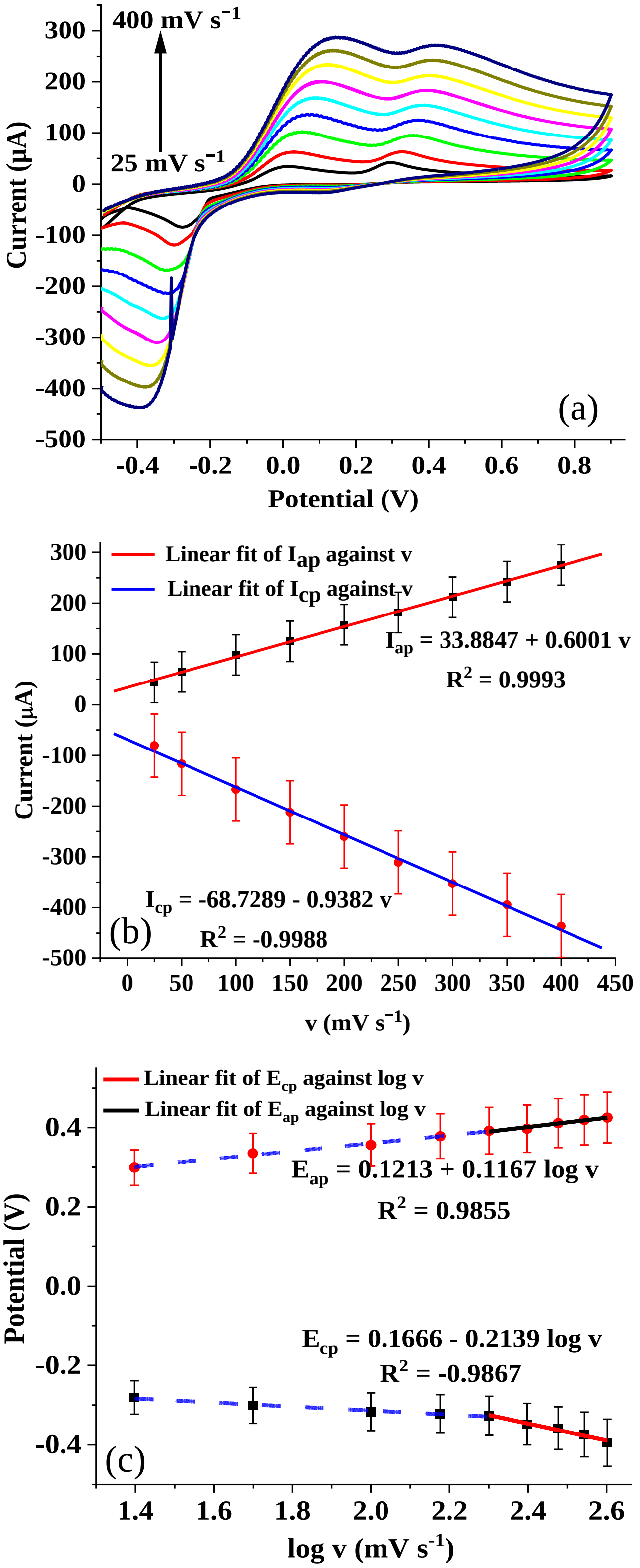

Figure 4.23: (a) Cyclic voltammograms of GCE/CQDs/CNPs in NE over a scan rate range (25 – 400 mV s-1) at pH 7 (b) plot of the anodic and cathodic peak current against the square root of the scan rate and (c) plot of the anodic and cathodic peak potential against log v

Table 4.12: Kinetic parameters of CQDs/CNPs and bCQDs/CNPs in NE

Electrode	α	n	k (s^{-1})	b (mV dec^{-1})
GCE/CQDs/CNPs	0.34	1.83	0.55	232
GCE/bCQDs/CNPs	0.75	0.12	0.27	184

Using Equations 4.28 and 4.29, the values of n and the charge transfer coefficient (α) at GCE/bCQDs/CNPs were calculated as 1.12 and 0.75, respectively. This value of α (0.75) is higher than that of GCE/CQDs/CNPs (0.34) and the value reported for some NE sensors in literature [343-345]. The Tafel slope (b) for GCE/bCQDs/CNPs was found to be 184 mV dec^{-1}. The fact that this Tafel slope is higher than 120 mV dec^{-1} suggested adsorption at the surface of the electrode [317]. The electron transfer rate constant (k_s) obtained with GCE/bCQDs/CNPs is 0.27 s^{-1}. This k_s value was lower than the value recorded at GCE/CQDs/CNPs (Table 4.12). Again, the lack of correlation between the anodic peak current and ΔE_p and the relationship between log k_s and ΔE_p (Equation 4.13) made it difficult to directly link the value of k_s with the electron transfer kinetics at the modified electrodes. Also, the lower value of α at GCE/CQDs/CNPs did not accurately support the significantly higher anodic peak current recorded at GCE/CQDs/CNPs.

$$I_{ap} = -6.6662 + 3.3349\, v^{1/2} \qquad (R^2 = 0.9982) \qquad \text{(Eqn 4.26)}$$

$$I_{cp} = -2.8250 - 1.7916\, v^{1/2} \qquad (R^2 = -0.9991) \qquad \text{(Eqn 4.27)}$$

$$E_{ap} = 0.1850 + 0.0918 \log v \qquad (R^2 = 0.9896) \qquad \text{(Eqn 4.28)}$$

$$E_{cp} = -0.0714 - 0.0305 \log v \qquad (R^2 = -0.9951) \qquad \text{(Eqn 4.29)}$$

4.4.4 Effect of pH

The effect of pH on NE redox processes at CQDs/CNPs and bCQDs/CNPs modified GCE was investigated over a pH range of 3-9 at a scan rate of 25 mV s^{-1}. Figure 4.25 (a) showed the CV of NE electroanalysis at GCE/CQDs/CNPs within the selected pH range. Figure 4.25 (b) revealed that the highest anodic current (I_{a1}) response was obtained at pH 7.01. On the other hand, the lowest I_{a1} value was recorded at a pH of 5.2. The sharp anodic peak current (I_{a2} at 0.05 V) recorded at pH 3 suggested that the conversion of 2,3,5,5-tetrahydro-1H-indole-3,5,6-triol (THT) to 3-hydroxy-2,3-dihydro-1H-indole-5,6-dione (HID) was more favourable at

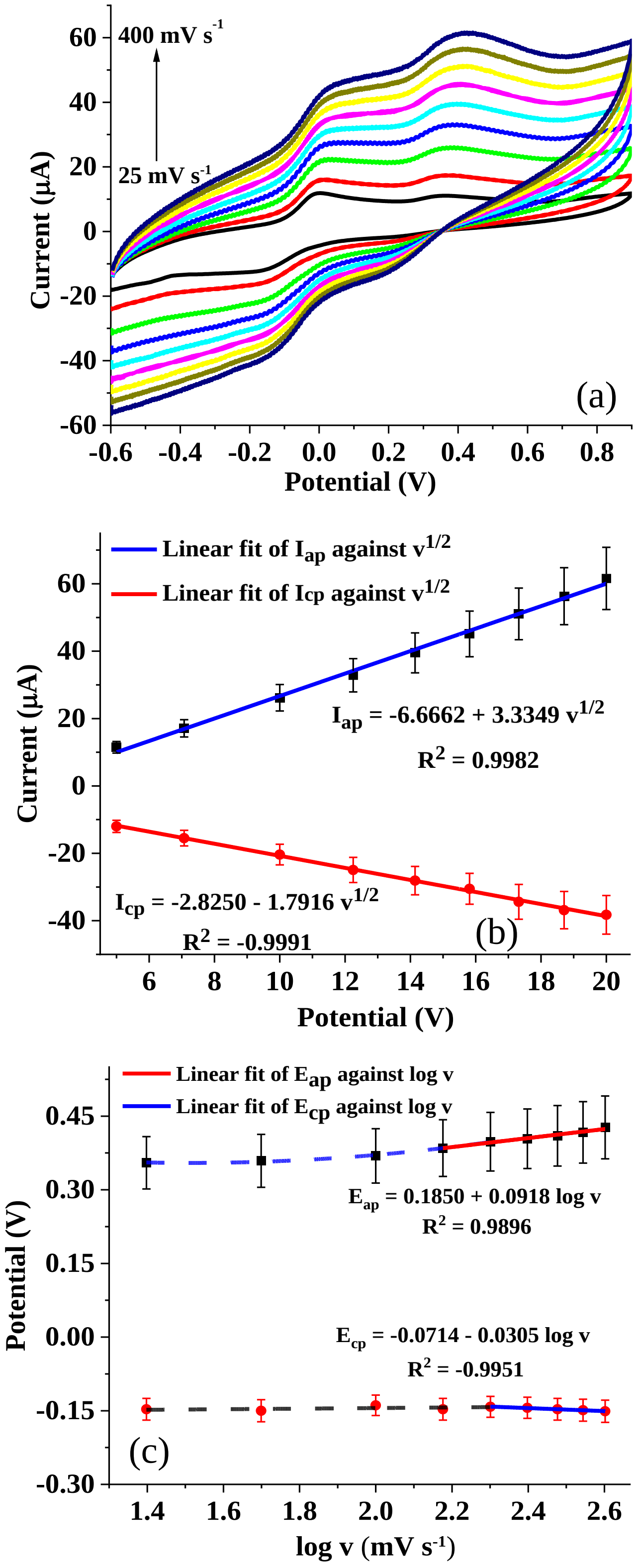

Figure 4.24: (a) Cyclic voltammograms of GCE/bCQDs/CNPs in NE over a scan rate range (25 – 400 mV s^{-1}) at pH 7 (b) plot of the anodic and cathodic peak current against the square root of the scan rate and (c) plot of the anodic and cathodic peak potential against log v

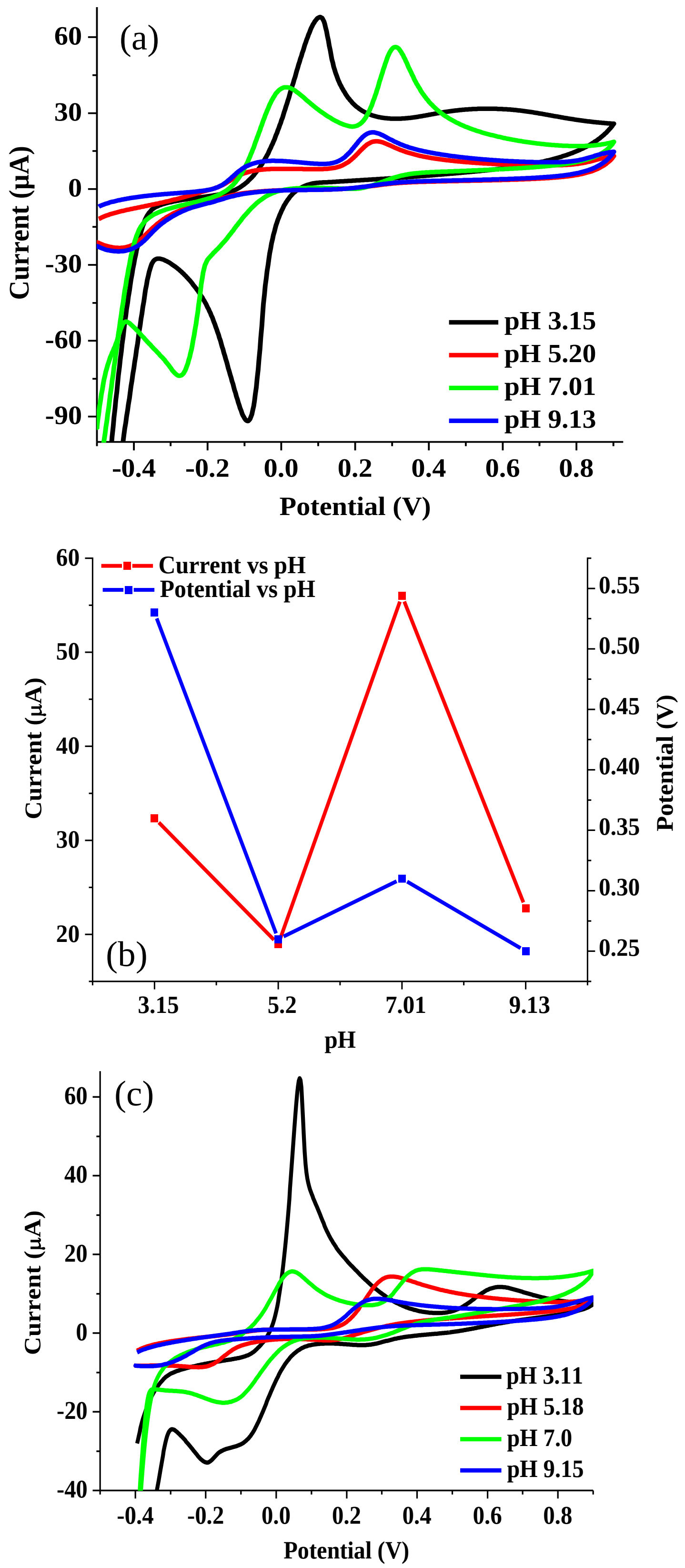
(a)
Current (µA)
60
30
0
-30
-60
-90
Potential (V)
-0.4
-0.2
0.0
0.2
0.4
0.6
0.8
pH 3.15
pH 5.20
pH 7.01
pH 9.13
Current vs pH
Potential vs pH
Current (µA)
60
50
40
30
20
Potential (V)
0.55
0.50
0.45
0.40
0.35
0.30
0.25
(b)
3.15
5.2
7.01
9.13
pH
(c)
Current (µA)
60
40
20
0
-20
-40
pH 3.11
pH 5.18
pH 7.0
pH 9.15
-0.4
-0.2
0.0
0.2
0.4
0.6
0.8
Potential (V)

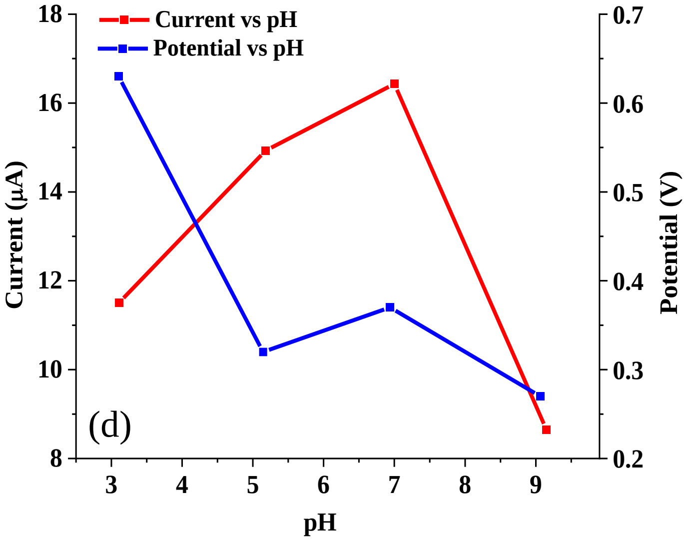

Figure 4.25: (a, c) Cyclic voltammograms of GCE/CQDs/CNPs and GCE/bCQDs/CNPs in 0.4 mM NE at pH 3-9 (scan rate: 25 mV s^{-1}) (b,d) plot of the anodic peak current and potential of NE against pH, recorded at GCE/CQDs/CNPs and GCE/bCQDs/CNPs

pH 3. Unfortunately, the diagnostic anodic peak (I_{a1}) recorded at higher potential (0.54 V) was much weaker. The significantly high current response recorded at neutral pH can be attributed to the cationic nature of NE which supported the electrostatic interaction between NE and the anionic CQDs. Also, possible prevalence of π-π interaction between NE and the graphitic carbon dots could have substantially contributed to the current response recorded at pH 7. The analysis of NE at similar pH has been reported in several publications [83, 346, 347]. Figure 4.25 (b) depicted the change in the anodic peak potential over the pH range under consideration. Beyond the extremely high peak potential recorded at pH 3.15 (0.54 V), NE anodic peak currents were recorded within a peak potential range of 0.2-0.3 V (Fig. 4.25 (b)).

Figure 4.25 (c) showed the CV for the changes in the NE anodic peak current and potential over a pH range of 3-9 at GCE/bCQDs/CNPs. The graphical representation of the current and potential trend at different pH values is depicted in Figure 4.25 (d). The variation in peak potential with pH at GCE/bCQDs/CNPs followed the same trend as that of GCE/CQDs/CNPs. Again, the highest anodic peak was recorded at pH 7.01. It is also noteworthy that the transformation of 2,3,5,5-tetrahydro-1H-indole-3,5,6-triol (THT) to 3-hydroxy-2,3-dihydro-1H-indole-5,6-dione (HID) was also dominant at pH 3.33, such that the diagnostic peak at 0.64 V was about a quarter of the strong peak at 0.02 V. Contrary to what was obtained at GCE/CQDs/CNPs, the anodic peak current (I_{a1}) at pH 3.11 was lower than the value obtained at pH 9 (Fig. 4.25 (d)). The possible repulsion between the anionic NE at high pH and the anionic CQDs could be responsible for the low current response recorded at pH 9.15. Like the electroanalysis of NE at GCE/CQDs/CNPs, the highest current response recorded with GCE/bCQDs/CNPs was obtained at pH 7, probably for the same reason given for GCE/CQDs/CNPs (electrostatic and π-π interactions). Because the highest NE anodic current (I_{a1}) response was recorded at pH 7, further electroanalysis of NE at GCE/CQDs/CNPs and GCE/bCQDs/CNPs were carried out at this pH.

4.4.5 Effect of concentration

The effect of concentration changes on the current response recorded at GCE/CQDs/CNPs and GCE/bCQDs/CNPs was investigated for NE electroanalysis at pH 7 using the square wave voltammetry (SWV) technique. Using GCE/CQDs/CNPs, the NE current response with increase in concentration was recorded (Fig. 4.26 (a)). The current response (I) and the concentration of NE have a linear relationship over a range of 10-126.4 µM (Fig. 4.26 (b)). The linear relationship has been mathematically represented in Equation 4.30.

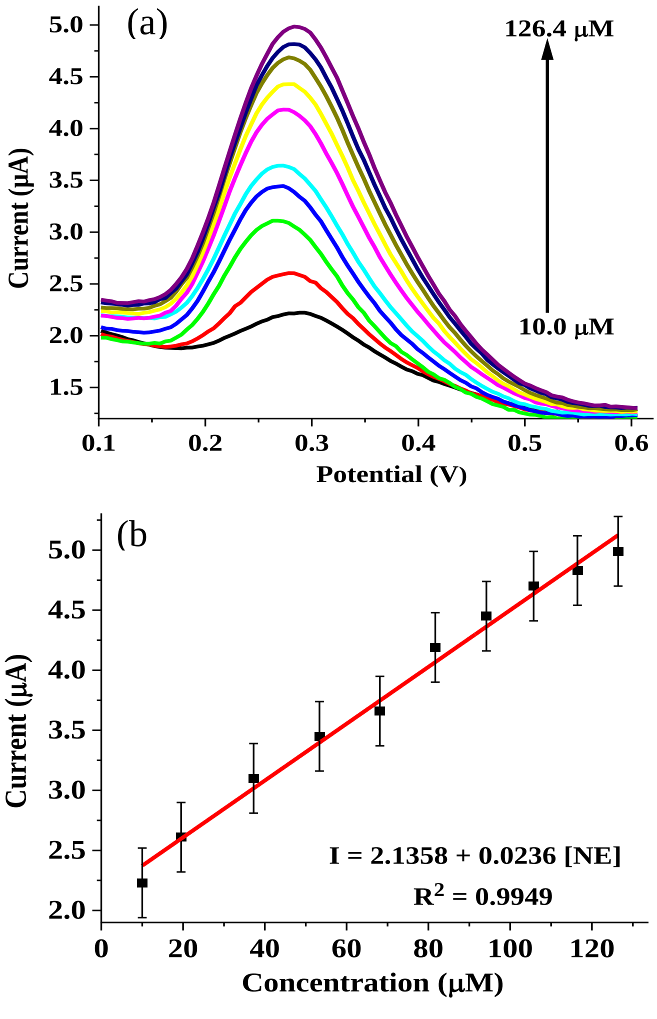

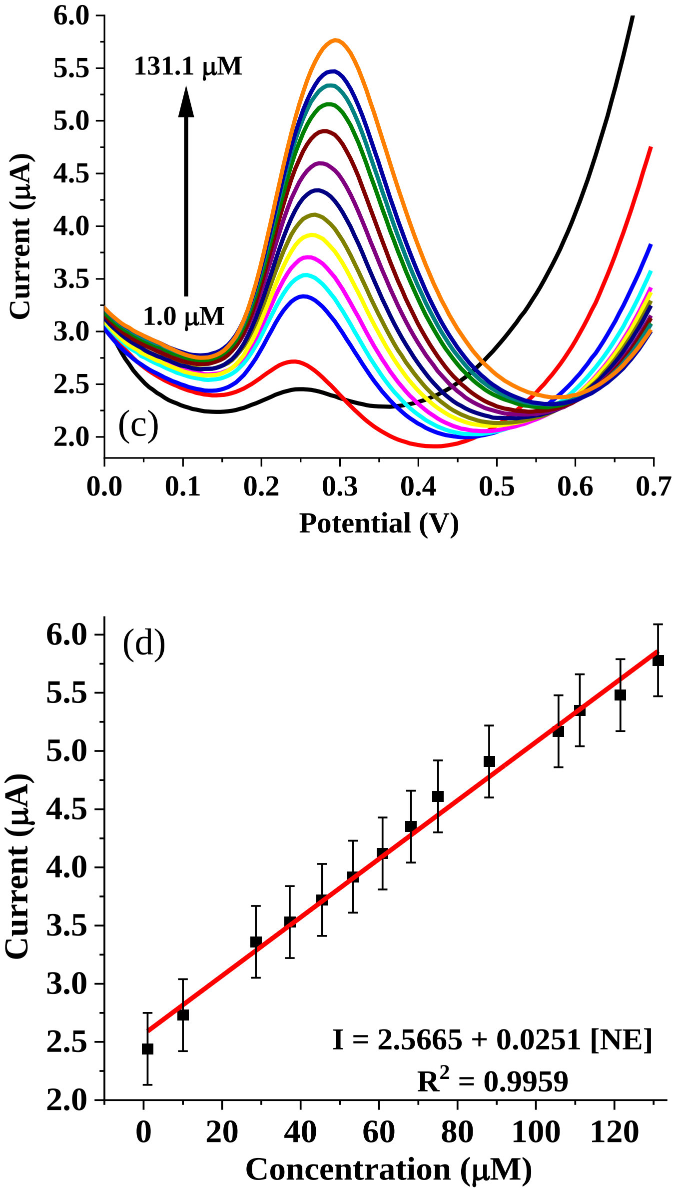

Figure 4.26: (a, c) Square wave voltammograms of GCE/CQDs/CNPs and GCE/bCQDs/CNPs over NE concentration range of 10-126.4 μM and 1-131.1 μM, respectively at pH 7 (b,d) plot of current versus concentration extracted from (a) and (c), respectively.

$$I = 2.1358 + 0.0236\,[NE] \qquad \text{(Eqn 4.30)}$$

$$I = 2.5665 + 0.0251\,[NE] \qquad \text{(Eqn 4.31)}$$

The LoD of GCE/CQDs/CNPs for NE detection was calculated as14.47 μM. The detection limit is higher than the value reported for some previously fabricated NE sensors (Table 4.13). This sensor's limit of quantitation (LoQ) was calculated as 43.86 μM.

Figure 4.26 (c) showed the square wave voltammogram of NE response to variation in concentration over a concentration range of 1-131.1 µM at GCE/bCQDs/CNPs. Fortuitously, the relationship between the current response and NE concentration was linear over the entire concentration range. Equation 4.31 showed the mathematical representation of this linear relationship. The LoD of GCE/bCQDs/CNPs for NE detection was calculated as 14.66 µM. This LoD is slightly higher than the value obtained with GCE/CQDs/CNPs and some previously fabricated NE sensors (Table 4.13). On the other hand, the dynamic linear range (LDR) obtained at GCE/bCQDs/CNPs (1-131 µM) was wider than the value recorded at GCE/CQDs/CNPs. The two sensors collectively possessed wider linear ranges than some in literature [83, 348]. The LoQ recorded at GCE/bCQDs/CNPs is 44.42 µM. The value was higher than the LoQ calculated for GCE/CQDs/CNPs (43.86 µM). The detection limits and the LoQ calculated for these two sensors showed that they are suitable for NE detection at the micromolar level.

Table 4.13 compares the figures of merit of GCE/CQDs/CNPs with that of GCE/bCQDs/CNPs and some other NE sensors in literature.

4.4.6 Interference studies

Norepinephrine (NE), like most neurotransmitters (NTs) exists in extracellular fluid with other biomolecules such as ascorbic acid (AA) and uric acid (UA). It has been reported that these biomolecules (AA and UA) existed at some much higher concentrations than the NTs. Also, the interference of the signal from these interfering molecules with NTs signals in voltammetric studies carried out with bare electrodes has been documented [43]. As a result, the ability of modified electrodes to achieve discriminatory detection of NTs such as NE in the presence of interfering molecules was considered a valuable figure of merit for NE sensors. In this study, the detection of NE in the presence of UA was attempted using GCE/CQDs/CNPs and GCE/bCQDs/CNPs as the working electrodes at pH 7. Figure 4.27 (a) showed the cyclic voltammogram of bare GCE and GCE/CQDs/CNPs in a mixture of 0.4 mM NE and 1 mM UA.

The CV of this mixture at bare GCE is similar to the voltammogram of NE alone. On the other hand, the CV of GCE/CQDs/CNPs in the mixture gave a similar voltammogram with a much broader peak (at -0.17 and 0.35 V) (Fig. 4.27 (a)). The outcome indicated that the CV could not be used for discriminatory NE detection in the presence of UA. With SWV, a single peak which suggested that the inability of square wave voltammetry to resolve NE and UA peaks was recorded (Fig. 4.27 (b)). The result showed that the UA peak interferes with the NE peak

Table 4.13: Figures of merit of the past and current NE sensors

Electrode	Methods	LoD (µM)	LDR (µM)	Sensitivity (µA µM $^{-1}$)	References
ATO-silica/GCE-SWNTs	CV	0.03	0.09-15	0.320	[348]
SiTi/AuNP/CPE	SWV	0.26	20-180	0.130	[349]
GCE-MWCNT/Fe_3O_4/Nc	DPV	6.0	7.5-48	-	[324]
MWNTs-ZnO/CHT/SPE	SWV	0.2	1-30	0.059	[350]
BH-TiO_2/CPE	DPV	0.5	4-1100	0.199	[344]
GCE/CQDs/CNPs	SWV	14.47	10-126	0.024	This work
GCE/bCQDs/CNPs	SWV	14.66	1-131	0.025	This work

SWNTs- Single walled carbon nanotube; MWNTs-Multi-walled carbon nanotube; GCE-glassy carbon electrode; CPE-Carbon paste electrode; SPE-Screen printed electrode; ATO-silica/GCE-SWNTs-Antimony doped tin oxide-silica composite modified SWNTs decorated GCE; SiTi/AuNP/CPE – silica-titania and gold nanoparticles modified CPE; GCE-MWCNT/Fe_3O_4/Nc - Multi-walled carbon nanotubes, 2,3-naphthalocyanine and iron oxide nanocomposite modified GCE; MWNTs-ZnO/CHT/SPE- MWNTs-ZnO nanoparticles and chitosan composite modified SPE; Nano Au-Ag - nanoporous gold-silver alloy electrode; BH-TiO_2/CPE‑2,2′-[1,2 buthanediylbis (nitriloethylidyne)]-bis-hydroquinone (BH) and TiO_2 nanoparticles modified CPE

at the bare and the modified electrodes. Interestingly, two peaks at 0.26 V and 0.52 V corresponding to the NE and UA peaks were obtained using the differential pulse voltammetry (DPV) (Fig. 4.27 (c)). The NE-UA peak separation (260 mV) is wider than the value reported for the discriminatory NE detection in the presence of UA using some previously fabricated chemically modified electrodes [86, 351, 352]. The peak separation confirmed the excellent sensitivity and peak resolution capabilities of DPV reported in literature [353, 354].

The suitability of GCE/CQDs/CNPs for NE analysis in the presence of UA was investigated using varying concentrations of NE (12.9 – 66.7 µM) in the presence of 1 mM UA. Figure 4.27 (d) showed the increase in NE peak currents with the increase in NE concentration while UA concentration remained constant. The result suggested that the discriminatory detection of NE in the presence of UA can be achieved using DPV.

The detection of NE in the presence of UA was also investigated using GCE/bCQDs/CNPs. Like what was obtained at GCE/CQDs/CNPs, CV could not provide the desired NE and UA peak resolution (Fig. 4.28 (a)). Also, the SWV gave a single peak when GCE/bCQDs/CNPs was used to analyze of 0.4 mM NE in the presence of 1 mM UA (Fig. 4.28 (b)). The result

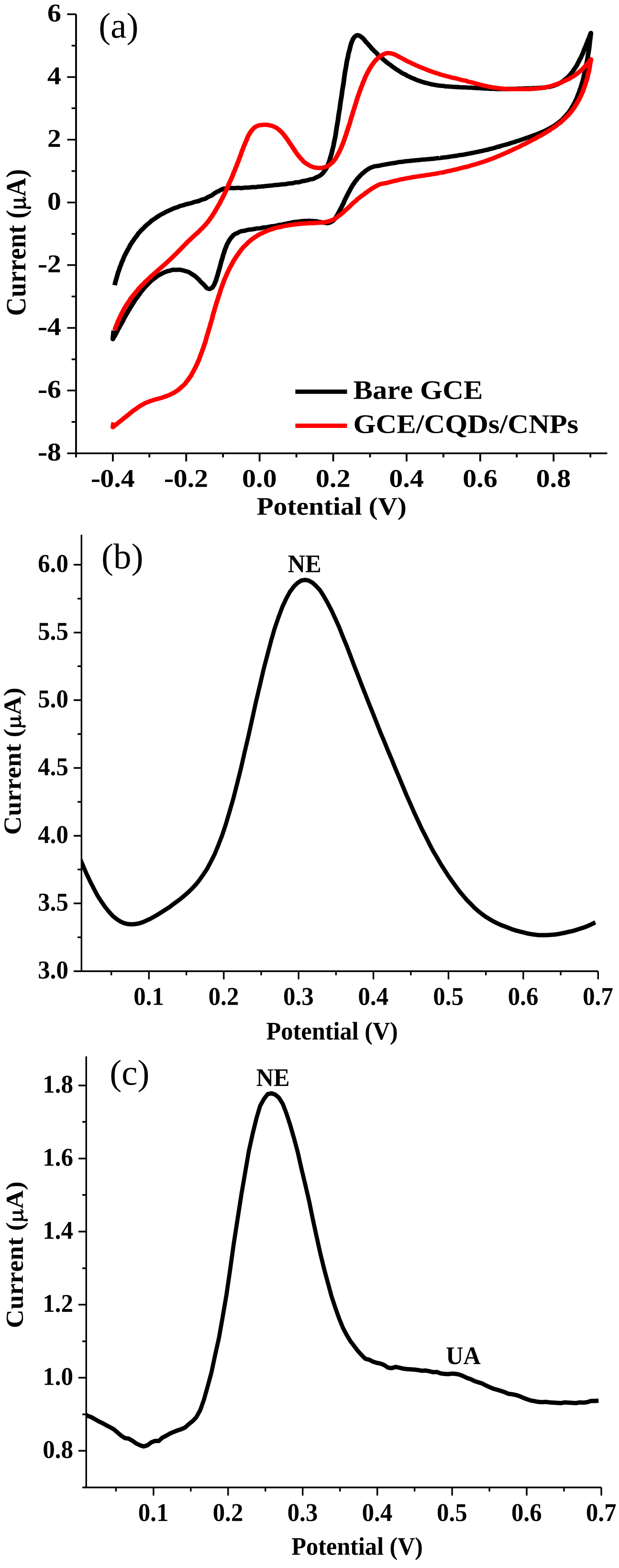
(a)
6
4
2
0
-2
-4
-6
-8
Current (µA)
-0.4
-0.2
0.0
0.2
0.4
0.6
0.8
Potential (V)
Bare GCE
GCE/CQDs/CNPs
(b)
NE
6.0
5.5
5.0
4.5
4.0
3.5
3.0
Current (µA)
0.1
0.2
0.3
0.4
0.5
0.6
0.7
Potential (V)
(c)
NE
UA
1.8
1.6
1.4
1.2
1.0
0.8
Current (µA)
0.1
0.2
0.3
0.4
0.5
0.6
0.7
Potential (V)

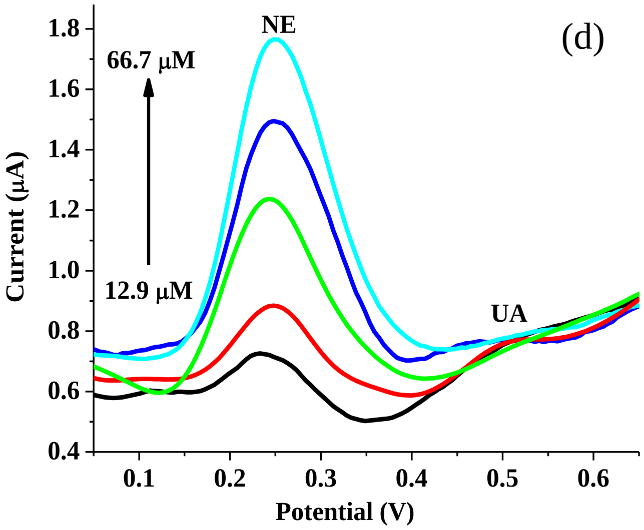

Figure 4.27: (a) Cyclic voltammograms of bare GCE and GCE/CQDs/CNPs, (b) square wave voltammogram and (c) differential pulse voltammogram of GCE/CQDs/CNPs in 0.4 mM NE and 1 mM UA (d) differential pulse voltammograms of NE concentration increase (12.9 – 66.7 µM) with constant AA concentration (1 mM) at GCE/CQDs/CNPs (pH 7, scan rate: 25 mV s^{-1}).

suggested that SWV could not be used for NE detection in a solution containing AA using bCQDs/CNPs modified GCE. The analysis of this mixture with DPV gave a very sharp peak for NE (at 0.31 V) and a weak peak at 0.56 V, belonging to UA (Fig. 4.28 (c)). The peak separation (250 mV) implied that DPV can be successfully used for discriminatory NE detection in the presence of UA. It is also noteworthy that this NE-UA peak-to-peak separation was wider than the value reported in literature for notable NE sensors (Table 4.14). With DPV, the electroanalysis of varying concentrations of NE (12.9 – 57.1 µM) in a constant UA

Table 4.14: UA-EP peak signal difference of past and present NE sensors

Electrode	Method	NE-UA peak difference (mV)	References
MCPE	DPV	139	[86]
p-ATD/GCE	LSV	130	[351]
PAA-MWCNTs/SPCE	DPV	112	[352]
Ce-HA/GCE	DPV	172	[355]
GCE/bCQDs/CNPs	DPV	260	This work
GCE/CQDs/CNPs	DPV	250	This work

CPE – carbon paste electrode; GCE – glassy carbon electrode; MCPE – poly(glutamic acid) modified CPE; poly(2-amino-1,3,4-thiadiazole) modified GCE; SPCE – screen printed carbon electrode; PAA-MWCNTs/SPCE –poly(acrylic acid)-multi-walled carbon nanotubes composite modified SPCE; Ce-HA/GCE – cerium doped hydroxyapatite modified GCE

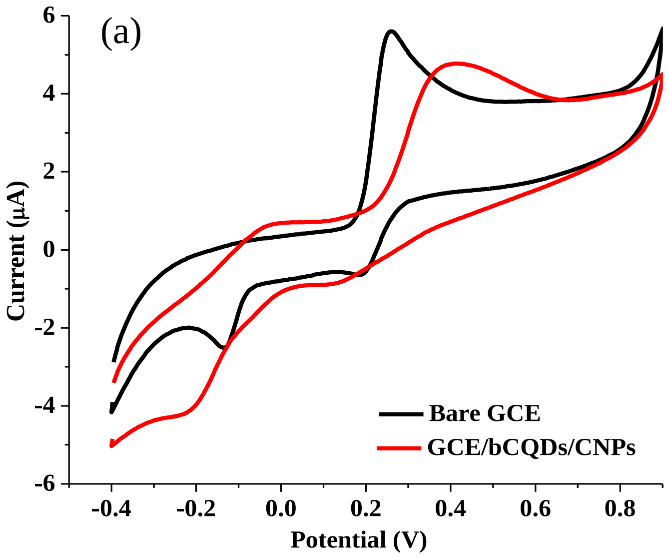
(a)
Current (μA)
6
4
2
0
-2
-4
-6
-0.4
-0.2
0.0
0.2
0.4
0.6
0.8
Potential (V)
Bare GCE
GCE/bCQDs/CNPs

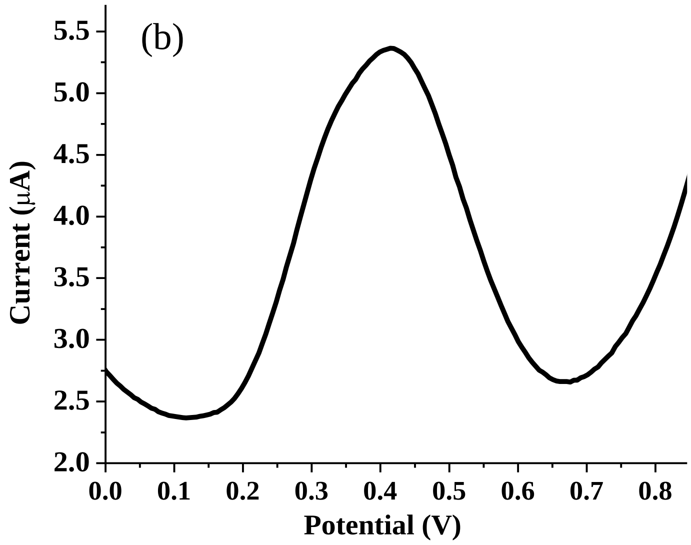
(b)
Current (μA)
5.5
5.0
4.5
4.0
3.5
3.0
2.5
2.0
0.0
0.1
0.2
0.3
0.4
0.5
0.6
0.7
0.8
Potential (V)

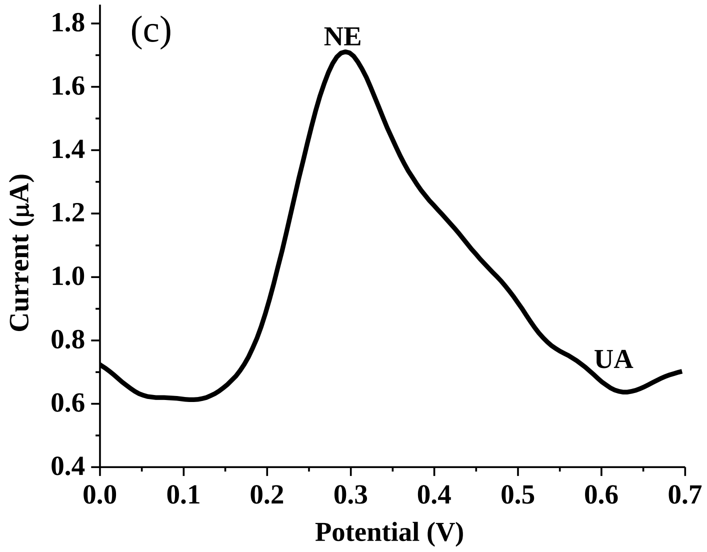
(c)
NE
UA
Current (μA)
1.8
1.6
1.4
1.2
1.0
0.8
0.6
0.4
0.0
0.1
0.2
0.3
0.4
0.5
0.6
0.7
Potential (V)

(d)

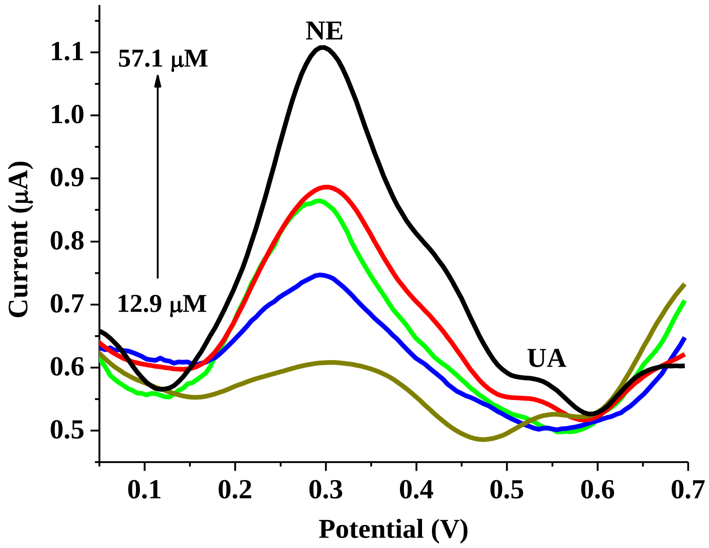

Figure 4.28: (a) Cyclic voltammograms of bare GCE and GCE/CQDs/CNPs, (b) square wave voltammogram and (c) differential pulse voltammogram of GCE/CQDs/CNPs in 0.4 mM NE and 1 mM UA (d) square wave voltammograms of NE concentration increase (12.9 – 57.1 µM) with constant AA concentration (1 mM) at GCE/CQDs/CNPs (pH 7, scan rate: 25 mV s^{-1})

concentration (1 mM) was attempted. The voltammograms recorded after these experiments revealed that the UA peaks slightly increased after the introduction of higher concentrations of NE. In addition, at a high NE concentration, the voltammograms recorded for the mixture (NE and UA) showed the emergence of a weak peak at about 0.45 V (Fig. 4.28 (d)). Although the source of this peak was unclear, it could as well be due to a complementary redox process to the one that led to the emergence of the prominent peak at 0.56 V (Scheme 3). In contrast, this peak did not emerge at GCE/CQDs/CNPs (Fig. 4.27 (d)).

4.4.7 Real sample analysis

The real sample analysis of NE in banana peel was investigated with the two fabricated sensors via the standard addition method. About 1 g of fresh banana peel was mashed in a mortar and made into a homogeneous paste using distilled water as solvent. The resultant paste was sufficiently diluted and allowed to stand for 24 h. The solution was filtered and centrifuged at 3000 rpm to get a clear supernatant. A mixture of the supernatant was spiked with 14.83 µM NE and the resultant mixture was subjected to electroanalysis using square wave voltammetry. Using GCE/CQDs/CNPs, the mean percentage recovery of NE from banana peel after a triplicate determination is 98.11 %, with a percentage relative standard deviation (% RSD) of 4.47 %.

Meanwhile, the GCE/bCQDs/CNPs working electrode gave a mean percentage recovery of 101.4 % with % RSD of 9.03 % (Table 4.15). Although GCE/bCQDs/CNPs offered a higher percentage recovery than GCE/CQDs/CNPs, its % RSD was almost twice that of the CQDs/CNPs modified electrode. The two sensors jointly offered % recovery, which was comparable to the recovery reported for some earlier fabricated NE sensors in various real samples [351, 356]. The outcome suggested that the GCE/CQDs/CNPs and GCE/bCQDs/CNPs can be reliably applied for the analysis of NE in fruits and possibly vegetables since it has been established that some fruits and vegetables contain a considerable amount of NE [357, 358].

Table 4.15: Real sample analysis of NE in banana peel

Electrode	Sample	Amount added (µM)	Amount found (µM)	% recovery	% RSD
GCE/CQDs/CNPs	Banana peel	14.83	13.79	92.99	4.47
		14.83	15.01	101.21	
		14.83	14.85	100.13	
GCE/bCQDs/CNPs	Banana peel	14.83	46.6	91.26	9.03
		14.83	42.1	104.27	
		14.83	42.2	108.60	

4.4.8 Stability and reproducibility

The stability of the electrodes in the presence of 0.4 mM NE (pH 7) was investigated by subjecting the modified electrodes (GCE/CQDs/CNPs and GCE/bCQDs/CNPs) to 22 consecutive CV scans. At GCE/CQDs/CNPs, the current response (I_{a1}) recorded at the end of the 22 scans dropped to about 33.48 % of the initial current response (after the first scan). In addition, the anodic peak potential for I_{a1} witnessed a significant increase from 0.31 to 0.61 V (Fig. 4.29 (a)). The voltammograms recorded with GCE/bCQDs/CNPs revealed that the bCQDs/CNPs modified electrode retained about 72.5 % of the initial current response (I_{a1}) without a significant change in the potential of the reference peak (I_{a1}) (Fig. 4.29 (b)). The outcomes confirmed the instability of the CQDs/CNPs modified electrode towards NE electrocatalytic oxidation due to possible fouling of the modified electrodes by NE oxidation products after several CV scans. The results also showed that GCE/bCQDs/CNPs is more stable than GCE/CNPs/CNPs. Collectively, these two electrodes offered lower stability than some previously fabricated NE sensors [83, 359].

The reproducibility of the modified electrodes was investigated using cyclic voltammetry in the presence of 0.4 mM NE (pH 7). The cyclic voltammogram was recorded by modifying the bare electrodes with CQDs/CNPs three different times prior to the electroanalysis of NE. The same process was repeated with GCE/bCQDs/NE. Figure 4.30 (a) and (b) show the cyclic voltammograms recorded with GCE/CQDs/CNPs and GCE/bCQDs/CNPs, respectively. The percentage relative standard deviation (% RSD) of the anodic current responses (I_{a1}) recorded after the three trials with GCE/CQDs/CNPs is 19.8 %. On the other hand, the bCQDs/CNPs composite modified electrode gave voltammograms with anodic peak currents (I_{a1}) that gave a % RSD of 29.1 %. Like it was with EP, the GCE/CQDs/CNPs electrode offered a lower % RSD than GCE/bCQDs/CNPs, suggesting that the CQDs/CNPs composite modified electrode

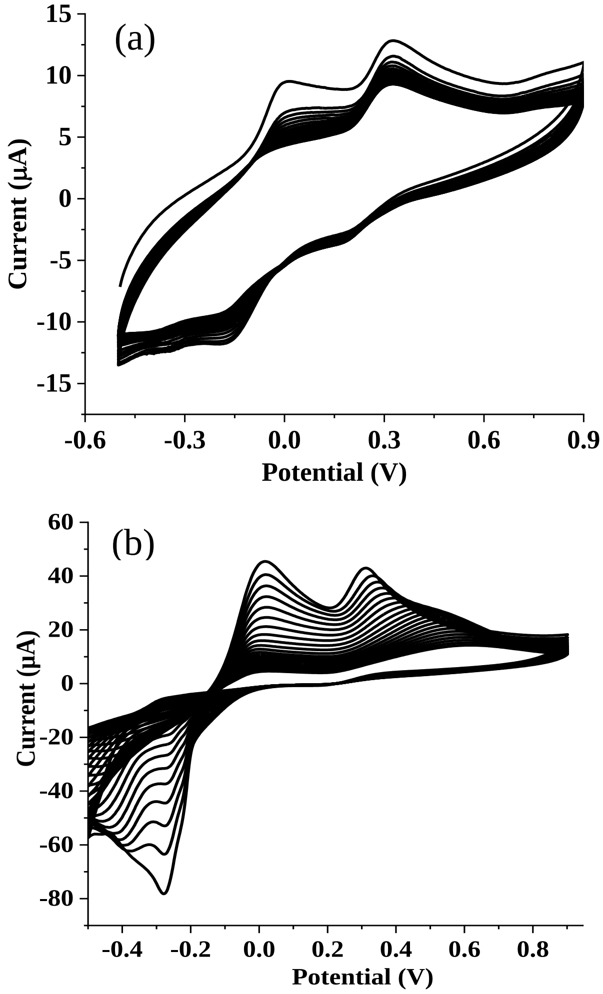

Figure 4.29: Cyclic voltammograms of (a) GCE/CQDs/CNPs and (b) GCE/bCQDs/CNPs in 0.4 mM NE (pH 7) after 22 scans (scan rate: 25 mV s^{-1})

offered a more reproducible result. Compared to the results obtained with EP, the two sensors have poor reproducibility. Also, compared to various NE sensors in literature, the sensors offer poor reproducibility [332, 345]. Beyond the statistical treatment of the data from the voltammograms, a visual inspection of Figures 4.30 (a) and (b) showed that a proper replication of the voltammograms after three trials is difficult. This could be due to the low stability of the electrodes in the presence of NE.

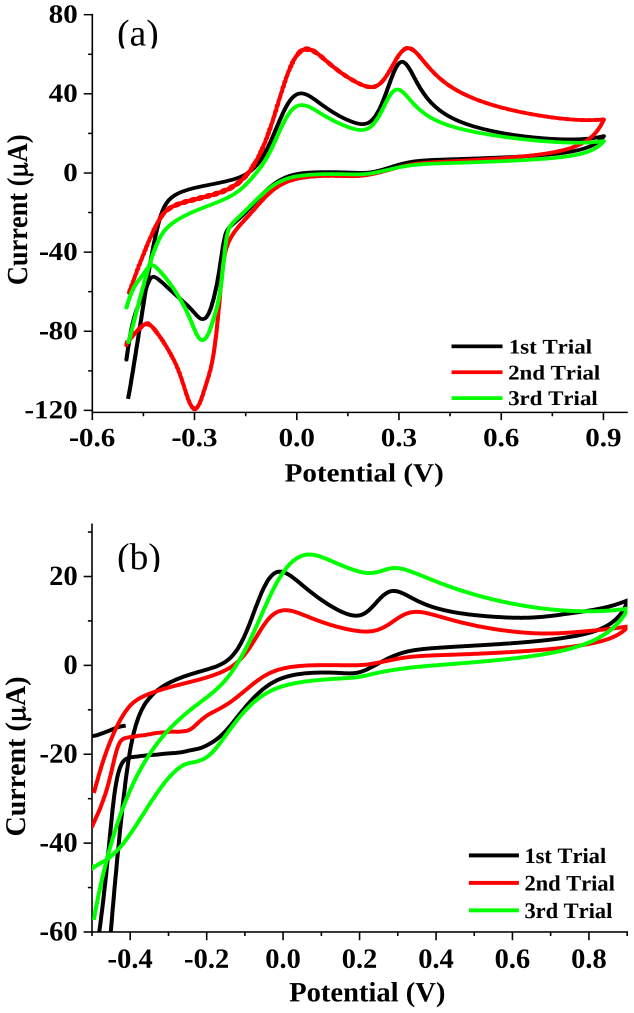

Figure 4.30: Cyclic voltammograms of (a) GCE/CQDs/CNPs and (b) GCE/bCQDs/CNPs in 0.4 mM NE (pH 7, scan rate: 25 mV s^{-1}) for three different trials of electrode modification

4.5 Electrochemical detection of dopamine

4.5.1 Electroanalysis of dopamine at bare and modified electrodes

The electroanalysis of dopamine (DA) was conducted at a scan rate of 25 mV s^{-1} using cyclic voltammetry. The mechanism of DA oxidation include a reversible loss of two protons and two electrons by DA to form dopamine-o-quinone (Scheme 5). Cyclic voltammograms of 0.4 mM DA at bare GCE, GCE/CNPs, GCE/CQDs, GCE/bCQDs, bCQDs/CNPs and CQDs/CNPs modified electrodes showed the current responses of the electrodes (Figure 4.31). The anodic peak currents (I_{ap}) (peak potential in parenthesis) obtained at bare GCE, GCE/CNPs, GCE/CQDs, GCE/bCQDs, GCE/CQDs/CNPs, and GCE/bCQDs/CNPs were 6.33 µA (0.21 V), 66.44 µA (0.25 V), 3.04 µA (0.2 V), 11.74 µA (0.42 V), 344.93 µA (0.34 V), and 95.43 µA (0.21 V), respectively. The respective cathodic peak currents were -1.29 µA (0.18 V), -61.52 µA (-0.16 V), -2.98 µA (-0.12 V), -1.34 µA (0.31 V), -255.04 µA (-0.26 V), -34.25 µA (0.13 V). The results showed that the highest current response was obtained at GCE/CQDs/CNPs. The value of I_{ap}/I_{cp} recorded at bare GCE, GCE/CNPs, GCE/CQDs, GCE/bCQDs, GCE/CQDs/CNPs, GCE/bCQDs/CNPs and GCE/CQDs/TNPs were 4.91, 1.08, 1.02, 8.76, 1.35, and 2.79, respectively. Also, the anodic-cathodic peak separation (ΔE_p) recorded at these electrodes were 30, 90, 32, 110, 600, and 80 mV, respectively.

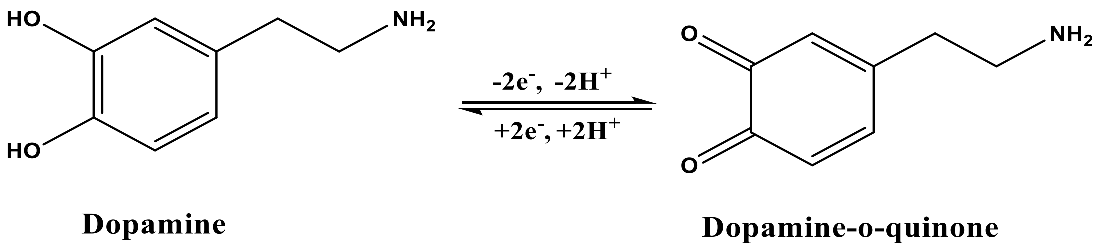

Scheme 5: Mechanism of dopamine oxidation

Using the value of I_{ap}/I_{cp} as the index of reversibility, the most reversible voltammogram was obtained at GCE/CQDs. Similarly, the voltammogram of GCE/CNPs with I_{ap}/I_{cp} values of 1.08 also showed significant reversibility. Although the voltammogram of GCE/CQDs/CNPs showed a relatively poor reversibility, its significantly high current response made it the selected candidate for further DA electroanalysis. Also, going by the anodic peak current (I_{ap}) recorded at all the electrodes, the bCQDs/CNPs and CQDs/CNPs modified electrodes were chosen as the working electrodes for comparative DA electroanalysis.

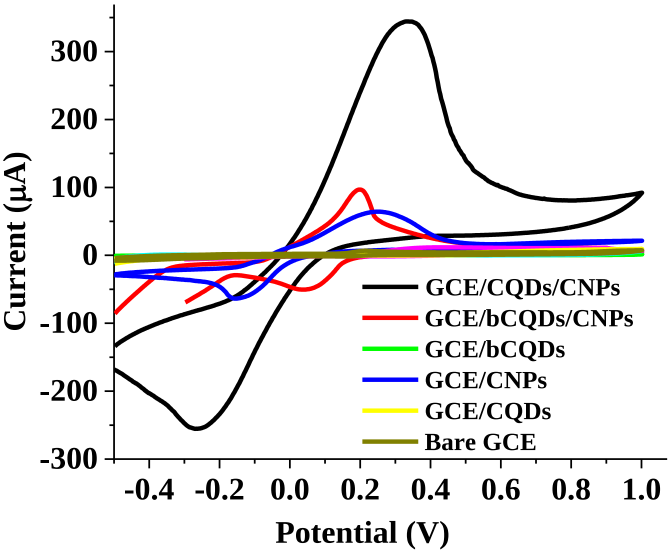

Figure 4.31: Cyclic voltammograms of the bare GCE, CQDs, bCQDs, CNPs, bCQDs/CNPs and CQDs/CNPs modified GCE in 0.4 mM DA (scan rate: 25 mV s^{-1}, pH 7)

Figures 4.32 (a) and (b) depict a vivid comparison between the voltammograms of the bare electrode, CNPs, bCQDs, CQDs, bCQDs/CNPs and CQDs/CNPs composite modified electrodes. Figure 4.32 (a) showed that the I_{ap} was in the order: GCE/CQDs/CNPs (344.93 µA) > GCE/CNPs (66.44 µA) > bare GCE (6.33 µA) > GCE/CQDs (3.04 µA). The lower current response obtained at GCE/CQDs relative to bare GCE suggested that the CQDs retards the electron transfer across GCE. On the contrary, GCE/CNPs offered a significantly higher I_{ap} than bare GCE, suggesting that CNPs improved the conductivity of the bare electrode. Noteworthy, the I_{ap} recorded at GCE/CQDs/CNPs is about fifty and five times the value recorded at GCE/CNPs and bare GCE, respectively. Figure 4.32 (a) also showed that the DA anodic peak potential obtained at GCE/CQDs/CNPs shifted to the positive side compared to GCE/CNPs and the bare GCE. Contrary to expectations that reduced over potential and small ΔE_p value suggest better DA electrocatalytic oxidation [336], GCE/CQDs/CNPs possessed the highest ΔE_p and over potential compared to other electrodes and offered the highest I_{ap} regardless. The fact that the highest current response was recorded at GCE/CQDs/CNPs indicates a synergy between CQDs and CNPs, culminating in improved electrocatalytic activity of CQDs/CNPs nanocomposite towards DA oxidation.

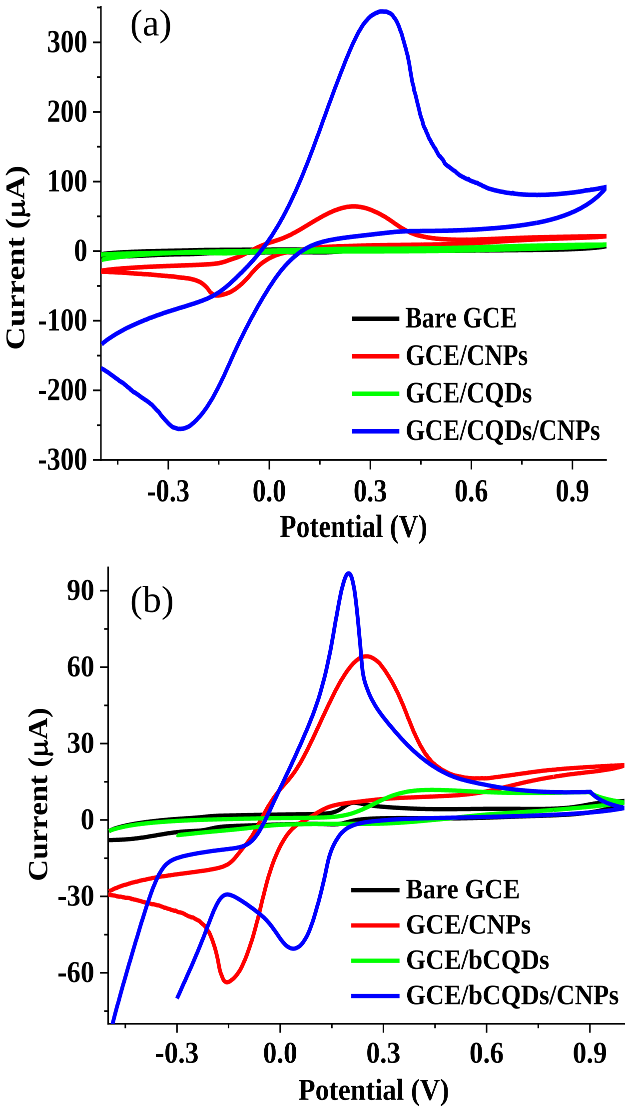

Figure 4.32: Cyclic voltammograms of (a) bare GCE, GCE/CQDs, GCE/CNPs and GCE/CQDs/CNPs and (b) bare GCE, GCE/bCQDs, GCE/CNPs and GCE/bCQDs/CNPs in 0.4 mM DA (scan rate: 25 mV s^{-1}, pH 7).

Similarly, the I_{ap} recorded at the bare electrode, CNPs, bCQDs and bCQDs/CNPs modified electrode followed the order: GCE/bCQDs/CNPs (95.43 µA) > GCE/CNPs (66.44 µA) > bare GCE (6.33 µA) > GCE/bCQDs (1.92 µA). This trend also showed that the bCQDs and CNPs offered a synergy that resulted in the improved electrocatalytic activity of the bCQDs/CNPs modified electrode. Compared to GCE/CNPs and GCE/bCQDs, the bCQDs/CNPs modified electrode possesses a lower ΔE_p, suggesting a faster electron transfer at GCE/bCQDs/CNPs [336]. On the other hand, the bare GCE gave a lower ΔE_p value than GCE/bCQDs/CNPs (Table 4.16). The occurrence suggested that the low ΔE_p recorded at GCE/bCQDs/CNPs and the attendant fast electron transfer could not have been the sole reason for the outstanding I_{ap}

recorded at GCE/bCQDs/CNPs. It is also noteworthy that the DA anodic peak current at the bare GCE and GCE/bCQDs/CNPs emerged at the same potential (0.21 V), suggesting no change in the over potential after GCE modification with bCQDs/CNPs. Considering these outcomes, it is therefore important to further investigate electronic properties of the electrodes through EIS to better understand the interaction between DA and the modified electrodes. The same applied to GCE/CQDs/CNPs and the electrodes modified by its components (CQDs and CNPs modified GCE).

Table 4.16: Cyclic voltammetry data of bare GCE and modified GCE in 0.4 mM DA

Electrodes	I_{ap} (µA)	I_{cp} (µA)	E_{ap} (V)	E_{cp} (V)	I_{ap}/I_{cp}	ΔE_p (mV)
Bare GCE	6.33	-1.29	0.21	0.18	4.91	30
GCE/CNPs	66.44	-61.52	0.25	-0.16	1.08	90
GCE/CQDs	3.04	-2.98	0.20	-0.12	1.02	32
GCE/bCQDs	11.74	-1.34	0.42	0.31	8.76	110
GCE/CQDs/CNPs	344.93	-255.04	0.34	-0.26	1.35	600
GCE/bCQDs/CNPs	95.43	-34.25	0.21	0.13	2.79	80

Meanwhile, as it was with CQDs/CNPs, bCQDs possessed a large surface area which complemented the conductivity of the CNPs in the composite (bCQDs/CNPs). Such synergy between materials has been reported for several composites targeted toward dopamine detection [87, 89, 199, 360]. Specifically, carbon nanomaterials and metal oxide nanoparticles have shown beneficial synergy for DA electroanalysis [87, 199, 360]. It is important to reiterate that the superiority of GCE/CQDs/CNPs and GCE/bCQDs/CNPs in terms of I_{ap} recorded for DA electroanalysis with the sensors made them the chosen candidate for further DA analysis.

4.5.2 Electrochemical impedance spectroscopy

The electrochemical impedance spectroscopy (EIS) data for the bare and modified electrodes were obtained using 0.4 mM DA (pH 7). Figure 4.33 (a) showed the Nyquist plot of the EIS spectra of the bare GCE, GCE/CQDs, GCE/bCQDs, GCE/CNPs, GCE/bCQDs/CNPs, and GCE/CQDs/CNPs.

The EIS parameters used for fitting the EIS spectra are the charge transfer resistance (R_{ct}), solution resistance (R_s), constant phase element (CPE), Warburg impedance (W), and double layer capacitance (C). The equivalents circuits X was used for fitting the EIS data for bare

GCE, GCE/CNPs, GCE/CQDs/CNPs, and GCE/bCQDs. On the other hand, the equivalent circuit Y was used for fitting the data for GCE/CQDs and GCE/bCQDs/CNPs (Fig. 4.33 (b)).

To fully understand how the EIS data validate the results obtained from cyclic voltammetry and some electronic properties of the electrodes, a comparison between the EIS data of the bare GCE, GCE/CNPs, GCE/CQDs, and GCE/CQDs/CNPs is essential. The R_{ct} values obtained at the electrodes were 12.45, 32.41, 91.20 and 9.83 kΩ, respectively (Table 4.17). The results show that the R_{ct} values are in the order: GCE/CQDs/CNPs < bare GCE < GCE/CNPs < GCE/CQDs. This trend showed that the CQDs modified electrode has the highest R_{ct} compared to the other electrodes. This indicates that the CQDs impede charge transfer across GCE. This result agreed with the CV result, which showed that GCE/CQDs gave the lowest I_{ap}. Surprisingly, the CNPs modified electrode gave a higher R_{ct} than the bare electrode. In contrast, GCE/CNPs gave a higher I_{ap} than the bare GCE. This suggested that the conductivity of CNPs is probably not the main reason why a higher I_{ap} was recorded with CV (compared to the bare electrode). The other reason could have been the large surface area of CNPs. The very low R_{ct} obtained at GCE/CQDs/CNPs can be attributed to the synergy between CNPs and CQDs, which resulted in improved surface area and conductivity of the composite. Similar synergy between composites components has been reported [361, 362].

The EIS data for bare GCE, GCE/CNPs, GCE/bCQDs and GCE/bCQDs/CNPs showed that these electrodes have R_{ct} values of 12.45, 32.41, 132.07 and 6.07 kΩ, respectively (Table 4.17). The results imply that the R_{ct} of the electrodes follow the order: GCE/bCQDs/CNPs < bare GCE < GCE/CQDs < GCE/bCQDs. Again, the bare electrode had a lower R_{ct} than GCE/bCQDs and GCE/CNPs. Like the CQDs, the bCQDs offered a high resistance to charge transfer across the electrode. The R_{ct} trend evident from the very high R_{ct} recorded at GCE/bCQDs. Surprisingly, GCE/bCQDs/CNPs possess R_{ct} lower than that of every other electrode, including GCE/CQDs/CNPs, suggesting that bCQDs and CNPs had a synergy that improves the charge transfer of the composite. It is important to note that CNPs increased the conductivity of the modified electrodes (GCE/bCQDs/CNPs and GCE/CQDs/CNPs), thus improving the electron transfer kinetics between the neurotransmitters and the sensors. It is also noteworthy that GCE/CQDs/CNPs possessed higher DA oxidation peak current (I_{ap}) than GCE/bCQDs/CNPs, suggesting that the current response recorded at the electrodes was due to

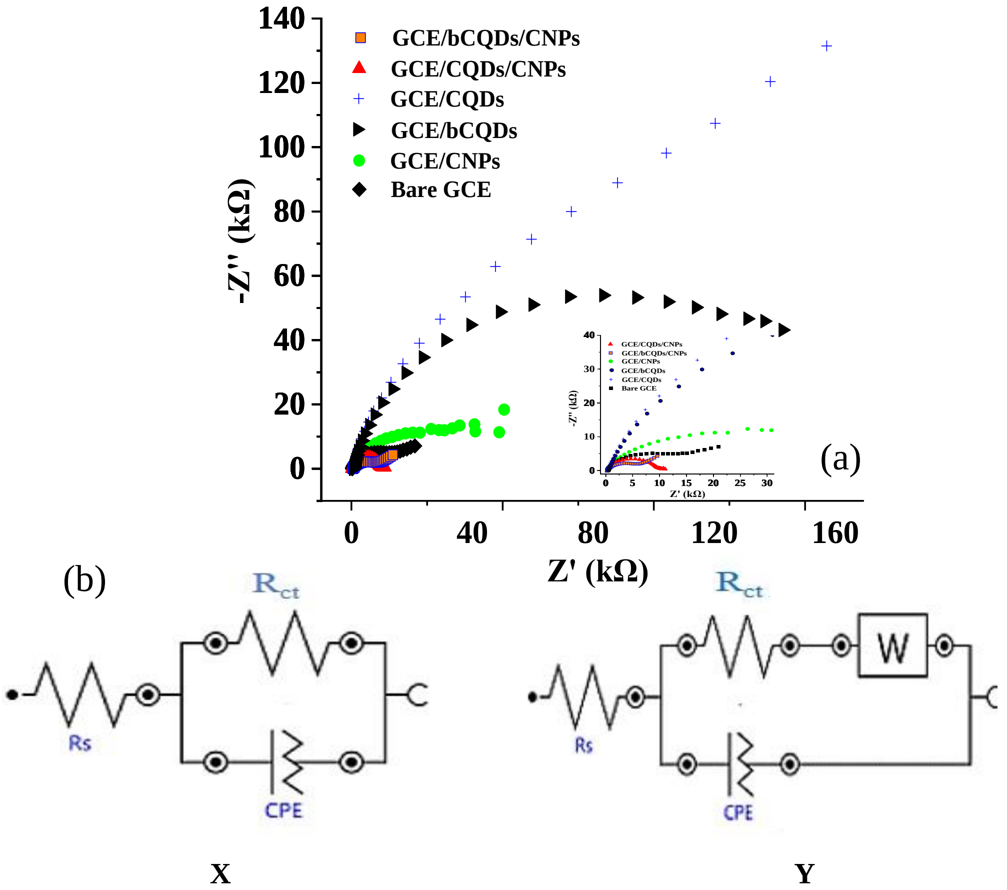

Figure 4.33: EIS spectra (Nyquist plot) of (a) Bare GCE, CQDs, bCQDs, CNPs and CQDs/CNPs modified GCE in 0.4 mM DA (pH 7) (inset: zoomed EIS spectra) (b) equivalent electrochemical circuits of the EIS data at (a)

reasons beyond the charge transfer resistance of the composites. The surface area and the electrocatalytic activity of the composites towards DA oxidation could have contributed to the current response recorded at the respective electrodes.

Table 4.17: EIS parameters of bare and modified electrode in DA

Electrode	R_s (kΩ)	R_{ct} (kΩ)	Y_o ($\mu\Omega^{-1}.s^{\wedge}N$)	N	W ($\mu\Omega^{-1}.s$)	X^2
Bare GCE	0.25 (1.18)	12.45 (2.77)	4.27 (4.41)	0.81 (0.82)	145.00 (5.63)	0.0825
GCE/CNPs	0.28 (2.19)	32.41(5.211)	3.51 (5.89)	0.75 (1.16)	59.00 (12.66)	0.2063
GCE/CQDs	0.23 (1.46)	91.20 (20.89)	5.83 (13.59)	0.74 (2.106)	7.34 (10.32)	0.1051
GCE/bCQDs	0.77 (4.28)	132.07 (8.6)	4.38 (6.98)	0.64 (1.92)	-	0.0741
GCE/CQDs/CNPs	0.31 (1.65)	9.83 (1.45)	2.99 (5.94)	0.81 (1.005)	-	0.1318
GCE/bCQDs/CNPs	0.22 (2.69)	5.59 (5.77)	2.74 (12.80)	0.77 (2.48)	-	0.3531

4.5.3 Effect of pH

The effect of pH on the electrocatalysis of DA was investigated over a pH range of 3-9 using cyclic voltammetry at a scan rate of 25 mV s^{-1}. Figure 4.34 (a) showed the CV of the electrocatalysis of DA over this pH range using GCE/CQDs/CNPs as the working electrode. The anodic peak current (I_{ap}) recorded at GCE/CQDs/CNPs followed the order: pH 7 > pH 3 > pH 5 > pH 9. The anodic peak potential change also follow the same trend (Fig. 4.34 (b)). The highest current response was obtained at pH 7. On the other hand, the lowest anodic peak current (I_{ap}) was recorded at pH 9. Recording the highest I_{ap} at pH 7 agrees with several reports on DA electroanalysis [41, 363]. The result suggested that at neutral pH, DA assumes a cationic nature, making electrostatic interaction between the analyte and the anionic CQDs possible. The combined effect of this electrostatic interaction and possible π-π interaction between the graphitic core of the CQDs and the analyte (DA) lead to the high I_{ap} obtained at pH 7. In addition, there is a possibility of a more favourable DA adsorption at pH 7 compared to other pH values. The assertion agreed with a report on the influence of adsorption on DA analysis [364]. At high pH, DA gets deprotonated, thus inducing an electrostatic repulsion between DA and the CQDs. The repulsion probably resulted in the low I_{ap} recorded at pH 9, thus explaining why further DA analysis was done at pH 7.

Figure 4.34 (c) showed the CV for the electroanalysis of DA over a pH range of 3-9 using GCE/bCQDs/CNPs as a working electrode. The change in the anodic peak current (I_{ap}) with pH follows the same order as the results obtained with GCE/CQDs/CNPs (Fig. 4.34 (b) and (d)). The highest current response was also obtained at pH 7, probably for the same reason as

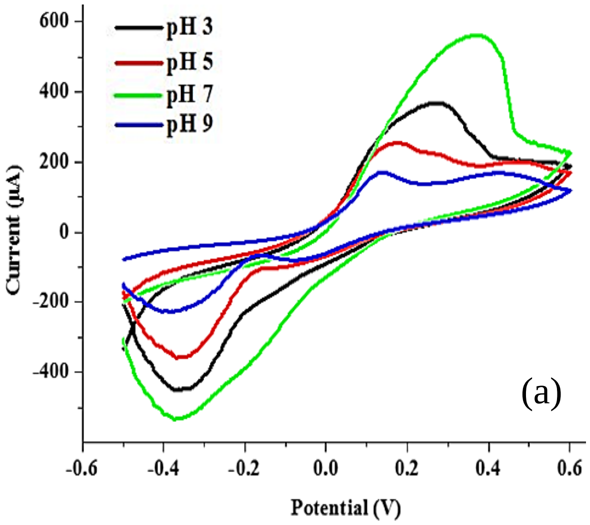

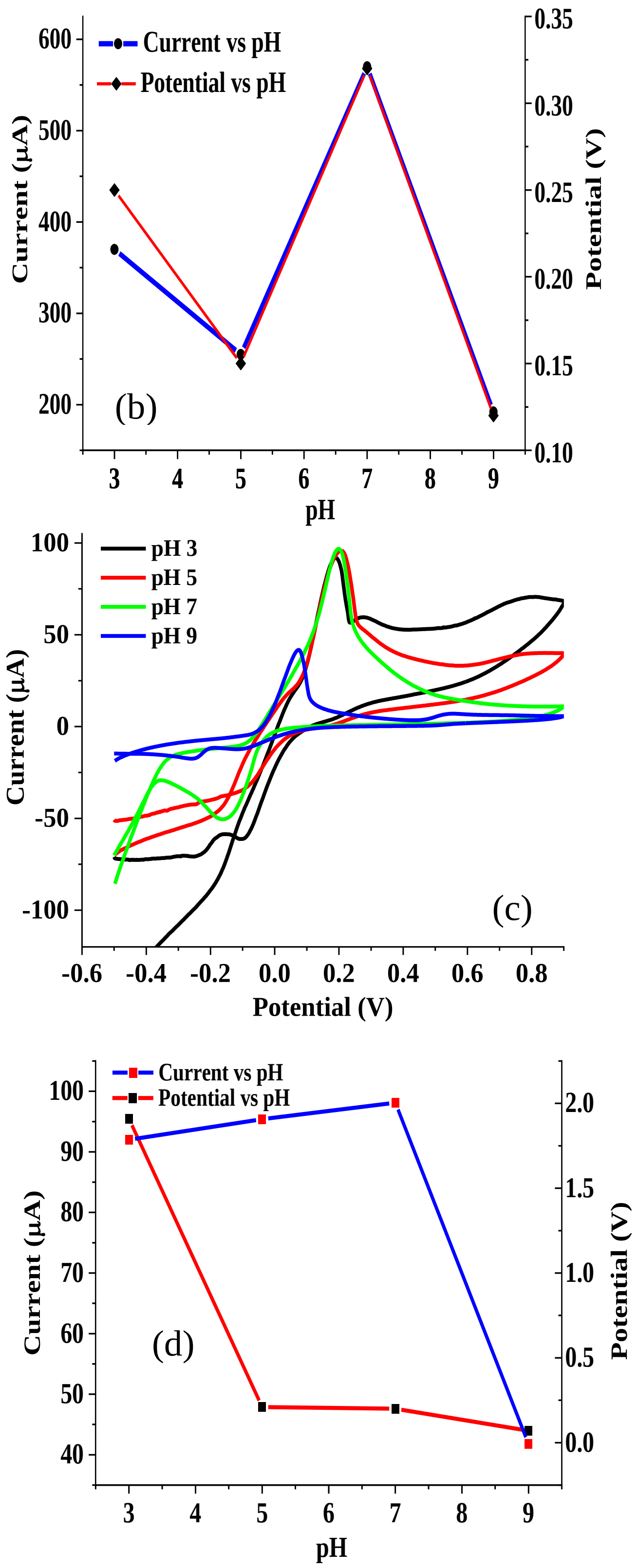

Figure 4.34: (a, c) Cyclic voltammograms of GCE/CQDs/CNPs and GCE/bCQDs/CNPs in 0.4 mM EP at pH 3-9 (scan rate: 25 mV s^{-1}) (b, d) plot of the anodic peak current and potential of DA against pH, recorded at GCE/CQDs/CNPs and GCE/bCQDs/CNPs

the current response recorded at GCE/CQDs/CNPs. Also, the lowest current response was recorded at pH 9 using GCE/bCQDs/CNPs, suggesting possible repulsion between the electrode modifiers and the analyte (DA) at this pH. The effect of pH on DA detection at green catalyst-mediated sensors has been reported. The best DA detection at many of these sensors has been recorded at a neutral pH [99, 217, 365]. Based on the superior performance of GCE/CQDs/CNPs and GCE/bCQDs/CNPs at pH 7 and significance of DA detection at physiological pH, further DA electroanalysis was conducted at pH 7.

4.5.4 Effect of scan rate on DA oxidation

The effect of scan rate on DA oxidation was investigated using 0.2 mM DA for cyclic voltammetry over a scan rate range of 25-400 mV s^{-1} (pH 7). Figure 4.35 (a) showed the cyclic voltammograms of GCE/CQDs/CNPs over the selected scan rate range. The anodic peak current (I_{ap}) increased with the increase in the scan rate. Also, the potential was shifted to the positive side with every increase in the scan rate (v). The increase in the current response (I_{ap}) with the increase in scan rate (v) was linear over the entire linear range. The relationship suggested that the DA oxidation at GCE/CQDs/CNPs was a surface-confined process and agrees with several reports on the surface-confined mechanism for DA oxidation at chemically modified electrodes [366, 367]. Equations 4.32 and 4.33 show the mathematical relationship between v and the peak currents (anodic and cathodic). Noteworthy, the cathodic peak current also showed a linear relationship with v. The logarithm of the anodic and cathodic peak potentials (E_{ap} and E_{cp}) also had a linear relationships with the logarithm of the scan rate (log v), especially at higher scan rate (> 200 mV s^{-1}). Using Equations 4.34 and 4.35, the values of the number of electrons transferred (n) and the charge transfer coefficients (α) were calculated as 2.03 and 0.51, respectively. The value of the electron transfer rate constant (k_s) was also calculated from Equation 4.13 as 0.11 s^{-1}. The rate constant is comparable with the value reported for the electrochemical detection of DA at a modified electrode [368-370]. Also, the Tafel slope obtained from Equation 4.12 and the slope of Equation 4.33 was 520 mV s^{-1}. The Tafel slope is higher than 120 mV dec^{-1}, suggesting an adsorptive process at the surface of the CQDs/CNPs modified electrode [317].

$$I_{ap} = 71.5311 + 0.6022\, v \qquad (R^2 = 0.9966) \qquad \text{(Eqn 4.32)}$$

$$I_{cp} = -22.1423 - 0.6061\, v \qquad (R^2 = -0.9971) \qquad \text{(Eqn 4.33)}$$

$$E_{ap} = -0.3976 + 0.2598 \log v \qquad (R^2 = 0.9932) \qquad \text{(Eqn 4.34)}$$

$$E_{cp} = 0.4280 - 0.2471 \log v \qquad (R^2 = -0.9982) \qquad \text{(Eqn 4.35)}$$

The effect of scan rate on the electrocatalytic oxidation of DA was also investigated using 0.2 mM DA (pH 7) at GCE/bCQDs/CNPs over the same scan rate range (25- 400 mV s^{-1}) (Fig. 4.36). Similar to the trend at GCE/CQDs/CNPs, there was an increase in current responses (I_{ap} and I_{cp}) with the increase in scan rate (v). Contrary to the linear relationship between I_{ap} and v recorded at GCE/CQDs/CNPs, linear relationships between the square root of the scan rate ($v^{1/2}$) and the current responses (I_{ap} and I_{cp}) were recorded at GCE/bCQDs/CNPs (Equations 4.36 and 4.37). This relationship between the current response and the square root of the scan rate ($v^{1/2}$) suggested a diffusion-controlled process at GCE/bCQDs/CNPs. A similar mechanism has been reported for DA electrocatalytic oxidation at quantum dots modified electrodes [218, 368]. Also, a linear relationship was observed between the peak potentials (E_{ap} and E_{cp}) and the logarithm of the scan rate at high scan rates (> 200 mV s^{-1}). The linear relationship was depicted by Equations 4.38 and 4.39. Using the slope of these linear equations and Equations 4.38 and 4.39, the values of n and α were calculated as 0.29 and 0.56, respectively. Also, the electron transfer rate constant was calculated from Equation 4.13 as 0.64 s^{-1}. This value is about six times the value recorded at GCE/CQDs/CNPs (Table 4.18). It is also noteworthy that the Tafel slope obtained from Equation 4.12 and the slope of Equation 4.38 was 400 mV. The fact that the value exceeds 200 mV dec^{-1} suggested adsorption at the surface of the modified electrode.

$$I_{ap} = -28.4985 + 8.2471\, v^{1/2} \qquad (R^2 = 0.9911) \qquad \text{(Eqn 4.36)}$$

$$I_{cp} = 5.9445 - 6.8099\, v^{1/2} \qquad (R^2 = -0.9918) \qquad \text{(Eqn 4.37)}$$

$$E_{ap} = -0.2186 + 0.2003 \log v \qquad (R^2 = 0.9899) \qquad \text{(Eqn 4.38)}$$

$$E_{cp} = 0.1327 - 0.1571 \log v \qquad (R^2 = -0.9869) \qquad \text{(Eqn 4.39)}$$

Table 4.18: Kinetic parameters of CQDs/CNPs and bCQDs/CNPs modified electrode in DA

Electrode	α	n	k (s^{-1})	b (mV dec^{-1})
GCE/CQDs/CNPs	0.69	2.03	0.11	520
GCE/bCQDs/CNPs	0.56	2.90	0.64	400

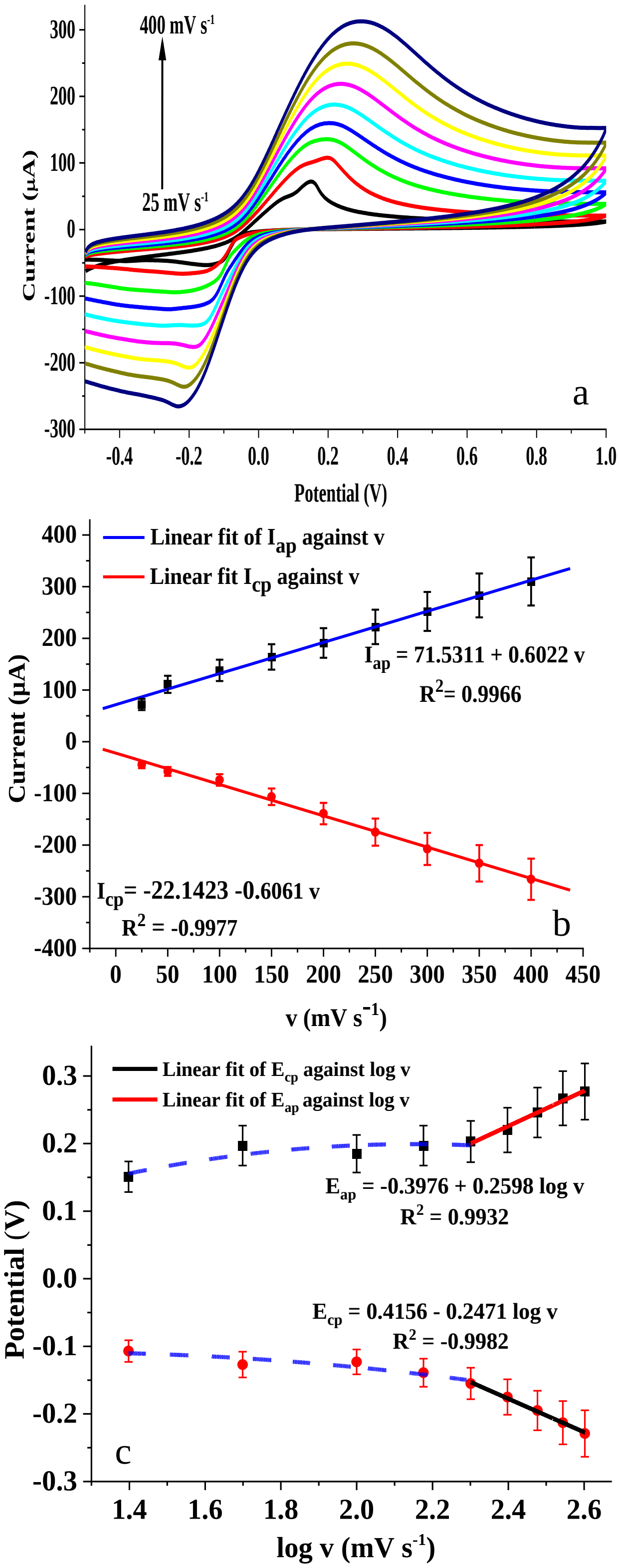

Figure 4.35: Cyclic voltammograms of GCE/CQDs/CNPs in DA over a scan rate range (25 – 400 mV s^{-1}) at pH 7 (b) plot of the anodic and cathodic peak current against the square root of the scan rate and (c) plot of the anodic and cathodic peak potential against log v

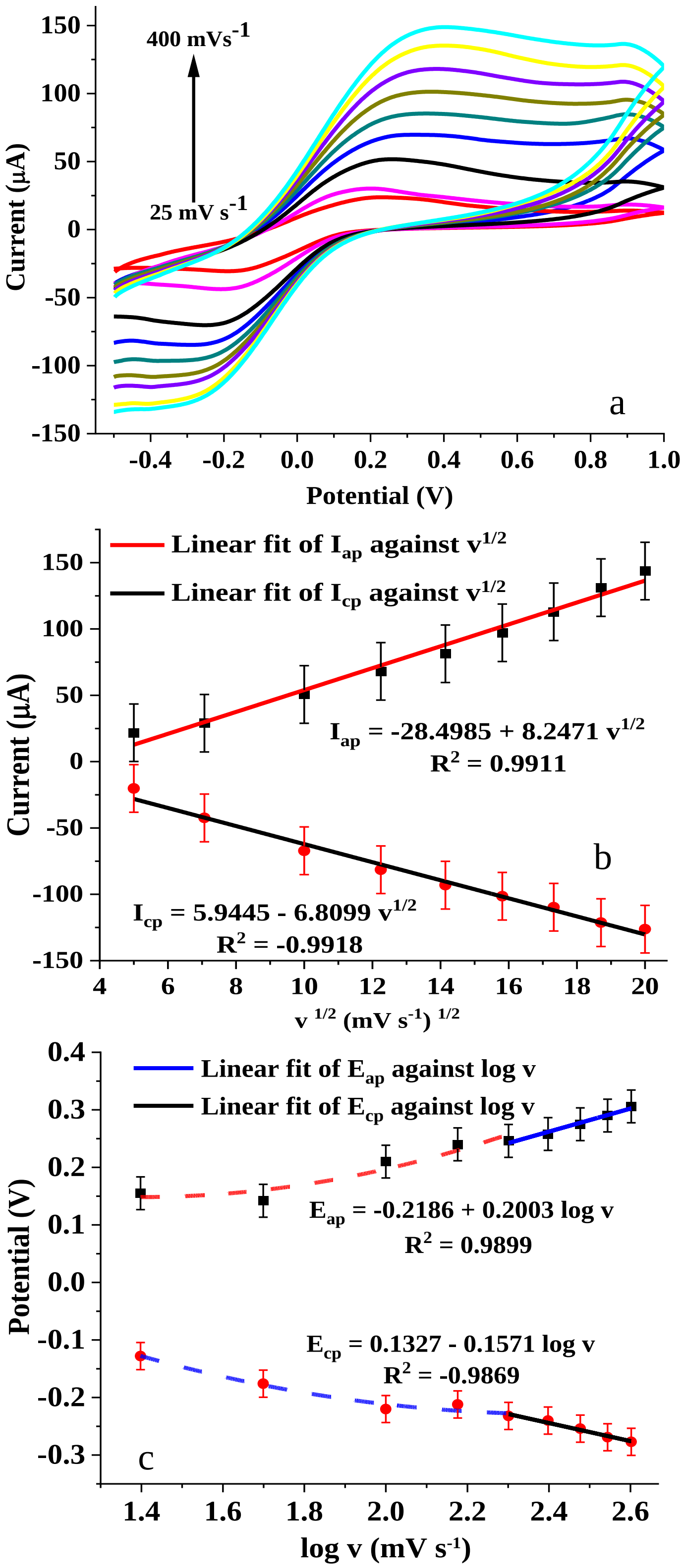

Figure 4.36: Cyclic voltammograms of GCE/bCQDs/CNPs in DA over a scan rate range (25 – 400 mV s^{-1}) at pH 7 (b) plot of the anodic and cathodic peak current against the square root of the scan rate and (c) plot of the anodic and cathodic peak potential against log v

4.5.5 Concentration studies

The effect of concentration on the electroanalysis of DA at the selected modified electrodes was studied using square wave voltammetry at a scan rate of 25 mV s^{-1} (pH 7). Figure 4.37 (a) showed the square wave voltammogram of GCE/CQDs/CNPs in the presence of 10-180 µM DA. The peak current increased with the increase in the DA concentration. Figure 4.37 (b) showed the linear relationship between the current response (I) and DA concentration. Fortuitously, the relationship between I and the concentration of DA ([DA]) was linear over the entire concentration range (10-180 µM). The LoD calculated for this sensor from Equation 4.19 and the mathematical representation of the linear relationship between I and [DA] (Equation 4.40) was 13.27 µM. The detection limit was comparable to the LoD reported for DA detection at some chemically modified electrodes (Table 4.19). On the other hand, the linear dynamic range (LDR) recorded at this electrode was wider than that of some previously fabricated DA electrochemical sensors [97, 371, 372]. The LoQ of this sensor (GCE/CQDs/CNPs) was calculated as 40.21 µM.

$$\mathrm{I} = 3.2711 + 0.0561\ [\mathrm{DA}] \qquad \text{(Eqn 4.40)}$$

$$\mathrm{I} = 0.2424 + 0.0194\ [\mathrm{DA}] \qquad \text{(Eqn 4.41)}$$

The effect of concentration on DA electroanalysis at GCE/bCQDs/CNPs was also investigated using SWV under similar conditions as that of GCE/CQDs/CNPs over a concentration range of 50-200 µM (Fig. 4.37 (c)). The relationship between I and [DA] was linear over the entire concentration range as with GCE/CQDs/CNPs (Fig. 4.37 (d)). The linear relationship was represented by Equation 4.41. The LDR for this sensor is similar to that of GCE/CQDs/CNPs and wider than that of some chemically fabricated sensor in literature [97, 371, 372]. Also, the detection limit obtained at GCE/bCQDs/CNPs was 21.11 µM.

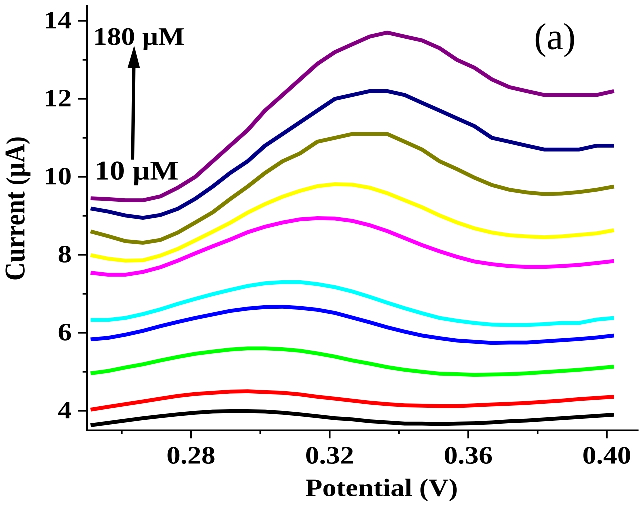

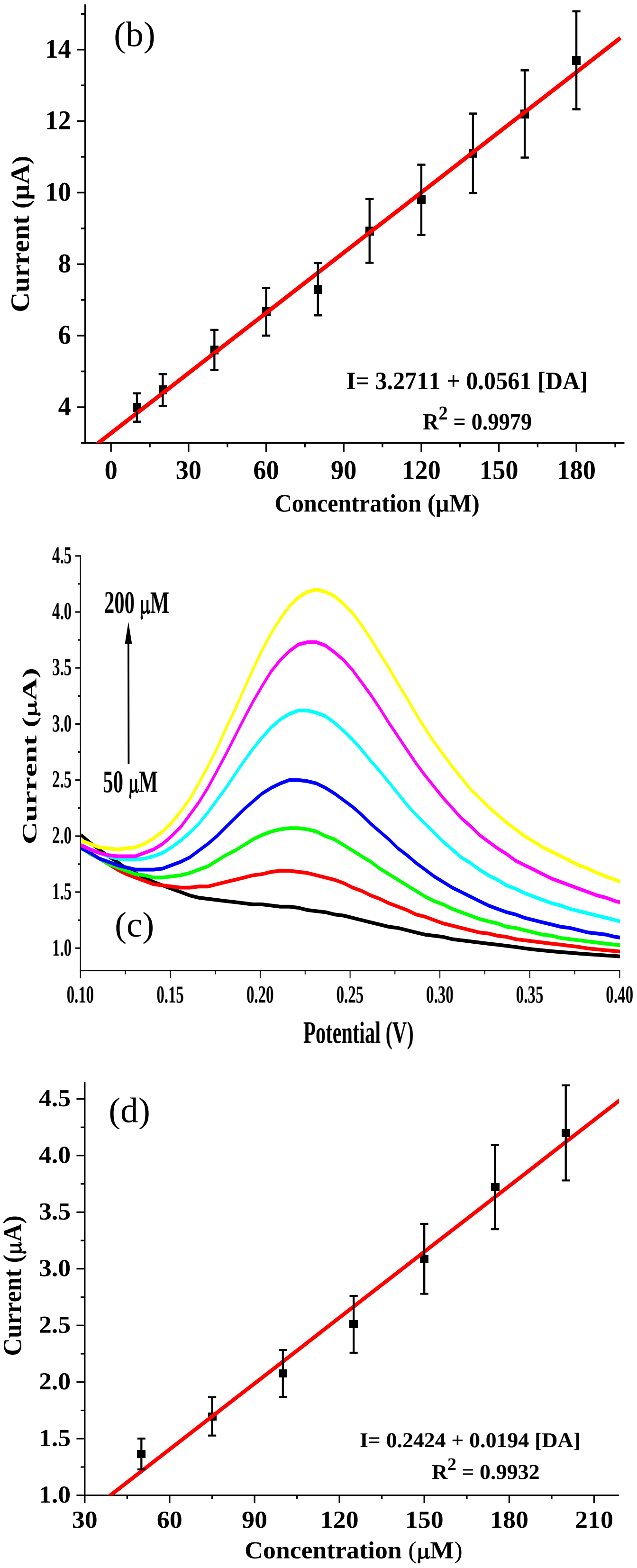

Figure 4.37: Square wave voltammograms of GCE/CQDs/CNPs and GCE/bCQDs/CNPs over DA concentration range of 10-180 µM and 50-200 µM, respectively at pH 7 (a) and (c). (b,d) plot of current versus concentration extracted from (a) and (c), respectively.

Table 4.19: Comparison of the proposed sensors with past DA sensors

Electrode	Technique	Linear range (µM)	LOD (µM)	Sensitivity (µA µM^{-1})	References
PANI-NF/Pt	SWV	62.5-603	33.3	0.002	[373]
AuNPs/DNA/o-PD/SPCE	CV	-	1000	-	[374]
Silanized graphene	DPV	0.2-25	0.01	-	[371]
PANI/GO/GCE	DPV	2-18	0.5	2.000	[372]
Nano-Au/SAMs/Au	DPV	200-1200	90.0	0.003	[375]
GCE/MWCNTs/pFA	AP	5-120	2.2	0.037	[323]
Poly-β-CD(f-MWCNTs)/PANI/GCE	DPV	2-24	0.0164	2.116	[97]
β-CD-MWCNTs/Plu-AuNPs/GCE	DPV	1-56	0.19	0.019	[376]
GCE/CQDs/CNPs	SWV	10-180	13.27	0.056	This work
GCE/bCQDs/CNPs	SWV	50-200	25.41	0.019	This work

PANI-NF/Pt – polyaniline/nafion composite modified platinum electrode; AuNPs/DNA/o-PD/SPCE- gold nanoparticles/deoxyribonucleic acid/o-phenylenediamine composite modified screen printed electrode; PANI/GO- polyaniline/graphene oxide composite modified glassy carbon electrode; Nano-Au/SAMs/Au – Nanoporous gold nanoparticles/self-assembly monolayer modified gold electrode; GCE/MWCNTs/pFA – Multiwalled-carbon nanotubes/poly(Feluric acid) composite modified glassy carbon electrode; Poly-β-CD(f-MWCNTs)/PANI – poly(β-cyclodextrin) decorated functionalized multi-walled carbon nanotube and polyaniline composite modified electrode; β-CD-MWCNTs/Plu-AuNPs/GCE – β-cyclodextrin decorated MWCNTs and gold nanoparticles modified glassy carbon electrode.

The LoD of this sensor is higher than that of GCE/CQDs/CNPs but lower than that of some sensors highlighted in Table 4.19 [373, 375]. The LoQ recorded at GCE/bCQDs/CNPs was 76.97 µM. Collectively, the figures of merit, such as recorded at GCE/CQDs/CNPs and GCE/bCQDs/CNPs are much better than the values reported for some sensors in literature, indicating that these sensors are suitable for micromolar DA detection.

4.5.6 Interference studies

The interference studies were done using ascorbic acid (AA) as the interfering molecule. The cyclic voltammogram of 0.2 mM DA in a solution containing 5 mM AA showed that the bare GCE was incapable of AA and DA peak resolution (Fig. 4.38 (a)). Using GCE/CQDs/CNPs, the cyclic voltammogram showed AA and DA peaks at 0.21 V and 0.43 V, respectively (Fig. 4.38 (b)). The differential pulse voltammetry (DPV) showed well-resolved AA and DA peaks at 0.11 V and 0.25 V, respectively (Fig. 4.38 (c)). This AA-DA peak difference (140 mV) was comparable with the values recorded at some of the previously fabricated DA sensors (Table 4.20). The DPV of GCE/CQDs/CNPs in a solution containing 1 mM AA and varying concentrations of DA (100-125 μM) at pH 7 revealed no significant change in the AA peak with the increase in DA concentration (Fig. 4.38 (d)). On the other hand, the DA current response increased with every increase in DA concentration. It is also noteworthy that AA peak initially reduced in intensity with increase in DA concentration and outrightly disappeared at very high DA concentration (Fig. 4.38 (d)), suggesting that GCE/CQDs/CNPs is selective for DA at the experimental pH (pH 7).

Table 4.20: AA-DA peak difference of past and present DA sensors

Electrode	Method	AA-DA Peak difference	References
PCN/GO/GCE	DPV	190	[377]
rGO/Pd@Ppy-GCE	DPV	150	[240]
PRB/CPE	CV	123	[378]
PGE/GCE	DPV	208	[379]
GCE/bCQDs/CNPs	DPV	130	This work
GCE/CQDs/CNPs	DPV	140	This work

GCE – glassy carbon electrode; CPE – carbon paste electrode; PCN/GO/GCE – porous graphitic carbon nitride modified glassy carbon electrode; rGO/Pd@Ppy-GCE – palladium supported poly(pyrrole)/graphene oxide composite modified GCE; PRB/CPE - poly (Reactive Blue) modified CPE; PGE/GCE – porous graphene modified GCE

The behavior of AA and DA in this mixture could be ascribed to the ionic nature of the analytes at neutral pH. It has been reported that DA and AA assumed cationic and anionic at physiological pH. The fact that CQDs possess negatively charged oxygen-containing functionalities supported the electrostatic interaction between DA and the modified electrode. This interaction improved with the increase in DA concentration. Conversely, the anionic nature of AA led to repulsion between AA and the CQDs in the CQDs/CNPs modified electrode. This interaction and repulsion between the modified electrode and these analytes led to the drop in the AA peak with the increase in DA concentration.

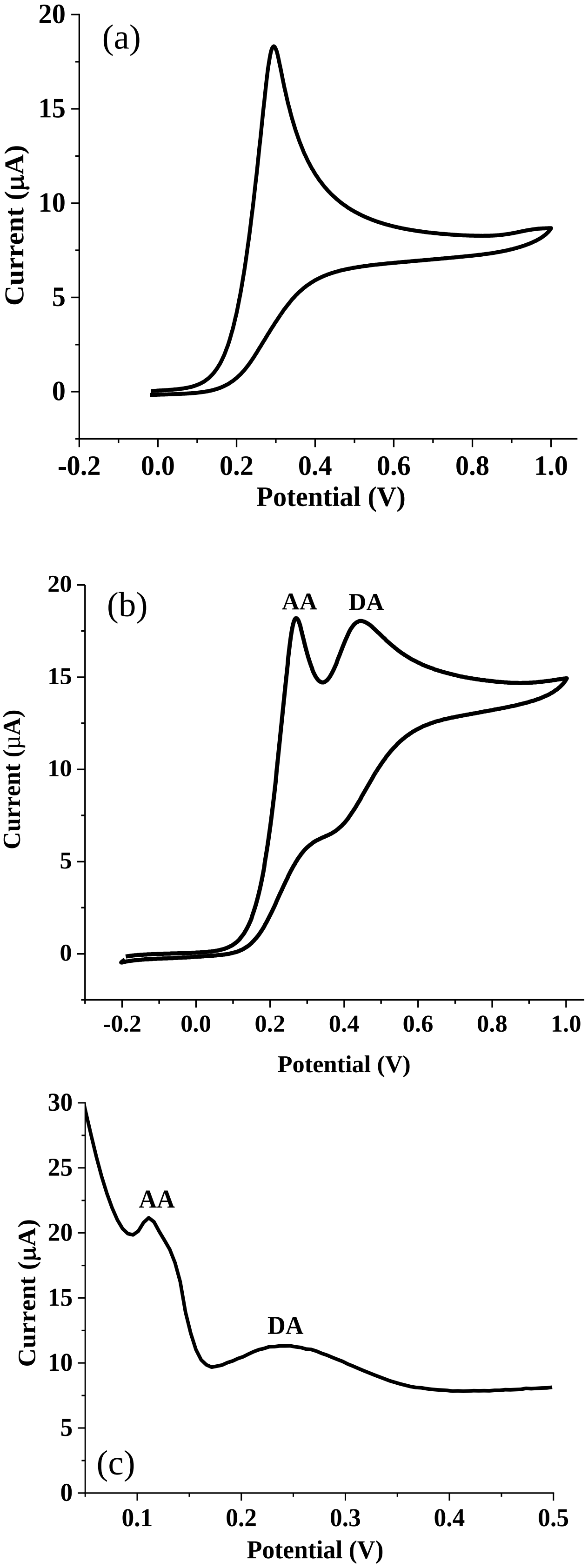
(a)
20
15
10
5
0
Current (μA)
-0.2
0.0
0.2
0.4
0.6
0.8
1.0
Potential (V)
(b)
AA
DA
20
15
10
5
0
Current (μA)
-0.2
0.0
0.2
0.4
0.6
0.8
1.0
Potential (V)
AA
DA
(c)
30
25
20
15
10
5
0
Current (μA)
0.1
0.2
0.3
0.4
0.5
Potential (V)

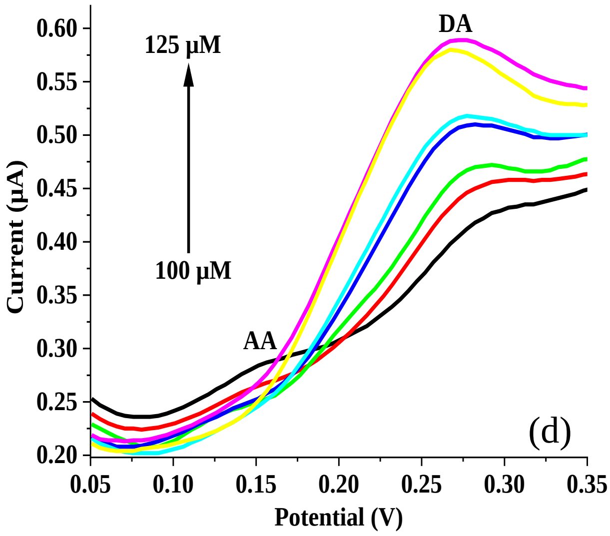

Figure 4.38: Cyclic voltammograms of (a) bare GCE and (b) GCE/CQDs/CNPs, (c) differential pulse voltammogram of GCE/CQDs/CNPs in 0.4 mM DA and 1 mM AA (d) Differential pulse voltammograms of EP concentration increase (100 – 125 µM) with constant AA concentration (1 mM) at GCE/CQDs/CNPs (pH 7, scan rate: 25 mV s^{-1})

The interference of AA with DA signal in a mixture of the two analytes was also investigated with GCE/bCQDs/CNPs under the same condition as GCE/CQDs/CNPs. Using cyclic voltammetry, the bare GCE and GCE/bCQDs/CNPs gave only one peak (Fig. 4.39 (a) and (b)). The major difference between the peaks is that the fused AA-DA peak at GCE/bCQDs/CNPs was broader than that of the bare GCE. With DPV, the well-resolved AA and DA peaks appeared at 0.08 V and 0.21 V, respectively (Fig. 4.39 (c)). The peak-to-peak separation (130 mV) was wider than the value recorded at GCE/bCQDs/CNPs and comparable to the peak differences recorded at notable DA sensors (Table 4.20). Similar to the behavior of DA in a mixture containing a constant concentration of AA and varying AA concentration at GCE/CQDs/CNPs, the DA peak current increased with increase in DA concentration. Noteworthy, there was a total disappearance of AA peak at higher DA concentration (Fig. 4.39 (d)). The disaapperance can be attributed to the same reason for the disappearance of the AA peak at high DA concentration when GCE/CQDs/CNPs was used as the working electrode. The outcome suggested that GCE/CQDs/CNPs and GCE/bCQDs/CNPs are suitable for DA detection in the presence of ascorbic acid.

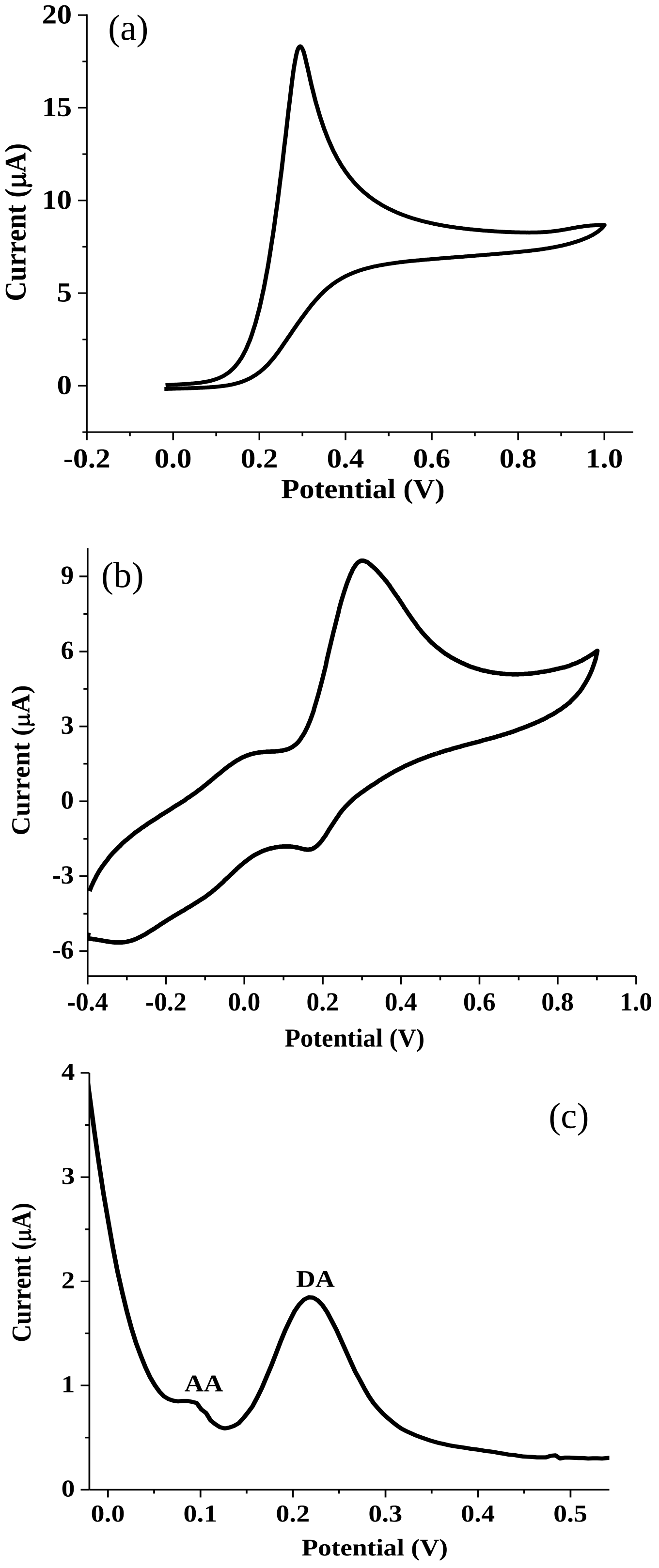
(a)
20
15
10
5
0
Current (μA)
-0.2
0.0
0.2
0.4
0.6
0.8
1.0
Potential (V)
(b)
9
6
3
0
-3
-6
Current (μA)
-0.4
-0.2
0.0
0.2
0.4
0.6
0.8
1.0
Potential (V)
(c)
4
3
2
1
0
Current (μA)
DA
AA
0.0
0.1
0.2
0.3
0.4
0.5
Potential (V)

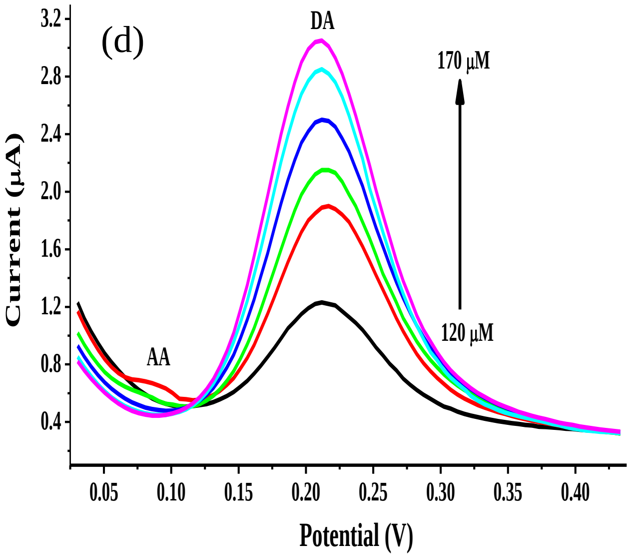

Figure 4.39: Cyclic voltammograms of bare GCE and GCE/CQDs/CNPs, (a and b), (c) differential pulse voltammogram of GCE/CQDs/CNPs in 0.4 mM DA and 1 mM AA (d) square wave voltammograms of EP concentration increase (120 – 170 µM) with constant AA concentration (1 mM) at GCE/CQDs/CNPs (pH 7, scan rate: 25 mV s^{-1}).

4.5.7 Real sample analysis

The real sample analysis of DA was done using dopamine hydrochloride injection, following the standard addition method. The dopamine hydrochloride injection (200 mg/5 mL) was prepared for real sample analysis by 1000-fold dilution of 5 mL of the injection. The diluted injection was spiked with 50 µM DA. The concentration of DA in the unspiked and spiked DA injection solution was used for calculating the percentage DA recovery from the DA injection sample. The percentage DA recovery from the injection sample after the triplicate determination was 95.1 %, with percentage relative standard deviation (% RSD) of 6.51 % (Table 4.21). The DA recovery in the injection sample was comparable with the % recovery reported for DA detection at poly(Reactive Blue) modified electrode [378].

The real sample analysis was also carried out under the same condition using GCE/bCQDs/CNPs as the working electrode. The % DA recovery recorded with GCE/bCQDs/CNPs after triplicate measurement was 94.77 % with a % RSD of 15.13 % (Table 4.21). The average % recovery was similar to the value recorded at GCE/bCQDs/CNPs. On the contrary, the % RSD recorded at GCE/bCQDs/CNPs was more than twice the value recorded at GCE/CQDs/CNPs and some previously fabricated DA sensors [380, 381]. The result indicated that GCE/bCQDs/CNPs was less sensitive for DA detection in DA hydrochloride injection than GCE/CQDs/CNPs. The outcome could be ascribed to the disparity in the sensitivity of the two electrodes.

Table 4.21: Dopamine analysis in dopamine hydrochloride injection

Electrode	Sample	Amount added (µM)	Amount found (µM)	% recovery	% RSD
GCE/CQDs/CNPs	DA injection	50	46.52	93.01	6.51
		50	50.98	102.04	
		50	45.10	90.21	
GCE/bCQDs/CNPs	DA injection	50	47.01	94.02	15.13
		50	55.13	110.26	
		50	40.01	80.02	

4.5.8 Stability and reproducibility

The stability of the current response recorded at the selected modified electrodes was investigated using cyclic voltammetry (CV) in the presence of 0.2 mM DA at a scan rate of 25 mV s^{-1} (pH 7). After 22 CV scans, the current response recorded at GCE/CQDs/CNPs dropped to about 31.4 % of the current response recorded after the first scan (Fig 4.40 (a)). With GCE/bCQDs/CNPs, the current response dropped to 20 % of the current response recorded for the first scan (Fig. 4.40 (b)). These outcomes indicate that GCE/CQDs/CNPs was more stable than GCE/bCQDs/CNPs. The superior stability of GCE/CQDs/CNPs can be ascribed to the lower % RSD recorded for DA recovery from dopamine hydrochloride injection relative to the % RSD recorded with GCE/bCQDs/CNPs.

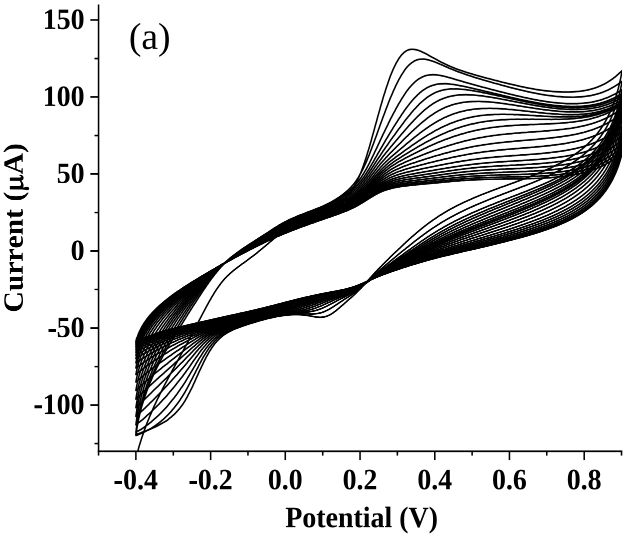

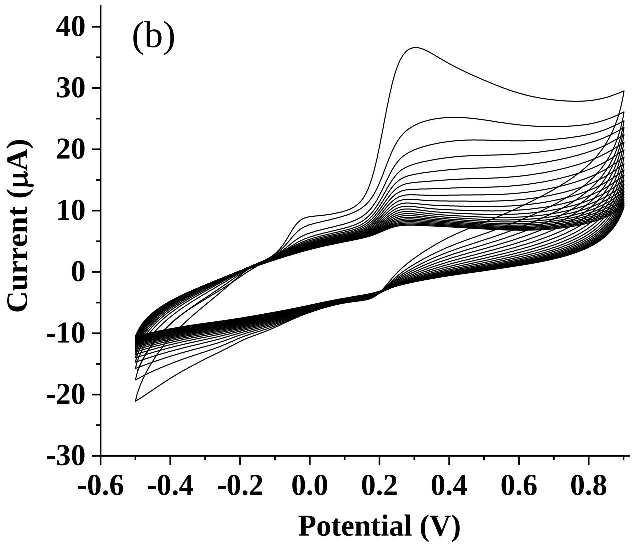

Figure 4.40: Cyclic voltammogram of (a) GCE/CQDs/CNPs and (b) GCE/bCQDs/CNPs in 0.2 mM DA (pH 7) after 22 scans (scan rate: 25 mV s^{-1})

The reproducibility of the two selected modified electrodes for DA electrocatalytic oxidation was investigated by modifying the bare electrode with the modifiers three times for 0.2 mM DA electroanalysis. Using GCE/CQDs/CNPs for cyclic voltammogram at a scan rate of 25 mV s^{-1}, the % RSD of the current response after the three trials was 9.53 % (Fig. 4.41 (a)). The reproducibility study with GCE/bCQDs/CNPs in a similar manner revealed that the DA anodic peak current response of the three trials had a % RSD of 13.88 % (Fig. 4.41 (b)). The results also suggested that GCE/CQDs/CNPs can produce a more reproducible current response than GCE/bCQDs/CNPs.

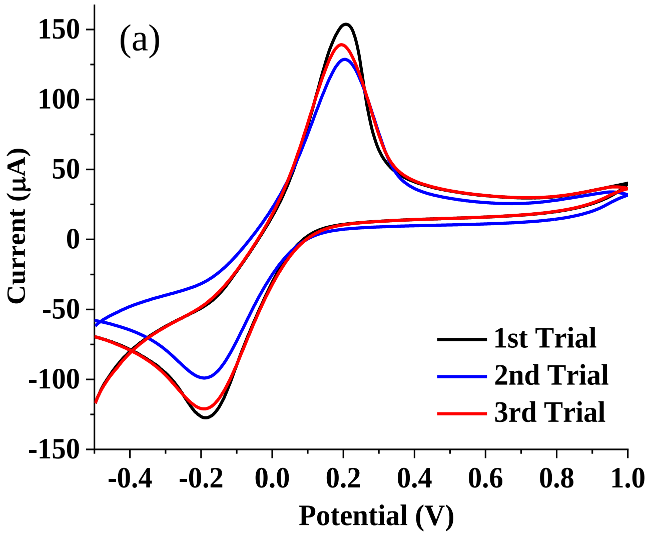

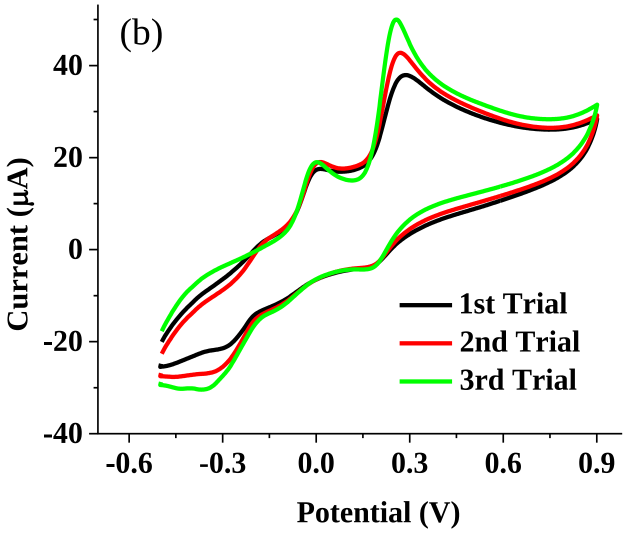

Figure 4.41: Cyclic voltammograms of (a) GCE/CQDs/CNPs and (b) GCE/bCQDs/CNPs in 0.2 mM DA (pH 7, scan rate: 25 mV s^{-1}) for three different trials of electrode modification

CHAPTER FIVE

CONCLUSION AND RECOMMENDATIONS

5.0 Conclusion and recommendations

5.1 Conclusion

Electrochemical detection of catecholamine neurotransmitters at the carbon-based quantum dots/copper oxide nanocomposite glassy carbon modified electrode was investigated in the study. The two carbon-based quantum dots were prepared through hydrothermal synthesis from pencil graphite and banana peel precursors and tagged CQDs and bCQDs, respectively. Some of the developed sensors studied are the bare GCE, GCE/CQDs, GCE/bCQDs, GCE/CNPs, GCE/bCQDs/CNPs, and GCE/CQDs/CNPs, with GCE/bCQDs/CNPs and GCE/CQDs/CNPs emerging as the best performing electrodes towards the detection and electrocatalytic oxidation of the neurotransmitters (dopamine (DA), epinephrine (EP), and norepinephrine (NE)) at a physiological pH of 7 using these sensors.

The comparative epinephrine detection at GCE/CQDs/CNTs and GCE/bCQDs/CNTs done using voltammetric techniques revealed that GCE/CQDs/CNTs offered a lower detection limit than GCE/bCQDs/CNTs. It is worth noting that GCE/CQDs/CNTs also offered better sensitivity to EP detection than the green carbon quantum dots supported sensor (GCE/bCQDs/CNPs). Also, GCE/CQDs/CNPs offered a wider AA-EP peak separation than GCE/bCQDs/CNPs. The superior performance of CQDs supported sensor to GCE/bCQDs/CNPs in the electroanalysis of EP supports the poor electrochemical properties of bCQDs/CNPs relative to that of CQDs/CNPs nanocomposite recorded in the $[Fe(CN)_6]^{3-/4-}$ redox probe. On the other hand, the two sensors have shown the ability to detect epinephrine only at the micromolar level and with low error margin in epinephrine hydrochloride injection. The mechanism of EP interaction with the surface of the modified electrodes (GCE/CQDS/CNPs and GCE/bCQDs/CNPs) was found to be diffusion-controlled. The % RSD (8% for GCE/CQDs/CNPs and 11 % for GCE/bCQDs/CNPs) recorded for the reproducibility of the sensors and the stability of the two sensors showed that the two sensors had similar reproducibility and stability. It can therefore be concluded from these experimental data that GCE/CQDs/CNPs was a better sensor for EP electroanalysis compared to the green carbon quantum dots mediated sensor.

The electrochemical detection of norepinephrine at the two sensors showed that the two sensors possessed similar detection limit and sensitivity. On the other hand, the green carbon quantum dots-based sensor offered a wider linear range than GCE/CQDs/CNPs. Interestingly, the green carbon quantum dots-based sensor also offered a wider NE-UA peak separation than

GCE/CQDs/CNPs, suggesting a better NE and UA peak resolution at bCQDs/CNPs modified electrode. The real sample analysis of NE at the two sensors showed that the recovery of NE from banana peel was achieved with a much lower % RSD at GCE/CQDs/CNPs. On the other hand, GCE/bCQDs/CNPs offered better stability even though the current response at GCE/CQDs/CNPs was more reproducible. The mechanism of NE oxidation at the GCE/CQDs/CNPs and GCE/bCQDs/CNPs was found to be diffusion controlled and surface-confined, respectively. Considering the similarities in sensitivity and detection limit of the two sensors and the superior stability of GCE/bCQDs/CNPs, the green carbon quantum dots-based electrodes was considered a better NE sensor than GCE/CQDs/CNPs.

The electroanalysis of dopamine at the two sensors showed that the GCE/CQDs/CNPs had a much lower detection limit and significantly higher sensitivity than the green carbon quantum dots-based sensor. The wider AA-DA peak separation recorded at GCE/CQDs/CNPs relative to the green carbon quantum dots-based sensor confirmed that DA was detected in the presence of AA with greater ease. Like the results obtained with NE, the analysis of the scan rate's effect on the sensor's current response confirmed that the mechanism of DA redox process was diffusion-controlled and surface-confined at GCE/bCQDs/CNPs and GCE/CQDs/CNPs, respectively. The CQDs-based electrode also showed a much lower % RSD for DA recovery from dopamine hydrochloride injection. The stability and reproducibility of the two electrodes also confirmed that GCE/CQDs/CNPs is more stable with more reproducible current response than the green carbon quantum dots modified electrode.

5.2 Recommendations

Considering the experimental data recorded with the CQDs/CNPs and bCQDs/CNPs modified electrodes for catecholamine neurotransmitters (NTs) detection, the following recommendations should be considered.

i. The synthesis of carbon quantum dots from various biomass for subsequent sensor fabrication should be considered to enable easy waste management while providing cheap starting material for catecholamine NTs sensors fabrication.

ii. The performance of the green carbon quantum dots based sensor in detecting the catecholamine NTs underscores its potential for the electroanalysis of other class of NTs and some other biomolecules. Therefore, the performance of GCE/bCQDs/CNPs in the detection of other NTs and biomolecules should be investigated.

iii. Simultaneous detection of catecholamine NTs (DA, EP and NE) and the selective detection of the NTs in the presence of other NTs at CQDs/CNPs and bCQDs/CNPs modified electrodes should be considered.

iv. The substitution of CNPs for another metal or metal oxide nanoparticles with proven synergy with carbon quantum dots should be attempted to actualize a better sensing platform than the current sensors.

v. Compared to CQDs/CNPs modified electrode, the green carbon quantum dots based sensor offered very close and sufficient sensitivity for the catecholamine NTs detection up to the micromolar level with reasonable recovery of these NTs from real sample. Commercialization of a cheap analytical tool from waste biological materials is therefore recommended for fast point-of-care catecholamine NTs analysis from extracellular fluids.

vi. The electrochemical properties of both carbon quantum dots (banana peel and pencil graphite based) showed that they possess high charge transfer resistance, suggesting that they could be better applied as protective barriers against corrosion of metallic substrates.

APPENDIX

Preparation of the analytes

The three analytes used for the study were prepared as follows:

(a) 0.4 mM dopamine was prepared by dissolving dopamine in 50 mL of 0.1 M PBS (pH 7). Every other concentrations of dopamine required for the study were obtained through dilution of the 0.4 mM dopamine solution.

(b) 0.4 mM epinephrine was prepared by dissolving epinephrine in 50 mL of 0.1 M PBS (pH 7). Every other epinephrine concentrations were prepared through dilution of the 0.4 mM epinephrine solution.

(c) 0.4 mM norepinephrine was prepared by dissolving norepinephrine in 50 mL of 0.1 M PBS (pH 7). Every other norepinephrine concentrations were prepared through dilution of the 0.4 mM norepinephrine solution.

Preparation of drug samples for real sample analysis

The drug samples (dopamine hydrochloride injection) were prepared using the serial dilution approach. A 0.5 mL of the injection samples were transferred into a 100 mL volumetric flask and made up to the 100 mL mark with 0.1 M PBS (pH 7). The procedure was followed by a 100 fold dilution of 0.5 mL of this stock solution. Afterwards, 10 mL of the diluted drug samples were transferred into four different 50 mL volumetric flask. One of the four flasks containing the diluted drug sample was spiked with the desired amount of dopamine and the other sample was left unspiked. The same procedure was repeated for epinephrine hydrochloride injection.

Articles

1. Elugoke, S.E., Adekunle, A.S., Fayemi, O.E., Mamba, B.B., Sherif, E.S.M. and Ebenso, E.E., 2020. Carbon-based quantum dots for electrochemical detection of monoamine neurotransmitters. *Biosensors*, *10*(11), p.162.

2. Saheed E. Elugoke, Omolola E. Fayemi, Abolanle S. Adekunle, Thabo Nkambule, Bhekie B. Mamba and Eno E. Ebenso (2021). Conductive Nanodiamond based Detection of Neurotransmitters: One Decade, Few Sensors. ACS Omega 6, 29, 18548–18558.

3. Saheed E. Elugoke, Omolola E. Fayemi, Abolanle S. Adekunle, Bhekie B. Mamba, Thabo T.I. Nkambule d, Eno E. Ebenso (2022). Electrochemical sensor for the detection of dopamine using carbon quantum dots/copper oxide nanocomposite modified electrode. *FlatChem* 33 (2022) 100372.

4. Highly sensitive and selective neurotransmitter epinephrine detection at a novel carbon quantum dots/copper oxide nanocomposite: experimental and theoretical studies (submitted for publication to Journal of Electroanalytical Chemistry, Elsevier).

5. Electrochemical sensor for the detection of adrenaline at poly(crystal violet) modified electrode: optimization and voltammetric studies (submitted for publication to Heliyon, Elsevier).

6. Elugoke, S.E., Adekunle, A.S., Fayemi, O.E., Akpan, E.D., Mamba, B.B., Sherif, E.S.M. and Ebenso, E.E., 2021. Molecularly imprinted polymers (MIPs) based electrochemical sensors for the determination of catecholamine neurotransmitters–Review. *Electrochemical Science Advances*, *1*(2), p.e2000026.

Conferences attended

1. American chemical society (ACS) spring meeting (virtual). Poster Title: Electrochemical epinephrine detection based on carbon dots/copper oxide nanocomposite: Voltammetric, spectroscopic and theoretical studies (March, 2022).

2. Virtual conference on chemistry and its applications (VCCA), University of Mauritius. Paper presented: Electrochemical detection of epinephrine at green carbon dots/ copper oxide nanocomposite modified electrode (August 2022).

3. International Society for Electrochemistry (ISE)-Sponsored Meeting: 12th International Symposium on Electrochemical Impedance Analysis (virtual). Paper presented: Impedance spectroscopy characterization of carbon quantum dots/copper oxide composite in epinephrine (November, 2021).

4. SACI: 2nd Commonwealth Chemistry Posters 2021 (virtual). Poster Title: Graphitic carbon dot/copper oxide nanocomposite based electrochemical sensor for dopamine detection (September 2021).

5. 240th electrochemical society (ECS) meeting (virtual). Paper presented**:** Poly(crystal-violet) Films Modified Electrode for Adrenaline Detection: Optimization and Voltammetric Studies (October 2021).

References

[1] P. A. Rutecki, "Neuronal excitability: voltage-dependent currents and synaptic transmission," *Journal of clinical neurophysiology: official publication of the American Electroencephalographic Society,* vol. 9, no. 2, pp. 195-211, 1992.

[2] S. E. Elugoke, A. S. Adekunle, O. E. Fayemi, B. B. Mamba, E. M. Sherif, and E. E. Ebenso, "Carbon-Based Quantum Dots for Electrochemical Detection of Monoamine Neurotransmitters-Review," *Biosensors (Basel),* vol. 10, no. 11, Oct 31 2020.

[3] N. F. Atta, H. Ekram, Y. M. Ahmed, and A. Galal, "Determination of some neurotransmitters at cyclodextrin/ionic liquid crystal/graphene composite electrode," *Electrochimica Acta,* vol. 199, pp. 319-331, 2016.

[4] J. R. Cooper, F. E. Bloom, and R. H. Roth, *The biochemical basis of neuropharmacology*. Oxford University Press, USA, 2003.

[5] A. Gutiérrez, E. N. Primo, M. Eguílaz, C. Parrado, M. D. Rubianes, and G. A. Rivas, "Quantification of neurotransmitters and metabolically related compounds at glassy carbon electrodes modified with bamboo-like carbon nanotubes dispersed in double stranded DNA," *Microchemical Journal,* vol. 130, pp. 40-46, 2017.

[6] D. Yu, Y. Zeng, Y. Qi, T. Zhou, and G. Shi, "A novel electrochemical sensor for determination of dopamine based on AuNPs@ SiO2 core-shell imprinted composite," *Biosensors and Bioelectronics,* vol. 38, no. 1, pp. 270-277, 2012.

[7] A. Babaei, M. Sohrabi, and M. Afrasiabi, "A sensitive simultaneous determination of epinephrine and piroxicam using a glassy carbon electrode modified with a nickel hydroxide nanoparticles/multiwalled carbon nanotubes composite," *Electroanalysis,* vol. 24, no. 12, pp. 2387-2394, 2012.

[8] N. Shafi, J. Midgley, D. Watson, G. Smail, R. Strang, and R. MacFarlane, "Analysis of biogenic amines in the brain of the American cockroach (Periplaneta Americana) by gas chromatography-negative ion chemical ionisation mass spectrometry," *Journal of Chromatography B: Biomedical Sciences and Applications,* vol. 490, pp. 9-19, 1989.

[9] K. Vuorensola, H. Sirén, and U. Karjalainen, "Determination of dopamine and methoxycatecholamines in patient urine by liquid chromatography with electrochemical detection and by capillary electrophoresis coupled with spectrophotometry and mass spectrometry," *Journal of Chromatography B,* vol. 788, no. 2, pp. 277-289, 2003.

[10] C. Muzzi *et al.*, "Simultaneous determination of serum concentrations of levodopa, dopamine, 3-O-methyldopa and α-methyldopa by HPLC," *Biomedicine & pharmacotherapy,* vol. 62, no. 4, pp. 253-258, 2008.

[11] F. B. Salem, "Spectrophotometric and titrimetric determination of catecholamines," *Talanta,* vol. 34, no. 9, pp. 810-812, 1987.

[12] S. E. Elugoke *et al.*, "Progress in electrochemical detection of neurotransmitters using carbon nanotubes/nanocomposite based materials: A chronological review," *Nano Select,* vol. 1, no. 6, pp. 561-611, 2020.

[13] S. E. Elugoke, O. E. Fayemi, A. S. Adekunle, T. T. Nkambule, B. B. Mamba, and E. E. Ebenso, "Conductive Nanodiamond-Based Detection of Neurotransmitters: One Decade, Few Sensors," *ACS Omega,* 2021.

[14] S. Zheng, "A Highly Sensitive Dopamine Sensor Based on Graphene Quantum Dots Modified Glassy Carbon Electrode," *International Journal of Electrochemical Science,* pp. 5723-5735, 2018.

[15] T. C. Canevari, M. Nakamura, F. H. Cincotto, F. M. de Melo, and H. E. Toma, "High performance electrochemical sensors for dopamine and epinephrine using

nanocrystalline carbon quantum dots obtained under controlled chronoamperometric conditions," *Electrochimica Acta,* vol. 209, pp. 464-470, 2016.

[16] J. Tashkhourian, S. F. Nami-Ana, and M. Shamsipur, "Designing a modified electrode based on graphene quantum dot-chitosan application to electrochemical detection of epinephrine," *Journal of Molecular Liquids,* vol. 266, pp. 548-556, 2018.

[17] Y. Wang and A. Hu, "Carbon quantum dots: synthesis, properties and applications," *Journal of Materials Chemistry C,* vol. 2, no. 34, pp. 6921-6939, 2014.

[18] G. S. Selopal *et al.*, "Highly stable colloidal “giant” quantum dots sensitized solar cells," *Advanced Functional Materials,* vol. 27, no. 30, p. 1701468, 2017.

[19] J. Chen *et al.*, "14.3: Quantum dots: optimizing LCD systems to achieve Rec. 2020 color performance," in *SID Symposium Digest of Technical Papers,* 2015, vol. 46, no. 1, pp. 173-175: Wiley Online Library.

[20] A. J. Sutherland, "Quantum dots as luminescent probes in biological systems," *Current Opinion in Solid State and Materials Science,* vol. 6, no. 4, pp. 365-370, 2002.

[21] D. Sun, R. Ban, P.-H. Zhang, G.-H. Wu, J.-R. Zhang, and J.-J. Zhu, "Hair fiber as a precursor for synthesizing of sulfur-and nitrogen-co-doped carbon dots with tunable luminescence properties," *Carbon,* vol. 64, pp. 424-434, 2013.

[22] S. Liu *et al.*, "Hydrothermal treatment of grass: a low-cost, green route to nitrogen-doped, carbon-rich, photoluminescent polymer nanodots as an effective fluorescent sensing platform for label-free detection of Cu (II) ions," *Advanced materials,* vol. 24, no. 15, pp. 2037-2041, 2012.

[23] N. Wang, Y. Wang, T. Guo, T. Yang, M. Chen, and J. Wang, "Green preparation of carbon dots with papaya as carbon source for effective fluorescent sensing of Iron (III) and Escherichia coli," *Biosensors and Bioelectronics,* vol. 85, pp. 68-75, 2016.

[24] Z. Zhang, Y. Duan, Y. Yu, Z. Yan, and J. Chen, "Carbon quantum dots: synthesis, characterization, and assessment of cytocompatibility," *Journal of Materials Science: Materials in Medicine,* vol. 26, no. 7, pp. 1-7, 2015.

[25] W.-F. Hsu and T.-M. Wu, "Electrochemical sensor based on conductive polyaniline coated hollow tin oxide nanoparticles and nitrogen doped graphene quantum dots for sensitively detecting dopamine," *Journal of Materials Science: Materials in Electronics,* vol. 30, no. 9, pp. 8449-8456, 2019.

[26] H. Beitollahi, Z. Dourandish, M. R. Ganjali, and S. Shakeri, "Voltammetric determination of dopamine in the presence of tyrosine using graphite screen-printed electrode modified with graphene quantum dots," *Ionics,* vol. 24, no. 12, pp. 4023-4031, 2018.

[27] M. Algarra *et al.*, "Enhanced electrochemical response of carbon quantum dot modified electrodes," *Talanta,* vol. 178, pp. 679-685, 2018.

[28] M. Jagannathan *et al.*, "Green synthesis of white light emitting carbon quantum dots: Fabrication of white fluorescent film and optical sensor applications," *Journal of Hazardous Materials,* vol. 416, p. 125091, 2021.

[29] A. Tyagi, K. M. Tripathi, N. Singh, S. Choudhary, and R. K. Gupta, "Green synthesis of carbon quantum dots from lemon peel waste: applications in sensing and photocatalysis," *RSC advances,* vol. 6, no. 76, pp. 72423-72432, 2016.

[30] Z. Li *et al.*, "A fluorescence probe based on the nitrogen-doped carbon dots prepared from orange juice for detecting Hg2+ in water," *Journal of Luminescence,* vol. 187, pp. 274-280, 2017.

[31] N. Chaudhary, P. K. Gupta, S. Eremin, and P. R. Solanki, "One-step green approach to synthesize highly fluorescent carbon quantum dots from banana juice for selective detection of copper ions," *Journal of Environmental Chemical Engineering,* vol. 8, no. 3, p. 103720, 2020.

[32] D. G. Dastidar, P. Mukherjee, D. Ghosh, and D. Banerjee, "Carbon quantum dots prepared from onion extract as fluorescence turn-on probes for selective estimation of Zn2+ in blood plasma," *Colloids and Surfaces A: Physicochemical and Engineering Aspects,* vol. 611, p. 125781, 2021.

[33] C. Wang *et al.*, "Facile synthesis of novel carbon quantum dots from biomass waste for highly sensitive detection of iron ions," *Materials Research Bulletin,* vol. 124, p. 110730, 2020.

[34] L. Komalavalli, P. Amutha, and S. Monisha, "A facile approach for the synthesis of carbon dots from Hibiscus sabdariffa & its application as bio-imaging agent and Cr (VI) sensor," *Materials Today: Proceedings,* vol. 33, pp. 2279-2285, 2020.

[35] M. Jayanthi, S. Megarajan, S. B. Subramaniyan, R. K. Kamlekar, and A. Veerappan, "A convenient green method to synthesize luminescent carbon dots from edible carrot and its application in bioimaging and preparation of nanocatalyst," *Journal of Molecular Liquids,* vol. 278, pp. 175-182, 2019.

[36] C. Cheng, Y. Shi, M. Li, M. Xing, and Q. Wu, "Carbon quantum dots from carbonized walnut shells: structural evolution, fluorescence characteristics, and intracellular bioimaging," *Materials Science and Engineering: C,* vol. 79, pp. 473-480, 2017.

[37] R. Atchudan, T. N. J. I. Edison, M. Shanmugam, S. Perumal, T. Somanathan, and Y. R. Lee, "Sustainable synthesis of carbon quantum dots from banana peel waste using hydrothermal process for in vivo bioimaging," *Physica E: Low-dimensional Systems and Nanostructures,* vol. 126, p. 114417, 2021.

[38] G. Muthusankar *et al.*, "In situ assembly of sulfur-doped carbon quantum dots surrounded iron (III) oxide nanocomposite; a novel electrocatalyst for highly sensitive detection of antipsychotic drug olanzapine," *Journal of Molecular Liquids,* vol. 268, pp. 471-480, 2018.

[39] Y. Li, Y. Zhong, Y. Zhang, W. Weng, and S. Li, "Carbon quantum dots/octahedral Cu2O nanocomposites for non-enzymatic glucose and hydrogen peroxide amperometric sensor," *Sensors and Actuators B: Chemical,* vol. 206, pp. 735-743, 2015.

[40] Q. Huang, X. Lin, C. Lin, Y. Zhang, S. Hu, and C. Wei, "A high performance electrochemical biosensor based on Cu2O–carbon dots for selective and sensitive determination of dopamine in human serum," *RSC Advances,* vol. 5, no. 67, pp. 54102-54108, 2015.

[41] S. K. Arumugasamy, S. Govindaraju, and K. Yun, "Electrochemical sensor for detecting dopamine using graphene quantum dots incorporated with multiwall carbon nanotubes," *Applied Surface Science,* vol. 508, p. 145294, 2020.

[42] S. Ben Aoun, "Nanostructured carbon electrode modified with N-doped graphene quantum dots-chitosan nanocomposite: a sensitive electrochemical dopamine sensor," *R Soc Open Sci,* vol. 4, no. 11, p. 171199, Nov 2017.

[43] J. A. Ribeiro, P. M. V. Fernandes, C. M. Pereira, and F. Silva, "Electrochemical sensors and biosensors for determination of catecholamine neurotransmitters: A review," *Talanta,* vol. 160, pp. 653-679, Nov 1 2016.

[44] O. E. Fayemi, A. S. Adekunle, and E. E. Ebenso, "Electrochemical determination of serotonin in urine samples based on metal oxide nanoparticles/MWCNT on modified glassy carbon electrode," *Sensing and Bio-Sensing Research,* vol. 13, pp. 17-27, 2017.

[45] N. G. Mphuthi, A. S. Adekunle, O. E. Fayemi, L. O. Olasunkanmi, and E. E. Ebenso, "Phthalocyanine Doped Metal Oxide Nanoparticles on Multiwalled Carbon Nanotubes Platform for the detection of Dopamine," *Sci Rep,* vol. 7, p. 43181, Mar 3 2017.

[46] S. Campuzano, P. Yanez-Sedeno, and J. M. Pingarron, "Carbon Dots and Graphene Quantum Dots in Electrochemical Biosensing," *Nanomaterials (Basel),* vol. 9, no. 4, Apr 19 2019.

[47] M. Liu, Y. Xu, F. Niu, J. J. Gooding, and J. Liu, "Carbon quantum dots directly generated from electrochemical oxidation of graphite electrodes in alkaline alcohols and the applications for specific ferric ion detection and cell imaging," *Analyst,* vol. 141, no. 9, pp. 2657-2664, 2016.

[48] D. Purves *et al.*, "Circuits within the basal ganglia system," in *Neuroscience. 2nd edition*: Sinauer Associates, 2001.

[49] J. Moini and P. Piran, *Functional And Clinical Neuroanatomy: A Guide for Health Care Professionals*. Academic Press, 2020.

[50] J. Mendoza and A. Foundas, *Clinical neuroanatomy: a neurobehavioral approach*. Springer Science & Business Media, 2007.

[51] G. M. Kapalka, *Nutritional and herbal therapies for children and adolescents: a handbook for mental health clinicians*. Academic Press, 2009.

[52] L. R. Doblado, C. Martínez-Ramos, and M. M. Pradas, "Biomaterials for Neural Tissue Engineering," *Frontiers in Nanotechnology,* vol. 3, p. 21, 2021.

[53] H. Lodish and S. L. Zipursky, "Molecular cell biology," *Biochem Mol Biol Educ,* vol. 29, pp. 126-133, 2001.

[54] M. Carter and J. C. Shieh, *Guide to research techniques in neuroscience*. Academic Press, 2015.

[55] S. W. Jones, "On the resting potential of isolated frog sympathetic neurons," *Neuron,* vol. 3, no. 2, pp. 153-161, 1989.

[56] R. Schmidt, "The transmission of excitation from cell to cell," in *Human Physiology*: Springer, 1983, pp. 51-70.

[57] J. P. Vessey, M. R. Lalonde, H. A. Mizan, N. C. Welch, M. E. Kelly, and S. Barnes, "Carbenoxolone inhibition of voltage-gated Ca channels and synaptic transmission in the retina," *Journal of neurophysiology,* vol. 92, no. 2, pp. 1252-1256, 2004.

[58] M. K. Gupta, R. Khanna, and K. Rangra, "Study and analysis of human nervous system and effects of external em signals on conduction in human nerves," *International Journal on Recent and Innovation Trends in Computing and Communication,* vol. 4, no. 4, pp. 448-458.

[59] F. Nadim and D. Bucher, "Neuromodulation of neurons and synapses," *Current opinion in neurobiology,* vol. 29, pp. 48-56, 2014.

[60] R. A. Johnson and F. K. Johnson, "The effects of carbon monoxide as a neurotransmitter," *Current opinion in neurology,* vol. 13, no. 6, pp. 709-713, 2000.

[61] Y. Yan *et al.*, "Electrochemical behavior of amino-modified multi-walled carbon nanotubes coordinated with cobalt porphyrin for the oxidation of nitric oxide," *Applied surface science,* vol. 258, no. 1, pp. 58-63, 2011.

[62] R. Mittal *et al.*, "Neurotransmitters: The critical modulators regulating gut–brain axis," *Journal of cellular physiology,* vol. 232, no. 9, pp. 2359-2372, 2017.

[63] S. E. Hyman, "Neurotransmitters," *Current biology,* vol. 15, no. 5, pp. R154-R158, 2005.

[64] S. K. Ogawa, J. Y. Cohen, D. Hwang, N. Uchida, and M. Watabe-Uchida, "Organization of monosynaptic inputs to the serotonin and dopamine neuromodulatory systems," *Cell reports,* vol. 8, no. 4, pp. 1105-1118, 2014.

[65] A. Brown and S. Gershon, "Dopamine and depression," *Journal of Neural Transmission/General Section JNT,* vol. 91, no. 2, pp. 75-109, 1993.

[66] E. H. Cook Jr *et al.*, "Association of attention-deficit disorder and the dopamine transporter gene," *American journal of human genetics,* vol. 56, no. 4, p. 993, 1995.

[67] K. L. Davis, R. S. Kahn, G. Ko, and M. Davidson, "Dopamine in schizophrenia: a review and reconceptualization," *The American journal of psychiatry,* 1991.

[68] J. Lotharius and P. Brundin, "Pathogenesis of Parkinson's disease: dopamine, vesicles and α-synuclein," *Nature reviews neuroscience,* vol. 3, no. 12, pp. 932-942, 2002.

[69] J. A. Bourgeois, J. S. Seaman, and M. E. Servis, "Delirium, Dementia, and Amnestic Disorders," 2003.

[70] S. C. Daubner, T. Le, and S. Wang, "Tyrosine hydroxylase and regulation of dopamine synthesis," *Archives of biochemistry and biophysics,* vol. 508, no. 1, pp. 1-12, 2011.

[71] R. Katzenschlager and A. J. Lees, "Treatment of Parkinson's disease: levodopa as the first choice," *Journal of neurology,* vol. 249, no. 2, pp. ii19-ii24, 2002.

[72] C. W. Olanow, "Levodopa: effect on cell death and the natural history of Parkinson's disease," *Movement Disorders,* vol. 30, no. 1, pp. 37-44, 2015.

[73] X. Zhang, J.-M. Beaulieu, T. D. Sotnikova, R. R. Gainetdinov, and M. G. Caron, "Tryptophan hydroxylase-2 controls brain serotonin synthesis," *Science,* vol. 305, no. 5681, pp. 217-217, 2004.

[74] J. E. Blundell and J. C. Halford, "Serotonin and appetite regulation," *CNS drugs,* vol. 9, no. 6, pp. 473-495, 1998.

[75] J. M. W. Bradford, "The treatment of sexual deviation using a pharmacological approach," *Journal of Sex Research,* vol. 37, no. 3, pp. 248-257, 2000.

[76] S. Hatta *et al.*, "Effects of Selective Serotonin Reuptake Inhibitors (SSRIs) therapy on the female sexual response cycle of women with major depression," *La Clinica Terapeutica,* vol. 164, no. 1, pp. 11-15, 2013.

[77] W. K. Goodman *et al.,* "Specificity of serotonin reuptake inhibitors in the treatment of obsessive-compulsive disorder: comparison of fluvoxamine and desipramine," *Archives of General Psychiatry,* vol. 47, no. 6, pp. 577-585, 1990.

[78] N. Kaludercic *et al.*, "Monoamine oxidase A–Mediated enhanced catabolism of norepinephrine contributes to adverse remodeling and pump failure in hearts with pressure overload," *Circulation research,* vol. 106, no. 1, pp. 193-202, 2010.

[79] P. D. Skosnik, R. T. Chatterton Jr, T. Swisher, and S. Park, "Modulation of attentional inhibition by norepinephrine and cortisol after psychological stress," *International Journal of Psychophysiology,* vol. 36, no. 1, pp. 59-68, 2000.

[80] C. Ziegler *et al.*, "monoamine oxidase a gene methylation and its role in posttraumatic stress disorder: first evidence from the South Eastern Europe (SEE)-PTSD Study," *International Journal of Neuropsychopharmacology,* vol. 21, no. 5, pp. 423-432, 2018.

[81] M. A. Schiele, C. Thiel, J. Deckert, M. Zaudig, G. Berberich, and K. Domschke, "Monoamine Oxidase A hypomethylation in obsessive-compulsive disorder: reversibility by successful psychotherapy?," *International Journal of Neuropsychopharmacology,* vol. 23, no. 5, pp. 319-323, 2020.

[82] J. D. Fernstrom and M. H. Fernstrom, "Tyrosine, phenylalanine, and catecholamine synthesis and function in the brain," *The Journal of nutrition,* vol. 137, no. 6, pp. 1539S-1547S, 2007.

[83] N. G. Mphuthi, A. S. Adekunle, and E. E. Ebenso, "Electrocatalytic oxidation of Epinephrine and Norepinephrine at metal oxide doped phthalocyanine/MWCNT composite sensor," *Sci Rep,* vol. 6, p. 26938, Jun 1 2016.

[84] B. Levy *et al.*, "Epinephrine versus norepinephrine for cardiogenic shock after acute myocardial infarction," *Journal of the American College of Cardiology,* vol. 72, no. 2, pp. 173-182, 2018.

[85] A. Babaei and A. R. Taheri, "Nafion/Ni (OH) 2 nanoparticles-carbon nanotube composite modified glassy carbon electrode as a sensor for simultaneous determination

of dopamine and serotonin in the presence of ascorbic acid," *Sensors and Actuators B: Chemical,* vol. 176, pp. 543-551, 2013.

[86] P. Ganesh and B. K. Swamy, "Simultaneous electroanalysis of norepinephrine, ascorbic acid and uric acid using poly (glutamic acid) modified carbon paste electrode," *Journal of Electroanalytical Chemistry,* vol. 752, pp. 17-24, 2015.

[87] T. Peik-See, A. Pandikumar, H. Nay-Ming, L. Hong-Ngee, and Y. Sulaiman, "Simultaneous electrochemical detection of dopamine and ascorbic acid using an iron oxide/reduced graphene oxide modified glassy carbon electrode," *Sensors,* vol. 14, no. 8, pp. 15227-15243, 2014.

[88] S. S. Shankar and B. K. Swamy, "Detection of epinephrine in presence of serotonin and ascorbic acid by TTAB modified carbon paste electrode: a voltammetric study," *Int J Electrochem Sci,* vol. 9, no. 3, pp. 1321-1339, 2014.

[89] Z.-N. Huang *et al.*, "A novel electrochemical sensor based on self-assembled platinum nanochains-multi-walled carbon nanotubes-graphene nanoparticles composite for simultaneous determination of dopamine and ascorbic acid," *Ecotoxicology and environmental safety,* vol. 172, pp. 167-175, 2019.

[90] B. Álvarez-Lario and J. Macarrón-Vicente, "Uric acid and evolution," *Rheumatology,* vol. 49, no. 11, pp. 2010-2015, 2010.

[91] B. Alvarez-Lario and J. Macarron-Vicente, "Is there anything good in uric acid?," *QJM: An International Journal of Medicine,* vol. 104, no. 12, pp. 1015-1024, 2011.

[92] B. Patella *et al.*, "Electrochemical detection of dopamine with negligible interference from ascorbic and uric acid by means of reduced graphene oxide and metals-NPs based electrodes," *Analytica Chimica Acta,* vol. 1187, p. 339124, 2021.

[93] T.-Q. Xu *et al.*, "Simultaneous determination of dopamine and uric acid in the presence of ascorbic acid using Pt nanoparticles supported on reduced graphene oxide," *Electrochimica Acta,* vol. 115, pp. 109-115, 2014.

[94] S. Jahani and H. Beitollahi, "Selective detection of dopamine in the presence of uric acid using NiO nanoparticles decorated on graphene nanosheets modified screen-printed electrodes," *Electroanalysis,* vol. 28, no. 9, pp. 2022-2028, 2016.

[95] S. Immanuel, T. Aparna, and R. Sivasubramanian, "A facile preparation of Au—SiO2 nanocomposite for simultaneous electrochemical detection of dopamine and uric acid," *Surfaces and Interfaces,* vol. 14, pp. 82-91, 2019.

[96] A. Arroquia, I. Acosta, and M. P. G. Armada, "Self-assembled gold decorated polydopamine nanospheres as electrochemical sensor for simultaneous determination of ascorbic acid, dopamine, uric acid and tryptophan," *Materials Science and Engineering: C,* vol. 109, p. 110602, 2020.

[97] Y. H. Chang, P. M. Woi, and Y. Alias, "The selective electrochemical detection of dopamine in the presence of ascorbic acid and uric acid using electro-polymerised-β-cyclodextrin incorporated f-MWCNTs/polyaniline modified glassy carbon electrode," *Microchemical Journal,* vol. 148, pp. 322-330, 2019.

[98] K. Ghanbari and A. Hajian, "Electrochemical characterization of Au/ZnO/PPy/RGO nanocomposite and its application for simultaneous determination of ascorbic acid, epinephrine, and uric acid," *Journal of Electroanalytical Chemistry,* vol. 801, pp. 466-479, 2017.

[99] P.-S. Hung, G.-R. Wang, W.-A. Chung, T.-T. Chiang, and P.-W. Wu, "Green synthesis of ni@ PEDOT and ni@ PEDOT/au (Core@ shell) inverse opals for simultaneous detection of ascorbic acid, dopamine, and uric acid," *Nanomaterials,* vol. 10, no. 9, p. 1722, 2020.

[100] F. Scholz, *Electroanalytical methods*. Springer, 2010.

[101] L. Dias, S. G. Meirinho, A. C. Veloso, L. Rodrigues, and A. M. Peres, "Electronic tongues and aptasensors," in *Bioinspired Materials for Medical Applications*: Elsevier, 2017, pp. 371-402.

[102] V. Vinoth, L. N. Natarajan, R. V. Mangalaraja, H. Valdes, and S. Anandan, "Simultaneous electrochemical determination of dopamine and epinephrine using gold nanocrystals capped with graphene quantum dots in a silica network," *Mikrochim Acta,* vol. 186, no. 10, p. 681, Sep 13 2019.

[103] L. Ruiyi, Q. Sili, L. Zhangyi, L. Ling, and L. Zaijun, "Histidine-functionalized graphene quantum dot-graphene micro-aerogel based voltammetric sensing of dopamine," *Sensors and Actuators B: Chemical,* vol. 250, pp. 372-382, 2017.

[104] D. Thomas, Z. Rasheed, J. S. Jagan, and K. G. Kumar, "Study of kinetic parameters and development of a voltammetric sensor for the determination of butylated hydroxyanisole (BHA) in oil samples," *Journal of food science and technology,* vol. 52, no. 10, pp. 6719-6726, 2015.

[105] F. G. Thomas and G. Henze, *Introduction to voltammetric analysis: theory and practice*. Csiro Publishing, 2001.

[106] N. Elgrishi, K. J. Rountree, B. D. McCarthy, E. S. Rountree, T. T. Eisenhart, and J. L. Dempsey, "A practical beginner's guide to cyclic voltammetry," *Journal of chemical education,* vol. 95, no. 2, pp. 197-206, 2018.

[107] N. G. Mphuthi, A. S. Adekunle, O. E. Fayemi, L. O. Olasunkanmi, and E. E. Ebenso, "Phthalocyanine doped metal oxide nanoparticles on multiwalled carbon nanotubes platform for the detection of dopamine," *Scientific reports,* vol. 7, no. 1, pp. 1-23, 2017.

[108] X. Zhuang, H. Wang, T. He, and L. Chen, "Enhanced voltammetric determination of dopamine using a glassy carbon electrode modified with ionic liquid-functionalized graphene and carbon dots," *Microchimica Acta,* vol. 183, no. 12, pp. 3177-3182, 2016.

[109] Q. Huang *et al.*, "Carbon dots and chitosan composite film based biosensor for the sensitive and selective determination of dopamine," *Analyst*, vol. 138, no. 18, pp. 5417-23, Sep 21 2013.

[110] B. Au, K. Chan, W. Pang, C. Lee, S. Wong, and A. Mustafa, "Effect of bias voltage on the electrochromic properties of WO3 films," in *Journal of Physics: Conference Series*, 2019, vol. 1349, no. 1, p. 012040: IOP Publishing.

[111] L. R. Faulkner, "Understanding electrochemistry: Some distinctive concepts," ed: ACS Publications, 1983.

[112] G. Baca and A. L. Dennis, "Electrochemistry in a nutshell A general chemistry experiment," *Journal of Chemical Education,* vol. 55, no. 12, p. 804, 1978.

[113] G. A. Mabbott, "An introduction to cyclic voltammetry," *Journal of Chemical education,* vol. 60, no. 9, p. 697, 1983.

[114] V. Mirceski, S. Skrzypek, and L. Stojanov, "Square-wave voltammetry," *ChemTexts,* vol. 4, no. 4, pp. 1-14, 2018.

[115] N. R. Devi, T. H. V. Kumar, and A. K. Sundramoorthy, "Electrochemically Exfoliated Carbon Quantum Dots Modified Electrodes for Detection of Dopamine Neurotransmitter," *Journal of The Electrochemical Society,* vol. 165, no. 12, pp. G3112-G3119, 2018.

[116] Q. Huang *et al.*, "A sensitive and reliable dopamine biosensor was developed based on the Au@carbon dots-chitosan composite film," *Biosens Bioelectron,* vol. 52, pp. 277-80, Feb 15 2014.

[117] H.-S. Jang, D. Kim, C. Lee, B. Yan, X. Qin, and Y. Piao, "Nafion coated Au nanoparticle-graphene quantum dot nanocomposite modified working electrode for voltammetric determination of dopamine," *Inorganic Chemistry Communications,* vol. 105, pp. 174-181, 2019.

[118] E. Laviron, "General expression of the linear potential sweep voltammogram in the case of diffusionless electrochemical systems," *Journal of Electroanalytical Chemistry and Interfacial Electrochemistry,* vol. 101, no. 1, pp. 19-28, 1979.

[119] J. Hanlan, "Principles of Instrumental Analysis," ed: JSTOR, 1973.

[120] L. R. Faulkner and J. Bard, "Fundamentals and Applications," *Electrochem. Methods,* vol. 2, pp. 580-632, 2001.

[121] F. Simões and M. Xavier, "Nanoscience and its Applications," ed: Elsevier BV Amsterdam, The Netherlands:, 2017.

[122] M. Geszke-Moritz and M. Moritz, "Quantum dots as versatile probes in medical sciences: synthesis, modification and properties," *Mater Sci Eng C Mater Biol Appl,* vol. 33, no. 3, pp. 1008-21, Apr 1 2013.

[123] W. Tisdale and X.-Y. Zhu, "Artificial atoms on semiconductor surfaces," *Proceedings of the National Academy of Sciences,* vol. 108, no. 3, pp. 965-970, 2011.

[124] D. R. Larson *et al.*, "Water-soluble quantum dots for multiphoton fluorescence imaging in vivo," *Science,* vol. 300, no. 5624, pp. 1434-1436, 2003.

[125] M. E. Mathew, J. C. Mohan, K. Manzoor, S. Nair, H. Tamura, and R. Jayakumar, "Folate conjugated carboxymethyl chitosan–manganese doped zinc sulphide nanoparticles for targeted drug delivery and imaging of cancer cells," *Carbohydrate polymers,* vol. 80, no. 2, pp. 442-448, 2010.

[126] J.-M. Li *et al.*, "Multifunctional QD-based co-delivery of siRNA and doxorubicin to HeLa cells for reversal of multidrug resistance and real-time tracking," *Biomaterials,* vol. 33, no. 9, pp. 2780-2790, 2012.

[127] J.-M. Shen, W.-J. Tang, X.-L. Zhang, T. Chen, and H.-X. Zhang, "A novel carboxymethyl chitosan-based folate/Fe3O4/CdTe nanoparticle for targeted drug delivery and cell imaging," *Carbohydrate polymers,* vol. 88, no. 1, pp. 239-249, 2012.

[128] R. Comparelli, F. Zezza, M. Striccoli, M. Curri, R. Tommasi, and A. Agostiano, "Improved optical properties of CdS quantum dots by ligand exchange," *Materials Science and Engineering: C,* vol. 23, no. 6-8, pp. 1083-1086, 2003.

[129] K. Sellami and S. Jaziri, "Piezoelectric coupling effect on exciton–phonon scattering rates in CdSe quantum dots embedded in glass matrix," *Materials Science and Engineering: C,* vol. 26, no. 2-3, pp. 555-558, 2006.

[130] M. Algarra, B. Campos, F. Aguiar, J. Rodriguez-Borges, and J. E. da Silva, "Novel β-cyclodextrin modified CdTe quantum dots as fluorescence nanosensor for acetylsalicylic acid and metabolites," *Materials Science and Engineering: C,* vol. 32, no. 4, pp. 799-803, 2012.

[131] B. O. Dabbousi *et al.*, "(CdSe) ZnS core− shell quantum dots: synthesis and characterization of a size series of highly luminescent nanocrystallites," *The Journal of Physical Chemistry B,* vol. 101, no. 46, pp. 9463-9475, 1997.

[132] P. Reiss, S. Carayon, J. Bleuse, and A. Pron, "Low polydispersity core/shell nanocrystals of CdSe/ZnSe and CdSe/ZnSe/ZnS type: preparation and optical studies," *Synthetic Metals,* vol. 139, no. 3, pp. 649-652, 2003.

[133] D. Jiang *et al.*, "Synthesis and luminescence properties of core/shell ZnS: Mn/ZnO nanoparticles," *Nanoscale research letters,* vol. 4, no. 1, pp. 78-83, 2009.

[134] S. Tajik *et al.*, "Carbon and graphene quantum dots: a review on syntheses, characterization, biological and sensing applications for neurotransmitter determination," *RSC Advances,* vol. 10, no. 26, pp. 15406-15429, 2020.

[135] K. Hola *et al.*, "Photoluminescence effects of graphitic core size and surface functional groups in carbon dots: COO− induced red-shift emission," *Carbon,* vol. 70, pp. 279-286, 2014.

[136] S. Paulo, E. Palomares, and E. Martinez-Ferrero, "Graphene and Carbon Quantum Dot-Based Materials in Photovoltaic Devices: From Synthesis to Applications," *Nanomaterials (Basel),* vol. 6, no. 9, Aug 25 2016.

[137] R. Das, R. Bandyopadhyay, and P. Pramanik, "Carbon quantum dots from natural resource: A review," *Materials today chemistry,* vol. 8, pp. 96-109, 2018.

[138] J. Zhou, Z. Sheng, H. Han, M. Zou, and C. Li, "Facile synthesis of fluorescent carbon dots using watermelon peel as a carbon source," *Materials Letters,* vol. 66, no. 1, pp. 222-224, 2012.

[139] Y. Dong *et al.*, "Polyamine-functionalized carbon quantum dots for chemical sensing," *Carbon,* vol. 50, no. 8, pp. 2810-2815, 2012.

[140] C. Wang *et al.*, "A novel nitrogen-doped carbon quantum dots as effective fluorescent probes for detecting dopamine," *Journal of Photochemistry and Photobiology A: Chemistry,* vol. 391, p. 112374, 2020.

[141] Y. Jiang, B. Wang, F. Meng, Y. Cheng, and C. Zhu, "Microwave-assisted preparation of N-doped carbon dots as a biosensor for electrochemical dopamine detection," *J Colloid Interface Sci*, vol. 452, pp. 199-202, Aug 15 2015.

[142] G. Jiang, T. Jiang, H. Zhou, J. Yao, and X. Kong, "Preparation of N-doped carbon quantum dots for highly sensitive detection of dopamine by an electrochemical method," *RSC Advances,* vol. 5, no. 12, pp. 9064-9068, 2015.

[143] N. Vasimalai *et al.*, "Green synthesis of fluorescent carbon dots from spices for in vitro imaging and tumour cell growth inhibition," *Beilstein journal of nanotechnology,* vol. 9, no. 1, pp. 530-544, 2018.

[144] R. Wang, K.-Q. Lu, Z.-R. Tang, and Y.-J. Xu, "Recent progress in carbon quantum dots: synthesis, properties and applications in photocatalysis," *Journal of Materials Chemistry A,* vol. 5, no. 8, pp. 3717-3734, 2017.

[145] M. Gomes, Y. Gomes, A. Lopes-Moriyama, E. de Barros Neto, and C. P. de Souza, "Design of carbon quantum dots via hydrothermal carbonization synthesis from renewable precursors," *Biomass Conversion and Biorefinery,* vol. 9, no. 4, pp. 689-694, 2019.

[146] T. Shen, Q. Wang, Z. Guo, J. Kuang, and W. Cao, "Hydrothermal synthesis of carbon quantum dots using different precursors and their combination with TiO2 for enhanced photocatalytic activity," *Ceramics International,* vol. 44, no. 10, pp. 11828-11834, 2018.

[147] B. C. Martindale, G. A. Hutton, C. A. Caputo, and E. Reisner, "Solar hydrogen production using carbon quantum dots and a molecular nickel catalyst," *Journal of the American Chemical Society,* vol. 137, no. 18, pp. 6018-6025, 2015.

[148] Y.-Q. Zhang *et al.*, "One-pot synthesis of N-doped carbon dots with tunable luminescence properties," *Journal of Materials Chemistry,* vol. 22, no. 33, p. 16714, 2012.

[149] N. R. Pires, C. M. Santos, R. R. Sousa, R. Paula, P. L. Cunha, and J. Feitosa, "Novel and fast microwave-assisted synthesis of carbon quantum dots from raw cashew gum," *Journal of the Brazilian Chemical Society,* vol. 26, no. 6, pp. 1274-1282, 2015.

[150] X. Hu *et al.*, "Green one-step synthesis of carbon quantum dots from orange peel for fluorescent detection of Escherichia coli in milk," *Food Chemistry,* vol. 339, p. 127775, 2021.

[151] L. Cui, X. Ren, J. Wang, and M. Sun, "Synthesis of homogeneous carbon quantum dots by ultrafast dual-beam pulsed laser ablation for bioimaging," *Materials Today Nano,* vol. 12, p. 100091, 2020.

[152] F. Chao-Mujica *et al.*, "Carbon quantum dots by submerged arc discharge in water: Synthesis, characterization, and mechanism of formation," *Journal of Applied Physics,* vol. 129, no. 16, p. 163301, 2021.

[153] M. Li, T. Chen, J. J. Gooding, and J. Liu, "Review of Carbon and Graphene Quantum Dots for Sensing," *ACS Sens,* vol. 4, no. 7, pp. 1732-1748, Jul 26 2019.

[154] Q. Li, Z. Xu, W. Tang, and Y. Wu, "Determination of dopamine with a modified carbon dot electrode," *Analytical Letters,* vol. 48, no. 13, pp. 2040-2050, 2015.

[155] M. Algarra *et al.*, "Enhanced electrochemical response of carbon quantum dot modified electrodes," *Talanta*, vol. 178, pp. 679-685, Feb 1 2018.

[156] J. Chen *et al.*, "Poly(β-cyclodextrin)/carbon quantum dots modified glassy carbon electrode: Preparation, characterization and simultaneous electrochemical determination of dopamine, uric acid and tryptophan," *Sensors and Actuators B: Chemical*, vol. 252, pp. 9-16, 2017.

[157] M. L. Yola and N. Atar, "Development of molecular imprinted sensor including graphitic carbon nitride/N-doped carbon dots composite for novel recognition of epinephrine," *Composites Part B: Engineering*, vol. 175, p. 107113, 2019.

[158] S. S. Shankar, R. M. Shereema, V. Ramachandran, T. V. Sruthi, V. B. S. Kumar, and R. B. Rakhi, "Carbon Quantum Dot-Modified Carbon Paste Electrode-Based Sensor for Selective and Sensitive Determination of Adrenaline," *ACS Omega,* vol. 4, no. 4, pp. 7903-7910, Apr 30 2019.

[159] D. Bharathi *et al.*, "Green and cost effective synthesis of fluorescent carbon quantum dots for dopamine detection," *Journal of Fluorescence,* vol. 28, no. 2, pp. 573-579, 2018.

[160] X. Cao *et al.*, "Yeast powder derived carbon quantum dots for dopamine detection and living cell imaging," *Analytical Methods,* vol. 14, no. 13, pp. 1342-1350, 2022.

[161] P. Pang *et al.*, "Graphene quantum dots and Nafion composite as an ultrasensitive electrochemical sensor for the detection of dopamine," *Analytical Methods,* vol. 8, no. 24, pp. 4912-4918, 2016.

[162] Y. Li, Y. Jiang, T. Mo, H. Zhou, Y. Li, and S. Li, "Highly selective dopamine sensor based on graphene quantum dots self-assembled monolayers modified electrode," *Journal of Electroanalytical Chemistry*, vol. 767, pp. 84-90, 2016.

[163] A. Medvedovici and V. David, "Spectrophotometry| Diode Array," 2019.

[164] Z. Wang, P. K. Nayak, J. A. Caraveo-Frescas, and H. N. Alshareef, "Recent developments in p-Type oxide semiconductor materials and devices," *Advanced Materials*, vol. 28, no. 20, pp. 3831-3892, 2016.

[165] D. C. Look, G. C. Farlow, P. Reunchan, S. Limpijumnong, S. Zhang, and K. Nordlund, "Evidence for native-defect donors in n-type ZnO," *Physical review letters,* vol. 95, no. 22, p. 225502, 2005.

[166] F. Tuomisto, V. Ranki, K. Saarinen, and D. C. Look, "Evidence of the Zn vacancy acting as the dominant acceptor in n-type ZnO," *Physical Review Letters,* vol. 91, no. 20, p. 205502, 2003.

[167] T. H. Tran and V. T. Nguyen, "Copper Oxide Nanomaterials Prepared by Solution Methods, Some Properties, and Potential Applications: A Brief Review," *Int Sch Res Notices,* vol. 2014, p. 856592, 2014.

[168] S. Baluta, A. Lesiak, and J. Cabaj, "Graphene Quantum Dots-based Electrochemical Biosensor for Catecholamine Neurotransmitters Detection," *Electroanalysis,* vol. 30, no. 8, pp. 1781-1790, 2018.

[169] M. L. Yola and N. Atar, "A novel detection approach for serotonin by graphene quantum dots/two-dimensional (2D) hexagonal boron nitride nanosheets with molecularly imprinted polymer," *Applied Surface Science,* vol. 458, pp. 648-655, 2018.

[170] A. Fajardo, D. Tapia, J. Pizarro, R. Segura, and P. Jara, "Determination of norepinephrine using a glassy carbon electrode modified with graphene quantum dots and gold nanoparticles by square wave stripping voltammetry," *Journal of Applied Electrochemistry,* vol. 49, no. 4, pp. 423-432, 2019.
[171] P. Mohammadzadeh Jahani, "Graphene quantum dots/ionic liquid-Modified Carbon Paste Electrode-Based Sensor for Simultaneous voltammetric determination of norepinephrine and acetylcholine," *International Journal of Electrochemical Science,* pp. 947-958, 2020.
[172] S. M. Dizaj, F. Lotfipour, M. Barzegar-Jalali, M. H. Zarrintan, and K. Adibkia, "Antimicrobial activity of the metals and metal oxide nanoparticles," *Mater Sci Eng C Mater Biol Appl,* vol. 44, pp. 278-84, Nov 2014.
[173] S. Pal, Y. K. Tak, and J. M. Song, "Does the antibacterial activity of silver nanoparticles depend on the shape of the nanoparticle? A study of the Gram-negative bacterium Escherichia coli," *Appl Environ Microbiol,* vol. 73, no. 6, pp. 1712-20, Mar 2007.
[174] R. K. Bera, S. M. Mandal, and C. R. Raj, "Antimicrobial activity of fluorescent Ag nanoparticles," *Lett Appl Microbiol,* vol. 58, no. 6, pp. 520-6, Jun 2014.
[175] Z. Allakhverdi *et al.*, "Thymic stromal lymphopoietin is released by human epithelial cells in response to microbes, trauma, or inflammation and potently activates mast cells," *J Exp Med,* vol. 204, no. 2, pp. 253-8, Feb 19 2007.
[176] K. Chetankumar, B. E. K. Swamy, and T. S. S. K. Naik, "A reliable electrochemical sensor for detection of catechol and hydroquinone at MgO/GO modified carbon paste electrode," *Journal of Materials Science: Materials in Electronics,* vol. 31, no. 22, pp. 19728-19740, 2020.
[177] A. S. Adekunle *et al.*, "Potential of cobalt and cobalt oxide nanoparticles as nanocatalyst towards dyes degradation in wastewater," *Nano-Structures & Nano-Objects,* vol. 21, p. 100405, 2020.
[178] S. Lakshmi, R. Renganathan, and S. Fujita, "Study on TiO2-mediated photocatalytic degradation of methylene blue," *Journal of Photochemistry and Photobiology A: Chemistry,* vol. 88, no. 2-3, pp. 163-167, 1995.
[179] E. Baeissa, "Photocatalytic degradation of malachite green dye using Au/NaNbO3 nanoparticles," *Journal of Alloys and Compounds,* vol. 672, pp. 564-570, 2016.
[180] L. A. Chanu, K. J. Singh, and K. N. Devi, "Study on the Photocatalytic Activity of Metal Oxide Nanoparticles towards the Degradation of Some Organic Dyes," *Integrated Ferroelectrics,* vol. 204, no. 1, pp. 90-99, 2020.
[181] M. Ahamed, H. A. Alhadlaq, M. Khan, P. Karuppiah, and N. A. Al-Dhabi, "Synthesis, characterization, and antimicrobial activity of copper oxide nanoparticles," *Journal of Nanomaterials,* vol. 2014, 2014.
[182] R. Prucek *et al.*, "The targeted antibacterial and antifungal properties of magnetic nanocomposite of iron oxide and silver nanoparticles," *Biomaterials,* vol. 32, no. 21, pp. 4704-4713, 2011.
[183] T. Yonezawa, K. Kamoshita, M. Tanaka, and T. Kinoshita, "Easy preparation of stable iron oxide nanoparticles using gelatin as stabilizing molecules," *Japanese journal of applied physics,* vol. 47, no. 2S, p. 1389, 2008.
[184] A. M. El Shafey, "Green synthesis of metal and metal oxide nanoparticles from plant leaf extracts and their applications: A review," *Green Processing and Synthesis,* vol. 9, no. 1, pp. 304-339, 2020.
[185] N. M. Ishak, S. Kamarudin, and S. Timmiati, "Green synthesis of metal and metal oxide nanoparticles via plant extracts: an overview," *Materials Research Express,* vol. 6, no. 11, p. 112004, 2019.

[186] P. Sutradhar, N. Debnath, and M. Saha, "Microwave-assisted rapid synthesis of alumina nanoparticles using tea, coffee and triphala extracts," *Advances in Manufacturing,* vol. 1, no. 4, pp. 357-361, 2013.

[187] P. P. N. V. Kumar, U. Shameem, P. Kollu, R. L. Kalyani, and S. V. N. Pammi, "Green Synthesis of Copper Oxide Nanoparticles Using Aloe vera Leaf Extract and Its Antibacterial Activity Against Fish Bacterial Pathogens," *BioNanoScience,* vol. 5, no. 3, pp. 135-139, 2015.

[188] M. Fernández-García and J. A. Rodriguez, "Metal Oxide Nanoparticles," 2011.

[189] K. Parveen, V. Banse, and L. Ledwani, "Green synthesis of nanoparticles: Their advantages and disadvantages," vol. 1249, p. 020048, 2016.

[190] K. G. Rao, C. Ashok, K. V. Rao, and C. S. Chakra, "Structural properties of MgO nanoparticles: synthesized by co-precipitation technique," *International Journal of Science and Research,* vol. 3, no. 12, pp. 43-46, 2014.

[191] N. Kandpal, N. Sah, R. Loshali, R. Joshi, and J. Prasad, "Co-precipitation method of synthesis and characterization of iron oxide nanoparticles," 2014.

[192] C. Dhand *et al.*, "Methods and strategies for the synthesis of diverse nanoparticles and their applications: a comprehensive overview," *RSC Advances,* vol. 5, no. 127, pp. 105003-105037, 2015.

[193] K. Amikura, T. Kimura, M. Hamada, N. Yokoyama, J. Miyazaki, and Y. Yamada, "Copper oxide particles produced by laser ablation in water," *Applied Surface Science,* vol. 254, no. 21, pp. 6976-6982, 2008.

[194] S. Peulon and D. Lincot, "Mechanistic study of cathodic electrodeposition of zinc oxide and zinc hydroxychloride films from oxygenated aqueous zinc chloride solutions," *Journal of the Electrochemical Society,* vol. 145, no. 3, p. 864, 1998.

[195] K. Arun, A. Batra, A. Krishna, K. Bhat, M. Aggarwal, and P. J. Francis, "Surfactant free hydrothermal synthesis of copper oxide nanoparticles," *Am. J. Mater. Sci,* vol. 5, pp. 36-38, 2015.

[196] C. Karuppiah *et al.*, "A simple hydrothermal synthesis and fabrication of zinc oxide–copper oxide heterostructure for the sensitive determination of nonenzymatic glucose biosensor," *Sensors and Actuators B: Chemical,* vol. 221, pp. 1299-1306, 2015.

[197] M. Divagar, R. Sriramprabha, N. Ponpandian, and C. Viswanathan, "Highly selective and sensitive electrochemical detection of dopamine with hydrothermally prepared β-MnO2 nanostructures," *Materials Science in Semiconductor Processing,* vol. 83, pp. 216-223, 2018.

[198] N. Roy, S. Yasmin, and S. Jeon, "Effective electrochemical detection of dopamine with highly active molybdenum oxide nanoparticles decorated on 2, 6 diaminopyridine/reduced graphene oxide," *Microchemical Journal,* vol. 153, p. 104501, 2020.

[199] O. E. Fayemi, A. S. Adekunle, and E. E. Ebenso, "Metal oxide nanoparticles/multi-walled carbon nanotube nanocomposite modified electrode for the detection of dopamine: comparative electrochemical study," *J. Biosens. Bioelectron,* vol. 6, no. 4, p. 10.4172, 2015.

[200] A. Dehdashti and A. Babaei, "Designing and characterization of a novel sensing platform based on Pt doped NiO/MWCNTs nanocomposite for enhanced electrochemical determination of epinephrine and tramadol simultaneously," *Journal of Electroanalytical Chemistry,* vol. 862, p. 113949, 2020.

[201] M. Mazloum-Ardakani, H. Beitollahi, M. K. Amini, F. Mirkhalaf, and M. Abdollahi-Alibeik, "New strategy for simultaneous and selective voltammetric determination of norepinephrine, acetaminophen and folic acid using ZrO2 nanoparticles-modified

carbon paste electrode," *Sensors and Actuators B: Chemical,* vol. 151, no. 1, pp. 243-249, 2010.

[202] M. Vinay and Y. A. Nayaka, "Iron oxide (Fe2O3) nanoparticles modified carbon paste electrode as an advanced material for electrochemical investigation of paracetamol and dopamine," *Journal of Science: Advanced Materials and Devices,* vol. 4, no. 3, pp. 442-450, 2019.

[203] R. Nurzulaikha *et al.*, "Graphene/SnO2 nanocomposite-modified electrode for electrochemical detection of dopamine," *Sensing and bio-sensing research,* vol. 5, pp. 42-49, 2015.

[204] N. Lavanya *et al.*, "Simultaneous electrochemical determination of epinephrine and uric acid in the presence of ascorbic acid using SnO2/graphene nanocomposite modified glassy carbon electrode," *Sensors and Actuators B: Chemical,* vol. 221, pp. 1412-1422, 2015.

[205] A. Üğe, D. K. Zeybek, and B. Zeybek, "An electrochemical sensor for sensitive detection of dopamine based on MWCNTs/CeO2-PEDOT composite," *Journal of Electroanalytical Chemistry,* vol. 813, pp. 134-142, 2018.

[206] V. Anbumannan, R. R. Kumar, and K. Suresh, "Enhanced electrochemical detection of dopamine by graphene oxide/tungsten trioxide nanocomposite," *Materials Science in Semiconductor Processing,* vol. 127, p. 105696, 2021.

[207] K. J. Samdani, J. S. Samdani, N. H. Kim, and J. H. Lee, "FeMoO4 based, enzyme-free electrochemical biosensor for ultrasensitive detection of norepinephrine," *Biosensors and Bioelectronics,* vol. 81, pp. 445-453, 2016.

[208] E. Marzi Khosrowshahi *et al.*, "Highly Sensitive Carbamazepine Electrochemical Sensor Based on CuO/ZnFe 2 O 4/rGO Nanocomposite: Application in Biological Fluids Analysis," 2021.

[209] T. Aparna and R. Sivasubramanian, "FeTiO3 nanohexagons based electrochemical sensor for the detection of dopamine in presence of uric acid," *Materials Chemistry and Physics,* vol. 233, pp. 319-328, 2019.

[210] Z. Lu *et al.*, "MOF-derived Co3O4/FeCo2O4 incorporated porous biomass carbon: Simultaneous electrochemical determination of dopamine, acetaminophen and xanthine," *Journal of Alloys and Compounds,* vol. 858, p. 157701, 2021.

[211] T. Kokulnathan, T.-J. Wang, E. A. Kumar, N. Duraisamy, and A.-T. Lee, "An electrochemical platform based on yttrium oxide/boron nitride nanocomposite for the detection of dopamine," *Sensors and Actuators B: Chemical,* vol. 349, p. 130787, 2021.

[212] Z. Anajafi *et al.*, "NdFeO3 as a new electrocatalytic material for the electrochemical monitoring of dopamine," *Analytical and bioanalytical chemistry,* vol. 411, no. 29, pp. 7681-7688, 2019.

[213] T. P. Tsele, A. S. Adekunle, O. E. Fayemi, and E. E. Ebenso, "Electrochemical detection of Epinephrine using Polyaniline nanocomposite films doped with TiO 2 and RuO 2 Nanoparticles on Multi-walled Carbon Nanotube," *Electrochimica Acta,* vol. 243, pp. 331-348, 2017.

[214] P. Lei, Y. Zhou, R. Zhu, C. Dong, S. Wu, and S. Shuang, "Facilely synthesized ultrathin Ni6MnO8@ C nanosheets: excellent electrochemical performance and enhanced electrocatalytic epinephrine sensing," *Sensors and Actuators B: Chemical,* vol. 326, p. 128863, 2021.

[215] S. Biswas, H. Naskar, S. Pradhan, Y. Wang, R. Bandyopadhyay, and P. Pramanik, "Simultaneous voltammetric determination of Adrenaline and Tyrosine in real samples by neodymium oxide nanoparticles grafted graphene," *Talanta,* vol. 206, p. 120176, 2020.

[216] S. Priyanka and K. Latha, "MnCr2O4 nanocomposite modified carbon paste electrode based electrochemical sensor for determination of Norepinephrine: A cyclic voltammetry study," *Chemical Data Collections,* vol. 35, p. 100769, 2021.

[217] S. Sundar, G. Venkatachalam, and S. J. Kwon, "Biosynthesis of Copper Oxide (CuO) Nanowires and Their Use for the Electrochemical Sensing of Dopamine," *Nanomaterials (Basel),* vol. 8, no. 10, Oct 12 2018.

[218] S. R. K. Kumar, G. P. Mamatha, H. B. Muralidhara, K. Y. Kumar, and M. K. Prashanth, "Electrochemical studies of dopamine using titanium dioxide nanoparticle modified carbon paste electrode," *Anal. Bioanal. Electrochem,* vol. 7, p. 175, 2015.

[219] D. Balram, "A Novel Electrochemical Sensor Based on Flower Shaped Zinc Oxide Nanoparticles for the Efficient Detection of Dopamine," *International Journal of Electrochemical Science,* pp. 1542-1555, 2018.

[220] N. Verma and N. Kumar, "Synthesis and Biomedical Applications of Copper Oxide Nanoparticles: An Expanding Horizon," *ACS Biomater Sci Eng,* vol. 5, no. 3, pp. 1170-1188, Mar 11 2019.

[221] J. Singh, G. Kaur, and M. Rawat, "A brief review on synthesis and characterization of copper oxide nanoparticles and its applications," *J. Bioelectron. Nanotechnol,* vol. 1, no. 9, 2016.

[222] M. Ahamed, H. A. Alhadlaq, M. A. M. Khan, P. Karuppiah, and N. A. Al-Dhabi, "Synthesis, Characterization, and Antimicrobial Activity of Copper Oxide Nanoparticles," *Journal of Nanomaterials,* vol. 2014, pp. 1-4, 2014.

[223] S. Jadhav, S. Gaikwad, M. Nimse, and A. Rajbhoj, "Copper Oxide Nanoparticles: Synthesis, Characterization and Their Antibacterial Activity," *Journal of Cluster Science,* vol. 22, no. 2, pp. 121-129, 2011.

[224] S. Pourbeyram, J. Abdollahpour, and M. Soltanpour, "Green synthesis of copper oxide nanoparticles decorated reduced graphene oxide for high sensitive detection of glucose," *Mater Sci Eng C Mater Biol Appl,* vol. 94, pp. 850-857, Jan 1 2019.

[225] H. Beitollai, F. Garkani Nejad, S. Tajik, S. Jahani, and P. Biparva, "Voltammetric determination of amitriptyline based on graphite screen printed electrode modified with a Copper Oxide nanoparticles," *International Journal of Nano Dimension,* vol. 8, no. 3, pp. 197-205, 2017.

[226] E. Bahrami, R. Amini, and S. Vardak, "Electrochemical detection of dopamine via pencil graphite electrodes modified by Cu/CuxO nanoparticles," *Journal of Alloys and Compounds,* vol. 855, p. 157292, 2021.

[227] R. Shashanka and B. E. Kumara Swamy, "Simultaneous electro-generation and electro-deposition of copper oxide nanoparticles on glassy carbon electrode and its sensor application," *SN Applied Sciences,* vol. 2, no. 5, 2020.

[228] H. Maaoui *et al.*, "Non-Enzymatic Glucose Sensing Using Carbon Quantum Dots Decorated with Copper Oxide Nanoparticles," *Sensors (Basel),* vol. 16, no. 10, Oct 18 2016.

[229] H. Razmi, H. Nasiri, and R. Mohammad-Rezaei, "Amperometric determination of L-tyrosine by an enzymeless sensor based on a carbon ceramic electrode modified with copper oxide nanoparticles," *Microchimica Acta,* vol. 173, no. 1-2, pp. 59-64, 2010.

[230] Q.-u.-a. Baloach *et al.*, "An amperometric sensitive dopamine biosensor based on novel copper oxide nanostructures," *Microsystem Technologies,* vol. 23, no. 5, pp. 1229-1235, 2016.

[231] S. Yang, G. Li, Y. Yin, R. Yang, J. Li, and L. Qu, "Nano-sized copper oxide/multi-wall carbon nanotube/Nafion modified electrode for sensitive detection of dopamine," *Journal of Electroanalytical Chemistry,* vol. 703, pp. 45-51, 2013.

[232] S. R. Kiran Kumar *et al.*, "Highly efficient multipurpose graphene oxide embedded with copper oxide nanohybrid for electrochemical sensors and biomedical applications," *Journal of Science: Advanced Materials and Devices,* vol. 2, no. 4, pp. 493-500, 2017.

[233] Y.-Y. Li, P. Kang, S.-Q. Wang, Z.-G. Liu, Y.-X. Li, and Z. Guo, "Ag nanoparticles anchored onto porous CuO nanobelts for the ultrasensitive electrochemical detection of dopamine in human serum," *Sensors and Actuators B: Chemical,* vol. 327, p. 128878, 2021.

[234] K. Ghanbari and N. Hajheidari, "ZnO-CuxO/polypyrrole nanocomposite modified electrode for simultaneous determination of ascorbic acid, dopamine, and uric acid," *Anal Biochem,* vol. 473, pp. 53-62, Mar 15 2015.

[235] Y. Huang, Y. Tan, C. Feng, S. Wang, H. Wu, and G. Zhang, "Synthesis of CuO/g-C3N4 composites, and their application to voltammetric sensing of glucose and dopamine," *Mikrochim Acta,* vol. 186, no. 1, p. 10, Dec 10 2018.

[236] J. Zou *et al.*, "An ultra-sensitive electrochemical sensor based on 2D g-C3N4/CuO nanocomposites for dopamine detection," *Carbon,* vol. 130, pp. 652-663, 2018.

[237] Y. Li *et al.*, "Supportless electrochemical sensor based on molecularly imprinted polymer modified nanoporous microrod for determination of dopamine at trace level," *Biosens Bioelectron,* vol. 78, pp. 308-314, Apr 15 2016.

[238] M. A. Sheikh-Mohseni and S. Pirsa, "Simultaneous determination of dopamine and acetaminophen by a carbon paste electrode doubly modified with poly (pyrrole) and CuO nanoparticles," *Anal. Bioanal. Electrochem,* vol. 8, no. 777, p. e789, 2016.

[239] S. Reddy, B. E. K. Swamy, B. N. Chandrashekar, S. Chitravathi, and H. Jayadevappa, "Cationic surfactants–assisted synthesis of ZnO nanoparticles and their modified carbon paste electrode for electrochemical investigation of dopamine," *Anal. Bioanal. Electrochem,* vol. 4, pp. 186-196, 2012.

[240] B. Demirkan *et al.*, "Palladium supported on polypyrrole/reduced graphene oxide nanoparticles for simultaneous biosensing application of ascorbic acid, dopamine, and uric acid," *Sci Rep,* vol. 10, no. 1, p. 2946, Feb 19 2020.

[241] B. Liu, X. Ouyang, Y. Ding, L. Luo, D. Xu, and Y. Ning, "Electrochemical preparation of nickel and copper oxides-decorated graphene composite for simultaneous determination of dopamine, acetaminophen and tryptophan," *Talanta,* vol. 146, pp. 114-21, 2016.

[242] G. Ashraf, M. Asif, A. Aziz, T. Iftikhar, and H. Liu, "Rice-Spikelet-like Copper Oxide Decorated with Platinum Stranded in the CNT Network for Electrochemical In Vitro Detection of Serotonin," *ACS Appl Mater Interfaces,* vol. 13, no. 5, pp. 6023-6033, Feb 10 2021.

[243] N. Alizadeh, S. Ghasemi, A. Salimi, T.-K. Sham, and R. Hallaj, "CuO nanorods as a laccase mimicking enzyme for highly sensitive colorimetric and electrochemical dual biosensor: Application in living cell epinephrine analysis," *Colloids and Surfaces B: Biointerfaces,* vol. 195, p. 111228, 2020.

[244] U. Sivasankaran and K. Girish Kumar, "A cost effective strategy for dual channel optical sensing of adrenaline based on 'in situ' formation of copper nanoparticles," *Spectrochim Acta A Mol Biomol Spectrosc,* vol. 223, p. 117292, Dec 5 2019.

[245] B. Li *et al.*, "Highly selective and sensitive determination of dopamine by the novel molecularly imprinted poly(nicotinamide)/CuO nanoparticles modified electrode," *Biosens Bioelectron,* vol. 67, pp. 121-8, May 15 2015.

[246] Y. J. Chabal, "Surface infrared spectroscopy," *Surface Science Reports,* vol. 8, no. 5-7, pp. 211-357, 1988.

[247] D. L. Pavia, G. M. Lampman, G. S. Kriz, and J. A. Vyvyan, *Introduction to spectroscopy*. Cengage Learning, 2014.

[248] D. A. Long, "Raman spectroscopy," *New York,* vol. 1, 1977.

[249] J. R. Ferraro, *Introductory raman spectroscopy*. Elsevier, 2003.

[250] E. Smith and G. Dent, *Modern Raman spectroscopy: a practical approach*. John Wiley & Sons, 2019.

[251] T. Inan, "Thermoplastic-based nanoblends: preparation and characterizations," in *Recent Developments in Polymer Macro, Micro and Nano Blends*: Elsevier, 2017, pp. 17-56.

[252] Z. Wang, J. Zhang, X. Wu, and K. Sheng, "Evaluation of reverse recovery characteristic of silicon carbide metal–oxide–semiconductor field-effect transistor intrinsic diode," *IET Power Electronics,* vol. 9, no. 5, pp. 969-976, 2016.

[253] S. K. Sen *et al.*, "X-ray peak profile analysis of pure and Dy-doped α-MoO3 nanobelts using Debye-Scherrer, Williamson-Hall and Halder-Wagner methods," *Advances in Natural Sciences: Nanoscience and Nanotechnology,* vol. 11, no. 2, p. 025004, 2020.

[254] Y. Saito, T. Yoshikawa, S. Bandow, M. Tomita, and T. Hayashi, "Interlayer spacings in carbon nanotubes," *Physical Review B,* vol. 48, no. 3, p. 1907, 1993.

[255] V. Mote, Y. Purushotham, and B. Dole, "Williamson-Hall analysis in estimation of lattice strain in nanometer-sized ZnO particles," *Journal of theoretical and applied physics,* vol. 6, no. 1, pp. 1-8, 2012.

[256] R. Sivakami, S. Dhanuskodi, and R. Karvembu, "Estimation of lattice strain in nanocrystalline RuO2 by Williamson–Hall and size–strain plot methods," *Spectrochimica Acta Part A: Molecular and Biomolecular Spectroscopy,* vol. 152, pp. 43-50, 2016.

[257] J. Abraham, B. Jose, A. Jose, and S. Thomas, "Characterization of green nanoparticles from plants," in *Phytonanotechnology*: Elsevier, 2020, pp. 21-39.

[258] S. S. Kumar, P. Venkateswarlu, V. R. Rao, and G. N. Rao, "Synthesis, characterization and optical properties of zinc oxide nanoparticles," *International Nano Letters,* vol. 3, no. 1, pp. 1-6, 2013.

[259] G. Instruments, "Basics of electrochemical impedance spectroscopy," *G. Instruments, Complex impedance in Corrosion,* pp. 1-30, 2007.

[260] K. K. Reddy, M. Satyanarayana, K. Y. Goud, K. V. Gobi, and H. Kim, "Carbon nanotube ensembled hybrid nanocomposite electrode for direct electrochemical detection of epinephrine in pharmaceutical tablets and urine," *Materials Science and Engineering: C,* vol. 79, pp. 93-99, 2017.

[261] B. Prakashaiah, D. V. Kumara, A. A. Pandith, A. N. Shetty, and B. A. Rani, "Corrosion inhibition of 2024-T3 aluminum alloy in 3.5% NaCl by thiosemicarbazone derivatives," *Corrosion Science,* vol. 136, pp. 326-338, 2018.

[262] D.-P. Burduhos-Nergis, P. Vizureanu, A. V. Sandu, and C. Bejinariu, "Evaluation of the corrosion resistance of phosphate coatings deposited on the surface of the carbon steel used for carabiners manufacturing," *Applied Sciences,* vol. 10, no. 8, p. 2753, 2020.

[263] D. Arenas-Lago, A. Rodríguez-Seijo, L. A. Couce, and F. A. Vega, "A Multianalytical Approach for the Assessment of Toxic Element Distribution in Soils From Mine and Quarry Areas," in *Assessment, Restoration and Reclamation of Mining Influenced Soils*: Elsevier, 2017, pp. 33-62.

[264] T. Kerdcharoen and C. Wongchoosuk, "Carbon nanotube and metal oxide hybrid materials for gas sensing," in *Semiconductor Gas Sensors*: Elsevier, 2013, pp. 386-407.

[265] V. Vaiano, D. Sannino, and O. Sacco, "Heterogeneous photocatalysis: how doping with nitrogen can improve the performance of semiconductor nanoparticles under visible

light irradiation," in *Nanomaterials for the Detection and Removal of Wastewater Pollutants*: Elsevier, 2020, pp. 285-301.

[266] R. Bottom, "Thermogravimetric analysis," *Principles and applications of thermal analysis,* vol. 1, pp. 87-118, 2008.

[267] V. Mortezaeikia, O. Tavakoli, and M. S. Khodaparasti, "A review on kinetic study approach for pyrolysis of plastic wastes using thermogravimetric analysis," *Journal of Analytical and Applied Pyrolysis,* vol. 160, p. 105340, 2021.

[268] P. Gałka, J. Kowalonek, and H. Kaczmarek, "Thermogravimetric analysis of thermal stability of poly (methyl methacrylate) films modified with photoinitiators," *Journal of Thermal Analysis and Calorimetry,* vol. 115, no. 2, pp. 1387-1394, 2014.

[269] J. Rami, C. Patel, C. Patel, and M. Patel, "Thermogravimetric analysis (TGA) of some synthesized metal oxide nanoparticles," *Materials Today: Proceedings,* vol. 43, pp. 655-659, 2021.

[270] K. Y. Hwa and P. Karuppaiah, "Comparative Studies on the Synthesis of Copper Oxide Nano-Structures," in *Materials Science Forum*, 2019, vol. 962, pp. 51-56: Trans Tech Publ.

[271] J. R. Memon, S. Q. Memon, M. Bhanger, G. Z. Memon, A. El-Turki, and G. C. Allen, "Characterization of banana peel by scanning electron microscopy and FT-IR spectroscopy and its use for cadmium removal," *Colloids and surfaces B: Biointerfaces,* vol. 66, no. 2, pp. 260-265, 2008.

[272] D. Manyasree, K. M. Peddi, and R. Ravikumar, "CuO nanoparticles: synthesis, characterization and their bactericidal efficacy," *Int J Appl Pharmaceut,* vol. 9, no. 6, pp. 71-74, 2017.

[273] M. Zhou, Z. Zhou, A. Gong, Y. Zhang, and Q. Li, "Synthesis of highly photoluminescent carbon dots via citric acid and Tris for iron (III) ions sensors and bioimaging," *Talanta,* vol. 143, pp. 107-113, 2015.

[274] D. Kumar, K. Singh, V. Verma, and H. Bhatti, "Synthesis and characterization of carbon quantum dots from orange juice," *Journal of Bionanoscience,* vol. 8, no. 4, pp. 274-279, 2014.

[275] B. De and N. Karak, "A green and facile approach for the synthesis of water soluble fluorescent carbon dots from banana juice," *Rsc Advances,* vol. 3, no. 22, pp. 8286-8290, 2013.

[276] D. Berra, S. Laouini, B. Benhaoua, M. Ouahrani, D. Berrani, and A. Rahal, "Green synthesis of copper oxide nanoparticles by Pheonix dactylifera L leaves extract," *Digest Journal of Nanomaterials and Biostructures,* vol. 13, no. 4, pp. 1231-1238, 2018.

[277] S. Sukumar, A. Rudrasenan, and D. Padmanabhan Nambiar, "Green-synthesized rice-shaped copper oxide nanoparticles using Caesalpinia bonducella seed extract and their applications," *ACS omega,* vol. 5, no. 2, pp. 1040-1051, 2020.

[278] A. A. Badawy, N. A. Abdelfattah, S. S. Salem, M. F. Awad, and A. Fouda, "Efficacy assessment of biosynthesized copper oxide nanoparticles (CuO-NPs) on stored grain insects and their impacts on morphological and physiological traits of wheat (Triticum aestivum L.) plant," *Biology,* vol. 10, no. 3, p. 233, 2021.

[279] A. E. D. Mahmoud, K. M. Al-Qahtani, S. O. Alflaij, S. F. Al-Qahtani, and F. A. Alsamhan, "Green copper oxide nanoparticles for lead, nickel, and cadmium removal from contaminated water," *Scientific Reports,* vol. 11, no. 1, pp. 1-13, 2021.

[280] S. S. Jones, P. Sahatiya, and S. Badhulika, "One step, high yield synthesis of amphiphilic carbon quantum dots derived from chia seeds: a solvatochromic study," *New Journal of Chemistry,* vol. 41, no. 21, pp. 13130-13139, 2017.

[281] M. Saikia, T. Das, and B. K. Saikia, "A novel rapid synthesis of highly stable silver nanoparticle/carbon quantum dot nanocomposites derived from low-grade coal feedstock," *New Journal of Chemistry,* vol. 46, no. 1, pp. 309-321, 2022.

[282] H. Liang, H. Liu, B. Tian, R. Ma, and Y. Wang, "Carbon quantum Dot@ Silver nanocomposite–based fluorescent imaging of intracellular superoxide anion," *Microchimica Acta,* vol. 187, no. 9, pp. 1-9, 2020.

[283] J. Zhu *et al.*, "In situ growth of copper oxide-graphite carbon nitride nanocomposites with peroxidase-mimicking activity for electrocatalytic and colorimetric detection of hydrogen peroxide," *Carbon,* vol. 129, pp. 29-37, 2018.

[284] K. P. Sapkota, I. Lee, M. Hanif, M. Islam, J. Akter, and J. R. Hahn, "Enhanced visible-light photocatalysis of nanocomposites of copper oxide and single-walled carbon nanotubes for the degradation of methylene blue," *Catalysts,* vol. 10, no. 3, p. 297, 2020.

[285] S. Rai, R. Bhujel, J. Biswas, and B. P. Swain, "Effect of electrolyte on the supercapacitive behaviour of copper oxide/reduced graphene oxide nanocomposite," *Ceramics International,* vol. 45, no. 11, pp. 14136-14145, 2019.

[286] S. Suresh, S. Karthikeyan, and K. Jayamoorthy, "FTIR and multivariate analysis to study the effect of bulk and nano copper oxide on peanut plant leaves," *Journal of Science: Advanced Materials and Devices,* vol. 1, no. 3, pp. 343-350, 2016.

[287] A. Eslami, N. M. Juibari, S. G. Hosseini, and M. Abbasi, "Synthesis and characterization of CuO nanoparticles by the chemical liquid deposition method and investigation of its catalytic effect on the thermal decomposition of ammonium perchlorate," *Central European Journal of Energetic Materials,* vol. 14, no. 1, 2017.

[288] S. Mohan, Y. Singh, D. K. Verma, and S. H. Hasan, "Synthesis of CuO nanoparticles through green route using Citrus limon juice and its application as nanosorbent for Cr (VI) remediation: Process optimization with RSM and ANN-GA based model," *Process Safety and Environmental Protection,* vol. 96, pp. 156-166, 2015.

[289] Y. Wei *et al.*, "Detection of ascorbic acid using green synthesized carbon quantum dots," *Journal of Sensors,* vol. 2019, 2019.

[290] N. A. Alarfaj, M. F. El-Tohamy, and H. F. Oraby, "CA 19-9 pancreatic tumor marker fluorescence immunosensing detection via immobilized carbon quantum dots conjugated gold nanocomposite," *International journal of molecular sciences,* vol. 19, no. 4, p. 1162, 2018.

[291] Y. Zhao *et al.*, "Novel carbon quantum dots from egg yolk oil and their haemostatic effects," *Scientific reports,* vol. 7, no. 1, pp. 1-8, 2017.

[292] S. Anmei, Z. Qingmei, C. Yuye, and W. Yilin, "Preparation of carbon quantum dots from cigarette filters and its application for fluorescence detection of Sudan I," *Analytica Chimica Acta,* vol. 1023, pp. 115-120, 2018.

[293] A. Aboulkas and M. Nadifiyine, "Investigation on pyrolysis of Moroccan oil shale/plastic mixtures by thermogravimetric analysis," *Fuel processing technology,* vol. 89, no. 11, pp. 1000-1006, 2008.

[294] R. Pallasser, B. Minasny, and A. B. McBratney, "Soil carbon determination by thermogravimetrics," *PeerJ,* vol. 1, p. e6, 2013.

[295] N. A. Kumar, H.-J. Choi, Y. R. Shin, D. W. Chang, L. Dai, and J.-B. Baek, "Polyaniline-grafted reduced graphene oxide for efficient electrochemical supercapacitors," *ACS nano,* vol. 6, no. 2, pp. 1715-1723, 2012.

[296] A. D. Jara, G. Woldetinsae, A. Betemariam, and J. Y. Kim, "Mineralogical and petrographic analysis on the flake graphite ore from Saba Boru area in Ethiopia," *International Journal of Mining Science and Technology,* vol. 30, no. 5, pp. 715-721, 2020.

[297] B. Şenel, N. Demir, G. Büyükköroğlu, and M. Yıldız, "Graphene quantum dots: Synthesis, characterization, cell viability, genotoxicity for biomedical applications," *Saudi Pharmaceutical Journal,* vol. 27, no. 6, pp. 846-858, 2019.

[298] N. H. Z. Abidin *et al.*, "The effect of functionalization on rice-husks derived carbon quantum dots properties and cadmium removal," *Journal of Water Process Engineering,* vol. 38, p. 101634, 2020.

[299] H. Shahba and M. Sabet, "Two-step and green synthesis of highly fluorescent carbon quantum dots and carbon nanofibers from pine fruit," *Journal of Fluorescence,* vol. 30, no. 4, pp. 927-938, 2020.

[300] K. Zangeneh Kamali, P. Alagarsamy, N. M. Huang, B. H. Ong, and H. N. Lim, "Hematite nanoparticles-modified electrode based electrochemical sensing platform for dopamine," *The Scientific World Journal,* vol. 2014, 2014.

[301] U. Z. M. Azmi *et al.*, "Aptasensor for the Detection of Mycobacterium tuberculosis in Sputum Utilising CFP10-ESAT6 Protein as a Selective Biomarker," *Nanomaterials,* vol. 11, no. 9, p. 2446, 2021.

[302] P. Devi *et al.*, "Selective electrochemical sensing for arsenite using rGO/Fe3O4 nanocomposites," *Journal of hazardous materials,* vol. 322, pp. 85-94, 2017.

[303] Z. Cai *et al.*, "Morphology–dependent electrochemical sensing properties of iron oxide–graphene oxide nanohybrids for dopamine and uric acid," *Nanomaterials,* vol. 9, no. 6, p. 835, 2019.

[304] V. Velusamy *et al.*, "Novel electrochemical synthesis of copper oxide nanoparticles decorated graphene-β-cyclodextrin composite for trace-level detection of antibiotic drug metronidazole," *Journal of colloid and interface science,* vol. 530, pp. 37-45, 2018.

[305] C. Gu, Q. Wang, L. Zhang, P. Yang, Y. Xie, and J. Fei, "Ultrasensitive non-enzymatic pesticide electrochemical sensor based on HKUST-1-derived copper oxide@ mesoporous carbon composite," *Sensors and Actuators B: Chemical,* vol. 305, p. 127478, 2020.

[306] R. Sainz *et al.*, "Chemically synthesized chevron-like graphene nanoribbons for electrochemical sensors development: determination of epinephrine," *Scientific reports,* vol. 10, no. 1, pp. 1-11, 2020.

[307] T. Łuczak and M. Bełtowska-Brzezinska, "Quantitative determination of biogenic amine at gold in the presence of secondary amine during electrochemical oxidation in physiological solution containing ascorbic and uric acids," *Electrochimica Acta,* vol. 90, pp. 634-640, 2013.

[308] E. Wierzbicka and G. D. Sulka, "Nanoporous spongelike Au–Ag films for electrochemical epinephrine sensing," *Journal of Electroanalytical Chemistry,* vol. 762, pp. 43-50, 2016.

[309] P. Shaikshavali *et al.*, "A simple sonochemical assisted synthesis of nanocomposite (ZnO/MWCNTs) for electrochemical sensing of Epinephrine in human serum and pharmaceutical formulation," *Colloids and Surfaces A: Physicochemical and Engineering Aspects,* vol. 584, p. 124038, 2020.

[310] M. Safaei, H. Beitollahi, and M. R. Shishehbore, "Simultaneous determination of epinephrine and folic acid using the Fe3O4@ SiO2/GR nanocomposite modified graphite," *Russian Journal of Electrochemistry,* vol. 54, no. 11, pp. 851-859, 2018.

[311] Y. Wang and Z.-z. Chen, "A novel poly (taurine) modified glassy carbon electrode for the simultaneous determination of epinephrine and dopamine," *Colloids and surfaces B: biointerfaces,* vol. 74, no. 1, pp. 322-327, 2009.

[312] Y. Lu *et al.*, "MOFs-derived nano-CuO modified electrode as a sensor for determination of hydrazine hydrate in aqueous medium," *Sensors,* vol. 20, no. 1, p. 140, 2019.

[313] Q. He *et al.*, "A promising sensing platform toward dopamine using MnO2 nanowires/electro-reduced graphene oxide composites," *Electrochimica Acta,* vol. 296, pp. 683-692, 2019.

[314] M. Mahmoudian, Y. Alias, W. Basirun, P. M. Woi, and M. Sookhakian, "Facile preparation of MnO2 nanotubes/reduced graphene oxide nanocomposite for electrochemical sensing of hydrogen peroxide," *Sensors and Actuators B: Chemical,* vol. 201, pp. 526-534, 2014.

[315] A. S. Karimullah, D. R. Cumming, M. Riehle, and N. Gadegaard, "Development of a conducting polymer cell impedance sensor," *Sensors and Actuators B: Chemical,* vol. 176, pp. 667-674, 2013.

[316] K. I. Ozoemena, D. Nkosi, and J. Pillay, "Influence of solution pH on the electron transport of the self-assembled nanoarrays of single-walled carbon nanotube-cobalt tetra-aminophthalocyanine on gold electrodes: electrocatalytic detection of epinephrine," *Electrochimica acta,* vol. 53, no. 6, pp. 2844-2851, 2008.

[317] N. Ndebele, P. Sen, and T. Nyokong, "Electrochemical detection of dopamine using phthalocyanine-nitrogen-doped graphene quantum dot conjugates," *Journal of Electroanalytical Chemistry,* vol. 886, p. 115111, 2021.

[318] Y.-H. Fang and Z.-P. Liu, "Tafel kinetics of electrocatalytic reactions: from experiment to first-principles," *ACS Catalysis,* vol. 4, no. 12, pp. 4364-4376, 2014.

[319] H. Beitollahi, Z. Dourandish, S. Tajik, M. R. Ganjali, P. Norouzi, and F. Faridbod, "Application of graphite screen printed electrode modified with dysprosium tungstate nanoparticles in voltammetric determination of epinephrine in the presence of acetylcholine," *Journal of Rare Earths,* vol. 36, no. 7, pp. 750-757, 2018.

[320] L. I. Tomé and C. M. Brett, "Polymer/iron oxide nanoparticle modified glassy carbon electrodes for the enhanced detection of epinephrine," *Electroanalysis,* vol. 31, no. 4, pp. 704-710, 2019.

[321] W. Dong *et al.*, "Synthesis of tetrahexahedral Au-Pd core–shell nanocrystals and reduction of graphene oxide for the electrochemical detection of epinephrine," *Journal of colloid and interface science,* vol. 512, pp. 812-818, 2018.

[322] D. M. Fouad and W. A. El-Said, "Selective electrochemical detection of epinephrine using gold nanoporous film," *Journal of Nanomaterials,* vol. 2016, 2016.

[323] L. V. da Silva *et al.*, "Electropolymerization of ferulic acid on multi-walled carbon nanotubes modified glassy carbon electrode as a versatile platform for NADH, dopamine and epinephrine separate detection," *Microchemical Journal,* vol. 133, pp. 460-467, 2017.

[324] N. G. Mphuthi, A. S. Adekunle, and E. E. Ebenso, "Electrocatalytic oxidation of Epinephrine and Norepinephrine at metal oxide doped phthalocyanine/MWCNT composite sensor," *Scientific reports,* vol. 6, no. 1, pp. 1-20, 2016.

[325] D. L. Robinson, A. Hermans, A. T. Seipel, and R. M. Wightman, "Monitoring rapid chemical communication in the brain," *Chemical reviews,* vol. 108, no. 7, pp. 2554-2584, 2008.

[326] S. Shahrokhian and M. Khafaji, "Application of pyrolytic graphite modified with nano-diamond/graphite film for simultaneous voltammetric determination of epinephrine and uric acid in the presence of ascorbic acid," *Electrochimica Acta,* vol. 55, no. 28, pp. 9090-9096, 2010.

[327] T. Joseph, T. Thomas, and N. Thomas, "Graphene Oxide Modified Carbon Paste Electrode for Handy and Ultra-sensitive Determination of Epinephrine in the Presence of Uric and Ascorbic Acids," *Electroanalysis,* vol. 32, no. 11, pp. 2463-2473, 2020.

[328] I. G. Casella, D. Gioia, and M. Rutilo, "A multi-walled carbon nanotubes/cellulose acetate composite electrode (MWCNT/CA) as sensing probe for the amperometric determination of some catecholamines," *Sensors and Actuators B: Chemical,* vol. 255, pp. 3533-3540, 2018.

[329] R. Bavandpour, H. Karimi-Maleh, M. Asif, V. K. Gupta, N. Atar, and M. Abbasghorbani, "Liquid phase determination of adrenaline uses a voltammetric sensor employing CuFe2O4 nanoparticles and room temperature ionic liquids," *Journal of Molecular Liquids,* vol. 213, pp. 369-373, 2016.

[330] T. Thomas, R. J. Mascarenhas, P. Martis, Z. Mekhalif, and B. K. Swamy, "Multi-walled carbon nanotube modified carbon paste electrode as an electrochemical sensor for the determination of epinephrine in the presence of ascorbic acid and uric acid," *Materials Science and Engineering: C,* vol. 33, no. 6, pp. 3294-3302, 2013.

[331] M. Charithra and J. Manjunatha, "Electrochemical sensing of adrenaline using surface modified carbon nanotube paste electrode," *Materials Chemistry and Physics,* vol. 262, p. 124293, 2021.

[332] R. N. Goyal, M. A. Aziz, M. Oyama, S. Chatterjee, and A. R. S. Rana, "Nanogold based electrochemical sensor for determination of norepinephrine in biological fluids," *Sensors and Actuators B: Chemical,* vol. 153, no. 1, pp. 232-238, 2011.

[333] C. Bian, Q. Zeng, H. Xiong, X. Zhang, and S. Wang, "Electrochemistry of norepinephrine on carbon-coated nickel magnetic nanoparticles modified electrode and analytical applications," *Bioelectrochemistry,* vol. 79, no. 1, pp. 1-5, 2010.

[334] H. Chasta and R. N. Goyal, "Molecularly imprinted sensor based on o-aminophenol for the selective determination of norepinephrine in pharmaceutical and biological samples," *Talanta,* vol. 125, pp. 167-173, 2014.

[335] T. Łuczak, "1, 4-Michael Addition–The Analytical Way for Quantitative Sensing of Neurotransmitter at Bare Gold Electrode in Physiological Solution in the Presence of Interfering Biogenic Compounds," *Electroanalysis,* vol. 25, no. 9, pp. 2067-2074, 2013.

[336] S. Cheemalapati, S. Palanisamy, V. Mani, and S.-M. Chen, "Simultaneous electrochemical determination of dopamine and paracetamol on multiwalled carbon nanotubes/graphene oxide nanocomposite-modified glassy carbon electrode," *Talanta,* vol. 117, pp. 297-304, 2013.

[337] G. Venkataprasad *et al.*, "A facile synthesis of Fe3O4-Gr nanocomposite and its effective use as electrochemical sensor for the determination of dopamine and as anode material in lithium ion batteries," *Sensors and Actuators A: Physical,* vol. 293, pp. 87-100, 2019.

[338] J. Li *et al.*, "Facile surfactant-and template-free synthesis and electrochemical properties of SnO2/graphene composites," *Journal of Alloys and Compounds,* vol. 674, pp. 44-50, 2016.

[339] M. Yu, L. Wu, J. Miao, W. Wei, A. Liu, and S. Liu, "Titanium dioxide and polypyrrole molecularly imprinted polymer nanocomposites based electrochemical sensor for highly selective detection of p-nonylphenol," *Analytica Chimica Acta,* vol. 1080, pp. 84-94, 2019.

[340] J. M. Mohan, K. Amreen, A. Javed, S. K. Dubey, and S. Goel, "Highly selective electrochemical sensing of dopamine, xanthine, ascorbic acid and uric acid using a carbon fiber paper," *IEEE Sensors Journal,* vol. 20, no. 19, pp. 11707-11712, 2020.

[341] M. Mazloum-Ardakani, M. Sheikh-Mohseni, and A. Benvidi, "Electropolymerization of thin film conducting polymer and its application for simultaneous determination of

ascorbic acid, dopamine and uric acid," *Electroanalysis,* vol. 23, no. 12, pp. 2822-2831, 2011.

[342] S. K. Anand, M. R. Mathew, J. Radecki, H. Radecka, and K. G. Kumar, "Individual and simultaneous voltammetric sensing of norepinephrine and tyramine based on poly (L-arginine)/reduced graphene oxide composite film modified glassy carbon electrode," *Journal of Electroanalytical Chemistry,* vol. 878, p. 114531, 2020.

[343] M. Mazloum-Ardakani, H. Beitollahi, M. K. Amini, F. Mirkhalaf, and B.-F. Mirjalili, "A highly sensitive nanostructure-based electrochemical sensor for electrocatalytic determination of norepinephrine in the presence of acetaminophen and tryptophan," *Biosensors and Bioelectronics,* vol. 26, no. 5, pp. 2102-2106, 2011.

[344] M. Mazloum-Ardakani, H. Beitollahi, M. A. Sheikh-Mohseni, H. Naeimi, and N. Taghavinia, "Novel nanostructure electrochemical sensor for electrocatalytic determination of norepinephrine in the presence of high concentrations of acetaminophene and folic acid," *Applied Catalysis A: General,* vol. 378, no. 2, pp. 195-201, 2010.

[345] N. Lavanya and C. Sekar, "Electrochemical sensor for simultaneous determination of epinephrine and norepinephrine based on cetyltrimethylammonium bromide assisted SnO2 nanoparticles," *Journal of Electroanalytical Chemistry,* vol. 801, pp. 503-510, 2017.

[346] S. K. Yadav, B. Agrawal, M. Oyama, and R. N. Goyal, "Graphene modified Palladium sensor for electrochemical analysis of norepinephrine in pharmaceuticals and biological fluids," *Electrochimica Acta,* vol. 125, pp. 622-629, 2014.

[347] C. M. Kuskur, B. Kumara Swamy, H. Jayadevappa, and P. Ganesh, "Poly (rhodamine B) sensor for norepinephrine and paracetamol: a voltammetric study," *Ionics,* vol. 24, no. 11, pp. 3631-3640, 2018.

[348] Z. Wang *et al.*, "A novel sensor made of Antimony Doped Tin Oxide-silica composite sol on a glassy carbon electrode modified by single-walled carbon nanotubes for detection of norepinephrine," *Materials Science and Engineering: C,* vol. 80, pp. 180-186, 2017.

[349] F. M. Morawski *et al.*, "A novel electrochemical platform based on mesoporous silica/titania and gold nanoparticles for simultaneous determination of norepinephrine and dopamine," *Mater Sci Eng C Mater Biol Appl,* vol. 120, p. 111646, Jan 2021.

[350] Y. Wang *et al.*, "A disposable electrochemical sensor for simultaneous determination of norepinephrine and serotonin in rat cerebrospinal fluid based on MWNTs-ZnO/chitosan composites modified screen-printed electrode," *Biosensors and Bioelectronics,* vol. 65, pp. 31-38, 2015.

[351] P. Kalimuthu and S. A. John, "Selective determination of norepinephrine in the presence of ascorbic and uric acids using an ultrathin polymer film modified electrode," *Electrochimica acta,* vol. 56, no. 5, pp. 2428-2432, 2011.

[352] S.-H. Huang, H.-H. Liao, and D.-H. Chen, "Simultaneous determination of norepinephrine, uric acid, and ascorbic acid at a screen printed carbon electrode modified with polyacrylic acid-coated multi-wall carbon nanotubes," *Biosensors and Bioelectronics,* vol. 25, no. 10, pp. 2351-2355, 2010.

[353] I. Gualandi, D. Tonelli, F. Mariani, E. Scavetta, M. Marzocchi, and B. Fraboni, "Selective detection of dopamine with an all PEDOT: PSS organic electrochemical transistor," *Scientific reports,* vol. 6, no. 1, pp. 1-10, 2016.

[354] K. Reddaiah, K. Rao, and T. M. Reddy, "Electrochemical detection of serotonin in human serum sample and simultaneous resolution in presence of epinephrine," *Anal. Bioanal. Electrochem.,* vol. 10, pp. 175-191, 2018.

[355] P. Kanchana, M. Navaneethan, and C. Sekar, "Fabrication of Ce doped hydroxyapatite nanoparticles based non-enzymatic electrochemical sensor for the simultaneous determination of norepinephrine, uric acid and tyrosine," *Materials Science and Engineering: B,* vol. 226, pp. 132-140, 2017.

[356] X. Ma, M. Chen, X. Li, A. Purushothaman, and F. Li, "Electrochemical detection of norepinephrine in the presence of epinephrine, uric acid and ascorbic acid using a graphene-modified electrode," *Int. J. Electrochem. Sci,* vol. 7, no. 2, pp. 991-1000, 2012.

[357] H. T. Vu, C. J. Scarlett, and Q. V. Vuong, "Phenolic compounds within banana peel and their potential uses: A review," *Journal of Functional Foods,* vol. 40, pp. 238-248, 2018.

[358] R. Arcusa *et al.*, "Effects of a Fruit and Vegetable-Based Nutraceutical on Biomarkers of Inflammation and Oxidative Status in the Plasma of a Healthy Population: A Placebo-Controlled, Double-Blind, and Randomized Clinical Trial," *Molecules,* vol. 26, no. 12, p. 3604, 2021.

[359] M. Safaei, H. Beitollahi, and M. R. Shishehbore, "Synthesis and characterization of NiFe2O4 nanoparticles using the hydrothermal method as magnetic catalysts for electrochemical detection of norepinephrine in the presence of folic acid," *Journal of the Chinese Chemical Society,* vol. 66, no. 12, pp. 1597-1603, 2019.

[360] Y. Wang, L. Wang, and Q. Zhuang, "A ratiometric electrochemical sensor for dopamine detection based on hierarchical manganese dioxide nanoflower/multiwalled carbon nanotube nanocomposite modified glassy carbon electrode," *Journal of Alloys and Compounds,* vol. 802, pp. 326-334, 2019.

[361] G. Mathew *et al.*, "Direct electrochemical reduction of hematite decorated graphene oxide (α-Fe2O3@ erGO) nanocomposite for selective detection of Parkinson's disease biomarker," *Biosensors and Bioelectronics,* vol. 115, pp. 53-60, 2018.

[362] F. Ma, B. Yang, Z. Zhang, J. Kong, G. Huang, and Y. Mei, "Self-rolled TiO2 microscroll/graphene composite for electrochemical dopamine sensing," *Progress in Natural Science: Materials International,* vol. 30, no. 3, pp. 337-342, 2020.

[363] R. Ramachandran, X. Leng, C. Zhao, Z.-X. Xu, and F. Wang, "2D siloxene sheets: A novel electrochemical sensor for selective dopamine detection," *Applied materials today,* vol. 18, p. 100477, 2020.

[364] M. Palomar-Pardavé, S. Corona-Avendaño, M. Romero-Romo, G. Alarcón-Angeles, A. Merkoçi, and M. Ramírez-Silva, "Supramolecular interaction of dopamine with β-cyclodextrin: An experimental and theoretical electrochemical study," *Journal of Electroanalytical Chemistry,* vol. 717, pp. 103-109, 2014.

[365] V. Sreenivasulu *et al.*, "Biosynthesis of silver nanoparticles using Mimosa pudica plant root extract: characterization, antibacterial activity and electrochemical detection of dopamine," *Int. J. Electrochem. Sci,* vol. 11, pp. 9959-9971, 2016.

[366] B. Li *et al.*, "Highly selective and sensitive determination of dopamine by the novel molecularly imprinted poly (nicotinamide)/CuO nanoparticles modified electrode," *Biosensors and Bioelectronics,* vol. 67, pp. 121-128, 2015.

[367] S.-J. Li, D.-H. Deng, Q. Shi, and S.-R. Liu, "Electrochemical synthesis of a graphene sheet and gold nanoparticle-based nanocomposite, and its application to amperometric sensing of dopamine," *Microchimica Acta,* vol. 177, no. 3, pp. 325-331, 2012.

[368] O. E. Fayemi, A. S. Adekunle, B. K. Swamy, and E. E. Ebenso, "Electrochemical sensor for the detection of dopamine in real samples using polyaniline/NiO, ZnO, and Fe3O4 nanocomposites on glassy carbon electrode," *Journal of Electroanalytical Chemistry,* vol. 818, pp. 236-249, 2018.

[369] M. K. Kumar, R. Prataap, S. Mohan, and S. K. Jha, "Preparation of electro-reduced graphene oxide supported walnut shape nickel nanostructures, and their application to selective detection of dopamine," *Microchimica Acta,* vol. 183, no. 5, pp. 1759-1768, 2016.

[370] B. K. Swamy *et al.*, "Electrochemical detection of dopamine and tyrosine using metal oxide (MO, M= Cu and Ni) modified graphite electrode: a comparative study," *Biointerface Res. Appl. Chem,* vol. 10, pp. 6460-6473, 2020.

[371] S. Hou, M. L. Kasner, S. Su, K. Patel, and R. Cuellari, "Highly sensitive and selective dopamine biosensor fabricated with silanized graphene," *The Journal of Physical Chemistry C,* vol. 114, no. 35, pp. 14915-14921, 2010.

[372] P. Manivel, M. Dhakshnamoorthy, A. Balamurugan, N. Ponpandian, D. Mangalaraj, and C. Viswanathan, "Conducting polyaniline-graphene oxide fibrous nanocomposites: preparation, characterization and simultaneous electrochemical detection of ascorbic acid, dopamine and uric acid," *Rsc Advances,* vol. 3, no. 34, pp. 14428-14437, 2013.

[373] H. Yu, Y. Pang, and J. Tang, "Polyaniline Nanofiber Modified Platinum Electrode Used to Determination of Dopamine by Square Wave Voltammetry," *Int. J. Electrochem. Sci,* vol. 10, pp. 8353-8360, 2015.

[374] M. Ouellette, J. Mathault, S. D. Niyonambaza, A. Miled, and E. Boisselier, "Electrochemical Detection of Dopamine Based on Functionalized Electrodes," *Coatings,* vol. 9, no. 8, p. 496, 2019.

[375] J. B. Raoof, A. Kiani, R. Ojani, R. Valiollahi, and S. Rashid-Nadimi, "Simultaneous voltammetric determination of ascorbic acid and dopamine at the surface of electrodes modified with self-assembled gold nanoparticle films," *Journal of Solid State Electrochemistry,* vol. 14, no. 7, pp. 1171-1176, 2010.

[376] D. Jia, J. Dai, H. Yuan, L. Lei, and D. Xiao, "Selective detection of dopamine in the presence of uric acid using a gold nanoparticles-poly(luminol) hybrid film and multi-walled carbon nanotubes with incorporated beta-cyclodextrin modified glassy carbon electrode," *Talanta*, vol. 85, no. 5, pp. 2344-51, Oct 15 2011.

[377] L. Zhang, C. Liu, Q. Wang, X. Wang, and S. Wang, "Electrochemical sensor based on an electrode modified with porous graphitic carbon nitride nanosheets (C3N4) embedded in graphene oxide for simultaneous determination of ascorbic acid, dopamine and uric acid," *Microchimica Acta,* vol. 187, no. 2, pp. 1-10, 2020.

[378] J. Shashikumara and B. K. Swamy, "Electrochemical investigation of dopamine in presence of uric acid and ascorbic acid at poly (reactive blue) modified carbon paste electrode: a voltammetric study," *Sensors International,* vol. 1, p. 100008, 2020.

[379] Y. Wang, Y. Huang, B. Wang, T. Fang, J. Chen, and C. Liang, "Three-dimensional porous graphene for simultaneous detection of dopamine and uric acid in the presence of ascorbic acid," *Journal of Electroanalytical Chemistry,* vol. 782, pp. 76-83, 2016.

[380] Q.-j. Gong, H.-x. Han, Y.-d. Wang, C.-z. Yao, H.-y. Yang, and J.-l. Qiao, "An electrochemical sensor for dopamine detection based on the electrode of a poly-tryptophan-functionalized graphene composite," *New Carbon Materials,* vol. 35, no. 1, pp. 34-41, 2020.

[381] L. Yang, T. Wang, C. Bao, M. Shi, X. Huang, and H. Cheng, "A novel graphene quantum dots/choline chloride/gold nanoparticles-modified carbon fiber microelectrode for sensitive and selective determination of dopamine in the presence of a high concentration of ascorbic acid," *Journal of Electroanalytical Chemistry,* vol. 895, p. 115512, 2021.